2013

Atomistic simulations to micro-mechanisms of adhesion in automotive applications

Fatih Gurcag Sen
University of Windsor

ATOMISTIC SIMULATIONS TO MICRO-MECHANISMS OF ADHESION IN AUTOMOTIVE APPLICATIONS

By

Fatih Gurcag Sen

A Dissertation

Submitted to the Faculty of Graduate Studies

through Engineering Materials

in Partial Fulfillment of the Requirements for

the Degree of Doctor of Philosophy at the

University of Windsor

Windsor, Ontario, Canada

2013

Atomistic Simulations to Micro-Mechanisms of Adhesion in Automotive Applications

By

Fatih Gurcag Sen

APPROVED BY:

Marek Niewczas (External Examiner)

Materials Science and Engineering, McMaster University

S. Holger Eichhorn (Outside Department Reader)

Chemistry and Biochemistry

Vesselin Stoilov (Department Reader)

Mechanical, Automotive and Materials Engineering

A. Reza Riahi (Department Reader)

Mechanical, Automotive and Materials Engineering

Ahmet T. Alpas (Advisor)

Mechanical, Automotive and Materials Engineering

Yue Qi (Co-advisor)

General Motors Research and Development Center

Hans V. Hansen, (Chair of Defense)

Philosophy

13 May 2013

Declaration of Co-authorship / Previous Publication

Co-Authorship Declaration

I hereby declare that this thesis incorporates documentation of research performed by the author under the supervision of Prof. Ahmet T. Alpas and Dr. Yue Qi. The collection of electron images and diffraction patterns using transmission electron microscope was performed jointly by Dr. Xianying Meng-Burany (University of Windsor) and the interpretation of these images were carried out by the author himself. The ReaxFF force-field used in Chapters 5 and 6 were supplied by Prof. Adri C.T. van Duin (Pennsylvania State University). The vacuum tribological experiments were carried out under the guidance of Dr. Michael Lukitsch (General Motors R&D).

I am aware of the University of Windsor Senate Policy on Authorship and I certify that I have properly acknowledged the contribution of other researchers to my thesis, and have obtained written permission from each of the co-author(s) to include the above material(s) in my thesis.

I certify that, with the above qualification, this thesis, and the research to which it refers, is the product of my own work.

Declaration of Previous Publication

This thesis includes material from five original peer reviewed journal articles that have already been published and one more journal articles to be submitted for publication in peer reviewed journals.

Thesis chapter	Publication title and citation information	Publication status
Chapter 2	F.G. Sen, Y. Qi, A.T. Alpas, "Surface stability and electronic structure of hydrogen and fluorine terminated diamond surfaces: a first principles investigation", *Journal of Materials Research* 24, (2009) 2461-2470.	Published
Chapter 3	F.G. Sen, Y. Qi, A.T. Alpas, "Material transfer mechanisms between aluminum and fluorinated carbon interfaces", *Acta Materialia*, 59 (2011) 2601-2614.	Published
Chapter 4	F.G. Sen, X. Meng-Burany, M. Lukitsch, Y. Qi, A.T. Alpas, "Low friction and environmentally stable diamond-like carbon (DLC) coatings incorporating Si and F sliding against aluminum", *Surface and Coatings Technology*, 215 (2013) 340-349.	Published
Chapter 5	F.G. Sen, Y. Qi, A.C.T. van Duin, A.T. Alpas, "Oxidation induced softening in Al nanowires", *Applied Physics Letters*, 102 (2013) 051912.	Published
Chapter 6	F.G. Sen, Y. Qi, A.C.T. van Duin, A.T. Alpas, "Plastic deformation of Al in O_2 environment"	To be submitted
Chapter 7	F.G. Sen, Y. Qi, A.T. Alpas, "Anchoring Pt on graphene using metallic adatoms: A first principles investigation", *Journal of Physics Condensed Matter* 24 (2012) 225003.	Published

I certify that I have obtained a written permission from the copyright owner(s) to include the published material(s) in my thesis. I certify that the above material describes work completed during my registration as graduate student at the University of Windsor. I declare that, to the best of my knowledge, my thesis does not infringe upon anyone's copyright nor violate any proprietary rights and that any ideas, techniques, quotations, or any other material from the work of other people included in my thesis, published or otherwise, are

iv

fully acknowledged in accordance with the standard referencing practices. Furthermore, to the extent that I have included copyrighted material that surpasses the bounds of fair dealing within the meaning of the Canada Copyright Act, I certify that I have obtained a written permission from the copyright owner(s) to include such material(s) in my thesis.

I declare that this is a true copy of my thesis, including any final revisions, as approved by my thesis committee and the Graduate Studies office of University of Windsor, and that this thesis has not been submitted for a higher degree to any other University or Institution.

Abstract

This study aimed at depicting atomistic and microstructural aspects of adhesion and friction that appear in different automotive applications and manufacturing processes using atomistic simulations coupled with tribological tests and surface characterization experiments. Thin films that form at the contact interfaces due to chemical reactions and coatings that are developed to mitigate or enhance adhesion were studied in detail.

The adhesion and friction experiments conducted on diamond-like carbon (DLC) coatings against Al indicated that F incorporation into DLC decreased the coefficient of friction (COF) by 30% -with respect to H-DLC that is known to have low COF and anti-adhesion properties against Al- to 0.14 owing to formation of repulsive F-F interactions at the sliding interface as shown by density functional theory (DFT) calculations. F atoms transferred to the Al surface with an increase in the contact pressure, and this F transfer led to the formation of a stable AlF_3 compound at the Al surface as confirmed by XPS and cross-sectional FIB-TEM. The incorporation of Si and O in a F-containing DLC resulted in humidity independent low COF of 0.08 due to the hydration effect of the Si–O–Si chains in the carbonaceous tribolayers that resulted in repulsive OH-OH interactions at the contact interface.

At high temperatures, adhesion of Al was found to be enhanced as a result of superplastic oxide fibers on the Al surface. Molecular dynamics (MD) simulations of tensile deformation of Al nanowires in oxygen carried out with ReaxFF showed that native oxide of Al has an oxygen deficient, low density structure and in O_2, the oxygen diffusion in amorphous oxide healed the broken Al-O bonds during applied strain and resulted in the superplasticity. The oxide shell also provided nucleation sites for dislocations in Al crystal.

In fuel cell applications, where low Pt/carbon adhesion is causing durability problems, spin-polarized DFT showed that metals with unfilled d orbitals increase the Pt/graphene interface strength from 0.009 J/m^2 to above 0.5 J/m^2 . Ir, Os, Ru, Rh and Re were the most effective modifiers, as they distributed their electronic charges evenly between Pt and graphene surfaces.

To my mother, father and sister

Acknowledgements

Foremost, I would like to express my sincere gratitude to my adisor Dr. Ahmet T. Alpas for his continuous support, guidance, motivation, and enthusisasm throughout my Ph.D study. He always inspired me to go for the extra mile for doing good research and writing good papers. I would like to express my deepest gratitude to my industrial co-advisor Dr. Yue Qi for her continuous advice, encourgement, enthusiasm, motivation and mentorship throughout the course of this dissertation. She always encouraged me and gave confidence to be a good scientist rather than an ordinary student with her visions and insights. Without their guidance and persistent help, this dissertation would not have been possible.

I would like to thank my thesis committee: Dr. Reza Riahi, Dr. Vesselin Stoilov, Dr. Holger Eichhorn and Dr. Marek Niewcsaz for their insightful comments, and suggestions.

Financial support from Natural Sciences and Engineering Research Council of Canada (NSERC) and General Motors of Canada, and SHARCNET (Shared Hierarchical Academic Research Computing Network)/Compute Canada, where all the computations in this dissertations were carried out are greatly acknowledged.

I would like to thank Mark Biesinger from Surface Science group at the University of Western Ontario for his invaluable help in XPS analysis. The asssitance in the ERD and RBS analyses of coatings from Michigan Ion Beam Laboratory are greatly acknowledged.

I would like to acknowledge the invaluable help during the experiments from Dr. Michael Lukitsch and Michael Balogh from GM R&D Center, and my colleagues Dr. Xianying Meng-Burany, Ahmed Abou Gharam and Dr. Sukanta Bhowmick.

I am thankful to the faculty and staff at the Department of Mechanical, Automotive and Materials Engineering of the University of Windsor, and particularly to my colleagues at the Tribology of Materials Research Centre, for their support, encouragement and tolerance.

Last but not the least, I would like to thank to my mother, father and sister for their unconditional love and support.

Contents

List of Tables

List of Figures

Nomenclature

ΔH^{vap} Heat of vaporization

ΔZ^i Total charge transfer to species i

γ_{12} Interface energy between materials 1 and 2

γ_i Surface of energy of material i

$\hat{\Omega}$ Activation volume

μ Shear modulus

μ_i Chemical potential of i

ν Poisson's ratio

ν_0 Atomic vibration frequency

ψ Wavefunction

ρ Density

σ_{zz} Stress in the zz direction

ε Strain

A Surface area

a Lattice parameter

b Burgers vector

C_6 Dispersion coefficient

d_{i-j} Distance between i and j atoms

E Young's modulus

e Electronic charge density value

E^{ads} Adsorption energy

E_F Fermi energy

E_i Total energy of the slab i

$E_s(n)$ Surface energy of an n layered slab

E_{tot} Total energy of slab

F Force

$g(r)$ Radial distribution function

H Hardness

H^f Enthalpy of formation

$K(t)$ Kinetic energy at time t

k_B Boltzman constant

$n(r)$ Electron density at position r

n_{WS} Average electron density at the boundary of the Wigner-Seitz cell

Q Atomic charge values

Q^* Activation energy barrier

R_a Surface roughness

r_i Radius of i

T Temperature

t time

T_m Melting temperature

t_{oxide} Thickness of oxide

V_m Atomic volume

W_{dec} Work of decohesion

W_{sep} Work of separation

z_{cell} Cell dimension in the z direction

Z_i Bader charge of atom i

a-C   Amorphous carbon, non-hydrogenated diamond-like carbon

a-C:H Hydrogenated diamond-like carbon

a-C:H:F Fluorine and hydrogen containing diamond-like carbon

AFM   Atomic force microscopy

CNT   Carbon nanotube

COF   Coefficient of friction

CSP   Centro-symmetry parameter

CVD   Chemical vapour deposition

DC   Direct current

DFT   Density functional theory

DLC   Diamond-like carbon

DMFC Direct methanol fuel cell

DOS   Density of states

ECSA electrochemically active surface area

EDS   Energy-dispersive spectroscopy

EEM   Electron equilibration method

ELF   Electron localization function

ERD   Elastic recoil detection

F-DLC   Fluorinated diamond-like carbon

FFT   Fast Fourier transform

FIB   Focused-ion beam

GGA   Generalized gradient approximation

H-DLC   Hydrogenated diamond-like carbon

HRTEM   High-resolution transmission electron microscopy

HSS   High speed steels

LAMMPS   Large-scale Atomic/Molecular Massively Parallel Simulator

LDA   Local density approximation

LEED   Low-energy electron diffraction

MC   Monte Carlo

MD   Molecular dynamics

MEMS   Micro-electromechanical systems

MQL   Minimum quantity lubrication

ND   Nano-diamond

NEMS   Nano-electromechanical systems

NH-DLC   Non-hydrogenated diamond-like carbon

NW   Nanowire

PACVD Plasma-assisted chemical vapor deposition

PAW   Projector-augmented wave

PBC   Periodic boundary conditions

PDOS   Partial density of states

PECVD Plasma-enhanced chemical vapour deposition

PEMFC polymer electrolyte membrane fuel cell

PTFE   Polytetrafluoroethylene

PVD   Physical vapour deposition

QM   Quantum mechanics

QPF   Quick plastic forming

RBS   Rutherford backscattering spectroscopy

RDF   Radial distribution function

ReaxFF Reactive force field

RF   Radio frequency

RH   Relative humidity

RoM   Rule of mixtures

SD   Sliding direction

SEI   Secondary electron image

SEM   Scanning electron microscopy

SF   Stacking fault

SPF   Superplastic forming

TDOS   Total density of states

TEM   Transmission electron microscopy

TM   Transition metal

VASP Vienna Ab initio Simulation Package

VdW   Van der Waals

XPS   X-ray photoelectron spectroscopy

Chapter 1

Introduction

1.1 Background and motivation

Diminishing resources and an increase in the awareness of environmental protection have stimulated the automotive industry to design and manufacture new vehicles which are more fuel efficient, environmentally friendly, and sustainable. The use of lightweight materials such as aluminum alloys, magnesium alloys, and their composites (Si, SiC, and Al_2O_3) in various components [1–5], and the implementation of fuel cells and batteries in drive-train parts [6, 7], are not the only significant advancements, but represent major improvements in the use of advanced materials in automotive technology. The use of these advanced, lightweight, and energy efficient materials in automotive components brings new challenges for effective [8] manufacturing processes (traditional processes are often not applicable), and in the optimization of the durability and efficiency of the materials during their service lives. Most automotive components are used in contact with another component, either moving or stationary, therefore, one very important challenge is to control the adhesion of the materials, which plays a significant role in determining the performance of that material. The adhesion problem arises during both the operation and manufacturing of automotive components, and it needs to be addressed for the better design of advanced vehicles.

Adhesion is defined as the tendency of dissimilar materials to attach to each other as a result of the interatomic forces generated at the contact interface [9]. These interatomic forces can be strong, and may lead to the formation of chemical bonds (ionic, covalent,

and hydrogen), or they can be relatively weak in the form of van der Waals or electrostatic interactions. Thus, an atomic level knowledge of the bond structure between contacting pairs is essential in understanding the adhesion problem. One of the most common and accurate ways of gaining that knowledge is predicting the surface structures of contacting pairs and the adhesive transfer at the interface of contact using atomistic simulations.

Atomistic simulations have been used to predict material properties for many years, but their major leap into common research tools emerged after the development of (and still developing) advancements in computational power. Current computational power allows the simulation of a few hundreds of atoms in electronic structure based methods (density functional theory (DFT) , Hartree-Fock, etc) and a few millions of atoms in methods based on many-body interatomic interactions (molecular dynamics, Monte Carlo) [10]. Although these methods allow the study of many different and complex problems at the atomic scale, it is still impossible to exactly model macro-scale problems that are observed in real life using atomistic simulations. However, this should not be the cause of great concern, because *"Trying to mimic the actual physical system is almost never the best way to model it"* [11]. In a real system, the majority of the materials do uninteresting things, and do not play important roles in the studied problem. Adhesion occurs only at the immediate contact surfaces, and therefore the inclusion of all of the defects into a model that affects the bulk properties of materials will not provide any significant insight into the understanding of the adhesion, but will only increase the computational time. In order to use atomistic methods for real problems without suffering from computational inefficiencies, it is essential to use cautiously chosen approximations. To decide on the model of interest that is most contributional to the problem, it is crucial to carry out and evaluate laboratory experiments that are ingeniously constructed to reflect real conditions.

Atomistic simulations provide a useful and fundamental understanding of molecular scale events, however it is necessary to connect the information obtained at the molecular scale to real applications. Nevertheless, there is an important challenge to be faced, while connecting computed material properties with the results obtained from laboratory experiments, which is *"the quantities that are easy to compute are easy to measure, but quantities that are easy to measure are hard to compute"* [11]. In atomistic simulations, adhesion can be

evaluated by either calculating the interatomic forces at the interface, or by calculating the ideal work of separation, which is defined as the energy required to separate the interface into two free surfaces. Both of these quantities are calculated for ideal systems (excluding all defects in the structure, all environmental effects, etc.), which are far from real systems. This challenge can be partially overcome by down-scaling the problem, designing laboratory experiments that can mimic the actual conditions that the adhesion arises, and enlightening the mechanisms of adhesion, thereby providing essential information for modelling the system of interest. As the poet James Russell Powell suggested: "*The true ideal is not opposed to the real but lies in it; and blessed are the eyes that find it.*"; to idealize a problem to the fundamental level of understanding, it is critical to evaluate the existing observations of the problem in different atmospheres, temperatures, geometries, loading conditions, and materials from the literature. In addition, laboratory experiments give qualitative relationships and observations that support adhesion calculations at the atomic scale. The nature of the adhesion problem necessitates the geometry of the studied system (shape of the material, surface roughness, etc.) to have the least significant effect on adhesion when compared to other parameters, (and as long as two materials are in contact) in whatever shape and orientation they have or how large they are, provided that the other conditions fulfill the chemical attractions occurring between materials, they will adhere to each other. For this purpose, tribological experiments can provide the necessary, qualitative information to study adhesion in automotive components, because in these applications, the parts are usually in sliding contact with a counterface under an applied load. The ex-situ investigation of the microscopic and chemical properties of mating surfaces informs the changes in the surface chemistry during adhesion, and the shear forces measured in-situ suggest the strength of interaction between the surfaces, and both sets of information can be obtained by atomistic simulations. There are numerous works in literature that study the adhesion problem, either experimentally or computationally, but only a few studies have benefited the advantages of both experimental and computational tools to understand the adhesion problem. The aim of this study is to combine atomic scale simulations and laboratory scale experiments in order to provide a coherent picture of the events that occur during adhesion in automotive components, and finding a solution to the problem for real applications will

be suggested.

1.2 Scope

The adhesion problem in various automotive components and processes is different due to dissimilar materials that are in contact, environmental conditions, temperatures, and loading conditions. Therefore, for each process, there is a requirement to approach the adhesion problem from a different perspective, and it is essential to use carefully selected experimental methodologies and atomistic tools to study the problem. Experimental and computational methods are employed in a synergistic way to understand the adhesion and friction problem in the industry, as shown in Figure 1.1.

In the manufacturing of aluminum parts, an aluminum work piece is placed in contact with a tool piece under an applied load, speed, and temperature. During this process, due to the high contact pressures generated at the contact interface, native aluminum oxide on the aluminum surface is broken, and nascent aluminum is exposed, which leads to a chemical attraction between the aluminum and the tool piece that is commonly made of tool steel. Subsequently, the aluminum may detach, and some fragments may transfer to the steel surface. The adhesive transfer of aluminum results in the degradation of the tool surface, which drastically affects the efficiency of the manufacturing process and the quality of the final product. Accordingly, it is essential to prevent aluminum adhesion in the manufacturing process in order to obtain the effective production of lightweight materials in automotive components. The adhesion problem in different manufacturing processes has different causes and mechanisms due to the different contact conditions. For instance, in machining operations the work piece material is put in sliding contact against the tool at a high contact pressure and speed, but in sheet metal forming operations, the work piece and die are placed in intermittent contact at higher temperatures for a short time, at relatively lower contact pressure and speed.

The aluminum adhesion problem in machining and sliding applications has been overcome in the literature by the application of hard, adhesion mitigating coatings (including borides, carbides, nitrides) to tool surfaces. Among these studied systems, diamond-like
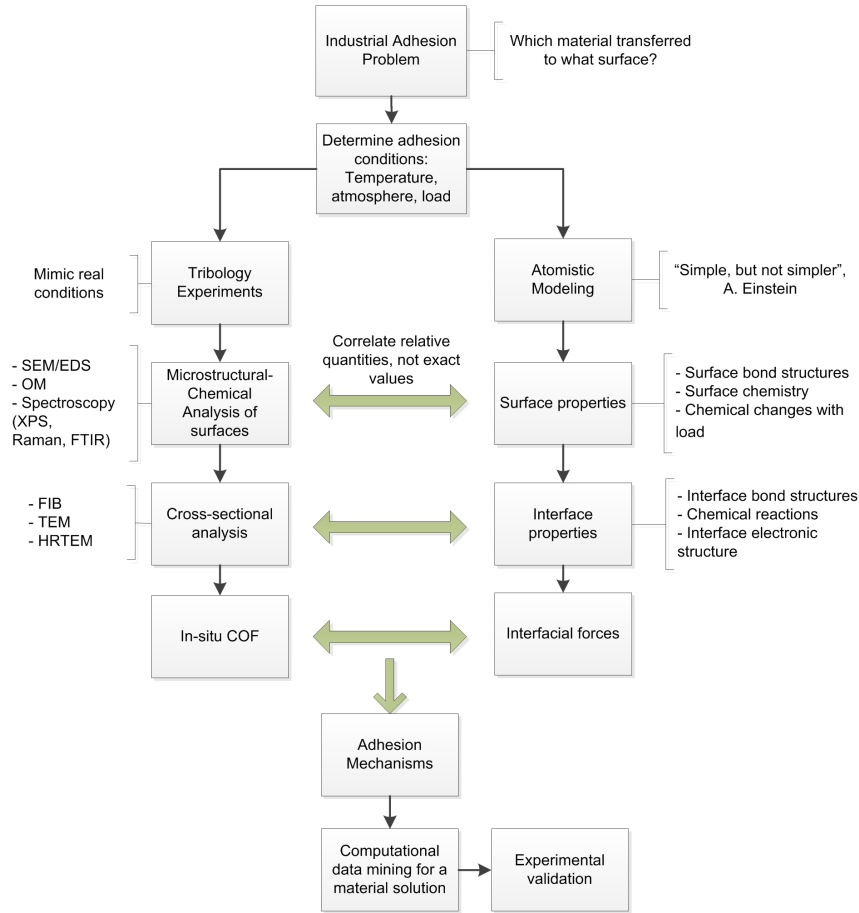
Figure 1.1: Overview of the methodology that was followed to solve the industrial adhesion problem. The results and analysis of tribological experiments were correlated with the material properties predicted using atomistic modeling methods, and the adhesion mechanisms were obtained. Following this, data mining of the materials based on the adhesion mechanism was pursued in order to design a materials solution to the problem, and the computational results were validated with experiments.

carbon (DLC) coatings provided the minimal adhesion against Al in tribological experiments [12–15]. The incorporation of F and Si has been shown in the literature to reduce the surface energy of DLC, and Si was shown to reduce the environmental dependence of the tribological properties of DLC. These additions can potentially decrease the adhesion between DLC and aluminum.

In Al sheet metal forming processes at high temperature conditions (> 400 ºC), where DLC coatings cannot be used due to degradation [16], superplastically elongated oxide fibers were observed on the Al sheet surface [17–19]. These fibers were particularly important for controlling adhesion because of the intimate contact that occurs between these fibers

and the steel tool surfaces during forming process. Cross-sectional transmission electron microscopy (TEM) experiments also confirmed that oxide fibers attach to the steel surface. The superplastically elongated oxide fibers were reported to be formed due to dynamic oxidation during deformation [20]. Therefore, at high temperature applications, oxidation has a drastic effect on the deformation and adhesion behavior of Al, however the effects of oxidation on the mechanical properties of Al are still unclear. The problem was addressed in this thesis by studying the oxidation and deformation of Al single crystals using atomistic simulation tools.

Energy efficient vehicles are not only produced by using lightweight materials, but also by using alternative drive-train parts, such as fuel cells and batteries. An important adhesion problem in automotive components appears in the electro-catalyst of the polymer electrolyte membrane fuel cells (PEMFCs). In the PEMFCs, Pt nanoparticles supported on carbon surfaces are used as catalysts for both in the cathode and the anode of the fuel cell [21]. During the operation of the fuel cell, Pt particles agglomerate on the carbon surface or dissolute [22], which causes a substantial performance reduction due to a decrease in the electrochemically active surface area (ECSA) [23]. The agglomeration of Pt particles occurs as a result of the weak binding between the Pt and carbon surfaces. Consequently, in order to retard the electro-catalyst degradation in PEMFCs, the weak adhesion at the Pt/carbon interface needs to be strengthened.

In summary, this thesis aims to solve different adhesion related problems in automotive applications by synergistically and systematically using various atomistic simulations and experimental methods. There have been various preventive measures undertaken in order to mitigate adhesion in these processes, such as using lubricants and the application of hard coatings on the tool surfaces. Although many of the lubricants and coatings partially meet the industrial needs for adhesion mitigation, the mechanisms of adhesion in these processes are still unclear, and do not bring a complete solution to the problem. Therefore, it is essential to study the adhesion problem at the fundamental level, which can done using tribological experiments at the laboratory scale between the tool and work piece materials to reveal the adhesion mechanisms, by following the principles initiated by earlier researchers including Cottrell [24], Bowden [25], Tabor and McFarlane [26]. Tribological experiments

generally do not represent the manufacturing conditions exactly, but these experiments allow the different contributing parameters to adhesion to vary, such as the environment, temperature, load, and speed in order to reveal the conditions that yield to adhesion in the particular system materials that are in contact. These derived mechanisms were used to construct atomistic models to understand the adhesion process at the fundamental level. Accordingly, this thesis is organized as such that it starts with an introductory chapter (Chapter 1) which presents some brief background information and our motivation to carry out this work (Section 1.1). Section 1.2 mentions the scope of this dissertation. Section 1.3 follows by defining our objectives, and in Section 1.4 a general literature review is provided. This thesis continues with the studies that were published or submitted in peer reviewed journals, such that Chapter 2 includes the results of the assessment of the changes in the surface stability and bond structure of diamond surfaces with F termination. These results were compared with those of H-termination, and the adhesion and friction between F- and H-terminated surfaces were compared. In Chapter 3 the adhesion mechanisms between Al and F-incorporated DLC coatings are presented, and their effects on the tribology between Al and F-DLC are discussed. In Chapter 4 the results of the tribological properties between Al and F, Si, and O-incorporated DLC are presented and the reasons for humidity independent friction characteristics are discussed. In Chapter 5 the results of the molecular dynamics simulations that show softening in the Al nanowires due to native oxide are given. In Chapter 6, the results of the molecular dynamics simulations show an increase in the plasticity of Al in an oxygen atmosphere. This chapter also reveals the superplastic deformation of native oxide on Al in an oxygen atmosphere. Chapter 7 includes the first principles calculations showing the systematic study carried out to find suitable metallic elements that can increase the strength of the Pt/carbon interface that is present in fuel cells. Finally Chapter 8 includes an overall summary and the conclusions of this dissertation.

1.3 Objectives

The general objectives of this thesis were:

- The elucidation of adhesion mechanisms in automotive applications using laboratory

scale tribological experiments and atomistic simulations.

- The design of a materials solution to the adhesion problem based on the derived mechanisms.

These objectives were achieved by undertaking three different "sub-studies", each with its own set of objectives. The objectives of the study to design coatings for Al adhesion mitigation in forming and machining applications were:

- A determination of the changes in the bond structure and stability of DLC surfaces with the incorporation of F using first principles calculations.

- An understanding of the differences between F- and H- terminated DLC surfaces in terms of adhesion and friction.

- An assessment of the material transfer mechanisms between Al and F-incorporated DLC coatings using first principles calculations and experiments.

- An assessment of the humidity independent material transfer and low friction mechanisms between Al and Si-, O-, and F-incorporated DLC coatings using tribological experiments.

The objectives of the study of the aluminum adhesion problem in high temperature forming applications due to oxidation were:

- The modeling of the effect of oxidation on the mechanical properties of Al using molecular dynamics simulations with a reactive force field (ReaxFF).

- An understanding of the effect of the native oxide on the nano-scale mechanical properties of Al.

- An understanding of the deformation characteristics of the native oxide, and an assessment of the reasons for observing superplasticity in an oxygen atmosphere.

The objectives of the study to find adatoms that can enhance the strength of the Pt/carbon interface were:

- A systematic search for suitable metallic adatoms sandwiched between Pt and carbon surfaces that can strengthen the weak Pt/carbon interface using first principles calculations.

- The understanding of the changes in the Pt/carbon interfacial bond strength with the metallic adatom incorporation.

- The selectiion of suitable elements based on the models developed for increasing the Pt/carbon interface strength.

1.4 Literature review

1.4.1 Fundamentals of adhesion

When two surfaces are placed in contact with each other, the attractive forces generated at the asperities lead to the bonding of tje surfaces to one another. Interactions at the contact interfaces can be strong as a result of the formation of chemical bonds (ionic, covalent, metallic, or hydrogen bonds) or they can be weak due to the generation of electrostatic and dispersive forces [9]. The bonding at the contact interface is referred to as *cohesion* if it occurs between similar materials. During the separation of two materials which are adhered to each other, if fracture occurs from any of the bulk regions, two surfaces are formed by the breaking of the cohesive bonds in the material. The cohesive strength of a material is characterized by the ideal work of decohesion (W_{dec}), which is the energy required to separate the interface into two free surfaces with the same surface energy of γ_1 (Figure 1.2a). Figure 1.2a also shows that the process of creating a unit area of surface is equivalent to separating two half-unit areas from contact so that [9]

$$W_{dec} = 2\gamma_1 \tag{1.1}$$

When the contact occurs between two dissimilar materials (1 and 2), the bonding formed at the interface is called *adhesion*. The adhesion strength of the interface can be characterized by the definition of the ideal work of separation (W_{sep}), which is the energy required

to break an interface reversibly into two free surfaces (when the plastic deformation is neglected). As illustrated in Figure 1.2b, W_{sep} is defined in terms of the surface and interface energies of the materials, which is the same as the difference between the total energy of the interface and the total energies of the isolated slabs

$$W_{sep} = \gamma_1 + \gamma_2 - \gamma_{12} = \frac{1}{A}[E_1 + E_2 - E_{12}] \tag{1.2}$$

where γ_i is the surface energy of material i, γ_{12} is the interface energy, E_i is the total energy of the slab i, and E_{12} is the total energy of the interface slab formed between 1 and 2 with an interfacial area of A.
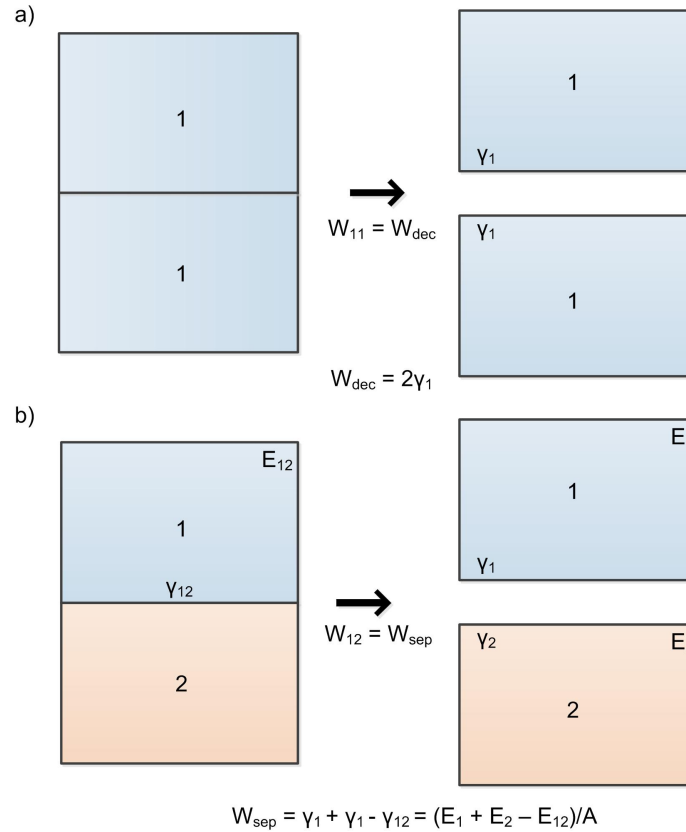
Figure 1.2: Definitions of a) the work of decohesion and b) the work of separation.

A comparison of the W_{sep} and W_{dec} values provides information about where the interface will break first during the separation of the adhered pair. When two solid surfaces are in contact, and if the interfacial bond is stronger than the cohesive bond in the cohesively weaker of the two materials (i.e. $W_{sep} > W_{dec}$), then, after the separation of the two solids,

the cohesively weaker material will transfer to the cohesively stronger material [27, 28].

Adhesion is a function of the material pair and the interface conditions, such as the crystal structure, crystallographic orientation, solubility of one material into another, chemical activity and separation of charges, surface cleanliness, normal load, temperature, duration of contact, and separation rate. For instance, the interfacial bonding between the two metals is usually stronger than the cohesive bonds in the weaker of the two metals so that the material transfer between the metal pairs is always observed when the two metals are brought into contact, and the fracture generally does not occur at the interface [27]. The formation of contaminants on the metal surface after exposure to the environment, and the formation of physisorbed, chemisorbed, and chemically reacted films on metal surfaces generally decreases the adhesion of two reactive surfaces [27–29]. The adhesive strength of a contact is also affected by the temperature. At high temperatures, a softening of the surfaces results in greater flow, ductility, and a larger real area of contact, which results in stronger adhesion. High temperatures can also result in diffusion across the interface. In a metal–metal contact, a high temperature may result in increased solubility, and in a polymer–polymer contact, inter-diffusion strengthens the contact, which results in stronger adhesion [28].

In nearly all practical systems where two solid surfaces are in solid-state contact some adhesion occurs, even under the most effectively lubricated situations. Therefore, both adhesion and cohesion are extremely important concepts to be studied in order to control the performance of materials in many industrial processes, such as in manufacturing and machine operations that involve contacts in bearings, gears, seals and electrical elements. In addition, adhesive wear is one of the most severe types of wear encountered in practical lubrication devices, and adhesion and cohesion are of fundamental importance to this wear mechanism [27]. In this chapter, adhesion problems and their detriment to Al manufacturing processes (machining, cutting and hot-forming) will be reviewed, in addition to the durability issues in fuel cells due to adhesion problems in the Pt electro-catalyst.

1.4.2   Adhesion problem in aluminum manufacturing and forming

In the manufacturing of aluminum products, cast aluminum alloy work pieces are subjected to various rolling, machining, and forming operations that are mostly carried out under extremely high loads and strain rates. In these processes tool steels are commonly used as the tool materials, and the contact interfaces are lubricated, either to reduce friction or to control the heat generated at the points of contact. For these processes, the contact interface formed between the lubricants and the oxides of steel and aluminum is shown for a typical aluminum rolling process [30] in Figure 1.3. As a result of the generation of high contact pressures at the contact interfaces during the forming processes, aluminum oxides are removed and the nascent Al surface is exposed. This exposed nascent aluminum reacts with the tool surfaces and some aluminum transfers to the tool surface. This adhesion and adhesive transfer of aluminum to the tool pieces under high contact pressures are some of the most important and common problems in the manufacturing and forming of aluminum products. The aluminum adhesion problem can be different in different forming processes due to the differences in the strain rate, load, and temperature, and the solution to the problem necessitates an understanding of the underlying adhesion mechanisms at these conditions.
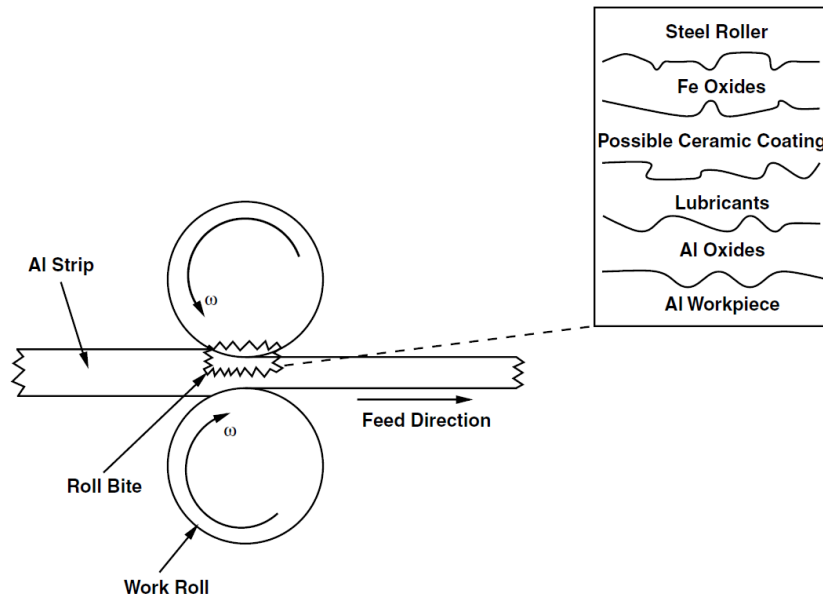
Figure 1.3: Aluminum rolling process showing the possible materials at the contact interface [30].

The machining of aluminum alloy products is generally carried out using steel made tools with the use of a liquid coolant. However, the detrimental health effects of coolant chemicals on the workers [31, 32], and the significant cost of the maintenance of machining fluid systems have led manufacturers to pursue alternative processes that can diminish the use of cutting fluids in machining operations, such as dry machining. In dry machining, the unwanted material is removed by a process involving intense plastic deformation at a high strain rate that generates high temperatures and pressures at the contact interface [33–35]. The main obstacle to the commercialization of dry machining for aluminum parts is the high wear rate of the tool pieces due to the adhesion of aluminum. For instance, aluminum chips generated during the drilling process build-up at the high speed steels (HSS) drill flutes [36] (Figure 1.4), and result in the rapid failure of the drills, and significant reduction in the machined surface quality. Similar failure mechanisms were also reported [37] when carbide tools were used in the orthogonal cutting of aluminum alloys.
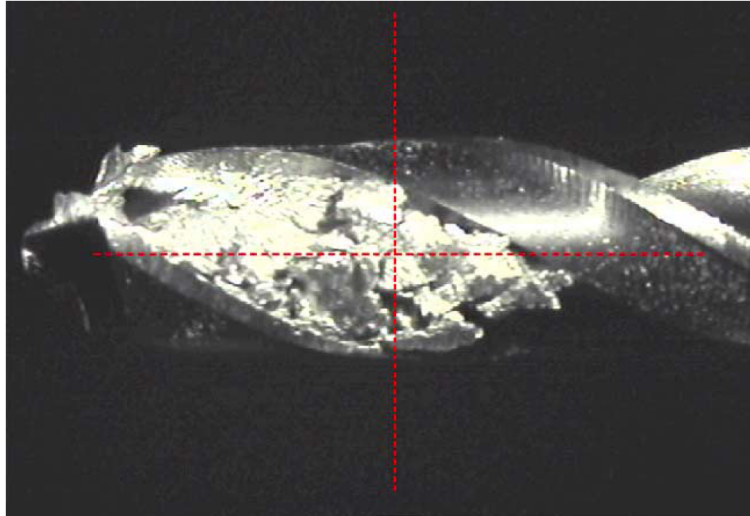
Figure 1.4: Drill flute covered with aluminum [36].

The aluminum adhesion problem of dry machining was overcome in the literature by various methods, such as the use of low melting temperature alloying elements in the aluminum [38], near-dry machining or minimum quantity lubrication (MQL) [39, 40], and hard coatings on tool surfaces that mitigate aluminum adhesion [13, 36]. The latter will be reviewed in Section 1.4.3.

In hot forming processes, as compared to machining processes, the aluminum is subjected

to relatively lower strain rates, and lower contact pressures are generated at the contact interface. For example, in the quick plastic forming (QPF) and superplastic forming (SPF) processes (at temperatures above 400 ºC) a hot gas is used as a pressurized fluid to deform an aluminum blank into a tool of the desired shape [17, 41, 42]. At high temperatures, aluminum easily conforms to the tool surface due to softening, but the presence of any surface imperfections on the tool surface results in a significant reduction in the surface quality of the final product [17]. In QPF, when lubricant film breakdown occurs, aluminum transfers and builds up on the tool surface [17], as shown in Figure 1.5, which causes surface imperfections on the final product that require additional metal finishing.
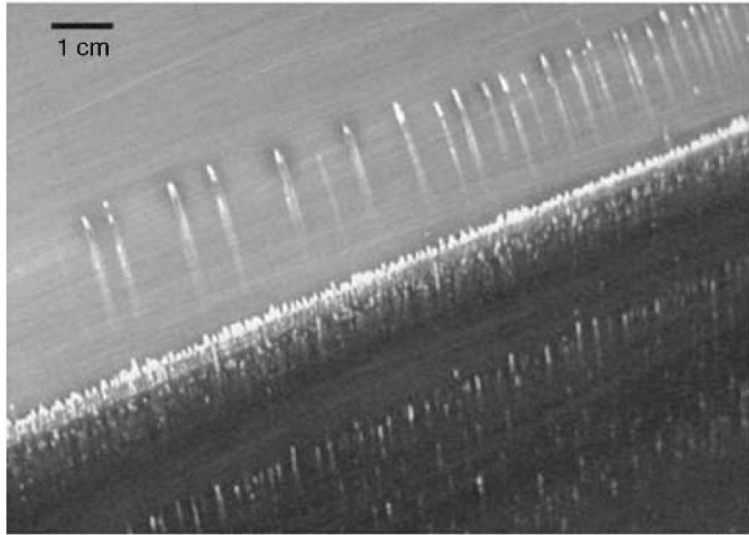
Figure 1.5: Aluminum particle buildup on QPF tools.

The tribological processes that result in aluminum adhesion have been studied using several methods, such as pin-on-disk type experiments. However, none of the conventional tribological tests represent the actual deformation and contact conditions in QPF or SPF since in conventional pin-on-disk experiments the contact between the aluminum and the tool occurs repeatedly over the same location, and also the aluminum is not stretched during frictional contact. In order to overcome these issues, new experimental methods that can capture the actual contact conditions in QPF were designed, such as the hot forming simulator developed by Das et. al [18], which had a tribometer that could measure the coefficient of friction (COF) during sheet aluminum forming. The experiments carried out

at different strain rates and temperatures using the hot forming simulator were used to generate deformation mechanism maps in relation to the changes in the COF between the aluminum strip and the tool steel. The changes in the deformation mechanisms of the aluminum according to the strain rate and temperature used were reported to drastically affect the surface roughness of the aluminum, and therefore the COF and adhesion of the aluminum. This study [18] revealed that the adhesion of aluminum in hot forming processes is complicated by the changes in the aluminum surface due to the extreme softening of aluminum, and its fast oxidation kinetics at high temperatures.

In the superplastic forming of aluminum, it has been shown by earlier studies [43] that elongated fibrous structures appear on the aluminum sheet surface. The fibrous structures form between the elongated grains as a result of grain boundary sliding [18, 19] (Figure 1.6), and the focused-ion beam (FIB)-TEM cross-sectional analysis has revealed [19] that oxide fibers are composed of mixed Al-Mg oxides, namely Al_2O_3, MgO, $MgAl_2O_4$. The HRTEM microstructure of the oxide fibers (Figure 1.7) showed that these fibers consisted of nano-sized grains with a very large grain boundary area [19]. The diffusional flow of grain boundaries was demonstrated to be the dominant deformation mechanisms of nano-crystalline oxides, which enabled the fibers to deform superplastically by viscous flow [19]. The subsurface of the oxide fibers on the Al given in Figure 1.8 shows that oxide fibers formed a core-shell structure on the Al. Thus, fibers were formed as a result of oxidation of the Al during the deformation process, and eventually the core Al in Figure 1.8 will also be oxidized and form an oxide fiber at the surface [44]. The formation of superplastically deformed oxide fibers on the sheet surface has a profound effect on the adhesion of aluminum during the hot forming processes.

The microscopic examination of the tool steel surface in hot forming simulator experiments has indicated that there is adhered aluminum on the steel counterface. The FIB-SEM (scanning electron microscopy) cross-sectional analysis [45] given in Figure 1.9 showed that the contact interface between the aluminum and the tool steel occurred between aluminum oxide fibers and the steel surface. As a result, in hot forming processes the oxidation of aluminum and the characteristics of the oxides formed at the surface had a profound effect on the adhesive transfer of the aluminum.
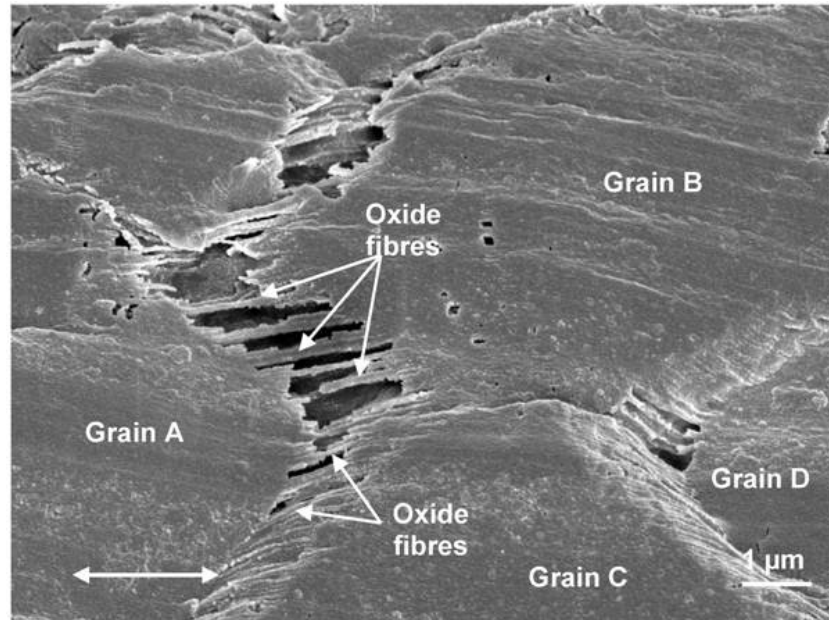
Figure 1.6: Oxide fibers elongated between aluminum grains as a result of grain boundary sliding when AA5083 alloy was deformed at 545 $^{\text{o}}$C and $4 \times 10^{-2}\text{s}^{-1}$ [19].

In a recent study, Chang et al. [20] subjected an AA5083 Al-Mg alloy to a series of tensile superplastic deformation processes under both ambient air and vacuum atmospheres. The formation of oxide fibers at the aluminum fracture surface was observed for the tests carried out at ambient air atmosphere, however no fibers were observed at the fracture surface when the test was carried out in a vacuum (Figure 1.10). Both of the aluminum samples tested (ambient air and vacuum) were exposed to air prior to the test and it is assumed that they had protective native oxide on their surfaces. It was revealed that the oxide fibers formed via the dynamic oxidation process during deformation [20].

1.4.3   Adhesion mitigating diamond-like carbon (DLC) coatings

The adhesion of aluminum on forming tools can be prevented by using a lubricant or applying a hard coating onto the tool surface. The temperature, atmosphere, and loading conditions in a particular forming process determine the applicable coating, which should mitigate the adhesion of the aluminum. Diamond-like carbon (DLC) coatings that are known to have good aluminum adhesion mitigation properties, and provide the lowest COF against aluminum in pin-on-disk experiments (compared to conventional industrial coatings
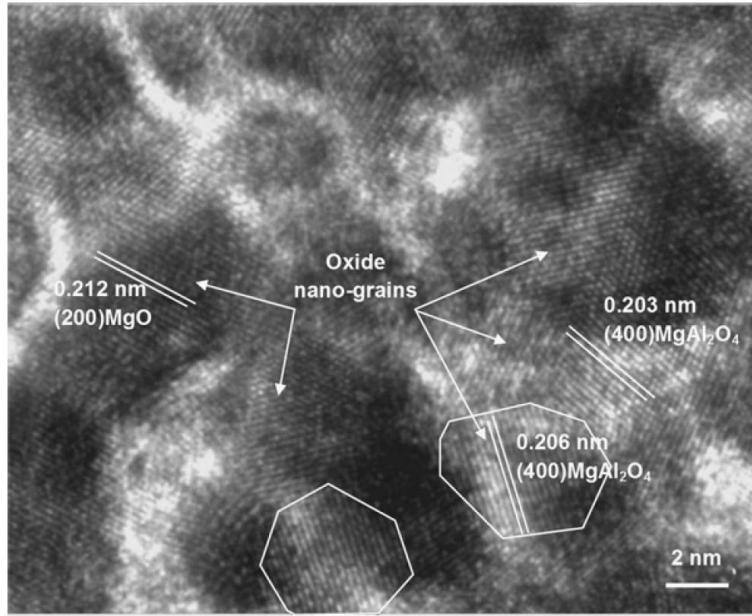
Figure 1.7: HRTEM micrograph taken from the fibre in Figure 1.6. The main phases in the fibres were found to be Al_2O_3, MgO and $MgAl_2O_4$, with a grain size of about 4.5 ± 0.7 nm [19].

based on nitride, boride, and carbide systems), have presented themselves as promising tool coatings for aluminum machining and shaping [12–14, 36, 46, 47].

The great engineering properties of diamond, which is the hardest and stiffest material available, is chemically inert, and has the highest thermal conductivity at room temperature attracted researchers to use diamond based materials, namely diamond-like carbon (DLC) in various applications [48], including optical windows, magnetic data storage, engine components [49], biomedical applications [50, 51], micro-electromechanical systems (MEMS) [52], and machine tools. The first DLC thin film was reported by Schmellenmeier [53] in 1953 and the first comprehensive study was presented by Aisenberg and Chabot [54] in 1971. Over the years, because of very good mechanical and chemical properties, extensive studies on the tribological and adhesion properties of DLC coatings have been reported in the literature [55–61].

In this section, beginning with the synthesis of DLC coatings, their characterization, and structural, mechanical, tribological, and chemical properties are reported. Additionally, the effects of F and Si doping on the properties of DLC films are reviewed.

17
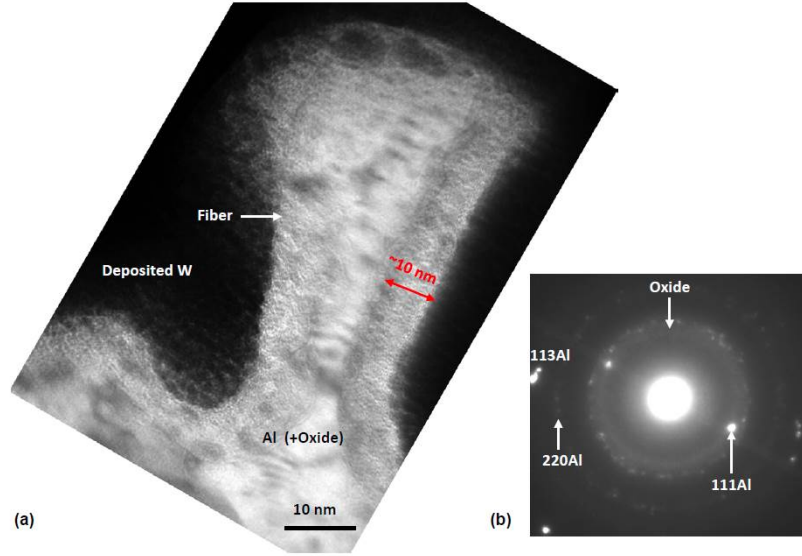
Figure 1.8: (a) A TEM cross-sectional micrographs of a fiber, (b) its electron diffraction pattern identified a oxide shell surrounding an Al fiber in AA5083 strip tensioned at 450 $^{\circ}$C [44].

1.4.3.1 Synthesis and classification of DLC coatings

DLC is an amorphous network of carbon atoms that contains fractions of sp^2 and sp^3 hybridized carbon atoms due to deposition conditions. DLC films with a high fraction of sp^2-bonded carbon atoms tend to be relatively soft and behave more graphite like, whereas a high fraction of sp^3-bonded carbons behave more diamond-like with regard to some of the properties [52]. DLC films are not only composed of carbon networks, but also contain significant amount of hydrogen (10-50 at.%), which is introduced during the production of the films. A comprehensive analysis of the structure and chemistry of DLC films was reported using Raman spectroscopy methods by Ferrari and Robertson [62]. They constructed a predominance area diagram of the types of DLC coatings, according to their bonding nature and hydrogen content. In Figure 1.11, a-C corresponds to amorphous carbon, which consists of a higher amount of sp^2-bonded carbon. The films that contain a higher sp^3/sp^2 ratio are described as tetrahedral amorphous carbon, ta-C [63]. Hydrogenated-DLC (H-DLC) films are designated by ta-C:H or a-C:H.

DLC coatings can be produced by various physical vapor deposition (PVD) and chemical vapor deposition (CVD) methods, and some of these methods are shown in Figure 1.12 [59].

18

In an ion beam deposition system, carbon ions are produced by the plasma sputtering of a graphite cathode in an ion source [54], or alternatively, a hydrocarbon gas (such as methane) is ionized in a plasma and ion beam then extracted through a grid from a plasma source by a bias voltage. The carbon ions are then accelerated to form an ion beam in a high vacuum deposition chamber [64]. In sputtering, which is the most widely used industrial process, a graphite target is bombarded by an Ar plasma using an RF or DC power supply. Alternatively, in ion beam sputtering, a beam of Ar ions can be used to sputter from the graphite target to create carbon flux. A second Ar ion beam can be used to bombard the growing film in order to densify the film or encourage sp^3 bonding [65]. Another method that is used to produce DLC films is the cathodic arc [63] in which an arc is initiated in a high vacuum by touching the graphite cathode with a small carbon striker electrode and then withdrawing the striker. This produces energetic plasma with a high ion density of up to $10^{13} cm^3$ [59]. In pulsed laser deposition, a plasma is formed using an excimer laser on a graphite target (such as ArF), which gives very short and intense energy pulses, following which the plasma expands towards the substrate. The kinetic energy of this expansion provides ion energy proportional to the laser fluence concentrated at the target spot [66,67]. The most widely used deposition process for DLC films is the plasma-enhanced CVD (PECVD) method, where the reactor consists of two electrodes of different areas, and the RF power is capacitively coupled to the smaller electrode on which the substrate is mounted, and the other electrode is grounded. The RF power produces a plasma between the electrodes [59,68].

DLC films can be coated to any surface, including polymers, ceramics, and metals, although there may be adhesion problems with some substrate materials. A strong adhesion of the films is important for tribological uses, otherwise the films may fracture and delaminate from the surface under high normal or shear forces. It was reported that the adhesion of DLC films to carbide or silicide forming substrates (Si, Ti, W, and Cr) can be attained easily, and that the adhesion of DLC to metals or ceramics is not very strong. Adhesion can be improved by coating these substrates with carbide or silicide formers (Si, Cr, W, and Nb) prior to DLC deposition [55].

Deposition conditions and methods determine the film structure and the bonding nature

of carbon (sp^3/sp^2 ratio), which affect the properties of films [56, 59, 69]. In addition, the deposition temperature, gas pressure, bias voltage, and other parameters specific to the applied method have considerable effects on the film structure.

1.4.3.2 Mechanical properties of DLC coatings

The mechanical properties of DLC are particularly important since these films are generally used as a protective coating. DLC coatings have a high hardness and high elastic modulus, similar to diamond (which has a hardness of 100 GPa and elastic modulus of 1100 GPa), but with high internal stress. Most of the mechanical properties of DLC films were measured using nano-indentation experiments [70]. In these experiments, a small diamond tip is progressively forced into the film, and then force-displacement curve is obtained. Since DLC films are relatively harder materials, they show both a plastic and elastic response to indentation. Hardness is a measure of the resistance of a material to plastic deformation, defined as the average pressure under the indenter, and it is given by dividing the applied load by the projected area of plastic deformation, which is found by estimating the area in the loaded condition from the curve versus the indent depth. Young's modulus is proportional to the slope of the tangent line that is drawn to the unloading curve at the maximum load, and extrapolated to zero load as described by the Oliver-Pharr method [71]. An accurate measurement of the mechanical properties for a hard film on a soft substrate system, such as DLC, can only be achieved when the indentation depth is limited to 10% of the thickness of the thin film [72].

The mechanical properties of DLC films were reported to be directly correlated with the sp^3/sp^2 ratio and the H content such that a-C/a-C:H coatings were reported to have hardness values in the range $10 - 30$ GPa with a corresponding Young's modulus of $60 - 300$ GPa [56]. The hardness of ta-C films can reach to the higher values of the $40 - 80$ GPa range [73], with a corresponding Young's modulus as high as 900 GPa [56]. The DLC films were reported to have internal compressive stresses in the range $0.5 - 7$ GPa for a-C films, while the compressive stress in the ta-C films can reach 13 GPa [74]. The compressive stresses were reduced by the incorporation of N, Si, O, or metals [75] in the films, or by the production of multi-layered structures [76, 77]. On the other hand, the reduction in the

stress also causes a reduction in the hardness of the films.

1.4.3.3 Tribological properties

In general harder materials exhibit higher wear resistance, therefore DLC coatings also have very good wear resistance with wear rates as low as 10^{-11}mm^{3}N^{-1}m^{-1} [55]. Additionally, DLC shows a low COF, when compared to other hard coatings, as shown in Figure 1.13, which is in the range of $0.001 - 0.7$ [55–57, 60, 61, 78, 79]. The COF and wear resistance of DLC films were reported to be affected by the material parameters of the substrate and counterface, contact pressure, nature of motion, speed, ambient temperature, and chemical environment during tribological testing, in addition to the structural properties of the DLC coating itself [55, 78].

The adhesion mitigating properties of DLC can be understood by the investigation of the friction properties of DLC in tribological experiments, since adhesion and friction are strongly correlated [26, 27]. In a simpler way, friction can be defined as the resisting force between materials sliding against each other [80], and the adhesive interactions between the sliding couple at the contact interface determine the degree of the friction. Therefore, the low COF in DLC coatings is observed as a result of weak adhesive interactions at the sliding contact interface in a tribological test. Any test parameter that can change the COF in a tribological test can be regarded as the result of a change that took place in the adhesive interactions at the sliding contact interface. Following this, the tribological properties of DLC coatings varied drastically with the environment, the alloying elements incorporated in the DLC structure, and among the different counterface materials sliding against DLC. Here, only the tribological properties of the DLC against Al will be the focus of this review.

Tribological tests with DLC sliding against different materials [55,58,61,81,82] show that the low friction is usually achieved after the formation of easy shearing carbonaceous transfer layers on the counterface, while the contact interface forms between these carbonaceous layers and the DLC [83–86]. These transfer layers were found to be significantly composed of sp^2 bonded carbon as the transfer layers were formed after the graphitization of carbon [87–89]. In earlier studies [87, 88], the low COF achieved with the DLC coating is believed to be due to the easy shearing of the graphitized transfer layers as a result of weak adhesive

interactions between the layers of the graphite structure. However, graphite exhibits a very high wear rate and a high COF of 0.6 in dry atmospheres and vacuum, when slid against itself, but the presence of a small amount of water vapor or large molecules that can enter between the carbon layers reduces the friction [90–93]. This result indicates that only the graphitization itself cannot reduce the friction of the DLC to lower levels, however the passivation of carbon layers or termination of carbon dangling bonds with -H, -OH, or other terminating molecular groups had a more significant contribution in reducing the COF in DLC coatings. The termination of dangling carbon bonds can be achieved either by the incorporation of hydrogen during production or the molecular groups in the environment can diffuse to the contact interface and terminate the dangling carbon bonds during the DLC operation.

When Al is placed in sliding contact against an a-C coating, a high COF of $0.56 - 0.74$ was observed in vacuum and inert atmospheres [14, 82, 94–96], however a very low COF of 0.11 [14, 82, 94, 95] was observed in ambient air and a COF of 0.03 was observved in H_2 [94, 95], as shown in Figure 1.14. In these studies a significant amount of adhered Al was detected on the wear tracks formed in vacuum and inert atmospheres (Figure 1.15), but no Al adhesion was reported on the wear tracks formed in the ambient air and H_2 atmospheres. In H_2, it was suggested that the a-C surface was H-terminated, and in air the a-C surface was H- and OH-terminated, which prevented Al adhesion. When tested in an atmosphere with high relative humidity (RH> 50%), the a-C showed a low COF due to the surface passivation by the -OH groups, formed as a result of the dissociation of water molecules into -H and -OH on the carbon surface [55, 95]. On the other hand, the COF of a-C:H increased with increasing humidity [55, 56].

The effect of the H- and OH-termination of carbon dangling bonds on Al adhesion mitigation was demonstrated in earlier studies using first principles calculations [95, 97]. The calculations at the Al/diamond:H interfaces [97] showed that Al forms strong covalent bonds with the clean diamond surface resulting in a high $W_{sep} = 4.08$ J/m^2. When the Al/diamond interface was separated, due to the low Al decohesion energy of $W_{dec} = 1.52$ J/m, the Al fractured and two Al layers transferred to the diamond surface, as can be seen in Figure 1.16(a). On the other hand, when the Al/diamond:H interface separated,

no Al transfer occurred (Figure 1.16(c)) due to the very low $W_{sep} = 0.02$ J/m^2. Similar results were reported for the Al/diamond:OH that did not show any adhesive transfer at the interface due to a low $W_{sep} = 0.2$ J/m^2. When carbon bonds at the surface were terminated by -H or -OH groups, and no adhesion of Al occurred, then the transfer of DLC to the Al counterface occurred due to the very weak adhesive interactions at the graphite interlayers. First principles calculations [98] predicted a $W_{sep} = 0.11$ J/m^2 at the Al/graphite interface, which was larger than the $W_{dec} = 0.08$ J/m^2 for graphite [98]. As a result, the transfer of graphite layers to the Al occurred, which is in agreement with the formation of carbonaceous transfer layers on Al counterfaces sliding against DLC coatings observed in the tribological experiments.

As shown in earlier first principles calculations [95], the -H and -OH terminations of the carbon dangling bonds can occur by the dissociation of water molecules that are present in the ambient air on the DLC surface. When the carbon surfaces are passivated by -H or -OH groups, and when the transfer layers are developed on the Al counterface during sliding, a sliding contact interface forms between two H- or OH-terminated diamond surfaces. First principles calculations showed that the interface formed between the two diamond:H surfaces had a very low $W_{sep} = 0.008$ J/m^2 [95], similar to the low $W_{sep} = 0.02$ J/m^2 [95] for the interface formed between the two diamond:OH surfaces, so that the DLC showed a very low COF when the carbon dangling bonds were terminated by -H and -OH.

In sliding contact experiments, a low COF was achieved after the formation of transfer layers on the Al surface, however in the Al manufacturing processes (such as in the forming and machining of Al alloys) the contact time between the tool surface and the Al work piece is so small that there is not enough time for the development of transfer layers on the Al surface. In these applications, the preferred coating should possess minimal Al adhesion. In the lubricant-free cold forming of the AA6016 Al alloy the use of a-C and a-C:H coatings was reported [99] to reduce the Al adhesion on the punch tool surface as shown in Figure 1.17. This figure also shows that for the un-coated 1.3343 punch material, the adhesive transfer of Al occurred at the tip edge, while the a-C and a-C:H coatings showed a preferred material transfer to the mantle surface. The highest adhesion was observed with the use of an a-C:H:Si coating. It is noted that in Figure 1.17, this is the lowest volume of the adhered

material observed for the a-C:H coating.

Dry machining experiments of Al alloys also showed a reduction in the amount of Al adhesion to tool surfaces with the use of DLC coatings [40, 47, 100]. In the dry cutting of an AlCu2.5Si18 alloy, the un-coated tool surface showed severe Al adhesion [47], but the DLC (ta-C) coated tool surface was reported to have almost no adhered Al on the rank and flank faces, as shown in Figure 1.18. The performance of the a-C (NH-DLC) and a-C:H (H-DLC) coatings in the dry drilling of the 319 Al alloy also reported [100] a considerable reduction in Al adhesion. The microstructural investigation of the drill flute areas (Figure 1.19(a)) showed severe Al adhesion for the un-coated steel tools (Figure 1.19(b)), which resulted in the failure of the drilling experiment in a short period of time. Conversely, the use of the a-C (Figure1.19(c)) and a-C:H (Figure 1.19(d)) coatings resulted in minimal Al adhesion and 150 holes could be easily drilled in dry conditions. The a-C:H coating showed less Al adhesion than the a-C coating. According to the first principles calculations reviewed above, it is assumed that the a-C:H coatings were passivated by the -H groups and a-C coatings were passivated by -OH and -H groups that were formed as a result of the dissociation of water molecules from the atmosphere, and therefore the Al adhesion to the carbon surface was prevented.

In summary, DLC coatings showed promising results in tribological experiments and the manufacturing processes of Al alloys. The adhesion mitigating properties of DLC coatings can be improved by the incorporation of different alloying elements into the amorphous DLC structure during deposition [75, 101, 102]. The surface energy of the DLC coatings was reduced, which can reduce the adhesion according to Eq. 1.2 by the incorporation of F and Si into the DLC structure, and the amount of the reduction in the surface energy was reported [102–111] to be proportional to the amount of F and Si in the DLC structure (Figure 1.20).

1.4.3.4   Effect of F on adhesion and friction

The doping of DLC coatings with F to produce fluorinated DLC (a-C:H:F) has generally been carried out using a reactive gas containing F, such as CF_4, C_2F_4, and C_2F_6 together with a hydrocarbon gas, such as CH_4, C_2H_2, or C_4H_{10} during the plasma production of

films [112–116]. An increase in the F concentration decreased the hardness of DLC, with the resulting hardness values being much lower than with a-C:H films [106, 107, 112]. The tribological properties of the films were reported to have optimum values for moderately $[0.1 < [F/(F+C)] < 0.2]$ fluorinated films [101], which was evidenced by sliding experiments against steel counterfaces with COF values between $0.10 - 0.15$ [106, 117]. The a-C:H:F coatings showed a superior adhesion mitigating performance when compared to a-C:H and other films, when used as a coating for mold surfaces in nanoimprinting lithography applications [118–121]. There are no studies reporting the performance of a-C:H:F coatings in tribological applications against Al, or when they are used in the manufacturing of Al alloys. In view of the results from the current literature, a-C:H:F is promising for reducing friction and mitigating the adhesion in Al manufacturing and sliding applications. Therefore, we have investigated the surface stability of a-C:H:F coatings, and studied the adhesion mechanisms between Al and a-C:H:F coatings using tribological experiments and first principles calculations, which will be presented in Chapters 2 and 3.

1.4.3.5 Effect of Si on adhesion and friction

In some manufacturing and sliding applications, a DLC coating that has less environmentally dependent tribological properties is preferred, and Si containing DLC coatings showed stable tribological properties in varying environmental conditions. Initially, Si incorporation in DLC films was carried out with the purpose of decreasing surface energy, decreasing internal stress, and increasing the DLC's adhesion to substrates. The addition of Si in a-C:H coatings was not only reported to decrease the COF from 0.2 to as low as 0.03 [102, 122–126] (when tested against steel in ambient air (30% RH)), but also to maintain the stability of the COF in varying humidity levels (0-85 %RH) [75, 101, 102, 122, 123, 127–130], as shown in Figure 1.21. The low COF values of a-C:H:Si were attributed to either a decrease in the surface energy [131] or the formation of a carbonaceous layer on the steel surface, incorporating SiO_x groups [124, 132]. However, the details of the mechanisms responsible for how the SiO_x groups facilitate the maintenance of a constant COF are yet to be clarified. Although Si incorporation reduced the sensitivity to humidity of the tribological properties of DLC against ferrous materials, Si containing DLC $(7 - 16 \text{ at.}\%)$ was not effective in preventing

Al adhesion to the coating surface during forming where more aluminum adhesion to tool surfaces occurred, when compared to DLC coatings without Si [99, 133]. The adhesion mechanisms and friction reducing effects of the SiO_x incorporation into DLC coatings against Al under varying atmospheric conditions are presented in this thesis in Chapter 4.

1.4.4 Pt/carbon electro-catalyst adhesion problem in fuel cells

Strong adhesion causes important problems in manufacturing processes as reviewed in previous sections, but sometimes it is low adhesion that creates a problem in automotive applications, such as in fuel cells. Platinum-carbon interfaces are present in various electrochemical systems, where carbon is used as a support material to conduct electrons to the Pt catalysts for specific electrochemical reactions. Such systems include direct methanol fuel cells (DMFCs), proton exchange membrane fuel cells (PEMFCs) [21], and lithium-air batteries [134, 135]. In these electrochemical environments, however, Pt-carbon interface degradation can limit the long term durability required by transportation applications [136]. For instance, in PEMFCs, the degradation of a carbon-supported Pt catalyst system results in the coarsening of Pt nanoparticles (Figure 1.22) [137], and causes a substantial performance reduction due to a decrease in the electrochemically active surface area (Figure 1.23) [23]. Both the dissolution of the Pt particles from the carbon support [22], and the agglomeration of the Pt particles during electrochemical cycling, are found to contribute to electro-catalyst degradation.

The agglomeration of Pt particles occurs via two equally interposed mechanisms: Ostwald ripening (the dissolution of small particles and their redeposition into larger particles) and the migration of Pt particles on the carbon support as schematically shown in Figure 1.24 [137]. The agglomeration of Pt particles due to migration on the carbon surface was believed to be a result of the weak binding between Pt and carbon. The weakest interface of Pt and carbon is formed between the Pt (111) and graphite basal planes. At the PEMFC electrodes, consisting of Pt deposited on carbon fibers and carbon black, high resolution transmission electron microscopy (HR TEM) investigations observed the formation of interfaces between the Pt (111) and graphite (0001) surfaces [138, 139]. X-ray absorp-

tion spectroscopy [140] and low-energy electron microscopy experiments [141] showed a very weak interaction between the Pt (111) and graphite (0001) surfaces, in accordance with the first principles calculations [142–146].

To avoid Pt particle agglomeration on the carbon surface, either the carbon surface or the Pt catalyst surface (or both) can be modified by enhancing the interfacial strength between Pt and C. To anchor Pt to the carbon surface, while maintaining or increasing the catalytic performance of Pt without sacrificing the electron conductivity of carbon, metallic elements can be incorporated at the Pt/C interface. The Pt catalyst surface can be alloyed with metals [147–149] that can increase the catalytic activity, and these metals are also shown to decrease the agglomeration of Pt particles [150–155]. The increase in the resistance of the Pt particles to agglomeration was attributed to the interaction of the alloying elements on the carbon support [156]. This was also confirmed with the first principles calculations that have shown that a Ru-alloyed Pt surface resulted in an increase in the Pt/C interface strength due to the strong interaction between Ru and carbon [142].

One disadvantage in modifying the Pt surface with metals is the difficulty in controlling the surface composition, since the alloyed Pt surfaces may be composed of only Pt atoms due to the surface segregation of Pt and near surface alloys [147, 149] that can form. Alternatively, the carbon surface was modified to enhance the interface adhesion between the Pt and the carbon without changing the catalytic properties of Pt [157]. The functionalizing of the carbon support by sulphur, nitrogen, and phosphorus yielded an increase in the binding of Pt, while nitrogen doping additionally improved the catalytic activity of the Pt particles [158]. The use of carbon nanotubes (CNTs) [159, 160] and graphene [161] as support materials was found to initiate stronger binding with the Pt particles. First principles calculations [162–165] were used to show the effect of different molecular groups on the enhancement of the Pt/C interface, but organic molecules may not sufficiently improve the electron conductivity between the carbon support and the Pt catalyst. Therefore, the modification of the carbon surface by metallic elements could be more effective when the focus is the interface strength and conductivity. However, there are no systematic studies available in the literature that compare the metallic modifications on the carbon surface. In this thesis a first principles investigation was carried out systematically to screen possible

metals that can anchor Pt on carbon surfaces and, the results are presented in Chapter 7.

1.5 Approach to industrial adhesion problem

To understand what could actually result in the adhesion between contacting pairs, we used atomistic modeling methods. When the atomistic models were constructed, and suitable methodologies were selected, the objective was not to simulate exactly the experimental or real conditions, and not to directly match the computed and the measured data. Instead, atomistic models that provided information about the chemical and physical properties of materials in contact were constructed, and by varying the parameters, it was examined if the predicted chemical changes were reflected in the experimental observations. For instance, when studying Al and a-C:H:F adhesion in Chapter 3, tribological experiments provided the COF data, but in the atomistic models, the interfacial forces between single crystal Al and diamond:F were estimated. The calculation of the COF between Al and a-C:H:F using atomistic methods would require the use of a very large, amorphous DLC structure against polycrystalline Al, including the effects of surface asperities, temperature, atmospheric gases, and loading conditions, and even using such a complex system would not necessarily give the correct prediction of the measured COF. Alternatively, more accurate adhesion measurement techniques could be used, such as an atomic force microscope (AFM), that could provide us with the atomic scale force between the Al and a-C:H:F coatings, which may then be directly compared to the results of the first principles calculations. In that case, the AFM experiments would measure only the interatomic forces at a nm scale between the Al asperity and the a-C:H:F surface, which would not be representative of the industrial adhesion problem. Instead, interfacial forces, calculated by first principle methods, between two F- and two H-passivated diamond surfaces were compared, and correlated perfectly the variation with the difference in the COF measured between the Al vs. the a-C:H:F and a-C:H.

When studying an industrial problem, and if one wants to benefit from the advantages of both the experimental and computational elements in order to solve the problem, the aim should not be to directly match the computed and measured data, unless the objective

was to validate the model or use the data in an upscale model in the multi-scale framework of materials modeling. In an industrial problem, the objective is generally an improvement in the material's performance in a corresponding application condition, which can either be achieved by replacing the material or by improving the performance of that material. Moreover, any individual data obtained from a materials model, even with the highest degree of accuracy (for accuracy calculations it also has to be compared with other data), will not be valuable, unless it is compared with other simulation data or an experimental result. The measured data from real observations will always be more valuable than the computed data from idealized unrealistic material models, so it would be a waste of computer resources to try to simulate an impossibly hard (and worthless) imaginary reality. Note that the leap in computational power in the last 20 years has only enabled the size of the system that can be studied to increase from approximately 1 nm to approximately 2–3 nm in quantum mechanics based methods. Therefore, in 20 years the system size will likely only be tripled, and even the roughest projections tell us that in the next couple of decades, we will still be far away from studying real size systems using atomistic models. Also, increase in computational power lead researchers to use more accurate and much slower methods. Therefore, for the adhesion problem, understanding the mechanisms of Al-DLC coating interactions, oxidation induced oxide fiber formation during Al hot forming, and Pt/carbon interactions is substantially useful for finding the solutions to industrial problems.

Once the mechanisms responsible for the industrial problem are found, the next step can be to identify a material solution (e.g. F incorporation to DLC coating) that can show better performance in the corresponding industrial conditions (better adhesion mitigation and low friction) than the existing materials. Data mining techniques can be used for this purpose in which the existing materials can be systematically replaced or modified with other possible elements. Data mining is a very efficient way to computationally design materials, since a vast number of materials can be screened and desired material properties can be calculated in a reasonable amount of time. The same research on this large number of materials systems would take tens of years to study when using experimental methods, and even better, data mining is free of charge. One can calculate many fundamental material properties using atomistic modeling tools for an infinite number of structures, as reported

in recently constructed material property databases, using atomistic modeling tools such as the Materials Project and AFLOWLIB. However, most easily calculated data from atomistic tools, although fundamentally valuable, are very hard to measure, and not directly related to or often do not give any insight into the industrial problem. Therefore, the data obtained may not fulfill the expectations of the industry. Industrial problems generally arise during the operation and processing of materials, and the mechanisms of the industrial problem should be known in advance, before searching for a material modification. Accordingly, data mining should be done in a systematic way that relies on the mechanisms of the problem, as we have demonstrated in this dissertation in order to find anchoring elements that can enhance the Pt/carbon interface strength in fuel cell applications. Also, future computational data mining methods should focus on the actual reasoning of a material property as the objective.

In summary, many different experimental results using different methods can be obtained, and a great deal of computational data can be generated to study a specific materials problem, which may in turn open up thousands of possibilities for a solution. However, in order to solve industrial problems, it is not desirable to prove the impossibilities of each of the many possibilities, but it is more valuable to reach the ultimate solution to the problem as directly as possible. This can be achieved by elucidating the mechanisms of the problem by combining carefully designed experiments and models with a goal to capture the quantitative changes, not the quantitative values, of the material properties, as demonstrated in this dissertation.
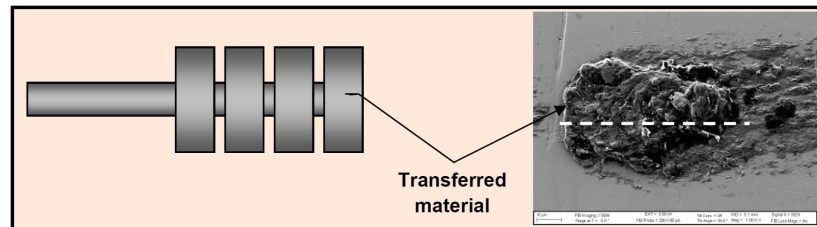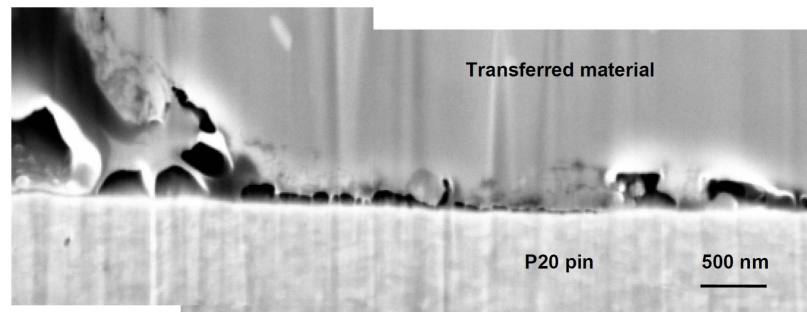
Figure 1.9: (a) Schematic representation of the P20 steel pin showing the location of the transferred material, (b) FIB cross-section of the transferred material showing the material attached to the pin surface. (c) Magnified image taken from the micrograph in plate (b) shows the interface between the transferred material and the P20 pin [45]. The direction of pin sliding against the AA5083 surface is along the cylindrical axis and towards the right side of the pin.
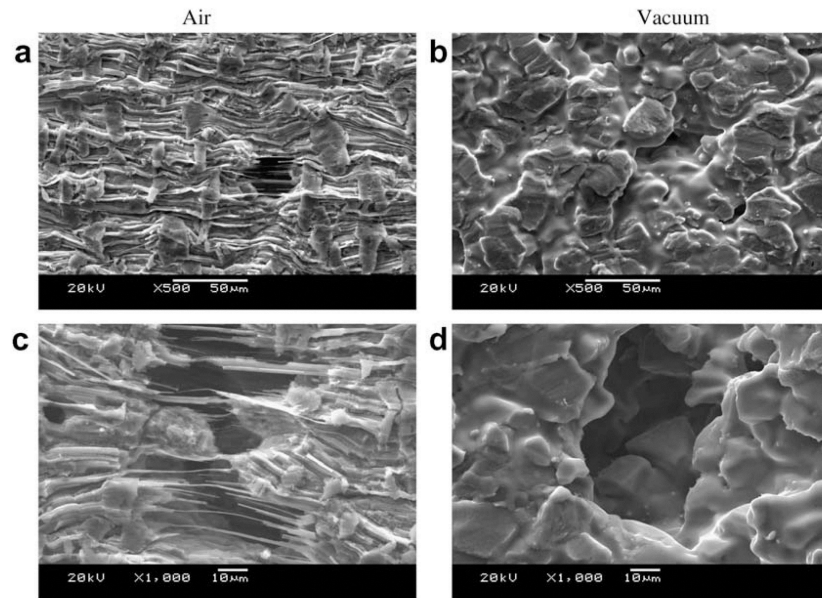
Figure 1.10: A series of photomicrographs from superplastically deformed AA5083 specimens tested in air (a and c) and in vacuum (b and d). The left column shows a specimen tested in air at (a) a continuous specimen surface, (c) a cavity opening and the fracture surface. The right column shows a specimen tested in vacuum at (b) a continuous specimen surface, (d) a cavity opening and the fracture surface. The tensile axis is approximately horizontal in all images [20].
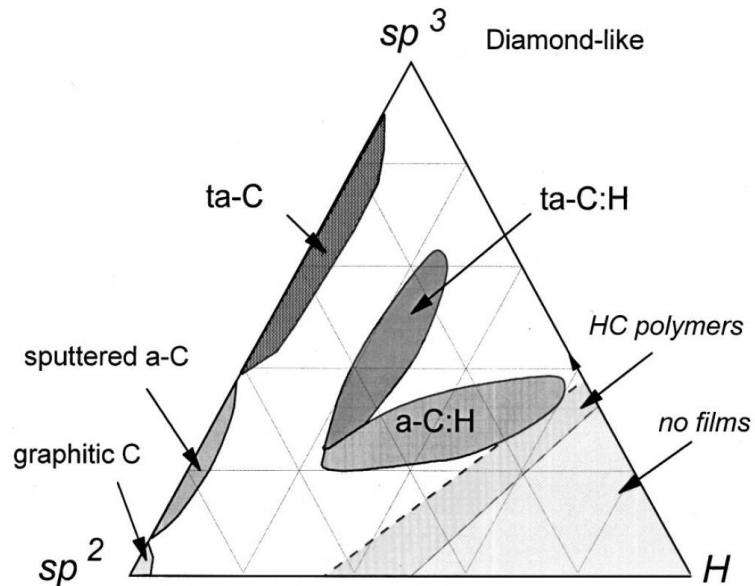
Figure 1.11: Ternary phase diagram of amorphous carbons. The three corners correspond to diamond, graphite, and hydrocarbons, respectively [59].
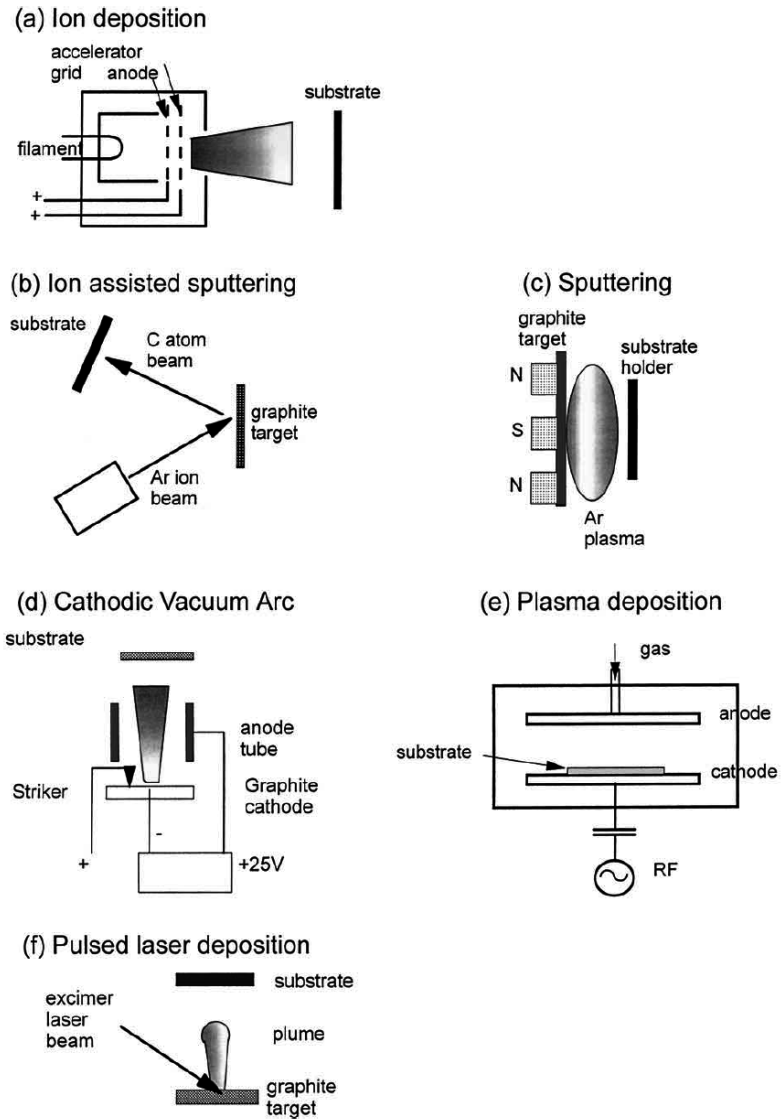
Figure 1.12: Schematics of various deposition systems for DLC production [59].
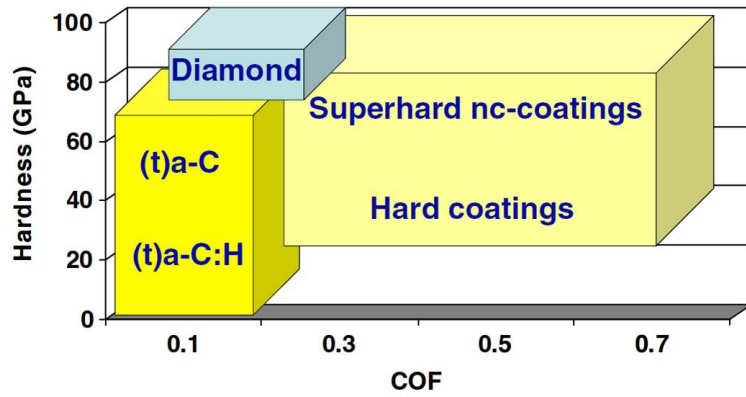
Figure 1.13: A schematic representation of hardness and the coefficients of friction (COF) of carbon-based and other hard coatings [55].
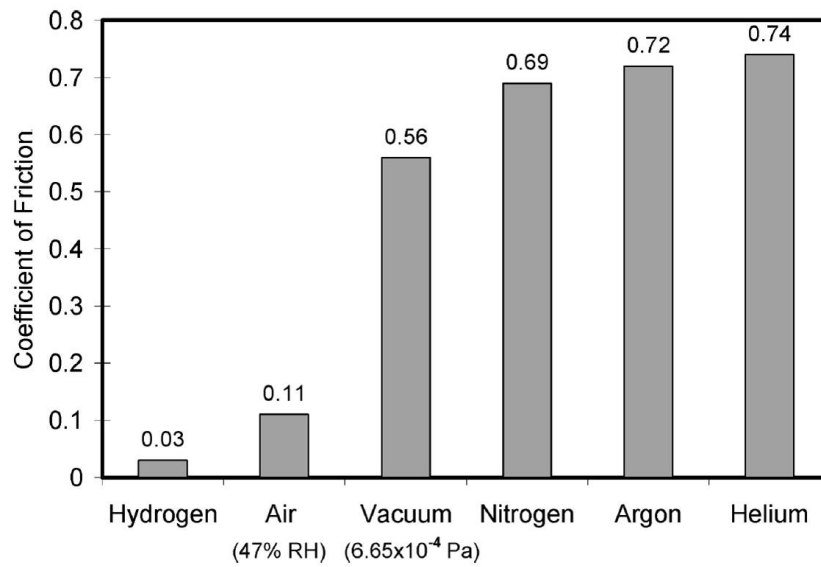
Figure 1.14: The average COF values between the a-C and the 319 Al pin under various test conditions. The sliding speed and the applied load were 0.12 m/s and 5 N in all tests [94].
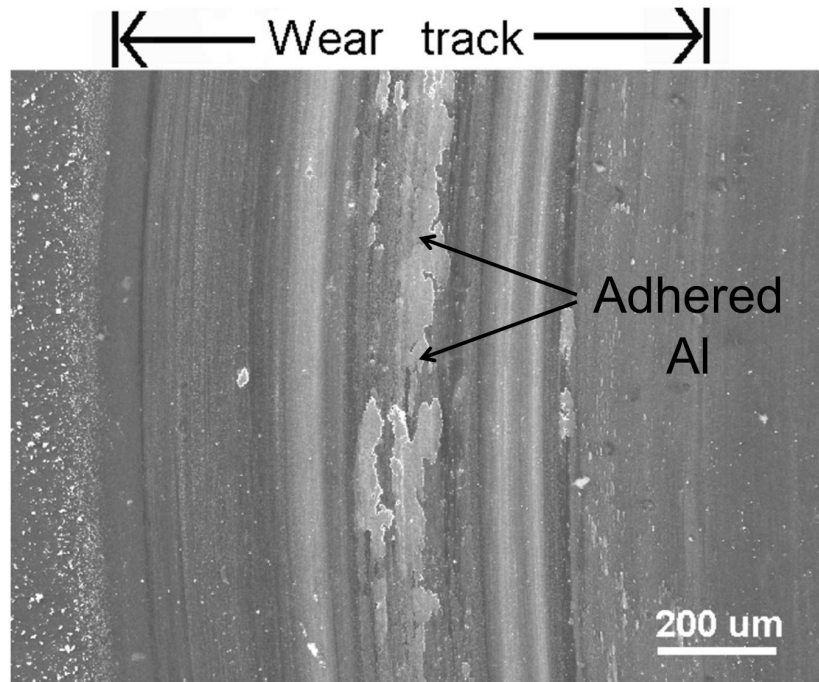
Figure 1.15: The secondary electron SEM images of a region of the wear track of the non-hydrogenated DLC (a-C) coating tested against the 319 Al pin in vacuum (6.65×10^{-4} Pa) for 10^4 revolutions under 5 N applied load. The DLC coating was worn down to the substrate (M2 steel), except in the middle, where it was mostly covered by the adhered aluminum [94].
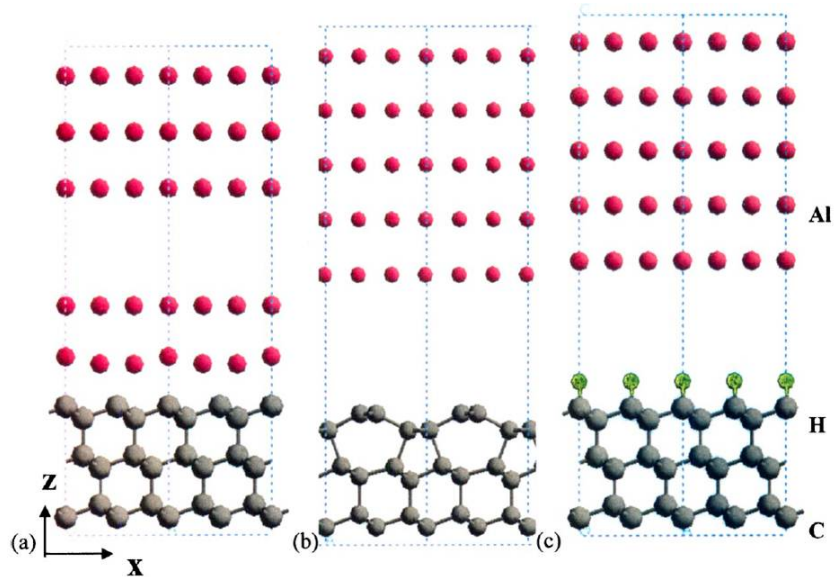
Figure 1.16: The fractured interface structure of (a) $Al(111)/C(111) - 1 \times 1$ showing two Al transfer layers, (b) $Al(111)/C(111) - 2 \times 1$, and (c) $Al(111)/C(111) - 1 \times 1$:H without adhesive transfer [97].
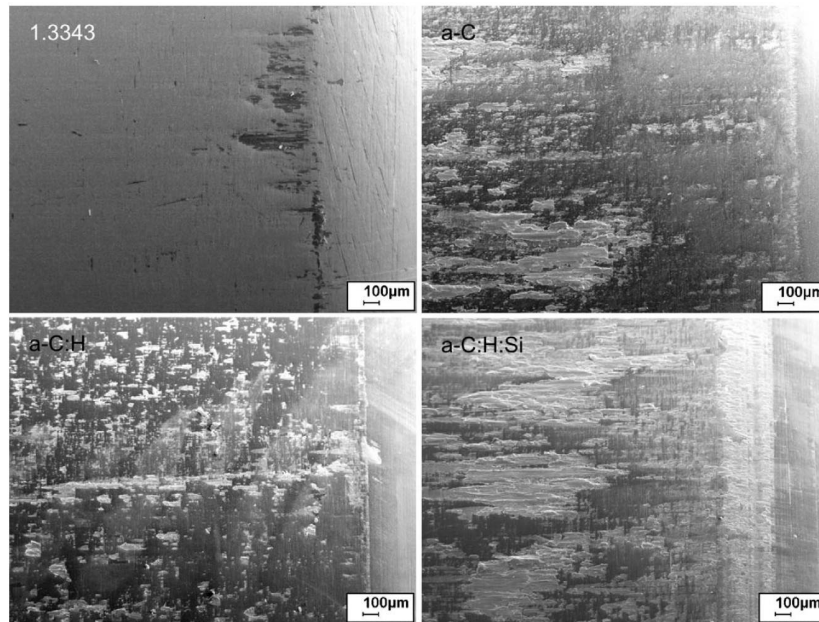
Figure 1.17: Transfer of AA6016 workpiece material to the punch tip edge [99].
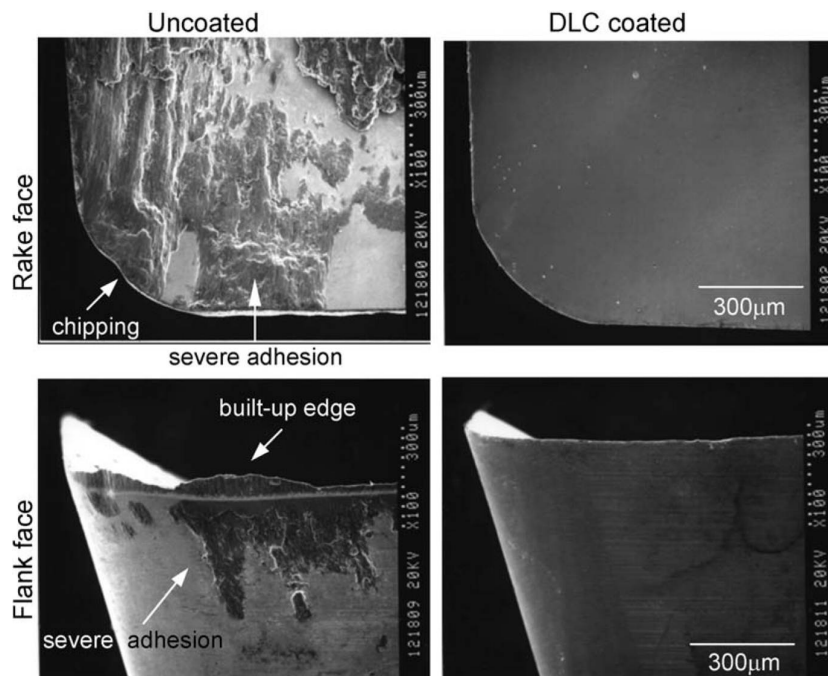
Figure 1.18: SEM micrographs of the rake and the flank faces of the tool after the dry milling test for the AlCu2.5Si18 alloy (cutting length 36 m) [47].
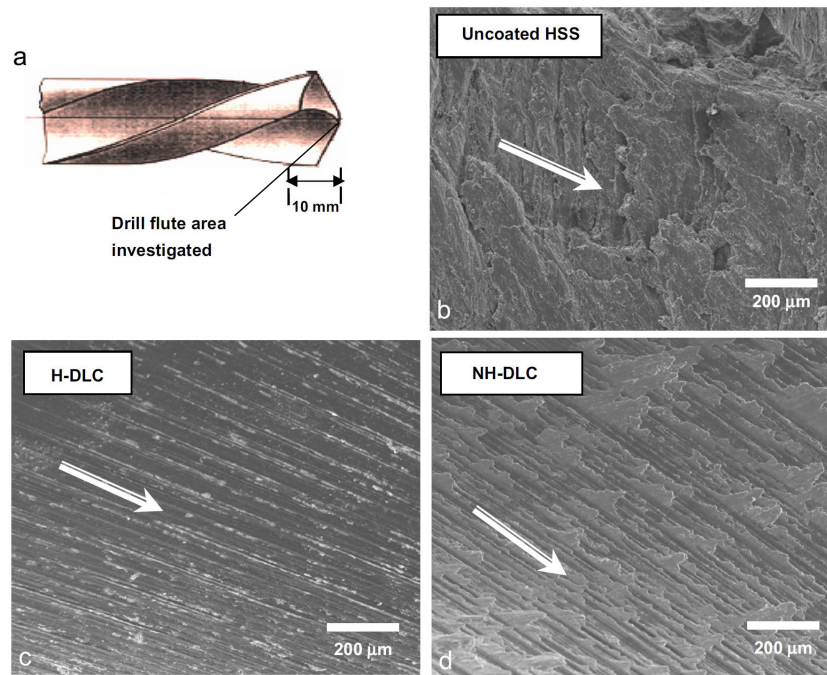
Figure 1.19: SEM secondary electron images showing the aluminum adhesion to the drill flutes: (a) schematic representation of drill flute showing the area investigated, (b) uncoated HSS tool, (c) H-DLC-coated tool, and (d) NHDLC-coated tool. The flute surface of the uncoated HSS drill was almost entirely covered by adhered aluminium. The direction of the chip flow is shown by the arrow [100].
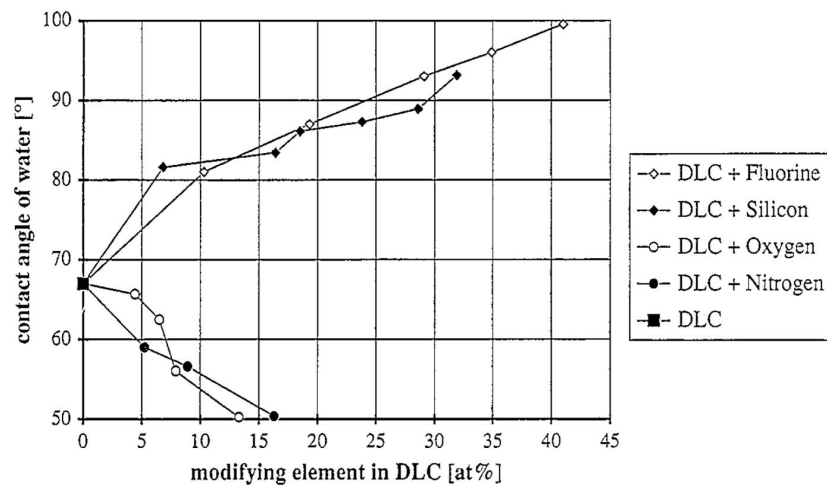
Figure 1.20: Change in the contact angle of water by adding different elements to DLC coatings [102].
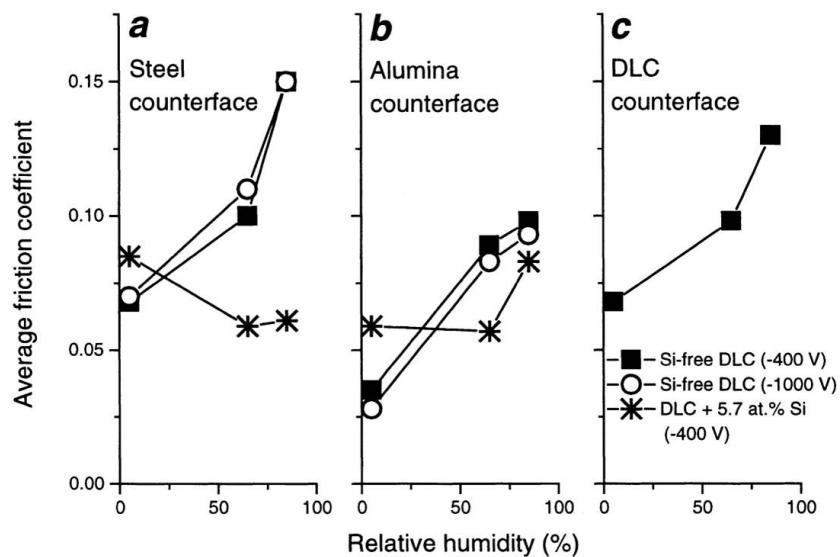
Figure 1.21: Evolution of the average coefficient of friction as a function of the ambient humidity for (a) steel, (b) alumina, and (c) DLC counterfaces rubbing against reference DLC (-400 V)., high-bias DLC (-1000 V). and Si-containing DLC (5.7 at.% Si). [128].
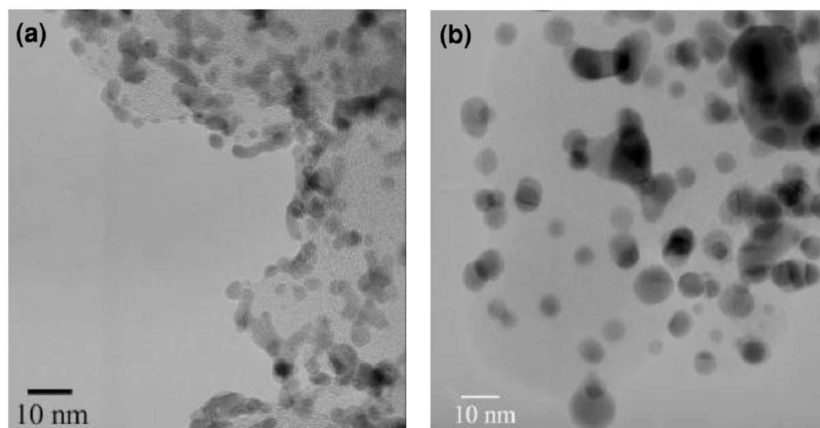
Figure 1.22: Typical TEM micrographs from (a) the pristine Pt/Vulcan samples powder sample, and (b) powders scraped away from the cathode surface of the cycled MEA sample. Considerable coarsening of the spherically shaped platinum nanoparticles was found after potential cycling [137].
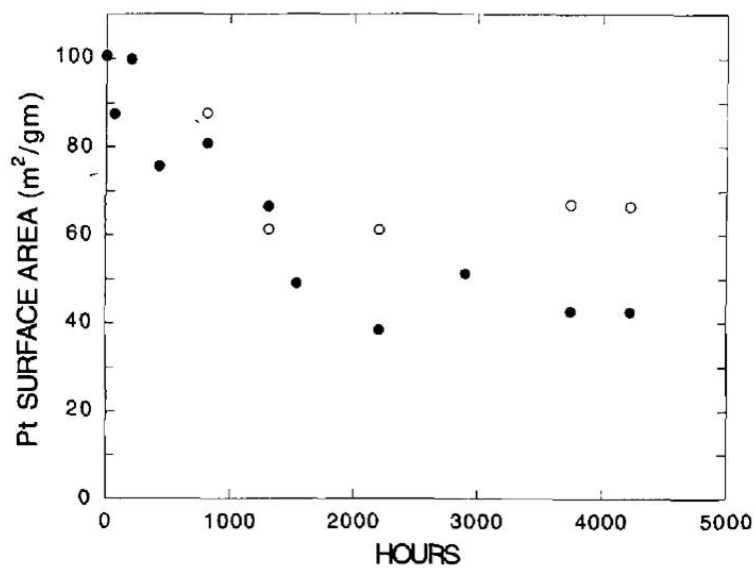
Figure 1.23: Specific Pt surface areas of PEM fuel cell electrode catalysts after life tests. (○) Anodes, (●) cathodes [23].
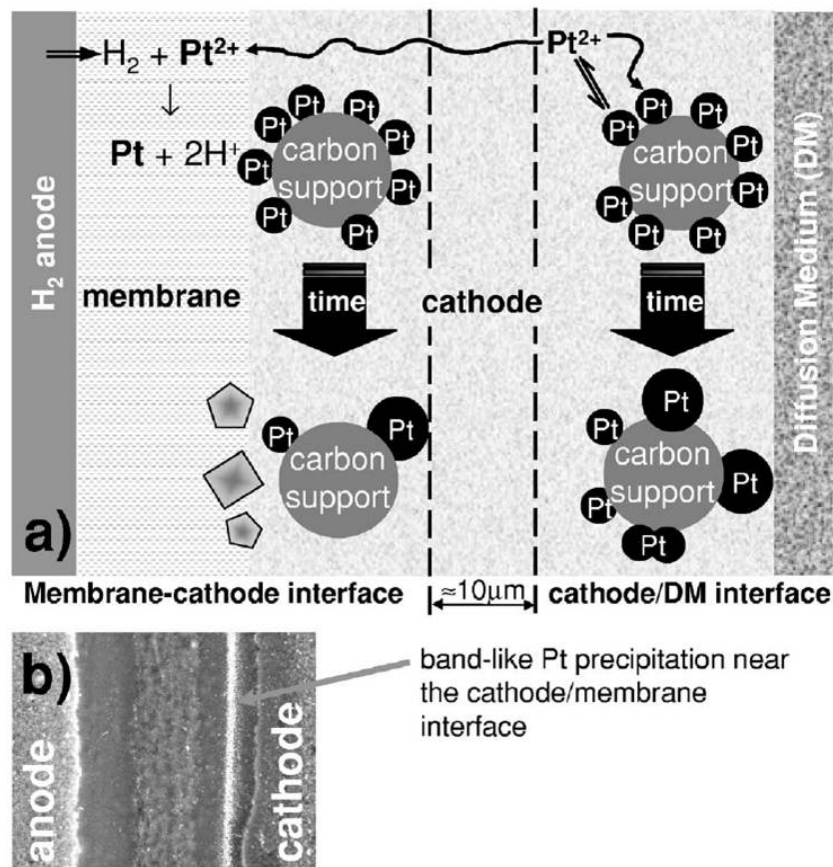
Figure 1.24: (a) Schematic representation of platinum surface area loss on (i) the nanometer scale, where platinum particles grow on carbon support via Ostwald ripening, and (ii) the micrometer scale, where dissolved platinum species diffuse toward the membrane, become reduced, and precipitate as platinum particles in the ionomer phase by crossover hydrogen molecules from the anode. (b) SEM cross section of a short-stack MEA operating at OCV for 2000 h, where the bright band in the image indicates platinum deposited in the membrane close to the membrane/cathode interface [137].

40

Bibliography

[1] C.L. Gray and F. Von Hippel. The fuel economy of light vehicles. *Sci. Am.*, 244(5):48–59, 1981.

[2] R. Wohlecker, M. Johannaber, and M. Espig. Determination of weight elasticity of fuel economy for ice, hybrid and fuel cell vehicles. *SAE 2007 World Congress*, 2103:2007010343, 2007.

[3] H.-J. Kim, C. McMillan, G.A. Keoleian, and S.J. Skerlos. Greenhouse gas emissions payback for lightweighted vehicles using aluminum and high-strength steel. *Journal of Industrial Ecology*, 14(6):929–946, 2010.

[4] H.-J. Kim, G.A. Keoleian, and S.J. Skerlos. Economic assessment of greenhouse gas emissions reduction by vehicle lightweighting using aluminum and high-strength steel. *Journal of Industrial Ecology*, 15(1):64–80, 2011.

[5] Lee Alonso, E., T.M., C. Bjelkengren, R. Roth, and R.E. Kirchain. Evaluating the potential for secondary mass savings in vehicle lightweighting. *Environmental Science and Technology*, 46(5):2893–2901, 2012.

[6] M.F. Mathias, R. Makharia, H.A. Gasteiger, J.J. Conley, T.J. Fuller, C.J. Gittleman, S.S. Kocha, D.P. Miller, C.K. Mittelsteadt, T. Xie, S.G. Van, and P.T. Yu. Two fuel cell cars in every garage? *Electrochemical Society Interface*, 14(3):24–35, 2005.

[7] J. Tollefson. Hydrogen vehicles: Fuel of the future? *Nature*, 464(7293):1262–1264, 2010.

[8] F. Field, R. Kirchain, and R. Roth. Process cost modeling: Strategic engineering and economic evaluation of materials technologies. *JOM*, 59(10):21–32, 2007.

[9] J. N. Israelachvili. *Intermolecular and Surface Forces*. Academic, San Diego, 2nd edition, 1992.

[10] S. Yip. *Handbook of materials modeling.* Springer, Dordrecht, The Netherlands, 2005.

[11] A. Van de Walle. *The Effect of Lattice Vibrations on Substitutional Alloy Thermodynamics.* PhD thesis, M.I.T., 2001.

[12] H. L. Coldwell, R. C. Dewes, D. K. Aspinwall, N. M. Renevier, and D. G. Teer. The use of soft/lubricating coatings when dry drilling BS L168 aluminium alloy. *Surface and Coatings Technology*, 177-178:716–726, 2004.

[13] E. Konca, Y. T. Cheng, A. M. Weiner, J. M. Dasch, A. Erdemir, and A. T. Alpas. Transfer of 319 Al alloy to titanium diboride and titanium nitride based (TiAlN, TiCN, TiN) coatings: Effects of sliding speed, temperature and environment. *Surface and Coatings Technology*, 200(7):2260–2270, 2005.

[14] E. Konca, Y. T. Cheng, A. M. Weiner, J. M. Dasch, and A. T. Alpas. Effect of test atmosphere on the tribological behaviour of the non-hydrogenated diamond-like carbon coatings against 319 aluminum alloy and tungsten carbide. *Surface and Coatings Technology*, 200(5-6):1783–1791, 2005.

[15] A. R. Riahi and A. T. Alpas. Adhesion of AA5182 aluminum sheet to dlc and TiN coatings at 25Â °C and 420Â °C. *Surface and Coatings Technology*, 202(4-7):1055–1061, 2007.

[16] D. R. Tallant, J. E. Parmeter, M. P. Siegal, and R. L. Simpson. The thermal stability of diamond-like carbon. *Diamond and Related Materials*, 4(3):191–199, 1995.

[17] P. E. Krajewski and A. T. Morales. Tribological issues during quick plastic forming. *Journal of Materials Engineering and Performance*, 13(6):700–709, 2004.

[18] S. Das, A. T. Morales, A. R. Riahi, X. Meng-Burany, and A. T. Alpas. Role of plastic deformation on elevated temperature tribological behavior of an Al-Mg alloy (AA5083): A friction mapping approach. *Metallurgical and Materials Transactions A*, 42(8):2384–2401, 2011.

[19] S. Das, A. R. Riahi, X. Meng-Burany, A. T. Morales, and A. T. Alpas. High temperature deformation and fracture of tribo-layers on the surface of AA5083 sheet aluminum-magnesium alloy. *Materials Science and Engineering A*, 531:76–83, 2012.

[20] J. K. Chang, E. M. Taleff, P. E. Krajewski, and J. R. Ciulik. Effects of atmosphere in filament formation on a superplastically deformed aluminum-magnesium alloy. *Scripta Materialia*, 60:459–462, 2009.

[21] G. Hooger. *Fuel Cell Technology Handbook*. CRC Press, Boca Raton, 2003.

[22] K. J. J. Mayrhofer, J. C. Meier, S. J. Ashton, G. K. H. Wiberg, F. Kraus, M. Hanzlik, and M. Arenz. Fuel cell catalyst degradation on the nanoscale. *Electrochemistry Communications*, 10(8):1144–1147, 2008.

[23] Mahlon S. Wilson, Fernando H. Garzon, Kurt E. Sickafus, and Shimshon Gottesfeld. Surface area loss of supported platinum in polymer electrolyte fuel cells. *Journal of the Electrochemical Society*, 140(10):2872–2877, 1993.

[24] A.H. Cottrell. *The Mechanical Properties of Matter*. John Wiley and Sons Inc., U.S.A., 1964.

[25] F.P. Bowden and D. Tabor. *The Friction and Lubrication of Solids*. Oxford University Press, Great Britain, 1950.

[26] J.S. McFarlane and D. Tabor. Relation between friction and adhesion. *Proceedings of the Royal Society of London. Series A*, 202(1069):244–253, 1950.

[27] D.H. Buckley. *Surface Effects in Adhesion, Friction, Wear and Lubrication*. Elsevier, Amsterdam, 1981.

[28] B. Bhushan. Adhesion and stiction: Mechanisms, measurement techniques, and methods for reduction. *Journal of Vacuum Science and Technology B*, 21(6):2262–2296, 2003.

[29] K.I. Johnson and D.V. Keller, Jr. Effect of contamination on the adhesion of metallic couples in ultra-high vacuum. *Journal of Applied Physics*, 38(4):1896–1904, 1967.

[30] J.B. Adams, L.G. Hector, Jr, D.J. Siegel, H. Yu, and J. Zhong. Adhesion, lubrication and wear on the atomic scale. *Surface and Interface Analysis*, 31:619–626, 2001.

[31] Occupational exposure to metalworking fluids: a criteria for a recommended standard, January 1998.

[32] ISO 14001 International Standard. Environmental management systems specification with guidance for use, 1996. 1996-09-01.

[33] S.P.F.C Jaspers and J.H Dautzenberg. Material behaviour in metal cutting: strains, strain rates and temperatures in chip formation. *Journal of Materials Processing Technology*, 121(1):123–135, 2002.

[34] H. Zhang and A.T. Alpas. Quantitative evaluation of plastic strain gradients generated during orthogonal cutting of an aluminum alloy. *Materials Science and Engineering A*, 332:249–254, 2002.

[35] H. Ni, M. Elmadagli, and A.T. Alpas. Mechanical properties and microstructures of 1100 aluminum subjected to dry machining. *Materials Science and Engineering A*, 385:267–278, 2004.

[36] J. M. Dasch, C. C. Ang, C. A. Wong, Y. T. Cheng, A. M. Weiner, L. C. Lev, and E. Konca. A comparison of five categories of carbon-based tool coatings for dry drilling of aluminum. *Surface and Coatings Technology*, 200(9):2970–2977, 2006.

[37] G. List, M. Nouari, D. Géhin, S. Gomez, J.P. Manaud, Y. Le Petitcorps, and F. Girot. Wear behaviour of cemented carbide tools in dry machining of aluminium alloy. *Wear*, 259:1177–1189, 2005.

[38] P. Chen, H. Hu, and A.T. Alpas. *Effect of Bismuth on the Tensile Properties and Dry Machining Performance of Al-12.7 wt% Si Alloy*, pages 215–223. John Wiley and Sons, Inc., 2009.

[39] Sukanta Bhowmick, Michael J. Lukitsch, and Ahmet T. Alpas. Dry and minimum quantity lubrication drilling of cast magnesium alloy (AM60). *International Journal of Machine Tools and Manufacture*, 50:444–457, 2010.

[40] S. Bhowmick and A. T. Alpas. Minimum quantity lubrication drilling of aluminium-silicon alloys in water using diamond-like carbon coated drills. *International Journal of Machine Tools and Manufacture*, 48:1429–1443, 2008.

[41] C.H. Hamilton and A.K. Ghosh, editors. *Metals Handbook Volume 14*. ASM International, Metals Park, Ohio, 1988.

[42] E.M. Taleff, P.A. Friedman, P.E. Krajewski, R.S. Mishra, and J.G. Schroth, editors. *Advances in Superplasticity and Superplastic Forming*. TMS, Warrendale, Pennsylvania, 2004.

[43] M. G. Zelin. On micro-superplasticity. *Acta Materialia*, 45(9):3533–3542, 1997.

[44] X. Meng-Burany, O. Gali, A.R. Riahi, and A.T. Alpas. unpublished. 2013.

[45] S. Das. *Plastic deformation and surface damage mechanisms during hot-forming of Al and Mg alloy sheets*. PhD thesis, University of Windsor, 2011.

[46] K. Kanda, S. Takehana, S. Yoshida, R. Watanabe, S. Takano, H. Ando, and F. Shimakura. Application of diamond-coated cutting tools. *Surface and Coatings Technology*, 73:115–120, 1995.

[47] Haruyo Fukui, Junya Okida, Naoya Omori, Hideki Moriguchi, and Keiichi Tsuda. Cutting performance of dlc coated tools in dry machining aluminum alloys. *Surface and Coatings Technology*, 187:70–76, 2004.

[48] P. W. May. The new diamond age? *Science*, 320(5883):1588, 2008.

[49] S.D.A. Lawes, M.E. Fitzpatrick, and S.V. Hainsworth. Evaluation of the tribological properties of DLC for engine applications. *Journal of Physics D: Applied Physics*, 40(18):5427–5437, 2007.

[50] Geoffrey Dearnaley and James H. Arps. Biomedical applications of diamond-like carbon (DLC) coatings: A review. *Surface and Coatings Technology*, 200(7):2518–2524, 2005.

[51] Ritwik Kumar Roy and Kwang-Ryeol Lee. Biomedical applications of diamond-like carbon coatings: A review. *Journal of Biomedical Materials Research Part B: Applied Biomaterials*, 83B(1):72–84, 2007.

[52] J.P. Sullivan, T.A. Friedmann, and K. Hjort. Diamond and amorphous carbon mems. *MRS Bulletin*, 26(04):309–311, 2001.

[53] H. Schmellenmeier. Die beeinflussung von festen oberflachen durch eine ionisierte gasatmosphare. *Experimentelle Technik der Physik*, 1:49–68, 1953.

[54] S. Aisenberg and R. Chabot. Ion-beam deposition of thin films of diamondlike carbon. *Journal of Applied Physics*, 42(7):2953–2958, 1971.

[55] A. Erdemir and C. Donnet. Tribology of diamond-like carbon films: recent progress and future prospects. *Journal of Physics. D: Applied Physics*, 39(18):R311–R327, 2006.

[56] A. Grill. Diamond-like carbon: State of the art. *Diamond and Related Materials*, 8(2-5):428–434, 1999.

[57] R. Hauert. An overview on the tribological behavior of diamond-like carbon in technical and medical applications. *Tribology International*, 37(11-12 SPEC.ISS.):991–1003, 2004.

[58] C. Donnet and A. Grill. Friction control of diamond-like carbon coatings. *Surface and Coatings Technology*, 94-95:456–462, 1997.

[59] J. Robertson. Diamond-like amorphous carbon. *Materials Science and Engineering R*, 37:129–281, 2002.

[60] A. Erdemir and J.M. Martin. *Superlubricity.* Elsevier Science, Amsterdam, Netherlands, 2007.

[61] C. Donnet and A. Erdemir, editors. *Tribology of diamond-like carbon films: fundamentals and applications.* Springer, New York, USA, 2008.

[62] A. C. Ferrari and J. Robertson. Interpretation of raman spectra of disordered and amorphous carbon. *Physical Review B*, 61(20):14095–14107, 2000.

[63] D.R. McKenzie. Tetrahedral bonding in amorphous carbon. *Reports on Progress in Physics*, 59:1611–1664, 1996.

[64] B. Druz, E. Ostan, S. Distefano, A. Hayes, V. Kanarov, V. Polyakov, A. Rukovishnikov, N. Rossukanyi, and A. Khomich. Diamond-like carbon films deposited using a broad, uniform ion beam from an RF inductively coupled ch_4-plasma source. *Diamond and Related Materials*, 7(7):965–972, 1998.

[65] J.J. Cuomo, J.P. Doyle, J. Bruley, and J.C. Liu. Sputter deposition of dense diamond-like carbon films at low temperature. *Applied Physics Letters*, 58(5):466–468, 1991.

[66] A.A. Voevodin and M.S. Donley. Preparation of amorphous diamond-like carbon by pulsed laser deposition: a critical review. *Surface and Coatings Technology*, 82(3):199–213, 1996.

[67] V.I. Merkulov, D.H. Lowndes, G.E. Jellison, A.A. Puretzky, and D.B. Geohegan. Structure and optical properties of amorphous diamond films prepared by ArF laser ablation as a function of carbon ion kinetic energy. *Applied Physics Letters*, 73(18):2591–2593, 1998.

[68] L. Holland. Deposition of hard and insulating carbonaceous films on an rf target in a butane plasma. *Thin Solid Films*, 38:L17–L19, 1976.

[69] M. Weiler, S. Sattel, T. Giessen, K. Jung, H. Ehrhardt, V.S. Veerasamy, and J. Robertson. Preparation and properties of highly tetrahedral hydrogenated amorphous carbon. *Physical Review B*, 53(3):1594–1608, 1996.

[70] W.C. Oliver and G.M. Pharr. Nanoindentation in materials research: Past, present, and future. *MRS Bulletin*, 35(11):897–907, 2010.

[71] W. C. Oliver and G. M. Pharr. Improved technique for determining hardness and elastic modulus using load and displacement sensing indentation experiments. *Journal of Materials Research*, 7(6):1564–1580, 1992.

[72] T. Y. Tsui, G. M. Pharr, W. C. Oliver, C. S. Bhatia, R. L. White, S. Anders, A. Anders, and I. G. Brown. Nanoindentation and nanoscratching of hard carbon coatings for magnetic disks. In *Proceedings of the 1995 MRS Spring Meeting*, volume 383, pages 447–452, Pittsburgh, PA, United States, 17 April 1995 through 20 April 1995 1995. Affiliation: Rice Univ, Houston, United States; Correspondence Address: Tsui, T.Y.; Rice Univ Houston, United States, Materials Research Society.

[73] B. Schultrich, H.-J. Scheibe, D. Drescher, and H. Ziegele. Deposition of superhard amorphous carbon films by pulsed vacuum arc deposition. *Surface and Coatings Technology*, 98:1097–1101, 1998.

[74] S. Xu, D. Flynn, B.K. Tay, S. Prawer, K.W. Nugent, S.R.P. Silva, Y. Lifshitz, and W.I. Milne. Mechanical properties and raman spectra of tetrahedral amorphous carbon films with high sp3 fraction deposited using a filtered cathodic arc. *Philosophical Magazine B*, 76(3):351–361, 1997.

[75] J. Sanchez-Lopez and A. Fernandez. *Doping and alloying effects on DLC coatings*, pages 311–338. Springer, 2008.

[76] J.W. Ager, S. Anders, I.G. Brown, M. Nastasi, and K.C. Walter. Multilayer hard carbon films with low wear rates. *Surface and Coatings Technology*, 91:91–94, 1997.

[77] S. Anders, D.L. Callahan, G.M. Pharr, T.Y. Tsui, and C.S. Bhatia. Multilayers of amorphous carbon prepared by cathodic arc deposition. *Surface and Coatings Technology*, 94:189–194, 1997.

[78] A. Grill. Tribology of diamondlike carbon and related materials: an updated review. *Surface and Coatings Technology*, 94-95:507–513, 1997.

[79] D. S. Grierson and R. W. Carpick. Nanotribology of carbon-based materials. *Nano Today*, 2(5):12–21, 2007.

[80] F. P. Bowden and D. Tabor. *The friction and lubrication of solids*. Oxford University Press, New York, 1950.

[81] E. Konca, Y. T. Cheng, and A. T. Alpas. Sliding wear of non-hydrogenated diamond-like carbon coatings against magnesium. *Surface and Coatings Technology*, 201(7 SPEC. ISS.):4352–4356, 2006.

[82] E. Konca, Y. T. Cheng, and A. T. Alpas. Dry sliding behaviour of non-hydrogenated DLC coatings against Al, Cu and Ti in ambient air and argon. *Diamond and Related Materials*, 15(4-8):939–943, 2006.

[83] K. Enke, H. Dimigen, and H. Hübsch. Frictional properties of diamondlike carbon layers. *Applied Physics Letters*, 36(4):291–292, 1980.

[84] H. Ronkainen, J. Koskinen, J. Likonen, S. Varjus, and J. Vihersalo. Characterization of wear surfaces in dry sliding of steel and alumina on hydrogenated and hydrogen-free carbon films. *Diamond and Related Materials*, 3(11-12):1329–1336, 1994.

[85] H. Ronkainen, J. Likonen, J. Koskinen, and S. Varjus. Effect of tribofilm formation on the tribological performance of hydrogenated carbon coatings. *Surface and Coatings Technology*, 79(1-3):87–94, 1996.

[86] H. Ronkainen, J. Koskinen, J. Likonen, S. Varjus, and J. Vihersalo. Characterization of wear surfaces in dry sliding of steel and alumina on hydrogenated and hydrogen-free carbon films. *Diamond and Related Materials*, 3(11-12):1329–1336, 1994.

[87] Y. Liu, A. Erdemir, and E. I. Meletis. An investigation of the relationship between graphitization and frictional behavior of DLC coatings. *Surface and Coatings Technology*, 86-87(1 -3 pt 2):564–568, 22 April 1996 through 26 April 1996 1996.

[88] Y. Liu, A. Erdemir, and E. I. Meletis. A study of the wear mechanism of diamond-like carbon films. *Surface and Coatings Technology*, 82(1-2):48–56, 1996.

[89] A. Erdemir, C. Bindal, J. Pagan, and P. Wilbur. Characterization of transfer layers on steel surfaces sliding against diamond-like hydrocarbon films in dry nitrogen. *Surface and Coatings Technology*, 76-77(PART 2):559–563, 1995.

[90] R.H. Savage. Graphite lubrication. *Journal of Applied Physics*, 19(1):1–10, 1948.

[91] F.P. Bowden and J.E. Young. Friction of diamond, graphite, and carbon and the influence of surface films. *Proceedings of the Royal Society of London A*, 208(1095):444–455, 1951.

[92] R.H. Savage and D.L. Schaefer. Vapor lubrication of graphite sliding contacts. *Journal of Applied Physics*, 27(2):136–138, 1956.

[93] P.J. Bryant, P.L. Gutshall, and L.H. Taylor. A study of mechanisms of graphite friction and wear. *Wear*, 7(1):118–126, 1964.

[94] E. Konca, Y. T. Cheng, A. M. Weiner, J. M. Dasch, and A. T. Alpas. The role of hydrogen atmosphere on the tribological behavior of non-hydrogenated DLC coatings against aluminum. *Tribology Transactions*, 50(2):178–186, 2007.

[95] Y. Qi, E. Konca, and A. T. Alpas. Atmospheric effects on the adhesion and friction between non-hydrogenated diamond-like carbon (DLC) coating and aluminum - A first principles investigation. *Surface Science*, 600(15):2955–2965, 2006.

[96] E. Konca, Y. T. Cheng, A. M. Weiner, J. M. Dasch, and A. T. Alpas. Vacuum tribological behavior of the non-hydrogenated diamond-like carbon coatings against aluminum: Effect of running-in in ambient air. *Wear*, 259(1-6):795–799, 2005.

[97] Yue Qi and L. G. Hector. Adhesion and adhesive transfer at aluminum/diamond interfaces: a first-principles study. *Physical Review B*, 69(23):235401, 06/15 2004.

[98] Yue Qi, Jr. L. G. Hector, N. Ooi, and J. B. Adams. A first principles study of adhesion and adhesive transfer at Al(111)/graphite(0001). *Surface Science*, 581(2-3):155–168, 05/01 2005.

[99] A. Wank, G. Reisel, and B. Wielage. Behavior of DLC coatings in lubricant free cold massive forming of aluminum. *Surface and Coatings Technology*, 201(3-4):822–827, 2006.

[100] S. Bhowmick and A. T. Alpas. The performance of hydrogenated and non-hydrogenated diamond-like carbon tool coatings during the dry drilling of 319 Al. *International Journal of Machine Tools and Manufacture*, 48:802–814, 2008.

[101] C. Donnet. Recent progress on the tribology of doped diamond-like and carbon alloy coatings: A review. *Surface and Coatings Technology*, 100-101(1-3):180–186, 1998.

[102] M. Grischke, K. Bewilogua, K. Trojan, and H. Dimigen. Application-oriented modifications of deposition processes for diamond-like-carbon-based coatings. *Surface and Coatings Technology*, 74-75:739–745, 1995.

[103] M. Ishihara, T. Kosaka, T. Nakamura, K. Tsugawa, M. Hasegawa, F. Kokai, and Y. Koga. Antibacterial activity of fluorine incorporated DLC films. *Diamond and Related Materials*, 15(4-8):1011–1014, 2006.

[104] X. M. He, M. Hakovirta, A. M. Peters, B. Taylor, and M. Nastasi. Fluorine and boron co-doped diamond-like carbon films deposited by pulsed glow discharge plasma immersion ion processing. *Journal of Vacuum Science and Technology A*, 20(3):638–642, 2002.

[105] M. Hakovirta, D. H. Lee, X. M. He, and M. Nastasi. Synthesis of fluorinated diamond-like carbon films by the plasma immersion ion processing technique. *Journal of Vacuum Science and Technology A*, 19(3):782–784, 2001.

[106] M. Hakovirta, X. M. He, and M. Nastasi. Optical properties of fluorinated diamond-like carbon films produced by pulsed glow discharge plasma immersion ion processing. *Journal of Applied Physics*, 88(3):1456–1459, 2000.

[107] K. P. Huang, P. Lin, and H. C. Shih. Structures and properties of fluorinated amorphous carbon films. *Journal of Applied Physics*, 96(1):354–360, 2004.

[108] G. Q. Yu, B. K. Tay, and Z. Sun. Fluorinated amorphous diamond-like carbon films deposited by plasma-enhanced chemical vapor deposition. *Surface and Coatings Technology*, 191(2-3):236–241, 2005.

[109] R. Prioli, L. G. Jacobsohn, M. E. H. Maia da Costa, and Jr. F. L. Freire. Nanotribological properties of amorphous carbon-fluorine films. *Tribology Letters*, 15(3):177–180, 2003.

[110] T. Nakamura, T. Ohana, M. Hasegawa, K. Tsugawa, M. Suzuki, M. Ishihara, A. Tanaka, and Y. Koga. Chemical modification of diamond surfaces with fluorine-containing functionalities. *New Diamond and Frontier Carbon Technology*, 15(6):313–324, 2005.

[111] S. A. Kulinich and M. Farzaneh. On wetting behavior of fluorocarbon coatings with various chemical and roughness characteristics. *Vacuum*, 79(3-4):255–264, 2005.

[112] L. G. Jacobsohn, D. F. Franceschini, M. E. H. Maia da Costa, and Jr. F. L. Freire. Structural and mechanical characterization of fluorinated amorphous-carbon films deposited by plasma decomposition of CF_4-CH_4 gas mixtures. *Journal of Vacuum Science and Technology A*, 18(5):2230–2238, 2000.

[113] R. S. Butter, D. R. Waterman, A. M. Lettington, R. T. Ramos, and E. J. Fordham. Production and wetting properties of fluorinated diamond-like carbon coatings. *Thin Solid Films*, 311(1-2):107–113, 1997.

[114] K. Trojan, M. Grischke, and H. Dimigen. Network modification of DLC coatings to adjust a defined surface energy. *Physica Status Solidi A*, 145(2):575–585, 1994.

[115] F. L. Freire Jr., M. E. H. Maia da Costa, L. G. Jacobsohn, and D. F. Franceschini. Film growth and relationship between microstructure and mechanical properties of a-C:H:F films deposited by PECVD. *Diamond and Related Materials*, 10(2):125–131, 2001.

[116] L. G. Jacobsohn, M. E. H. Maia da Costa, V. J. Trava-Airoldi, and Jr F. L. Freire. Hard amorphous carbon-fluorine films deposited by PECVD using C_2H_2-CF_4 gas mixtures as precursor atmospheres. *Diamond and Related Materials*, 12(10-11):2037–2041, 2003.

[117] C. Donnet, J. Fontaine, A. Grill, V. Patel, C. Jahnes, and M. Belin. Wear-resistant fluorinated diamondlike carbon films. *Surface and Coatings Technology*, 94-95:531–536, 1997.

[118] K. I. Nakamatsu, N. Yamada, K. Kanda, Y. Haruyama, and S. Matsui. Fluorinated diamond-like carbon coating as antisticking layer on nanoimprint mold. *Japanese journal of Applied Physics*, 45(33-36):L954–L956, 2006.

[119] N. Yamada, K. I. Nakamatsu, K. Kanda, Y. Haruyama, and S. Matsui. Surface evaluation of fluorinated diamond-like carbon thin film as an antisticking layer of nanoimprint mold. *Japanese Journal of Applied Physics*, 46(9B):6373–6374, 2007.

[120] M. Schvartzman and S. J. Wind. Plasma fluorination of diamond-like carbon surfaces: Mechanism and application to nanoimprint lithography. *Nanotechnology*, 20(14):145306, 2009.

[121] R. W. Fillman and R. R. Krchnavek. Ultrathin fluorinated diamondlike carbon coating for nanoimprint lithography imprinters. *Journal of Vacuum Science and Technology B*, 27(6):2869–2872, 2009.

[122] R. Gilmore and R. Hauert. Control of the tribological moisture sensitivity of diamond-like carbon films by alloying with F, Ti or Si. *Thin Solid Films*, 398-399:199–204, 2001.

[123] T. Hioki, Y. Itoh, A. Itoh, S. Hibi, and J. Kawamoto. Tribology of carbonaceous films formed by ion-beam- assisted deposition of organic material. *Surface and Coatings Technology*, 46(2):233–243, 1991.

[124] M. G. Kim, K. R. Lee, and K. Y. Eun. Tribological behavior of silicon-incorporated diamond-like carbon films. *Surface and Coatings Technology*, 112(1-3):204–209, 1999.

[125] S. Miyake, R. Kaneko, Y. Kikuya, and I. Sugimoto. Micro-tribological studies on fluorinated carbon films. *Journal of Tribology-Transactions of the ASME*, 113(2):384–389, 1991.

[126] T. W. Scharf, J. A. Ohlhausen, D. R. Tallant, and S. V. Prasad. Mechanisms of friction in diamondlike nanocomposite coatings. *Journal of Applied Physics*, 101(6):063521, 2007.

[127] A. K. Gangopadhyay, P. A. Willermet, M. A. Tamor, and W. C. Vassell. Amorphous hydrogenated carbon films for tribological applications i. development of moisture insensitive films having reduced compressive stress. *Tribology International*, 30(1):9–18, 1997.

[128] R. Gilmore and R. Hauert. Comparative study of the tribological moisture sensitivity of Si-free and Si-containing diamond-like carbon films. *Surface and Coatings Technology*, 133-134:437–442, 2000.

[129] K. Oguri and T. Arai. Tribological properties and characterization of diamond-like carbon coatings with silicon prepared by plasma-assisted chemical vapour deposition. *Surface and Coatings Technology*, 47(1-3):710–721, 1991.

[130] J. Meneve, R. Jacobs, L. Eersels, J. Smeets, and E. Dekempeneer. Friction and wear behaviour of amorphous hydrogenated $Si_{1-x}C_x$ films. *Surface and Coatings Technology*, 62(1-3):577–582, 1993.

[131] M. Grischke, A. Hieke, F. Morgenweck, and H. Dimigen. Variation of the wettability of DLC-coatings by network modification using silicon and oxygen. *Diamond and Related Materials*, 7(2-5):454–458, 1998.

[132] W. J. Wu, T. M. Pai, and M. H. Hon. Wear behavior of silicon-containing diamond-like carbon coatings. *Diamond and Related Materials*, 7(10):1478–1484, 1998.

[133] M. Murakawa and S. Takeuchi. Evaluation of tribological properties of DLC films used in sheet forming of aluminum sheet. *Surface and Coatings Technology*, 163-164:561–565, 2003.

[134] A. Débart, J. Bao, G. Armstrong, and P. G. Bruce. An O_2 cathode for rechargeable lithium batteries: The effect of a catalyst. *Journal of Power Sources*, 174(2):1177–1182, 2007.

[135] Y. C. Lu, H. A. Gasteiger, M. C. Parent, V. Chiloyan, and Y. Shao-Horn. The influence of catalysts on discharge and charge voltages of rechargeable Li-oxygen batteries. *Electrochemical and Solid-State Letters*, 13(6):A72, 2010.

[136] M. F. Mathias, R. Makharia, H. A. Gasteiger, J. J. Conley, T. J. Fuller, C. J. Gittleman, S. S. Kocha, D. P. Miller, C. K. Mittelsteadt, T. Xie, S. G. Van, and P. T. Yu. Two fuel cell cars in every garage? *Electrochemical Society Interface*, 14(3):24–35, 2005.

[137] P. J. Ferreira, G. J. La O', Y. Shao-Horn, D. Morgan, R. Makharia, S. Kocha, and H. A. Gasteiger. Instability of Pt/C electrocatalysts in proton exchange membrane fuel cells: A mechanistic investigation. *Journal of the Electrochemical Society*, 152(11):A2256–A2271, 2005.

[138] Y. Zhang, M. L. Toebes, A. D. Van Eerden, W. E. O'Grady, K. P. De Jong, and D. C. Koningsberger. Metal particle size and structure of the metal-support interface of carbon-supported platinum catalysts as determined with EXAFS spectroscopy. *Journal of Physical Chemistry B*, 108(48):18509–18519, 2004.

[139] J. T. Chou and K. Sasaki. Microstructural analysis of catalyst/catalyst support interfaces of PEFC electrocatalysts. *Solid State Ionics*, 179(27-32):1405–1408, 2008.

[140] A. B. Preobrajenski, M. L. Ng, A. S. Vinogradov, and N. Mårtensson. Controlling graphene corrugation on lattice-mismatched substrates. *Physical Review B*, 78(7):073401, 2008.

[141] P. Sutter, J. T. Sadowski, and E. Sutter. Graphene on Pt(111): Growth and substrate interaction. *Physical Review B*, 80(24):245411, 2009.

[142] Y. Okamoto. Density-functional calculations of graphene interfaces with Pt(111) and Pt(111)/RuML surfaces. *Chemical Physics Letters*, 407(4-6):354–357, 2005.

[143] K. Okazaki-Maeda, T. Akita, S. Tanaka, and M. Kohyama. First-principles calculations of M_{10}/graphene (M = Au, Pt) systems - atomic structures and hydrogen adsorption. *Materials Transactions*, 49(11):2441–2444, 2008.

[144] P. A. Khomyakov, G. Giovannetti, P. C. Rusu, G. Brocks, J. Van Den Brink, and P. J. Kelly. First-principles study of the interaction and charge transfer between graphene and metals. *Physical Review B*, 79(19):195425, 2009.

[145] G. Giovannetti, P. A. Khomyakov, G. Brocks, V. M. Karpan, J. Van Den Brink, and P. J. Kelly. Doping graphene with metal contacts. *Physical Review Letters*, 101(2):026803, 2008.

[146] C. K. Acharya and C. H. Turner. CO oxidation with Pt(111) supported on pure and boron-doped carbon: A DFT investigation. *Surface Science*, 602:3595–3602, 2008.

[147] J. Greeley and M. Mavrikakis. Alloy catalysts designed from first principles. *Nature Materials*, 3(11):810–815, 2004.

[148] V. R. Stamenkovic, B. S. Mun, M. Arenz, K. J. J. Mayrhofer, C. A. Lucas, G. Wang, P. N. Ross, and N. M. Markovic. Trends in electrocatalysis on extended and nanoscale Pt-bimetallic alloy surfaces. *Nature Materials*, 6(3):241–247, 2007.

[149] V. R. Stamenkovic, B. Fowler, B. S. Mun, G. Wang, P. N. Ross, C. A. Lucas, and N. M. Markovic. Improved oxygen reduction activity on $Pt_3Ni(111)$ via increased surface site availability. *Science*, 315(5811):493–497, 2007.

[150] F. A. De Bruijn, V. A. T. Dam, and G. J. M. Janssen. Review: Durability and degradation issues of PEM fuel cell components. *Fuel Cells*, 8(1):3–22, 2008.

[151] R. Borup, J. Meyers, B. Pivovar, Y. S. Kim, R. Mukundan, N. Garland, D. Myers, M. Wilson, F. Garzon, D. Wood, P. Zelenay, K. More, K. Stroh, T. Zawodzinski, J. Boncella, J. E. McGrath, M. Inaba, K. Miyatake, M. Hori, K. Ota, Z. Ogumi, S. Miyata, A. Nishikata, Z. Siroma, Y. Uchimoto, K. Yasuda, K. I Kimijima, and N. Iwashita. Scientific aspects of polymer electrolyte fuel cell durability and degradation. *Chemical Reviews*, 107(10):3904–3951, 2007.

[152] J. Wu, X. Z. Yuan, J. J. Martin, H. Wang, J. Zhang, J. Shen, S. Wu, and W. Merida. A review of PEM fuel cell durability: Degradation mechanisms and mitigation strategies. *Journal of Power Sources*, 184(1):104–119, 2008.

[153] Y. Shao, G. Yin, and Y. Gao. Understanding and approaches for the durability issues of Pt-based catalysts for PEM fuel cell. *Journal of Power Sources*, 171(2):558–566, 2007.

[154] X. Yu and S. Ye. Recent advances in activity and durability enhancement of Pt/C catalytic cathode in PEMFC. part ii: Degradation mechanism and durability enhancement of carbon supported platinum catalyst. *Journal of Power Sources*, 172(1):145–154, 2007.

[155] E. Antolini, J. R. C. Salgado, and E. R. Gonzalez. The stability of Pt-M (M = first row transition metal) alloy catalysts and its effect on the activity in low temperature fuel cells. a literature review and tests on a Pt-Co catalyst. *Journal of Power Sources*, 160(2 SPEC. ISS.):957–968, 2006.

[156] Z. Wei, H. Guo, and Z. Tang. Heat treatment of carbon-based powders carrying platinum alloy catalysts for oxygen reduction: Influence on corrosion resistance and particle size. *Journal of Power Sources*, 62(2):233–236, 1996.

[157] X. Yu and S. Ye. Recent advances in activity and durability enhancement of Pt/C catalytic cathode in PEMFC. part i. physico-chemical and electronic interaction between Pt and carbon support, and activity enhancement of Pt/C catalyst. *Journal of Power Sources*, 172(1):133–144, 2007.

[158] S. C. Roy, A. W. Harding, A. E. Russell, and K. M. Thomas. Spectroelectrochemical study of the role played by carbon functionality in fuel cell electrodes. *Journal of the Electrochemical Society*, 144(7):2323–2328, 1997.

[159] D. J. Guo and H. L. Li. High dispersion and electrocatalytic properties of Pt nanoparticles on SWNT bundles. *Journal of Electroanalytical Chemistry*, 573(1):197–202, 2004.

[160] Y. Shao, G. Yin, Y. Gao, and P. Shi. Durability study of Pt/C and Pt/CNTs catalysts under simulated PEM fuel cell conditions. *Journal of the Electrochemical Society*, 153(6):A1093–A1097, 2006.

[161] E. Yoo, T. Okata, T. Akita, M. Kohyama, J. Nakamura, and I. Honma. Enhanced electrocatalytic activity of Pt subnanoclusters on graphene nanosheet surface. *Nano Letters*, 9(6):2255–2259, 2009.

[162] W. Q. Deng, Y. Matsuda, and III W. A. Goddard. Bifunctional anchors connecting carbon nanotubes to metal electrodes for improved nanoelectronics. *Journal of the American Chemical Society*, 129(32):9834–9835, 2007.

[163] X. Lepró, E. Terrés, Y. Vega-Cantú, F. J. Rodríguez-Macías, H. Muramatsu, Y. A. Kim, T. Hayahsi, M. Endo, M. Torres R., and M. Terrones. Efficient anchorage of Pt clusters on N-doped carbon nanotubes and their catalytic activity. *Chemical Physics Letters*, 463(1-3):124–129, 2008.

[164] C. K. Acharya and C. Heath Turner. Stabilization of platinum clusters by substitutional boron dopants in carbon supports. *Journal of Physical Chemistry B*, 110(36):17706–17710, 2006.

[165] C. K. Acharya, W. Li, Z. Liu, G. Kwon, C. Heath Turner, A. M. Lane, D. Nikles, T. Klein, and M. Weaver. Effect of boron doping in the carbon support on platinum nanoparticles and carbon corrosion. *Journal of Power Sources*, 192(2):324–329, 2009.

Chapter 2

Surface Stability and Electronic Structure of Hydrogen and Fluorine Terminated Diamond Surfaces: A First Principles Investigation

2.1   Introduction

Diamond is known to be the hardest and stiffest material, chemically inert and has the highest thermal conductivity at the room temperature. Due to this remarkable set of properties, synthetic diamond films like diamond-like carbon (DLC), nano-diamond (ND) and amorphous carbon (a-C), have found wide range of applications. Some examples include hard and wear resistant coatings, biomedical applications, micro- and nano-electromechanical systems (MEMS/NEMS), optical windows, magnetic data storage, and electrodes for electrochemical processes [1]. DLC films are produced by either physical vapor deposition (PVD) or chemical vapor deposition (CVD) methods and their physical and chemical properties depend primarily on their sp^3/sp^2 bonding ratio of carbons and as well as their hydrogen

content [2]. The tribological properties of DLC films show diverse characteristics under various environmental conditions [3, 4]. Presence of dangling carbon bonds plays a role in controlling the friction characteristics. The passivation of dangling bonds by hydrogen or hydroxide group hinders interactions between surface carbon atoms and the environment, resulting in a more stable surface and low coefficient of friction (< 0.01) [4–6].

In order to improve tribological and mechanical properties, as well as thermal stability of DLC films, and to decrease internal stresses in films, doping elements were incorporated into the amorphous DLC structure [5,7,8]. Among them, fluorine incorporation is mainly inspired by the many special properties of PolyTetraFluoroEthylene (PTFE), which, in addition to features like extremely low friction and excellent chemical resistance, is simultaneously hydrophobic and oleophobic [9]. Studies revealed that the incorporation of fluorine caused an increase in the water contact angle, hence a decrease in surface energy, proportional to the fluorine content [10–18]. On the other hand, an increase in the fluorine concentration decreased film hardness with the resulting hardness values much lower than hydrogenated DLC films [11, 14, 19]. Tribological properties of films were reported to have optimum values for moderately $[0.1 < (F/F + C) < 0.2]$ fluorinated films [5] which was evidenced by sliding experiments [11, 20]. Meanwhile, atomic force microscopy (AFM) showed that both adhesive force and coefficient of friction (COF) decreased with an increase in fluorine concentration [16]. The COF of fluorinated DLC (F-DLC) films decreased with the relative humidity, and the lowest friction was achieved under distilled water [10]. The high water contact angle of F-DLC coatings led some researchers to consider this coating in anti-sticking moulds [21, 22].

Fluorination of diamond surfaces was achieved by exposing the surface to atomic F beams [23–25], F_2 [26], XeF_2 [27–29] and fluorocarbons [30, 31]. Surface fluorination can also be conducted by exposing the surface to CF_4 during plasma processing [32, 33]. The doping of DLC films with F was generally carried out using a reactive gas environment containing F, such as CF_4, C_2F_4, and C_2F_6 with a hydrocarbon gas like CH_4, C_2H_2, or C_4H_{10} during the plasma production of films. The fluorine concentration in the films was controlled by adjusting hydrocarbon to fluorine ratio of gas mixture. The selection of gas mixtures changes the surface properties of the films [34] which are also sensitive to

processing parameters including power and gas pressure [19, 35–37]. The incorporation of F into an amorphous carbon structure was believed to occur with the substitution of F atoms for the H atoms, since the C−F bond is stronger than the C−H bond [38]. This behavior was observed when the hydrogen content decreased with the addition of fluorine atoms in experimental studies [11–13,19].It was also reported that an increase in the fluorine concentration of DLC films caused the formation of −CF, −CF$_2$ and −CF$_3$ groups, which in turn reduced the surface energy [10, 11, 13, 15, 34, 39, 40]. It has been proposed that fluorine hinders interactions between surface carbon atoms and the environment more effectively than hydrogen, resulting in a more chemically stable surface for DLC coatings, due to its size, which is larger than H. The formation of fluorocarbons was also reported to break the cross-linked diamond structure [19, 35] and enhance sp^3 bonding [11, 14], suggesting that a higher F content would weaken the film's hardness.

Despite many experimental studies that have investigated fluorine's role in DLC films, the fundamental role that F plays on modifying the surface properties is still unclear. An important question is whether an optimal F concentration for DLC coatings exists, because there are many discrepancies regarding the role that source gases play on surface properties during the production of films. In order to address these questions, in this work, the surface stability phase diagram for mixed and fully H and F terminated diamond surfaces was calculated, using first principles methods. The calculated phase diagram provided guidance on how to control the surface termination by changing the reactive gas used in production. The electronic structure was also analyzed in an effort to better understand variations in the concentration of fluorine on modifying diamond surface properties. Finally, interactions between two H and two F terminated diamond surfaces are analyzed to determine their adhesion and friction properties.

2.2 Computational Methodology

First principles methods were used to determine the stability of H and/or F terminated diamond surfaces with the calculations based on density functional theory (DFT), where the ground state structures and energies were obtained by solving the single particle Kohn-

Sham [41] equation with a plane wave basis set. All computations were performed using a projector-augmented wave (PAW) method with exchange correlation energy approximated in the generalized gradient approximation (GGA) [42] to DFT as implemented in the Vienna Ab initio Simulation Package (VASP) [43–45]. Calculations were carried out by PAW-PBE [46, 47] potentials, supplied by VASP. The total energies were obtained by relaxing the system according to atomic positions and minimizing the Hellman-Feynman forces using a conjugate gradient method. In all calculations, energy convergence to $1 - 2$ meV was obtained using a plane wave cutoff energy of 600 eV. The electronic degrees of freedom for surface structures were converged to 10^{-5} eV/cell and Hellman-Feynman forces were relaxed to less than 10^{-4} eV/Å.

In order to validate the accuracy of computations, the lattice parameter of bulk diamond was calculated in the space group $FD\bar{3}M$ (no 227) as 3.572 Å compared to the experimental result of 3.567 Å [48] using a $30 \times 30 \times 30$ grid (816 k-points) of $\Gamma-$centered k-points. The cohesive energies and bond lengths for different gas molecules were calculated in a large $15 \times 15 \times 15$ Å box, and the corresponding parameters were then compared to the experimental values. The errors in these computations were less than 4%.

Chemical passivation of diamond surfaces successfully explained experimental observations of H content and gas effects in friction tests [4, 6]. Thus, although DLC is a mixture of sp^3 (diamond) and sp^2 (graphite) bonded carbon, diamond structure can represent the picture in the atomistic modeling.

Diamond structures are further complicated by surface reconstructions and surface terminations. Clean diamond $(111) - 1 \times 1$ surfaces are unstable due to dangling surface bonds. Consequently, clean diamond $(111) - 1 \times 1$ surfaces undergo a reconstruction to form a sp^2 hybridized $\pi-$bonded 2×1 structure that effectively passivates the clean surface through reorganization of its electronic structure [49–52]. Terminating the surface dangling bonds with various chemical species, such as H, CH_3, F, Cl, Br, O and OH changes the stability of the 1×1 and 2×1 surface constructions [50, 53–58]. In the first stage of current calculations, the stability of both diamond $(111) - 1 \times 1$ and diamond $(111) - 2 \times 1$ surfaces with H and F terminations were compared. Then, in the surface with stable construction, non-stoichiometric, mixed H and F terminated surfaces were created and a surface phase

diagram was constructed using the calculated surface energies.

All surface calculations were performed using a slab model with a total 10 Å vacuum, introduced symmetrically to the top and the bottom of the slab. Surface energies of diamond (111) surfaces for 2 to 10 layers of slabs were calculated in order to find the necessary slab thickness that simulates the bulk effect. A $10 \times 10 \times 1$ grid of $\Gamma-$centered k-points was used in order to achieve $1 - 2$ meV/atom energy convergence. The surface energies for the clean diamond surface were calculated using Boettger's [59] method. The surface energy, $E_s(n)$, was expressed as

$$E_s(n) = \frac{1}{2A} [E(n) - n(E(n) - E(n-1))] \tag{2.1}$$

where $E(n)$ is the energy of the n layer slab and A is the area of the surface.

Since there are four atomic positions at the (111) surface, there are also four F atoms at the fully F terminated surface, and four H at the fully H terminated surface. Replacing the H atoms, one by one, with F atoms provided different surface concentrations, such as 25% F, 50% F and 75% F terminated surfaces (Figure 2.1). Fully H and F terminated surfaces are designated as 4H and 4F, respectively, while mixed terminations are referred to as 3H1F, 2H2F and 1H3F. If surfaces contain chemical species that differ from the bulk elements of the structure, then the surface energies must be defined according to the chemical potentials of existing species. Therefore, the surface energy, E_s, is defined as a function of chemical potentials of H and F [60], and the corresponding equation is given by

$$E_s = \frac{1}{2A} [E_{slab} - (n_C \mu_C + n_H \mu_H + n_F \mu_F)] \tag{2.2}$$

where n_C, n_H and n_F are the number of C, H and F atoms in the slab. For $n_F = 0$, the surface is 100% H terminated and when $n_H = 0$, the surface is 100% F terminated. μ_C, μ_H and are the chemical potentials of C, H and F respectively and E_{slab} is the energy of the slab. The chemical potentials of H and F depend on the source gas that the surface is in equilibrium with.

The adhesion tendencies between the two F- terminated and two H-terminated diamond surfaces were modeled by constructing a fully coherent interface between them. Then, the
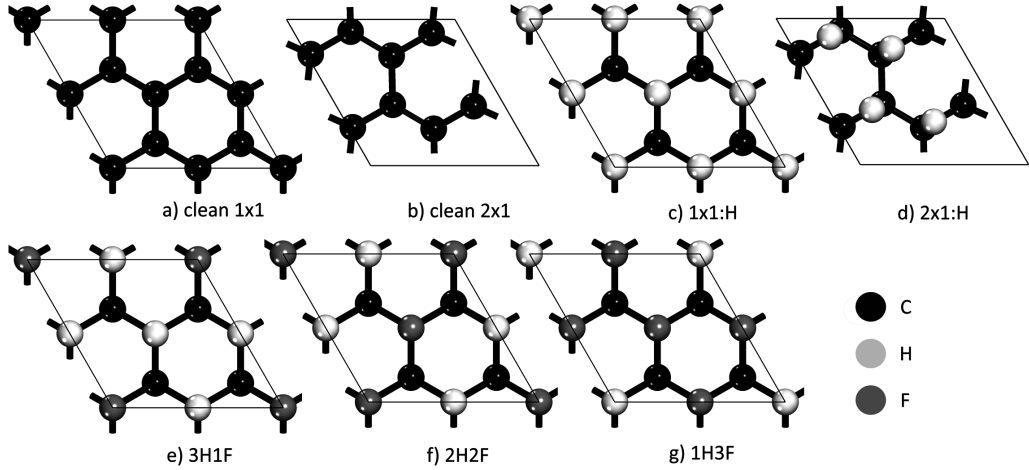
Figure 2.1: Surface construction of diamond (111) surfaces: (a) clean diamond (111)–1×1, (b) clean diamond (111)–2×1, (c) H-terminated diamond (111)–1×1, (d) H-terminated diamond (111)–2×1, and mixed H- and F-terminated surfaces: (e) 3H1F, (f) 2H2F, and (g) 1H3F.

interface separation distance, d, which is the distance between two F atoms in different surfaces, was gradually decreased from 3.7 to 1.6 Å and, for each 0.1 Å interval, the system was relaxed according to atomic positions and the total energy of the system was computed. According to the change in the energy due to interface separation, the normal force, F_N, exerted between surfaces was calculated numerically, as $F_N = -\frac{\partial E_{tot}}{\partial d}$ where E_{tot} is the total energy of the slab.

The energy computed by original DFT calculations cannot capture the Van der Waals (VdW) forces, originating from the long range dispersive interactions. Recently proposed theoretical studies addressed this issue and attempted to correct the dispersion energies for DFT calculations. These approaches include introducing new correlation functional [61], empirical methods which corrects the DFT energy with a dispersion relation with empirically determined coefficients [62, 63] and non-self consistent methods that take into account the dispersion relation by partitioning the electronic charge density [64]. In this study, we employed a practical DFT including dispersion corrections (DFT-D) method described by Grimme [63], where the dispersion relations to DFT were corrected using an empirical potential of the form $C_6 R^{-6}$ with a damping function, where R is the interatomic distance and C_6 is the dispersion coefficient. The determination of these parameters (including

C, H and F atoms) is described in detail in Ref. [63] where they were tested for various complex molecules. Following the DFT-D approach, the dispersion energy of the interface was calculated and added to DFT results. The interfacial force was determined as a function of separation distance in a similar way as described above.

2.3 Results and Discussion

2.3.1 Surface terminations and reconstructions

In the first step of the calculations, both $1\times1-$ and $2\times1-$reconstructed clean diamond (111) surfaces were built. Surface energies of these structures were computed using Boettger's [59] method, and results are listed in Table 2.1. The surface energy for the 1×1 construction converged for a six bi-layer slab to 5.66 J/m^2, and for the 2×1 reconstruction, surface energy converged for eight bi-layers of slab to 3.39 J/m^2. The diamond slab was not stable for slabs less than five layers thick, because a tendency toward graphitization occurred. Hence, the 2×1 reconstruction had a lower surface energy, which made it more stable than the 1×1 construction. The calculated values were in strong agreement with previous DFT results for clean diamond [65].

Table 2.1: Surface energy convergence of clean diamond (111) surfaces according to number of layers (n) in the surface structure.

n	No. of atoms	Diamond $(111) - (1 \times 1)$		Diamond $(111) - (2 \times 1)$	
		$E_s(n)$ (eV/atom)	$E_s(n)$ (J/m^2)	$E_s(n)$ (eV/atom)	$E_s(n)$ (J/m^2)
6	48	1.9531	5.6638	1.1143	3.2291
7	56	1.9638	5.6947	1.2272	3.5561
8	64	1.9556	5.6711	1.1731	3.3993
9	72	1.9548	5.6687		
10	80	1.9528	5.6629		

The surface energies of fully $F-$ and $H-$terminated diamond $(111) - 1 \times 1$ and -2×1 surfaces were calculated with respect to the chemical potential of F and H. It was found that both F and H terminations yielded surface C atoms that made sp^3-type bonding, resulting in a 1×1 constructed surface. For the H termination, this result was confirmed with previous DFT calculations reported by Kern et al. [50] and LEED experiments conducted by Schaich et al. [53], who observed the phase transformation from 2×1 to 1×1 construction around

990 K. For the F termination, direct LEED pattern evidence was provided by Freedman [24], who fluorinated the clean diamond $(111) - 2 \times 1$ surface with atomic F and observed that fluorination breaks the $p-$bonded chains on the surface of the 2×1 construction, resulting in the formation of the 1×1 construction. Computational work using empirical group additivity method showed that, even at low fluorine pressures, structures in the (111) plane prefer to be in an sp^3 bonding structure rather than an sp^2, which also indicates that the 1×1 constructed surface is more stable than the 2×1 construction for F$-$ and H$-$terminated surfaces [56].

2.3.2 Surface stability

Because the 1×1 constructed surfaces are more stable than 2×1 for both H and F terminations, the surface energies of mixed and completely F$-$ and H$-$terminated surfaces were calculated only for the $1 \times 1-$constructed surfaces. To determine which phase had the lower surface energy and hence was more stable for any given chemical potential of hydrogen and fluorine, a surface phase diagram was constructed that shows the predominant areas of the stable structures. The surface termination phase diagram constructed is shown in Figure 2.2, which is obtained by projecting the lowest surface free energies on the $\mu_H - \mu_H^0$ and $\mu_F - \mu_F^0$ planes. The limits of the phase diagram were set according to the energy of atomic F ($\mu_F - \mu_F^0 = 1.316$ eV/atom) and atomic H ($\mu_H - \mu_H^0 = 2.281$ eV/atom). According to Figure 2.2, the F$-$terminated surface is more stable in a much larger phase space than the H$-$terminated one. At zero chemical potential of H and F, which correspond to H_2 and F_2 gas sources, it can be seen that the stable surface is fully F terminated. Increasing the F concentration in the source gas makes a fully F-terminated surface formation more favorable. Similarly, an H-terminated surface can be achieved by increasing the chemical potential of H. The diagram shows that there is no 1H3F surface termination at any of the chemical potential combinations, suggesting that the 1H3F surface is thermodynamically unstable.

The transformation from a 2×1 clean diamond surface to a 1×1 H$-$terminated diamond occurs when the chemical potential of H increases to $\mu_H - \mu_H^0 > 1.52$ eV/ atom and to a 1×1 F$-$terminated diamond when F chemical potential increases to $\mu_F - \mu_F^0 = -2.91$ eV/atom.

It is noted that the chemical potential needed for the stable F termination is much lower than for the H termination. It is also important to note that the chemical potential required to form a fully passivated surface is considerably lower in an F environment than in an H environment.

According to Figure 2.2, the desired surface composition can be adjusted by varying the composition of the source gases. If the diamond (111) surface is exposed to HF, H_2 and F_2, or atomic H and F, it will be fully F terminated. Varying the ratio of the source gases would change the values of $\mu_H - \mu_H^0$ and $\mu_F - \mu_F^0$, hence providing various ways of controlling the final surface termination. The surface termination phase diagram also indicates the changes that may occur on the surface termination during surface modification after the deposition process of the coating. For example, exposing an H−terminated surface to an atomic F environment will produce an F-terminated surface. This is in agreement with the observation of Yamada et al. [29] that a fully F−covered monolayer was formed after exposing the H−terminated surface to XeF_2, whereas the 1×1 structure was maintained.

The surface termination map was calculated for the equilibrium conditions between the surface and the source gas. Although the deposition process (PVD or CVD) cannot be approximated into an equilibrium process, this phase diagram can nevertheless be used to provide a general trend for varying the source gas to modify the surface F concentration. Along the vertical and horizontal lines designating the chemical potentials of certain molecules, these molecules are formed with no energy cost, meaning that above the vertical lines and on the right side of the horizontal lines, the formation energy of these molecules is negative. Within this chemical potential range, the formation of compounds and growth of the surface should be considered a competing process during the deposition; however, it is still possible that higher H or F coverage can be formed as metastable states.

Finally, it is worth emphasizing that the surface energy was not plotted as a function of F content, because, from a thermodynamical point of view, the surface energy is referred to the environment. The surface energy decreases with increasing F content for the common reference states of H_2 and F_2, in agreement with the general experimental measurements. However, it needs to be pointed out that the surface energy is typically measured experimentally by measuring wetting angles made with various liquids and extrapolating to "critical

surface tension" according to the Zisman method [66]. The "critical surface tension" is not the surface energy of the solid itself. Therefore, the comparison may not be appropriate.

2.3.3 Electronic structure and bonding

The length of the C−H bond formed between surface C atoms and H atoms was found to be 1.1Å in the relaxed surface structures for all the surface compositions. The C–F bond was found to alter in different surface compositions such that the computed bond lengths for 3H1F, 2H2F, 1H3F, and 4F structures were 1.439, 1.414, 1.394, and 1.379 Å, respectively. The bond length between F and C at the surface decreases with increasing F content and reaches the minimum value for the fully fluorinated surface. The calculated C−F bond length for a CF_4 molecule in vacuum was 1.344 Å (experimental value is 1.323 Å [67]).

The reason behind the change in the surface energy (and other surface properties) with F doping can be rationalized by analyzing the electronic structure of the surfaces. Electron density distributions of the surfaces were mapped to determine the surface area coverage of F termination, as shown in Figure 2.3. The electron density coverage increases with an increase in the F content at the surface. The fully F−terminated surface has almost covered the entire diamond surface [Figure 2.3(e)] compared with the fully H−terminated surface [Figure 2.3(a)]. The charge density isosurface of $e = 0.1$ gives a diameter of 1.92 Å for H and 2.48 Å for F, which is almost equal to the distance between two C atoms (2.53 Å). One can think a fully F−terminated diamond surface as entirely covered by charges > 0.1. Consequently, the F−terminated surfaces can be considered to effectively block interactions between C atoms and the environment, providing better protection for the coating compared with the H−terminated surfaces.

Bader charge analysis [68, 69] was used to partition electrons and atoms, where atomic volume and charges were determined according to charge density distribution. The net charges on the H− and F−terminated diamond (111) surfaces with reference to H_2 and F_2 molecules and perfect diamond appear in Table 2.2. Calculated values of Bader charges for H_2 and F_2 molecules indicated that the fluctuation of net charge was around $e \sim 0.08$. The C atoms at the center of the slab were almost neutral ($e < 0.04$), which is comparable to the zero charge determined for the perfect diamond. Thus, the model slab is sufficiently

thick to maintain the bulk properties of diamond at the slab center.

Table 2.2: Bader charge analysis of H− and F−terminated diamond (111)–1 × 1 surfaces, bulk diamond, and H_2 and F_2 molecules. Values show the amount of charge transferred, with a positive value representing charge accumulation and a negative value representing charge depletion on the corresponding atom.

Configuration	Surface atoms				
	H	C below H	F	C below F	Bulk C
4H	0.057	−0.021			0.010
3H1F	0.013	−0.069	0.724	−0.611	0.029
2H2F	−0.032	−0.105	0.729	−0.701	0.034
1H3F	−0.139	−0.028	0.752	−0.734	0.008
4F			0.762	−0.829	0.043
Diamond					0
H_2	±0.881				
F_2			±0.0799		

There was not a significant charge accumulation on the fully H−terminated surface. Charges on both H and C atoms on the surface remained close to neutral ($e < 0.057$), indicating that no charge transfer occurred because of the covalent nature of the bond. In all F−containing surfaces, the F atom takes charges from the C atom underneath, resulting in negatively $0.7 - 0.8$ charged F and positively $0.6 - 0.8$ charged C atoms. In highly fluorinated configurations, H seems to donate a small amount of charge, resulting in an atomic charge of positive 0.1. The C−F bond is highly ionic, because of the large electronegativity difference, 1.45, between F, with an electronegativity of 4.00, and C, with an electronegativity of 2.55. The difference in electronegativity between C and H is as small as 0.3. The ionic character of the C−F bond might contribute to an increase in the stability of the F−terminated surface. Larsson and Lunell [57] found that the ionic character of the C−F bonding causes higher adsorption energies of F to the F−terminated diamond surface compared with adsorption of H to the H−terminated diamond surface.

The charge transfer and bonding formalism on the surfaces can be effectively shown using the charge density difference plots (Figure 2.4). The charge density differences were taken between the surface and the H, F, and C atoms in their corresponding structures. Positive regions in these plots represent charge accumulation and negative regions show charge depletion. In addition to the charge density difference plots taken from the xz plane for mixed H and F terminated surfaces in Figure 2.4, the charge transfer across the interface

are shown using slices taken from the xy plane from locations marked by an arrow. Because C−F bonds are longer than C−H bonds, it was impossible to have a slice cut through the atomic cores of both H and F. Plotting the charge density difference for both cross-sections results in a three-dimensional map of the charge transfer. In all structures, the surface C atoms lose charges, but in a C−H bond, the region between C and H atoms gains most of the charge. In a C−F bond, the F atom gains most of the electrons. These observations are consistent with the covalent nature of the C−H bond and the ionic character of the C−F bond. The p orbital on the xy plane of F atoms gains electrons with an increase in the F content. It is interesting to note that the mixed terminated surfaces featured orbitals of F atoms that take charge in the xy plane, p_x and p_y, directing to the other F atoms. In contrast, charge depletion in the p_z orbital that points to the carbon atoms located below is noted. The formation of F−F atomic bonds on the surface is counter intuitive, because the highly negatively charged F atoms would repel each other. The attraction between surface F atoms is consistent with previous [55] empirical group additivity studies, which have reported minor repulsion between neighboring F atoms that resulted in the fluorinated diamond (111) surface not being significantly strained.

The electron charge density difference plot suggested that pz orbitals of fluorine made $\sigma-$type bonding with carbon, and p_x and p_y orbitals of fluorine atoms interacted with each other through $p-$type bonding. The total density of states (TDOS) of the surface structures are plotted in Figure 2.5. TDOS clearly shows a new peak that appeared at 25 eV below the Fermi energy for configurations where more than two F atoms existed on the surface, indicating that this peak was probably caused by F−F interactions. Notice that the intensity of this peak decreased when three F atoms were considered and increased again in the presence of four F atoms, indicating that even numbers of F neighbors promoted the F−F bond formation. This observation provides a plausible explanation as to why the 1H3F surface was energetically unstable under any of the $\mu_H - \mu_H^0$ and $\mu_F - \mu_F^0$ combinations (Figure 2.2). Further investigation of partial DOS (PDOS) of surfaces indicated that these energy levels were mainly contributed from fluorine's orbitals. The formation of the F−F bond on a carbon structure was reported by Saito et al. [70], who investigated the effect of F termination on the graphene edge by quantum chemistry calculations and found that

having F atoms side by side rather than at the opposite edges was energetically favored. They attributed the interaction between F−F atoms to the formation of spin singlet states.

2.3.4   Adhesion between F−and H−terminated surfaces

When two F−terminated diamond surfaces approach each other, the negatively charged F atoms are expected to develop a large repulsive electrostatic interaction. This assumption was tested by performing adhesion simulations of a fully F−terminated surface against another fully F−terminated surface. Similarly, changes between two fully H−terminated surfaces were characterized. The normal force generated when two fully H− or F−terminated surfaces approached each other was computed and compared in Fig. 6. In addition to DFT calculated forces, we considered the effect of VdW forces caused by dispersion relations by adding them to the DFT-based forces using an empirical method [63]. The dispersion-corrected DFT forces are designated by DFT-D in Fig. 6. Considering the DFT force on its own, the repulsive force generated between two F−terminated surfaces increased sharply when the surfaces were brought closer than 2.8 Å. The repulsive force between two fully H−terminated surfaces rose at a much slower rate when they approached closer than 2.2 Å. It can be seen that the addition of the dispersion energy did not have a significant effect on the repulsion force. The interface separation, below which repulsive force increased sharply, was recalculated using the the DFT-D method, and it became only 0.2 Å larger than those predicted from the DFT results. Consequently, a much larger repulsive force between F−terminated diamond surfaces in comparison to the H−terminated surfaces was developed, and this large repulsive force prevented two fluorinated diamond surfaces from getting too close. This analysis infers that the anti-stickiness of DLC film would increase with an increase in the F content, especially when the F atoms are on the top surfaces. It also implies that the repulsive force between F atoms can better protect the diamond surface compared with the H-terminated DLC surface.

In a previous study [71], adhesion and friction between two hydrogenated diamond (100) surfaces were simulated, and the lower friction observed between the hydrogenated diamond surfaces was attributed to the repulsive force developed between H atoms on each surface. We can predict that the repulsive force between the F−terminated surfaces is even larger

than H−terminated surfaces. In addition, the C−F bond is stronger than the C−H bond, and fluorinated surfaces are more stable. Consequently, a lower friction between two fluorinated diamond surfaces is predicted compared with that between two hydrogenated diamond surfaces.

2.4   Conclusions

The chemical stability and electronic structure of F− and H−terminated diamond surfaces were investigated using first principles calculations. The following conclusions were reached:

1. Both F and H incorporation caused diamond (111) surface C atoms to make sp^3−type bonding, resulting in a more stable 1×1 construction than the 2×1.

2. According to the surface phase diagram constructed for mixed H and F terminations, the F−terminated surface was found to be stable in a substantially larger chemical potential phase space. A 75% F (25% H)−terminated surface was unstable.

3. Because of the strong bond between C and F atoms and the large size of F atoms, the F−terminated surfaces prevented interactions between C atoms and the environment, providing better chemical protection compared with the H−terminated surfaces.

4. Larger repulsive forces between two F−terminated diamond surfaces were predicted compared with those between two H−terminated surfaces, suggesting lower adhesion and friction between F−terminated surfaces.
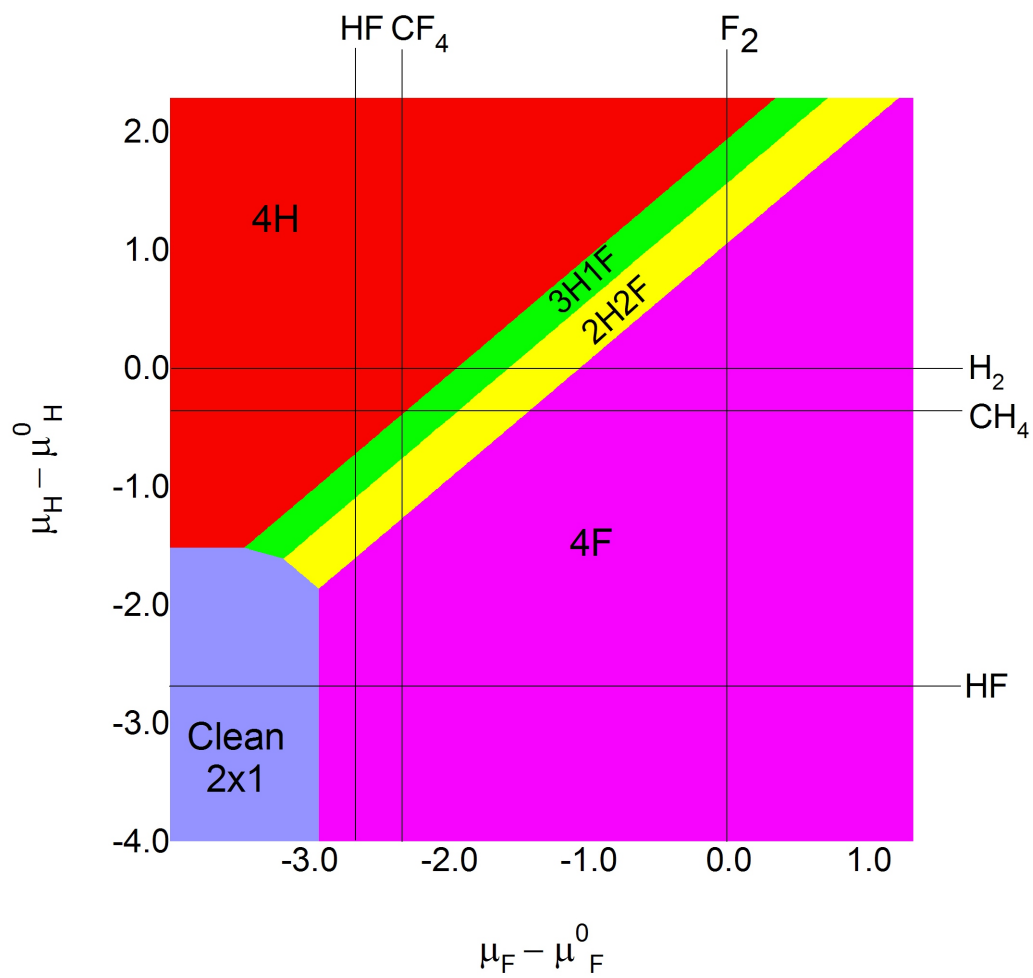
Figure 2.2: Surface phase diagram of stable H− and F−terminated diamond (111)–1 × 1 surface structures. The graph shows the predominant areas of stable surface terminations for a particular gas composition. The chemical potentials of H and F are limited to the formation of atomic H ($\mu_H - \mu_H^0 = 2.281$ eV/atom) and atomic F ($\mu_F - \mu_F^0 = 1.316$ eV/atom).
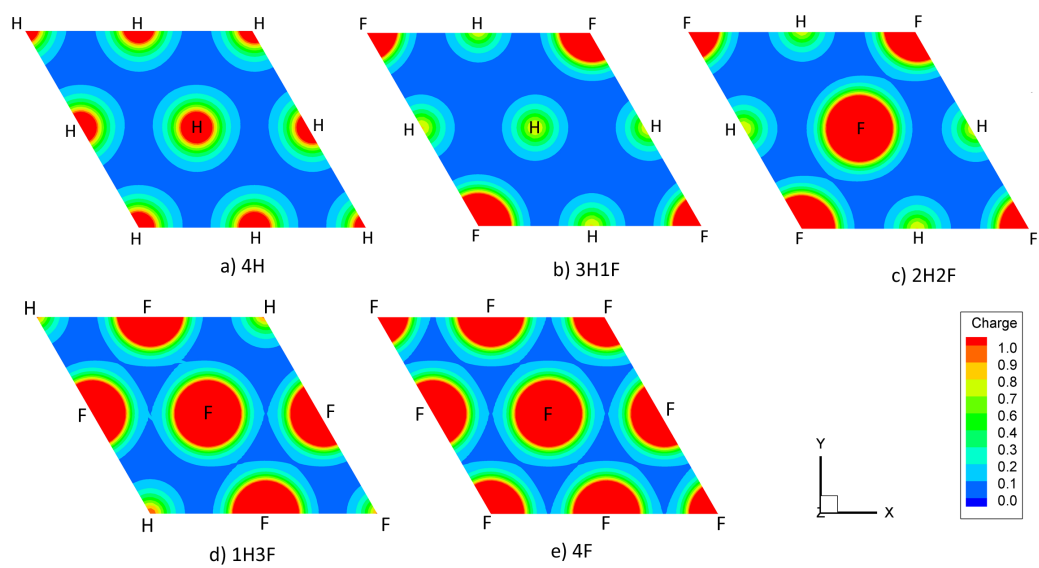
Figure 2.3: Electron charge density plots of hydrogenated and fluorinated diamond (111) − 1 × 1 surfaces showing the surface coverage of different terminations from (a)–(e).
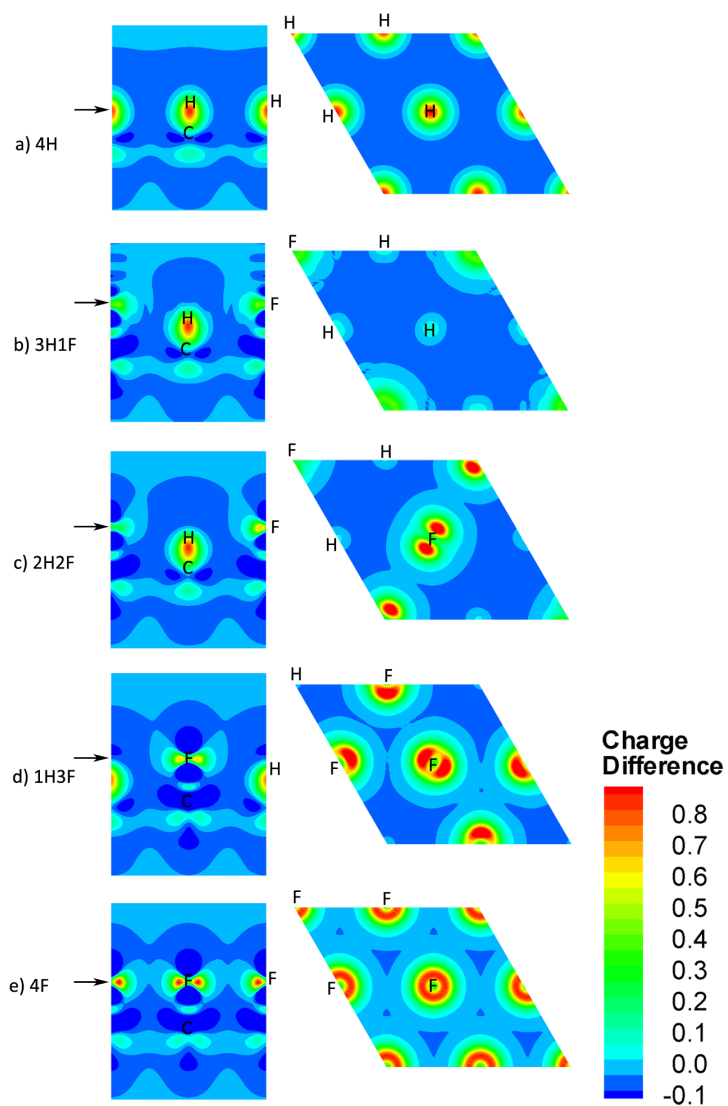
Figure 2.4: Charge density difference plots taken from the xz plane shown at the left and the xy plane shown at the right for H− and F−terminated diamond (111) surfaces with the following terminations: (a) 4H, (b) 3H1F, (c) 2H2F, (d) 1H3F, and (e) 4F.
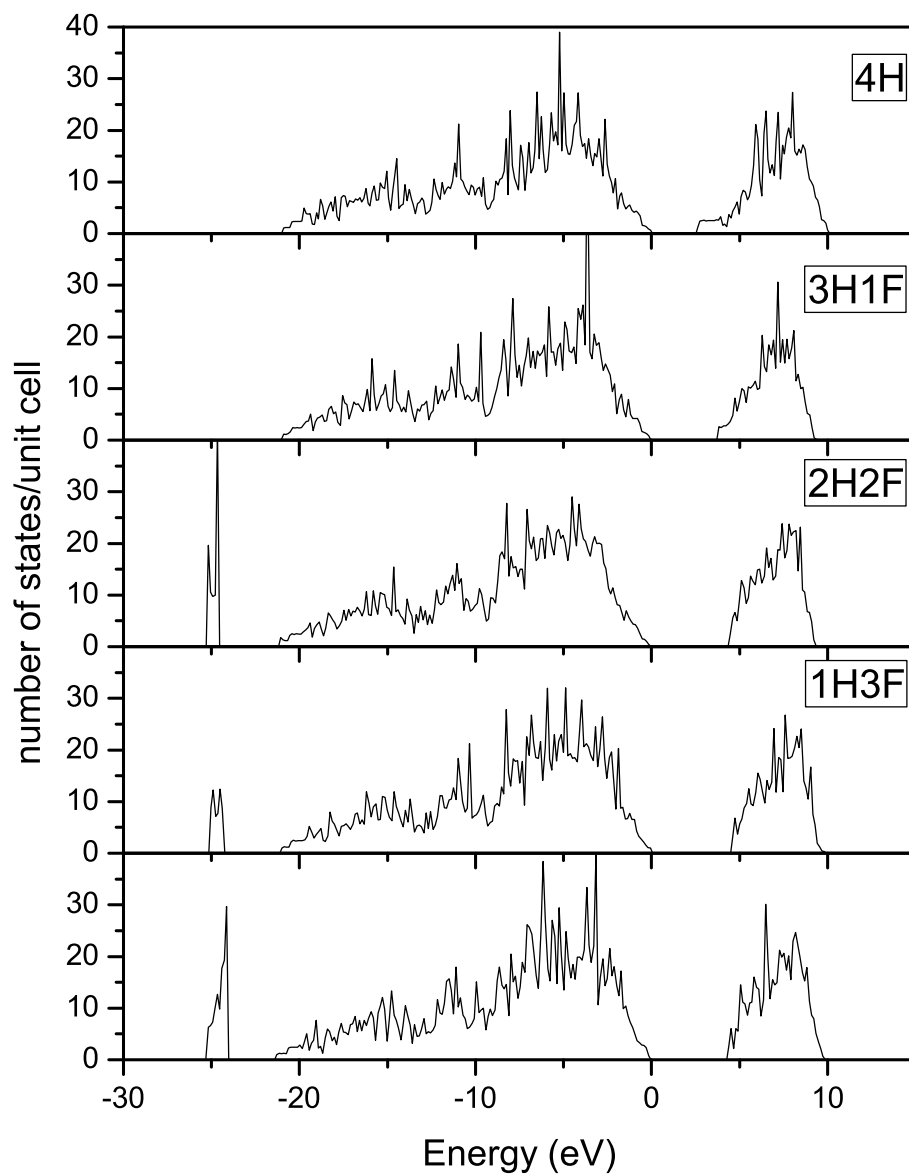
Figure 2.5: Total density of states (TDOS) for diamond (111) surfaces with the terminations 4H, 3H1F, 2H2F, 1H3F, and 4F as labeled (normalized such as $E_F = 0$).
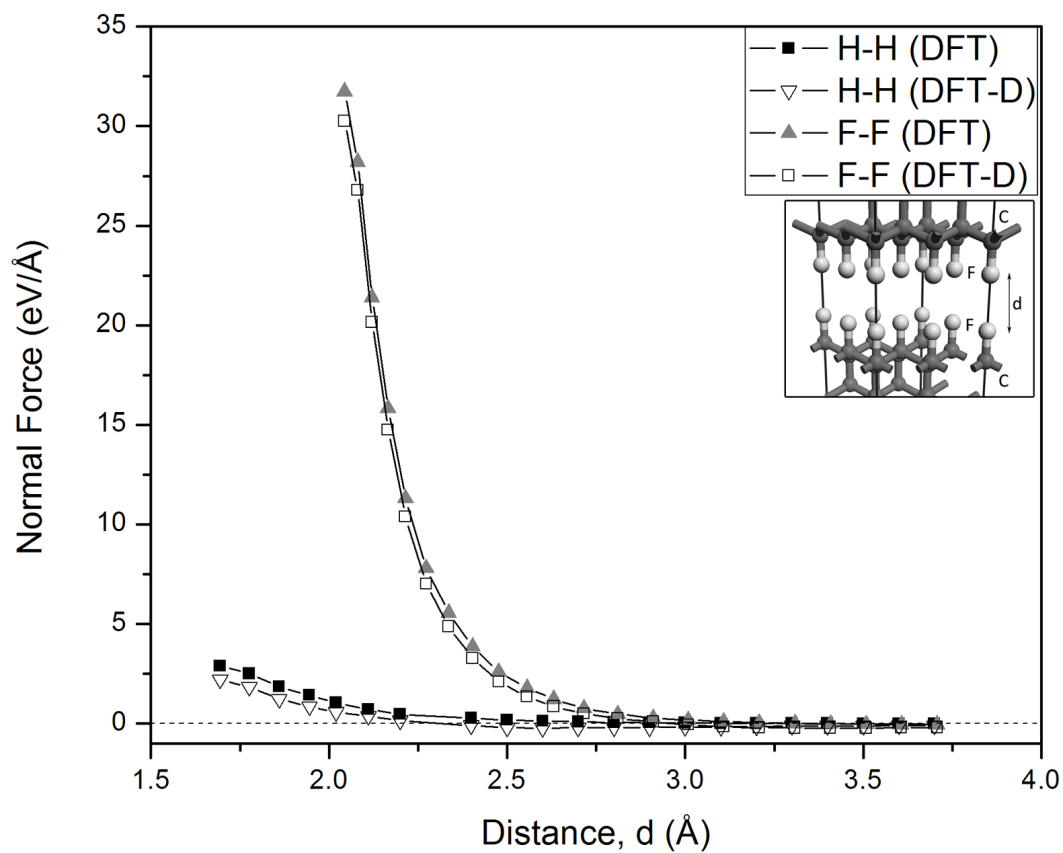
Figure 2.6: The variation of the normal force between H− and F−terminated diamond (111) surfaces with interfacial separation distance. The forces labeled "DFT" are the values calculated from DFT energy only, whereas the forces labeled "DFT-D" are the dispersion-corrected forces. The inset shows the interfacial distance that was taken into account while calculating the force.

Bibliography

[1] P. W. May. The new diamond age? *Science*, 320(5883):1588, 2008.

[2] J. Robertson. Diamond-like amorphous carbon. *Materials Science and Engineering R*, 37(4-6):129–281, 2002.

[3] J. Andersson, R. A. Erck, and A. Erdemir. Frictional behavior of diamondlike carbon films in vacuum and under varying water vapor pressure. *Surface and Coatings Technology*, 163-164:535–540, 2003.

[4] A. Erdemir. The role of hydrogen in tribological properties of diamond-like carbon films. *Surface and Coatings Technology*, 146-147:292–297, 2001.

[5] C. Donnet. Recent progress on the tribology of doped diamond-like and carbon alloy coatings: A review. *Surface and Coatings Technology*, 100-101(1-3):180–186, 1998.

[6] Y. Qi, E. Konca, and A. T. Alpas. Atmospheric effects on the adhesion and friction between non-hydrogenated diamond-like carbon (DLC) coating and aluminum - a first principles investigation. *Surface Science*, 600(15):2955–2965, 2006.

[7] M. Grischke, K. Bewilogua, K. Trojan, and H. Dimigen. Application-oriented modifications of deposition processes for diamond-like-carbon-based coatings. *Surface and Coatings Technology*, 74-75:739–745, 1995.

[8] J. Sanchez-Lopez and A. Fernandez. *Doping and alloying effects on DLC coatings*, pages 311–338. Tribology of Diamond-Like Carbon Films: Fundamentals and Applications. Springer, 2008.

[9] H. Touhara and F. Okino. Property control of carbon materials by fluorination. *Carbon*, 38(2):241–267, 2000.

[10] M. Ishihara, T. Kosaka, T. Nakamura, K. Tsugawa, M. Hasegawa, F. Kokai, and Y. Koga. Antibacterial activity of fluorine incorporated DLC films. *Diamond and Related Materials*, 15(4-8):1011–1014, 2006.

[11] M. Hakovirta, X. M. He, and M. Nastasi. Optical properties of fluorinated diamond-like carbon films produced by pulsed glow discharge plasma immersion ion processing. *Journal of Applied Physics*, 88(3):1456–1459, 2000.

[12] M. Hakovirta, D. H. Lee, X. M. He, and M. Nastasi. Synthesis of fluorinated diamond-like carbon films by the plasma immersion ion processing technique. *Journal of Vacuum Science and Technology A*, 19(3):782–784, 2001.

[13] X. M. He, M. Hakovirta, A. M. Peters, B. Taylor, and M. Nastasi. Fluorine and boron co-doped diamond-like carbon films deposited by pulsed glow discharge plasma immersion ion processing. *Journal of Vacuum Science and Technology A*, 20(3):638–642, 2002.

[14] K. P. Huang, P. Lin, and H. C. Shih. Structures and properties of fluorinated amorphous carbon films. *Journal of Applied Physics*, 96(1):354–360, 2004.

[15] G. Q. Yu, B. K. Tay, and Z. Sun. Fluorinated amorphous diamond-like carbon films deposited by plasma-enhanced chemical vapor deposition. *Surface and Coatings Technology*, 191(2-3):236–241, 2005.

[16] R. Prioli, L. G. Jacobsohn, M. E. H. Maia da Costa, and Jr. F. L. Freire. Nanotribological properties of amorphous carbon-fluorine films. *Tribology Letters*, 15(3):177–180, 2003.

[17] T. Nakamura, T. Ohana, M. Hasegawa, K. Tsugawa, M. Suzuki, M. Ishihara, A. Tanaka, and Y. Koga. Chemical modification of diamond surfaces with fluorine-containing functionalities. *New Diamond and Frontier Carbon Technology*, 15(6):313–324, 2005.

[18] S. A. Kulinich and M. Farzaneh. On wetting behavior of fluorocarbon coatings with various chemical and roughness characteristics. *Vacuum*, 79(3-4):255–264, 2005.

[19] L. G. Jacobsohn, D. F. Franceschini, M. E. H. Maia da Costa, and Jr. F. L. Freire. Structural and mechanical characterization of fluorinated amorphous-carbon films deposited by plasma decomposition of CF_4-CH_4 gas mixtures. *Journal of Vacuum Science and Technology A*, 18(5):2230–2238, 2000.

[20] C. Donnet, J. Fontaine, A. Grill, V. Patel, C. Jahnes, and M. Belin. Wear-resistant fluorinated diamondlike carbon films. *Surface and Coatings Technology*, 94-95:531–536, 1997.

[21] K. I. Nakamatsu, N. Yamada, K. Kanda, Y. Haruyama, and S. Matsui. Fluorinated diamond-like carbon coating as antisticking layer on nanoimprint mold. *Japanese journal of Applied Physics*, 45(33-36):L954–L956, 2006.

[22] N. Yamada, K. I. Nakamatsu, K. Kanda, Y. Haruyama, and S. Matsui. Surface evaluation of fluorinated diamond-like carbon thin film as an antisticking layer of nanoimprint mold. *Japanese Journal of Applied Physics*, 46(9B):6373–6374, 2007.

[23] A. Freedman and C. D. Stinespring. Fluorination of diamond (100) by atomic and molecular beams. *Applied Physics Letters*, 57(12):1194–1196, 1990.

[24] A. Freedman. Halogenation of diamond (100) and (111) surfaces by atomic beams. *Journal of Applied Physics*, 75(6):3112–3120, 1994.

[25] T. Ando, K. Yamamoto, M. Matsuzawa, Y. Takamatsu, S. Kawasaki, F. Okino, H. Touhara, M. Kamo, and Y. Sato. Direct interaction of elemental fluorine with diamond surfaces. *Diamond and Related Materials*, 5:1021–1025, 1996.

[26] D. E. Patterson, R. H. Hauge, and J. L. Margrave. Fluorinated diamond films, slabs, and grit. In L. E. Pope, L. Fehrenbacher, and W. O. Winer, editors, *Materials Research Society Symposium Proceedings*, volume 140, pages 351–356, 1989.

[27] J. F. Morar, F. J. Himpsel, G. Hollinger, J. L. Jordan, G. Hughes, and F. R. McFeely. C 1s excitation studies of diamond (111). ii. unoccupied surface states. *Physical Review B*, 33(2):1346–1349, 1986.

[28] J. F. Morar, F. J. Himpsel, G. Hollinger, J. L. Jordan, G. Hughes, and F. R. McFeely. C 1s excitation studies of diamond (111). i. surface core levels. *Physical Review B*, 33(2):1340–1345, 1986.

[29] T. Yamada, H. Seki, and T. J. Chuang. Adsorption of fluorine on bare, hydrogen- and hydrocarbon-covered diamond C(111) surfaces. *Japanese Journal of Applied Physics*, 39(4A):1826–1834, 2000.

[30] V. S. Smentkowski and Jr J. T. Yates. Fluorination of diamond surfaces by irradiation of perfluorinated alkyl iodides. *Science*, 271(5246):193–195, 1996.

[31] V. S. Smentkowski, Jr J. T. Yates, and III Chen W.A. X. Goddard. Fluorination of diamond - C_4F_9I and CF_3I photochemistry on diamond (100). *Surface Science*, 370(2-3):209–231, 1997.

[32] H. Kasai, M. Kogoma, T. Moriwaki, and S. Okazaki. Surface structure estimation by plasma fluorination of amorphous carbon, diamond, graphite and plastic film surfaces. *Journal of Physics D: Applied Physics*, 19(11):L225–L228, 1986.

[33] S. Miyake, R. Kaneko, Y. Kikuya, and I. Sugimoto. Micro-tribological studies on fluorinated carbon films. *Journal of Tribology-Transactions of the ASME*, 113(2):384–389, 1991.

[34] R. S. Butter, D. R. Waterman, A. M. Lettington, R. T. Ramos, and E. J. Fordham. Production and wetting properties of fluorinated diamond-like carbon coatings. *Thin Solid Films*, 311(1-2):107–113, 1997.

[35] K. Trojan, M. Grischke, and H. Dimigen. Network modification of DLC coatings to adjust a defined surface energy. *Physica Status Solidi A*, 145(2):575–585, 1994.

[36] F. L. Freire Jr., M. E. H. Maia da Costa, L. G. Jacobsohn, and D. F. Franceschini. Film growth and relationship between microstructure and mechanical properties of a-C:H:F films deposited by PECVD. *Diamond and Related Materials*, 10(2):125–131, 2001.

[37] L. G. Jacobsohn, M. E. H. Maia da Costa, V. J. Trava-Airoldi, and Jr F. L. Freire. Hard amorphous carbon-fluorine films deposited by PECVD using C_2H_2-CF_4 gas mixtures as precursor atmospheres. *Diamond and Related Materials*, 12(10-11):2037–2041, 2003.

[38] S. Liu, S. Gangopadhyay, G. Sreenivas, S. S. Ang, and H. A. Naseem. Infrared studies of hydrogenated amorphous carbon (a-C:H) and its alloys (a-C:H,N,F). *Physical Review B*, 55(19):13020–13024, 1997.

[39] K. L. Choy and J. Zhao. The mechanical properties of DLC and fluorinated DLC films deposited using unbalanced magnetron sputter ion plating method. *Scripta Materialia*, 39(7):839–845, 1998.

[40] H. S. Jung and H. H. Park. Structural and electrical properties of co-sputtered fluorinated amorphous carbon film. *Thin Solid Films*, 420-421:248–252, 2002.

[41] W. Kohn and L. J. Sham. Self-consistent equations including exchange and correlation effects. *Physical review*, 140:A1133–A1138, 1965.

[42] J. P. Perdew, J. A. Chevary, S. H. Vosko, K. A. Jackson, M. R. Pederson, D. J. Singh, and C. Fiolhais. Atoms, molecules, solids, and surfaces: Applications of the generalized gradient approximation for exchange and correlation. *Physical Review B*, 46(11):6671–6687, 1992.

[43] G. Kresse and J. Hafner. Ab initio molecular dynamics for open-shell transition metals. *Physical Review B*, 48(17):13115–13118, 1993.

[44] G. Kresse and J. Hafner. Ab initio molecular-dynamics simulation of the liquid-metalamorphous- semiconductor transition in germanium. *Physical Review B*, 49(20):14251–14269, 1994.

[45] G. Kresse and J. Furthmüller. Efficiency of ab-initio total energy calculations for metals and semiconductors using a plane-wave basis set. *Computational Materials Science*, 6(1):15–50, 1996.

[46] P. E. Blöchl. Projector augmented-wave method. *Physical Review B*, 50(24):17953–17979, 1994.

[47] G. Kresse and D. Joubert. From ultrasoft pseudopotentials to the projector augmented-wave method. *Physical Review B*, 59(3):1758–1775, 1999.

[48] Katsuji Haruna, Hiroshi Maeta, Kazutoshi Ohashi, and Takuro Koike. Thermal expansion coefficient of synthetic diamond single crystal at low temperatures. *Japanese Journal of Applied Physics*, 31(8):2527–2529, 1992.

[49] K. C. Pandey. New dimerized-chain model for the reconstruction of the diamond $(111)-(2\times1)$ surface. *Physical Review B*, 25(6):4338–4341, 1982.

[50] G. Kern, J. Hafner, and G. Kresse. Atomic and electronic structure of diamond (111) surfaces i. Reconstruction and hydrogen-induced de-reconstruction of the one dangling-bond surface. *Surface Science*, 366(3):445–463, 1996.

[51] A. Scholze, W. G. Schmidt, and F. Bechstedt. Structure of the diamond (111) surface: Single-dangling-bond versus triple-dangling-bond face. *Physical Review B*, 53(20):13725–13733, 1996.

[52] W. J. Huisman, J. F. Peters, S. A. De Vries, E. Vlieg, W. S. Yang, T. E. Derry, and J. F. Van Der Veen. Structure and morphology of the as-polished diamond$(111)-1\times1$ surface. *Surface Science*, 387(1-3):342–353, 1997.

[53] Th. Schaich, J. Braun, J. P. Toennies, M. Buck, and Ch Wöll. Structural changes accompanying the hydrogen desorption from the diamond C(111):H(1×1)-surface revisited by helium atom scattering. *Surface Science*, 385(2-3):L958–L964, 1997.

[54] Th Köhler, M. Sternberg, D. Porezag, and Th Frauenheim. Surface properties of diamond (111): 1×1, 2×1, and 2×2 reconstructions. *Physica Status Solidi A*, 154(1):69–89, 1996.

[55] S. J. Harris and D. N. Belton. Thermochemistry on a fluorinated diamond (111) surface. *Applied Physics Letters*, 59(16):1949–1951, 1991.

[56] W. Piekarczyk and S. Prawer. On the behavior of diamond crystal surfaces during heating in fluorine gas and fluorocarbon-fluorine gas mixtures. *Diamond and Related Materials*, 3:66–74, 1993.

[57] K. Larsson and S. Lunell. Stability of halogen-terminated diamond (111) surfaces. *The journal of physical chemistry A*, 101(1):76–82, 1997.

[58] D. Petrini and K. Larsson. Theoretical study of the thermodynamic and kinetic aspects of terminated (111) diamond surfaces. *Journal of Physical Chemistry C*, 112(8):3018–3026, 2008.

[59] J. C. Boettger. Nonconvergence of surface energies obtained from thin-film calculations. *Physical Review B*, 49(23):16798–16800, 1994.

[60] S. Hong and M. Y. Chou. Effect of hydrogen on the surface-energy anisotropy of diamond and silicon. *Physical Review B*, 57(11):6262–6265, 1998.

[61] M. Dion, H. Rydberg, E. Schroder, D.C. Langreth, and B.I. Lundqvist. Van der Waals density functional for general geometries. *Physical review Letters*, 92:246401, 2004.

[62] Q. Wu and W. Yang. Empirical correction to density-functional theory for van der Waals interactions. *Journal of Chemical Physics*, 116(2):515–524, 2002.

[63] S. Grimme. Accurate description of van der Waals complexes by density-functional theory including empirical corrections. *Journal of Computational Chemistry*, 25(12):1463–1473, 2004.

[64] P.L. Silvestrelli. Van der Waals interaction in DFT made easy by Wannier functions. *Physical Review Letters*, 100:053002, 2004.

[65] Yue Qi and L. G. Hector. Adhesion and adhesive transfer at aluminum/diamond interfaces: a first-principles study. *Physical Review B*, 69(23):235401, 06/15 2004.

[66] W. Zisman. Contact angle, wettability and adhesion. volume 43 of *Advances in Chemistry Series*, page 51. American Chemical Society, Washington D.C., 1964.

[67] D. R. Lide. *CRC Handbook of Chemistry and Physics*. Taylor and Francis, Boca Raton, FL, 2007.

[68] R. F. W. Bader. Atoms in molecules. *Accounts of Chemical Research*, 18(1):9–15, 1985.

[69] G. Henkelman, A. Arnaldsson, and H. Jónsson. A fast and robust algorithm for Bader decomposition of charge density. *Computational Materials Science*, 36(3):354–360, 2006.

[70] R. Saito, M. Yagi, T. Kimura, G. Dresselhaus, and M. S. Dresselhaus. Electronic structure of fluorine doped graphite nanoclusters. *The Journal of Physics and Chemistry of Solids*, 60(6):715–721, 1999.

[71] S. Dag and S. Ciraci. Atomic scale study of superlow friction between hydrogenated diamond surfaces. *Physical Review B*, 70(24):241401(R), 2004.

Chapter 3

Material Transfer Mechanisms between Aluminum and Fluorinated Carbon Interfaces

3.1 Introduction

The adhesive transfer of aluminum to tool and die surfaces is a significant manufacturing problem for the machining and forming processes of components made of Al alloys. Diamond-like carbon (DLC) coatings, which are known to have good Al adhesion mitigating properties and provide the lowest coefficient of friction (COF) against Al, compared to conventional industrial coatings based on nitride, boride and carbide systems, have presented themselves as promising tool coatings for machining and shaping of Al [1–4]. DLC coatings consist of a dense, amorphous structure characterized by a mixture of sp^2 and sp^3 type bonded carbon. The carbon hybridization state (i.e. the sp^3/sp^2 ratio) and the hydrogen content are the two major factors that control these coatings' mechanical and physico-chemical properties [5,6]. Studies have shown that during Al−Si alloy machining, improvements in tool life were achieved by using cutting tools with DLC coatings containing about 40 at.% H (H−DLC) instead of uncoated tool steel [7,8]. Tribological tests under various atmospheres, including ambient air, dry air and vacuum, have indicated that the

COF values of DLC coatings can vary over a broad range [5, 9–11]. When used in vacuum or under inert gas atmospheres, H−DLC coatings have displayed a consistently low COF of 0.001 [12–14], which increased to 0.07 in the presence of water vapor in the atmosphere [15, 16]. Testing non−hydrogenated DLC (NH−DLC) coatings that contained less than $1 - 2$ at.% H under inert atmospheres and in vacuum [3, 17] led to significant Al adhesion, with COF values as high as $0.6 - 0.9$, which were generally associated with the strong bonding formed between Al and the dangling bonds of C atoms on the DLC surface [13, 14].

The passivation of a surface C atom's dangling bonds by H and/or OH groups is thought to hinder interactions with the environment and counterface materials, resulting in a stable surface with a low COF and a negligible amount of Al adhesion [3, 18–20]. Thus, NH−DLC coatings display lower COFs when tested under high relative humidity atmospheres − an opposite trend to the environmental response of the tribological behavior of H−DLCs [3]. The temperature and the partial pressure of H_2 required to maintain a fully H−passivated diamond surface can be calculated using first-principles thermodynamic calculations, which allow the prediction of conditions that promote low friction during sliding contact [21].

First-principles calculations have been used in many studies to provide insight into the interactions between Al and various surfaces, including Al_2O_3 [22], WC [23], VN, VC [24], BN [25], graphite [26] and diamond [27]. In these studies, typically the energy required to separate an interface into two free surfaces—the work of separation, W_{sep} [28] − was calculated and used to predict the material transfer tendency by comparing the bulk materials' calculated decohesion energies with the interface's work of separation. It was reported that the passivation of diamond surfaces by −H [27] and −OH [20] radicals created repulsive interactions between these surfaces and Al atoms. On the other hand, it was shown that Al atoms formed covalent bonds with surfaces consisting of C atoms that had exposed dangling bonds, as well as with O−terminated diamond surfaces [29]. When iron surfaces that came in contact with −H and −OH terminated diamond surfaces were considered, first principles and molecular dynamics calculations indicated that a minimum quantity of adhesion occurred at the contact interface [30]. The formation of C−rich transfer layers on the counter surfaces that slid against H−DLC was identified as an important factor in attainment of low friction in DLC coatings [31–33].

DLC coatings with structures that contain between 2 and 35 at.% F (F−DLC) were reported to possess a lower surface energy than H−DLC coatings, and tended to form more thermodynamically stable surfaces [34–42]. The first principles calculations revealed that two F−terminated diamond surfaces facing each other would exert mutually higher repulsive forces than two H−terminated surfaces [43]. According to observations of the DLC-coated molds used for nanoimprinting polymers, F−DLC coatings displayed a more effective anti-sticking performance compared with the H−DLC-coated mold surfaces [44–46]. One study reported a slightly lower COF of 0.10 for F−DLC coatings tested against steel surfaces, compared to H−DLC coatings with a COF of 0.13 [39]. These measurements were consistent with atomic force microscopy observations of F−DLC coatings tested against Si_3N_4 [42], which provided a COF of 0.15, whereas a COF of 0.21 was obtained for the H−DLC coating. Studies also revealed that while increasing the relative humidity in the test atmosphere caused an increase in the COF values of H−DLC coatings [16, 47], higher humidity levels resulted in a decrease in the F−DLC's COF [48, 49] [48,49]−suggesting that differences exist between the roles that H− and F−terminated C bonds play in the passivation of DLC surfaces.

In summary, both experimental and computational studies suggested that the F−DLC coatings could provide an effective route to alleviate adhesion in the systems studied so far, most of which consisted of ferrous and ceramic surfaces. Experimental and computational studies that address material transfer and adhesion between F−DLC coatings and Al surfaces have yet to be undertaken, but remain vital to developing a comprehensive understanding of the surface properties of F−DLC coatings, as well as assessing the feasibility of applying these coatings on the surfaces of tools used in Al alloy shaping and forming operations.

This study, accordingly, investigates material transfer mechanisms between F−DLC and Al surfaces by using first principles calculations. The interfacial strength between F−terminated diamond and Al surfaces was estimated, and the effect that contact pressure had on the F transfer was determined. In order to corroborate the implications of the atomistic simulations on tribological applications, sliding contact experiments were performed on F−DLC-coated substrates (and H−DLC coatings, for comparison) run against commer-

cial purity Al counterfaces. The predictions of atomistic simulations at the interfaces were analyzed together with the results of the sliding contact experiments, which served to rationalize the effect that fluorine in carbon coatings has on adhesion and friction of metallic surfaces.

3.2 First principles calculations

3.2.1 Calculation methodology

Interactions between Al and F−DLC surfaces were modeled using first principles calculations based on the density functional theory (DFT). The single-particle Kohn-Sham [50] equation was solved with a plane-wave basis set in order to obtain the ground state energies of the model structures used. All computations were performed using a projector-augmented wave (PAW) method and a generalized gradient approximation (GGA) [51] of exchange correlation energy, as implemented in the Vienna Ab initio Simulation Package (VASP) [52, 53]. The total ground state energies were obtained by relaxing the positions of the atoms in the model structures and minimizing the Hellman-Feynman forces using a conjugate gradient method. Using a plane wave cut-off energy of 600 eV and a $10 \times 10 \times 1$ grid of $\Gamma-$centered k-points, an energy convergence to $1 - 2$ meV was obtained. The electronic degrees of freedom for the structures were set to converge at 10^{-5} eV/cell and the Hellman-Feynman forces were relaxed to 0.05 eV/Å or less for all atomic cells used in computations for bulk, surface and interface structures. The lattice parameters of Al and diamond were calculated with an error of less than 1% of their experimental values in their bulk experimental crystal structure [54, 55].

The F−DLC coating surface was represented by an F−terminated diamond surface − designated as diamond:F surface−by following the common practice outlined in the literature of employing diamond to model the passivation effects in DLC surfaces [20, 27, 30, 56]. A slab model was used to simulate the geometries of the Al and the diamond:F surfaces. The slabs consisted of 5−10 layers of atoms separated by a 10 Å vacuum gap. The minimum number of atomic layers necessary for simulating the bulk effect in each slab was determined by computing the convergence in surface energies for slabs representing Al and diamond:F

surfaces individually. The surface energy of the Al (111) surfaces each contained three atoms per layer and converged at 0.82 J m^{-2} in a slab consisting of eight layers—in agreement with previous DFT calculations [22]. Calculations carried out to estimate the surface stability of diamond:F surfaces indicated that a slab with six layers would be adequate. Details of these calculations can be found in the authors' previous work [43].

The interface model used is shown in Figure 3.1, and consisted of a periodic arrangement of alternating diamond:F and Al layers without vacuum that had, at minimum, an inversion symmetry to ensure that both interfaces were the same. The interface registry (Figure 3.1a) was constructed to minimize the large lattice mismatch (13%) between the Al and the diamond slabs. A construction that consisted of six bilayers of diamond:F $(111)-(2\times2)$ surface oriented in the $[01\bar{1}]$ direction and containing 4 F atoms at the surface and eight C atoms in each bilayer was considered. The diamond:F slab was matched with a slab consisting of 10 Al (111) surface layers oriented in the $[\bar{1}2\bar{1}]$ direction. This configuration formed a hexagonal interface structure described with an orientation relationship of $(111)\,[\bar{1}2\bar{1}]_{Al}\,\|\,(111)\,[01\bar{1}]_{C}$ and consisted of a total of 86 atoms. The structure constructed in this way is called an interface cell structure (Figure 3.1b). The interface registry was reported to have a negligible effect on the adhesion tendencies of Al/diamond interfaces [27], and hence no other orientation of Al and diamond surfaces was considered.

Given that the edge length of the Al (111) plane is 4.96 Å in the $[\bar{1}2\bar{1}]$ direction, and that the (2×2) diamond slab has a length of 5.05 Å along the $[01\bar{1}]$ direction, a lattice mismatch of less than 2% occurred at the interface. As such, the contribution of misfit dislocations can be ignored because a periodic interface structure that gives rise to an error in the computed work of separation less than 5% is considered a reasonable approximation [57, 58]. The in-plane cell dimension of the Al (111) slab was intentionally expanded to match that of the diamond surface (5.05 Å), which led to the generation of a negligible strain in the Al cell, prompting the total energy of the interface to remain virtually unchanged. Interface calculations were carried out under vacuum at 0 K and the effects of plastic deformation and diffusion were not considered.

Initially, atoms on Al and diamond:F surfaces were placed 8.8 Å apart, and then the interfacial separation distance $(d_{\text{Al-F}})$ was gradually decreased to 1.2 Å. The decrease in
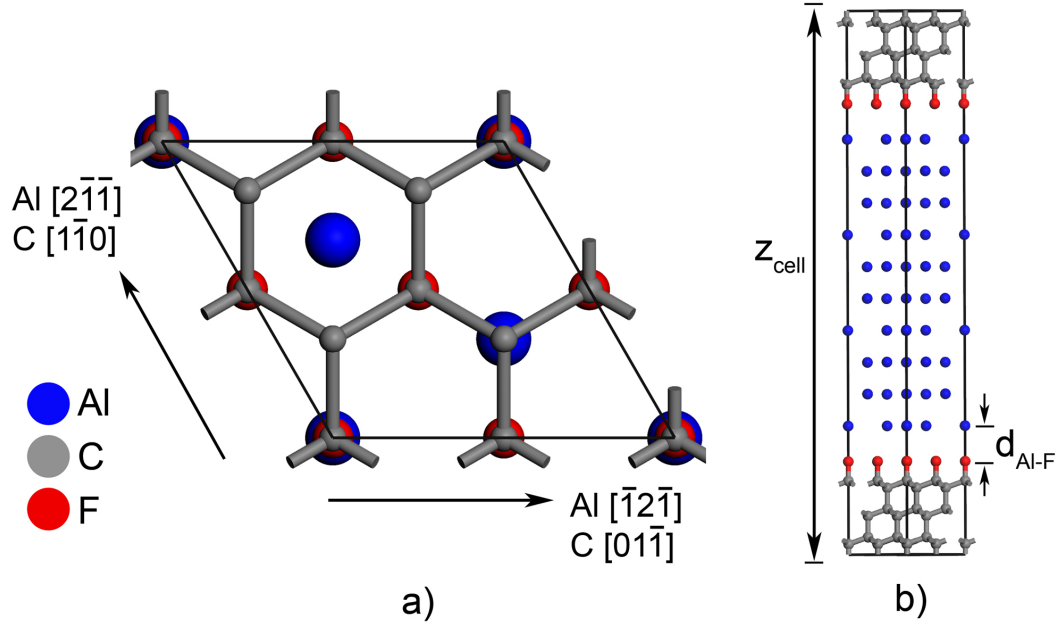
Figure 3.1: Al/diamond:F interface model used in the first principles calculations. (a) Top view of the interface registry, where the edge length of the cell is 5.05 Å. (b) Side view of the interface model formed between 10 layers of Al and 6 bilayers of diamond surface terminated with fluorine, where z_{cell} is the cell length in the $z-$direction and $d_{\text{Al-F}}$ is the distance between the Al and F atoms at the interface.

$d_{\text{Al-F}}$ was accompanied by a decrease in the $z-$direction of the interface cell structure. For each intermediate separation distance considered and defined in respect to cell dimension z_{cell}, the total energy of the system (E_{tot}) was computed by letting the atoms relax in their initial positions without allowing the constrained interface cell structure to relax. The change in E_{tot} was reported to be relative to that of the reference state E_{tot}^0 at the far separated interface of $d_{\text{Al-F}} = 8.8$ Å. The relative energy change $\Delta E_{tot} = \left(E_{tot} - E_{tot}^0\right)$ for the Al/diamond:H interfaces was calculated in the same way, by substituting the F atoms with the H atoms in Figure 3.1.

3.2.2   Interfacial energy calculations

Figure 3.2 plots the change in ΔE_{tot} as a function of decreasing the separation distance between the Al and diamond:F surfaces, expressed as a function of $z_{cell}-$compared with ΔE_{tot} vs. z_{cell} variations between the Al and diamond:H surfaces. It is pertinent to consider the variations of ΔE_{tot} between Al and diamond:H as a way of rationalizing the interactions

between Al and diamond:F. For $z_{cell} < 40.9$ Å, corresponding to $d_{Al-H} < 3.4$ Å, ΔE_{tot} started to assume increasingly positive values, hence Al and diamond:H surfaces exerted a progressively more repulsive force in relation to each other−a repulsive force that continued to increase with a further decrease in z_{cell}.
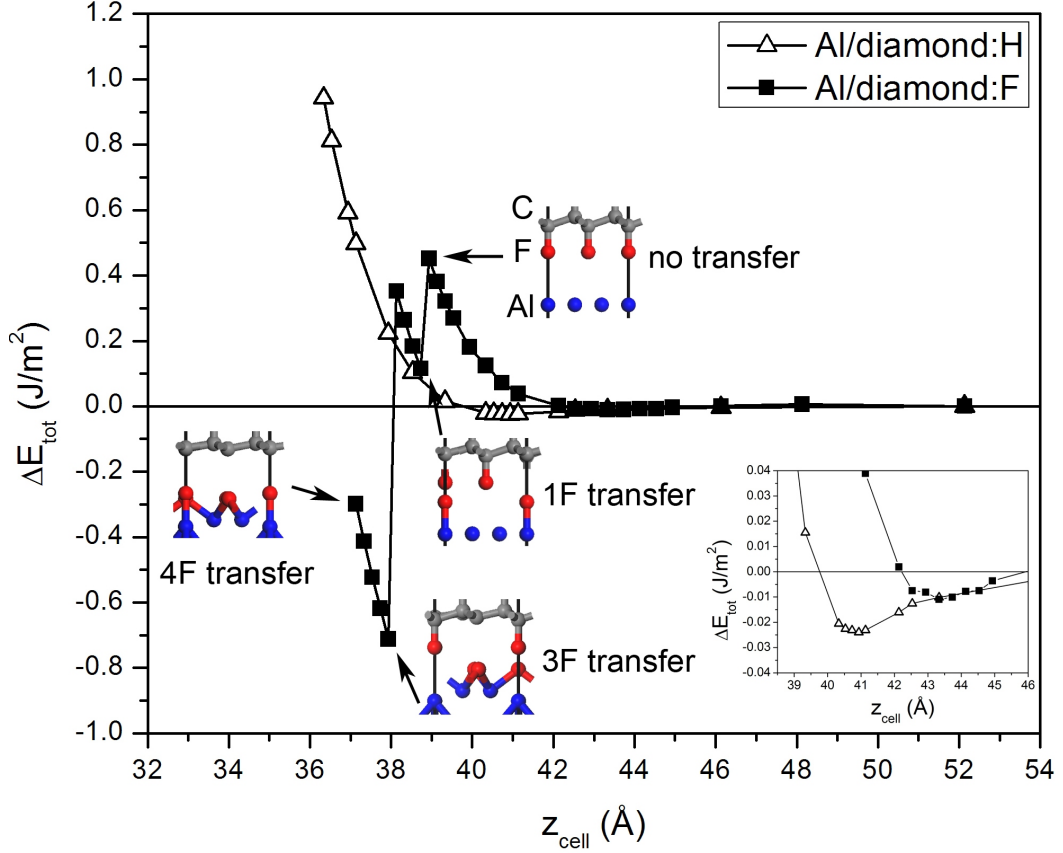
Figure 3.2: The relative energy change, ΔE_{tot}, when an Al surface approaches diamond:F and diamond:H surfaces. While bringing the surfaces together, the cell dimension, z_{cell} is reduced from $z_{cell}^0 = 52.1$ to 37.1 Å. The relaxed atomic structures of Al/diamond:F interfaces corresponding to 1 F, 3 F and 4 F atom transfers to the Al surface are illustrated at z_{cell} corresponding to the initiation of each transfer event. The inset shows details of ΔE_{tot} vs z_{cell} plot for $38.5 < z_{cell} < 46.0$ Å.

For Al/diamond:F, the increase in ΔE_{tot} was not continuous, but incremental increases in ΔE_{tot} were followed by local minima. ΔE_{tot} initially reached a local minimum of 0.01 J m^{-2} at $z_{cell} = 43.3$ Å (see the enlarged portion of the curve in the inset) corresponding to $d_{Al-F} = 4.4$ Å, below which ΔE_{tot} started to rise−indicating repulsion between Al and diamond:F. At $z_{cell} = 38.9$ Å ($d_{Al-F} = 2.8$ Å) ΔE_{tot} increased to a maximum of 0.45 J m^{-2} and then dropped to another local minimum value of 0.12 J m^{-2} at $z_{cell} = 38.7$ Å.

An analysis of the interface cell structure revealed that the energy minimum at $z_{cell} = 38.7$ Å is caused by the transfer of an F atom to the Al surface. The 1 F−transferred interface remained stable, while the ΔE_{tot} increased to 0.35 J m^{-2} with the reduction in z_{cell} to 38.1 Å. For the interfaces that were closer than this separation distance, the energy dropped to a global minimum of $\Delta E_{tot}^{min} = 0.71$ J m^{-2}. At this point, the transfer of 3 F atoms on the diamond surface to Al was realized. Further reduction in z_{cell} resulted in an increase in ΔE_{tot}, but the negative values of ΔE_{tot} indicated that the 3 F−transferred interface remained stable. Finally, all 4 F atoms on the diamond surface became transferred to the Al side at $z_{cell} = 37.5$ Å. Surfaces were brought closer until $z_{cell} = 37.3$ Å ($d_{Al-F} = 1.2$ Å) with no sign of the formation of another energy minimum.

Assuming that the process of bringing the surfaces closer was achieved by applying an external pressure to the interfaces, the stress in the $z-$direction, σ_{zz}, normal to interface plane can be calculated using:

$$\sigma_{zz} = -\frac{1}{A}\frac{\partial E_{tot}}{\partial z_{cell}} \tag{3.1}$$

where A, the area of interface plane shown in Figure 3.1a, is equal to 22.1 Å^2 and is plotted in Figure 3.3. This stress can be regarded as the contact pressure exerted on the Al/diamond: F interfaces. According to Figure 3.3, the transfer of 1 F atom from the diamond surface to the Al initiated when $\sigma_{zz} = 3.5$ GPa, while the transfer of 3 F atoms occurred when $\sigma_{zz} > 4.5$ GPa and all 4 F atoms became transferred to the Al when $\sigma_{zz} > 5.7$ GPa. When the same amount of pressure (Fig. 3) was applied to the Al/diamond:H interfaces, ΔE_{tot} increased continuously without an indication of H transfer to the Al.

To determine the stability of the interfaces with 1 F, 3 F and 4 F atoms transferred on the Al surface, each of the interfaces shown in Figure 3.2 was pulled apart from its equilibrium configuration until the interfacial separations (d_{F-F}) exceeded 8.0 Å. Figure 3.4 shows that ΔE_{tot} of the interfaces with the transferred F atoms were lower compared to the original Al/diamond:F interface−a clear indication that the F−transferred interfaces were more stable than the original interface structure. Figure 3.4 provides evidence that the
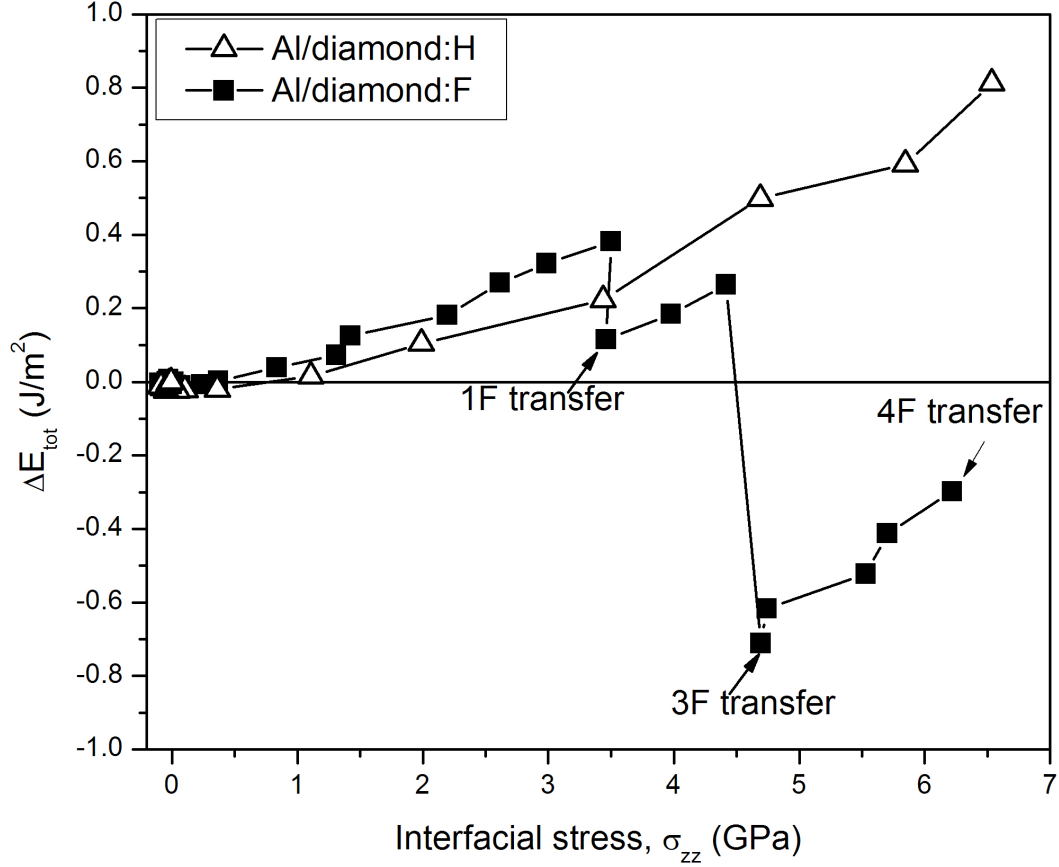
Figure 3.3: The variations in the relative energy, ΔE_{tot} at Al/diamond:F and Al/diamond:H interfaces with the stress, σ_{zz}, applied at the interface.

F transfer to the Al surface is thermodynamically feasible, and following the transfer of F atoms to Al, a repulsive interaction was maintained between this Al/diamond:F interface. Consequently, it can be concluded that F atoms can effectively passivate both surfaces.

According to Figure 3.4, the 3 F−transferred interface assumed the lowest energy and thus was the most stable, which is consistent with the global energy minimum ΔE_{tot}^{min} observed in Figure 3.2 for this configuration. A better insight was gained into the stability of F transferred Al/diamond: F interfaces, when the bonding structure of these interfaces was studied in more detail as described in Section 3.2.3.

3.2.3 Bonding structure of Al/diamond:F interfaces

Electron localization function (ELF) analyses were used to study the evolution of bonding structure generated at Al/diamond:F interfaces. ELF is a position-dependent function
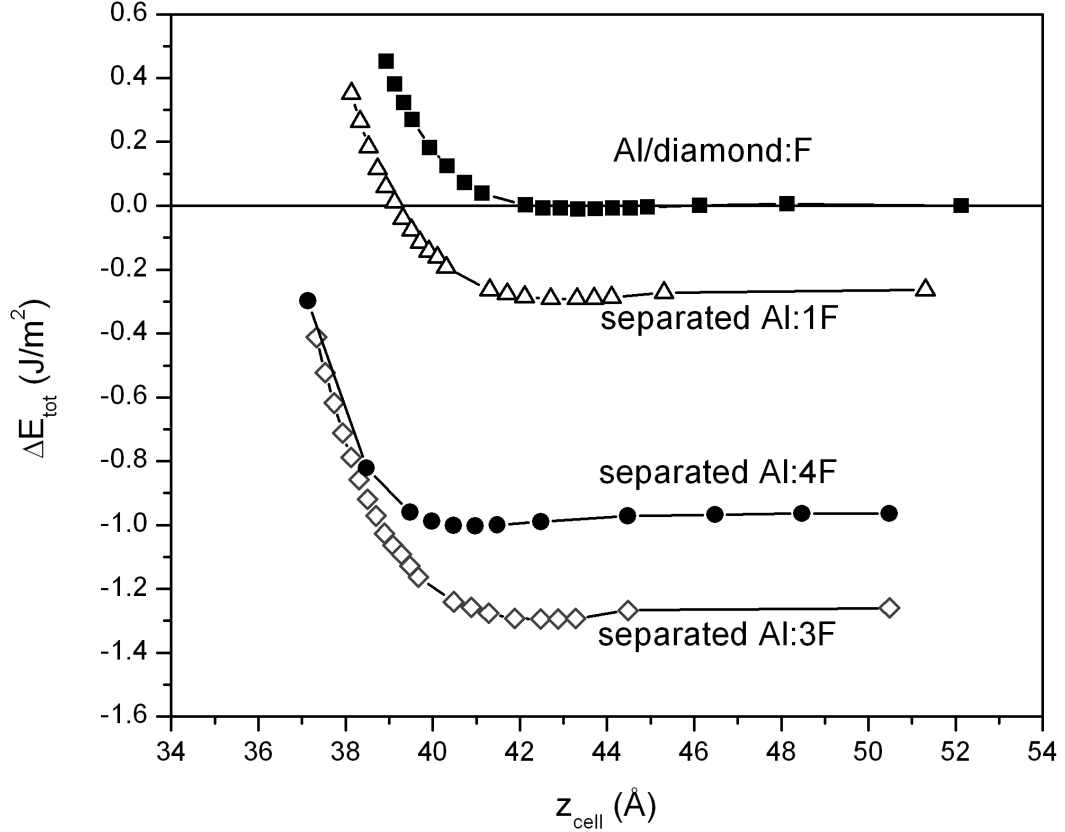
Figure 3.4: The relative energy change, ΔE_{tot} during separation of the F−transferred Al/diamond:F interfaces. All F−transferred interfaces had lower energy than the initial Al/diamond:F interface configuration with the 3 F−transferred interface being the most stable structure.

whose value varies in the range of $0 - 1$, with $\mathrm{ELF} = 1.0$ corresponding to covalent type bonding. $\mathrm{ELF} = 0.5$ corresponds to electron/gas-like pair probability, which is an indication of metallic bonding, and for $\mathrm{ELF} < 0.5$ the function is undefined [59]. The ELF plots of the Al/diamond:F interfaces with different concentrations of F atoms transferred to the Al surfaces appear in Figure 3.5. The covalent bonding that characterizes a diamond surface is clearly visible in locations where $\mathrm{ELF} \sim 1.0$ between the two C atoms. Al exhibited a metallic character, as expected, in locations where $\mathrm{ELF} \sim 0.5$. At the interfaces where $\mathrm{ELF} \sim 0$, the absence of any type of chemical bonding (covalent, metallic or ionic) was apparent. At the F−transferred interfaces (Figure 3.5b-d), the substantial electron localization generated around the F atoms and the corresponding charge depletion around the Al atoms were all indicative of the transfer of electrons from the Al to the F atoms. This observation also

inferred that an ionic bond was formed between Al and F.

The transfer of F to Al prompted a reconstruction of the Al surface structure. When 1 F atom was transferred to Al (Figure 3.5b), the F atom became bonded to the Al atom with a bond distance of 1.69 Å (i.e. a distance almost equal to the bond length observed in the gaseous state of AlF(g) reported as 1.65 Å [60]). The transfer of F caused the top layers of the diamond surface to expand and those of the Al surface to contract (the Al atom that bonded to an F atom was pushed away from the surface by 0.13 Å in Figure 3.5b). When 3 or 4 F atoms were transferred to Al, the subsequent surface changes were more noticeable. Figure 3.5c shows that following the transfer of 3 F atoms to the Al surface, two of the Al atoms shifted away from their initial positions on the surface to bond with the three available F atoms−leaving only 1 non-bonded Al atom at the surface. In this configuration, each Al atom was bonded to 3 F atoms, which implies the possibility that the AlF_3 compound forms. The structure of an interface with four transferred F atoms can be regarded as the combination of 1 F− and 3 F−transferred interfaces, but with all 4 F atoms staying in-plane in the z−direction. This observation can be attributed to the interactions existing between π orbitals of F atoms [43]. In summary, according to the ELF analysis, F transfer to the Al surface caused the passivation of the Al surface by F atoms, which in turn resulted in increasing the stability of Al/diamond:F interfaces. This increase in stability was due to the surface reconstruction that occurred on the Al (111) surface in the presence of fluorine. The characteristics of the F−transferred Al surface are investigated in Section 3.2.4.

3.2.4   Modification of Al surface and formation of AlF_3

The reconstructed Al (111) surface was examined in further detail to explain the formation of AlF_3 at the Al interface. The formation of this compound is an important aspect of the material transfer mechanisms at the Al/diamond: F interface. The atomic configuration of the 3 F-transferred Al surface is illustrated in Figure 3.6, which shows that the reconstruction resulted in a slightly weakened, near surface Al structure. The work of decohesion, for the Al layers−defined as the energy required to detach one layer from the Al surface−was calculated for the first three Al layers. The W_{dec} values of these layers are marked in Figure

3.6a. Accordingly, W_{dec} between the 3rd and 4th layers (1.69 J m^{-2}) was comparable to the W_{dec} of the atomic layers in bulk Al, which is twice the surface energy of Al (0.82 J m^{-2}). Less energy was required to separate the atomic layers that lay immediately below the surface incorporating the transferred F atoms (the separation of the 2nd and 3rd atomic layers W_{dec} = 1.26 J m^{-2}). It should be noted that, despite the weakening of the Al structure near the surface, the reduced W_{dec} was still higher than the interfacial strength of the 3 F−transferred Al/diamond:F interface, which was calculated as W_{sep} = 0.02 J m^{-2}. Consequently, Al decohesion is not expected to occur before the separation of the Al/diamond:F interface.

Figure 3.6b shows that each Al atom at the surface was bonded to 3 F atoms, suggesting the formation of an AlF$_3$ compound. The bond structure of the 3 F−transferred Al surface was compared with the bond structure of the AlF$_3$ compound by relaxing the AlF$_3$ crystal. We then calculated the lattice parameters of the thermodynamically stable phase, α−AlF$_3$ [61], which belongs to space group $R\bar{3}c$. In this unit cell, atoms were arranged in the forms of corner-sharing AlF$_6$ octahedra. The lattice parameters of this relaxed AlF$_3$ unit cell were calculated as a = 4.99 Å, c = 12.61 Å and x = 0.4266, which are in good agreement with the reported experimental values for α−AlF$_3$ [61]. In this structure, the Al−F bond distance was 1.82 Å and angles F− Al−F and Al−F−Al were 89.97 and 156.8, respectively. When comparing the atomic arrangements of the AlF$_3$ crystal with the 3 F−transferred Al surface, the Al−F bond distance (1.83 Å) and F−Al−F angle (88.4) values (Figure 3.6a) proved to be in excellent agreement. The only significant difference was that the Al−F−Al angle was higher in the AlF$_3$ crystal, because in the 3 F−transferred Al surface, only half of the AlF$_6$ octahedra were present.

To summarize the salient points of the results arising from first principles calculations, it was predicted that F transfer would occur at the Al/diamond:F interfaces under high contact pressure. The F transfer was found to yield an increase in the stability, which was attributed to the surface reconstruction that occurred on the Al surface in the presence of F atoms. Further analysis of the reconstructed Al surface showed that AlF$_3$ would form at the Al surface. The sliding contact experiments were carried out to corroborate the predictions from first principles calculations, and the results of these experiments are presented in the

next section.

3.3   Sliding contact experiments

3.3.1   Experimental procedure and material properties

The F−DLC-coated steel samples were placed in dry sliding contact against commercial purity (> 99%) Al 1100 counterfaces in the shape of 6.35 mm diameter spherical balls, using a ball-on-disk type tribometer (CSM, Switzerland) to record the change in COF that occurred with the sliding distance. Sliding tests were conducted using a constant speed of 0.12 m s^{-1}, and at a 5.0 N load under an ambient atmosphere with a relative humidity of $41 \pm 3\%$. During the tests, a sliding track with an average diameter of 5.0 cm and a width of 0.3 mm was formed.

   The DLC coatings−designated as F−DLC and H−DLC−were deposited using a plasma-assisted chemical vapor deposition (PACVD) technique on M2 grade tool steel coupons in the form of 25.4 mm diameter discs by Bekaert Advanced Coating Technologies, New York, USA. The carbon and fluorine contents of the coatings were determined using Rutherford backscattering spectroscopy (RBS), and their hydrogen content was determined using the elastic recoil detection (ERD) technique. The compositions of the F−DLC and H−DLC coatings are given in Table 3.1. Measurements taken from three separate locations each 1.0 mm in diameter were used to determine the average compositions. Pertinent properties of the coatings are listed in Table 3.1. The surfaces of Al balls (cold forged, supplied by Alfa Aesar) were electropolished in a 5% perchloric acid (HClO$_4$) containing methanol solution at 20 V for 5 min. The surface roughness, R_a, of the polished Al balls, measured using a WYKO NT1100 white light optical surface profilometer, was 50 nm. The grain size of the Al was 9.5 ± 5.2 μm and its Vickers hardness measured at a load of 10 g was 264.7 ± 18.7 MPa (26.9 ± 1.9 VHN) which is much lower than that of the DLC.

   Scanning electron microscopy (JEOL JSM-5800LV) combined with energy-dispersive spectroscopy (EDS) was used to examine the transfer layers generated on the Al surface. The composition of these layers was studied using X-ray photoelectron spectroscopy (XPS). A Kratos Axis Ultra model XPS with an Al X-ray source (characteristic energy = 1.4867

Table 3.1: Chemical compositions and properties of F−DLC and H−DLC coatings. The thickness, t, was determined by pressing a 20 mm diameter ball onto the coating surface using a CSM Calotest instrument. The surface roughness, R_a, was measured on a 0.269 mm^2 area using a white light optical interferometer (Wyko NT1100). Water contact angles (θ) were measured using the sessile-drop method (Kruss). The elastic modulus (E) and hardness (H) values of the coatings were measured using a Hysitron TI 900 Nanoindenter using a load of 5 mN providing a penetration depth $\leq 10\%$ of the coating thickness.

Coating	C (at.%)	H (at.%)	F (at.%)	t (μm)	R_a (nm)	θ (º)	E (GPa)	H (GPa)
F-DLC	72 ± 3	25 ± 2	3 ± 1	1.23 ± 0.05	20 ± 3	80 ± 3	175 ± 12	31 ± 4
H-DLC	71 ± 3	29 ± 3	−	1.21 ± 0.05	16 ± 3	67 ± 2	153 ± 8	27 ± 3

keV) was used, and survey scans of samples were carried out with a pass energy of 160 eV. High resolution analyses were carried out on the same area using a pass energy of 20 eV.

Cross-sectional TEM samples taken from the Al surface covered with the transfer layers were prepared using an H-bar focussed-ion beam (FIB) milling technique [62]. Briefly, a 40 μm thick Al plate was first sectioned perpendicular to the area covered by the transfer layer by mechanical polishing. The location of the transfer layer to be thinned to electron transparency was coated with a carbon patch 30×30 μm^2 in area and 2.0 μm in height inside a Carl Zeiss NVision Crossbeam workstation. The sample was ion milled, beginning at one side of the plate and continuing until the region of interest protected by the carbon layer was reached. Ion milling was then performed on the other side of the area protected by the carbon strip, so that the final thickness of the section was reduced to approximately 100 nm−ready for TEM examination. To minimize ion beam damage during cross-sectional ion milling, a low ion current (150 pA) was used. The microstructure across the interface between the Al and the transfer layer was studied using a JEOL JEM-2100F field emission electron microscope.

3.3.2 The coefficient of friction and formation of transfer layers on aluminum

The variation of the F−DLC coating's COF with the number of sliding cycles is shown in Figure 3.7 together with the COF of the H−DLC coating−both tested against Al. The inset shows the initial portion of the COF curves for the first 200 sliding cycles. The COF of the F−DLC increased abruptly at the beginning of the test, and reached a maximum value of

0.61 at the 24$^{\text{th}}$ sliding cycle. This initial running-in period of high COF lasted for 110 sliding cycles. The COF then reduced to 0.14 ± 0.01, and this steady-state value was maintained for the rest of a sliding test that lasted for 3000 sliding cycles. An SEM examination of the Al ball surface (Figure 3.8a) that was in contact with the F−DLC, combined with EDS elemental maps taken from this surface (Figures 3.8b−e) indicated that the Al surface was plastically deformed and the deformed area was covered with a carbonaceous material that incorporated F (Figures 3.8c−d). Some oxygen associated with C and/or Al was also present (Figure 3.8e). SEM and EDS analyses performed on the F−DLC's wear track at the end of the test did not show any evidence of Al adhesion. Similarly, the COF of H−DLC initially increased to a maximum value of 0.67. The running-in period lasted for about 80 sliding cycles and was followed by a steady-state COF of 0.20 ± 0.01. Evidence for the presence of C and O in the transfer layers generated on the Al surface is given in (Figures 3.9a–d).

3.3.3   Nanohardness values of transfer layers

The nanohardness values of the transfer layers were measured using a Hysitron TI 900 Nanoindenter with a Berkovich type tip at about 50 different locations. The applied load was varied between 50 and 5000 μN. Indentations made with the same load resulted in widely differing penetration depths because of non-uniform thickness of the layers, and because the layers had different degrees of adhesion to the underlying Al substrate. Consequently, the average nanohardness values measured at a given load showed large standard deviations. For the indentations at depths between 100 and 200 nm, it was observed that the mean nanohardness values were almost constant and their standard deviations were relatively low compared to those with penetration depths lower and higher than this particular depth range. According to these measurements, the nanohardness of the transfer layer formed on the Al contact surface after sliding against F−DLC (Figure 3.8a) was 0.26 ± 0.16 GPa. Similarly, the nanohardness of the transfer layers formed on the Al surface after sliding against H−DLC (Figure 3.9a) was 0.29 ± 0.12 GPa. The nanohardness of the Al ball (measured on the cross-sections away from the contact surface) was determined as 0.56 ± 0.29 GPa. Therefore, the nanohardness values of transfer layers derived from F−DLC and H−DLC were similar, and lower than the bulk hardness of the Al. In addition the

hardness of the extruded Al chips formed on the ball surface, as a result of sliding, was measured and found to be 2.05 ± 1.04 GPa. This indicated that Al was subjected to severe plastic deformation upon contact with DLC and the deformed Al surface's nanohardness was approximately four times higher than that of the bulk Al.

3.3.4 Characterization of transfer layers

The presence of F in the transfer layers was in good agreement with the prediction of the first principles calculations (Figure 3.2), warranting more comprehensive compositional and microstructural analyses of the transfer layers by XPS and TEM. According to the XPS analyses, the composition of the transfer layer formed on the Al consisted of 55.3 at.% C, 24.6 at.% O, 1.7 at.% Si, 0.7 at.% N and 12.8 at.% Al. The F content in the transfer layer was 4.9 at.%, making the F/C ratio in these transfer layers 0.09, which was higher than the $F/C = 0.04$ in the constitution of the as-deposited F$-$DLC coating$-$suggesting that F was accumulated on the Al surface during sliding.

High-resolution XPS spectra of the transfer layers that recorded the binding energies of C $1s$ and Al $2p$ are shown in Figures 3.10a and b. Accordingly, C was present in the transfer layer in the bonding states of C$-$C and C$-$H, and associated with some C$-$F and C$-$O bonds. The binding energies of 284.8, 286.3, 287.8, 289.1 and 290.5 eV were assigned to the $-$C$-$C/$-$C$-$H, $-$C$-$OH/$-$C$-$O$-$C, $-$C$-$C$-$F, $-$O$-$C=O and $-$CH$_2$C$-$F$_2$ bonding states, respectively [63–65]. The atomic ratio of C$-$F groups was very small (1 at.%) compared to the other carbon groups, suggesting that the F in the DLC was separated from the carbon during the formation of the transfer layer. For the Al $2p$ spectra, an $2p_{3/2}$ binding energy of 74.92 eV and $2p_{1/2}$ binding energy of 75.33 eV were assigned to the chemical state of Al$_2$O$_3$ (xH$_2$O) with the possible presence of hydride groups, which could be in the form of either Al(OH)$_3$ [66,67] or AlO(OH) [67,68]. Another important piece of information that the Al $2p$ spectra yielded was the presence of AlF$_3$ that corresponded to a $2p_{3/2}$ binding energy of 76.55 eV and a $2p_{1/2}$ binding energy of 76.96 eV, which matched that of AlF$_3$ reported in the literature [65, 69, 70]. The species were quantified according to the integral area of decomposed peaks. Deconvolution of the spectrum as in Figure 3.10b, and the integral area calculations of these decomposed peaks revealed that 84.2 at.% of Al was present in

the form of $Al_2O_3xH_2O$, and 15.8 at.% Al in the form of AlF_3, inferring that the fluorine present in the F−DLC coating promoted the formation of AlF_3. The high-resolution TEM investigation provided evidence for the presence of AlF_3 in the transfer layer, as described below.

The TEM samples were prepared from cross-sections taken normal to the transfer layer on the Al surface, using the FIB milling method described in Section 3.1. A typical high-resolution, cross-sectional TEM (HRTEM) image in Figure 3.11 clearly shows that an AlF_3 phase was formed at the Al surface. According to the calculated diffraction patterns using fast Fourier transform (FFT) of the HRTEM image, the Al (111) surface was aligned with the $\alpha-AlF_3$ ($\bar{1}012$) surface, which is in the same family of ($01\bar{1}2$) planes. Therefore, an interface structure of $(111)_{Al} \parallel (01\bar{1}2)_{AlF_3}$ was formed at the Al surface. This was in agreement with the previous computational [71] and X-ray diffraction experiments [72], which revealed that in $\alpha-AlF_3$ crystals, ($01\bar{1}2$) surfaces are the most stable. Another observation arising from Figure 3.11 is the absence of an oxide layer on the Al surface. It is well known that Al oxidizes readily even under normal atmospheric conditions and forms a protective oxide film on its surface. However, Figure 3.11 shows that the oxide layer on the Al surface was removed during the sliding experiment, allowing nascent Al to interact with F atoms and form AlF_3.

3.4 Discussion

Two principal results pertaining to the tribological behavior of F−DLC coatings have arisen from the observations reported in Section 3.3. The first is that the steady-state COF of F−DLC was 30% lower compared to H−DLC, and the second was evidence for F transfer to the Al counterface. The detection of F−containing transfer layers by XPS and EDS and the evidence for the formation of AlF_3 at the transfer layers generated at the contact surfaces supported the key predictions of the first principles calculations. According to these calculations, when an Al and a diamond:F surface were brought together, the sequence of atomic transfer events would occur in the manner described in Figure 3.2, and eventually all 4 F atoms at the diamond surface would transfer to the Al surface. Again, according

to the atomistic calculations, the number of F atoms transferred to the Al would increase with an increase in the contact pressure. The interface that consisted of 3 transferred F atoms proved to be the most stable state. The possibility of forming an AlF_3 compound was predicted from a consideration of the angular relationships and bond lengths of atoms at the reconstructed Al surface (Figure 3.6b). A thermodynamic argument can be made to support the formation of AlF_3. Considering that this compound was formed as a result of the following reaction:

$$\frac{8}{3}Al + C_{48}F_8 = C_{48} + \frac{8}{3}AlF_3 \tag{3.2}$$
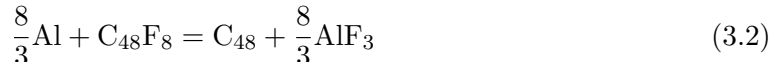
The enthalpy of formation for AlF_3, $H^f_{AlF_3}$, can then be calculated from:

$$H^f_{AlF_3} = \frac{3}{8}\left[E_{C_{48}} + \frac{8}{3}E_{AlF_3} - E_{C_{48}F_8} - \frac{8}{3}E_{Al}\right] \tag{3.3}$$

where $E_{C_{48}F_8}$ and $E_{C_{48}}$ designate the total energies of the six bilayers of diamond $(111) - 1 \times 1$ slabs with and without F termination. E_{Al} is the energy of one atom in a bulk Al face-centered cubic unit cell. E_{AlF_3} is the energy of one AlF_3 molecule, calculated in the $\alpha-AlF_3$ crystal. $H^f_{AlF_3}$ can then be calculated as 319.4 kJ mol^{-1}. The high negative value of $H^f_{AlF_3}$ indicates that the formation of AlF_3 is thermodynamically feasible under the conditions considered in this work. Experimental evidence for the formation of AlF_3 was shown by XPS results (Figure 3.10), and by the HRTEM observations (Figure 3.11).

Results of atomistic simulations and sliding experiments although not performed under identical contact and environmental conditions, complement each other, and when analyzed together they depict a coherent picture of the material transfer mechanisms. Accordingly, a model that accounts for the material transfer mechanisms between the F−DLC and the Al surfaces is proposed as shown in Figure 3.12, upon which implications of material transfer mechanisms on the COF between Al and F−DLC surfaces can be discussed.

Originally the Al surface was covered with a thin oxide layer and the initial COF was relatively low (Figure 3.12a). The subsequent steep increase in the COF during the early stages of the contact can be attributed to the plastic deformation of Al following removal of the surface oxide film and the breaking of C−C, C−H and C−F bonds. The bond breaking

process and the formation of new bonds with Al consume energy and may contribute to an increase in the COF during the running-in period [73] as depicted in Figure 3.12b. During sliding the occurrence of plastic deformation of Al was evident from the small extruded lips formed ahead of the contact area as shown in Figures 3.8 and 3.9a. The deformation microstructures that developed in Al in contact with DLC surfaces at similar loads were reported previously and shown to consist of ultrafine Al grains [62], and caused an increase in local hardness of the Al tip (Section 3.3.3). The transfer of Al fragments to the DLC surface contributed to the high friction, i.e. COF > 0.7 [18, 19].

The low COF values in the range of $0.1-0.2$ were reported to coincide with the formation of a carbonaceous transfer layer on the Al surface [12–14,31,33,74]. Some authors attributed the formation of transfer layers on the counterfaces sliding against the DLC coatings to the "structural transformation" of the sp^3 hybridized C atoms in the DLC to the sp^2 bonding state−a phenomenon referred as wear-induced graphitization [75, 76]. Bowden and Tabor [77] provided an analysis which demonstrated that low shear strength layers between two hard surfaces would produce low friction. The graphitized layers may be considered as low shear strength layers that serve to reduce the COF of the contacting surfaces. Provided the layers remain intact, the wear and plastic deformation of Al are prevented and a low COF value is expected to arise.

The DLC tribology literature also considers positive effects of −H and −OH passivation of carbon surfaces in reducing the COF [14, 18, 20]. Sliding tests carried out on non−hydrogenated DLC coatings under a vacuum environment (6.7×10^{-4} Pa) resulted in a high COF of 0.7, but introduction of H_2 or H_2O into the vacuum chamber reduced the COF to 0.1 [3, 14–18, 78]. It is well known that H atoms could be adsorbed by the transfer layers formed on Al [31] and the source of adsorbed H is either broken C−H bonds at the DLC surface or dissociation of H_2O molecules (in the ambient air) into H [20]. Atomistic simulations have shown that H_2O molecules can dissociate into −H and −OH groups on diamond surface [20] and effectively passivate the diamond surface, preventing adhesive interactions with Al [20, 27] (and Fe [30]). In the current study both F−DLC and H−DLC coatings were tested under ambient air conditions and the carbon layers became passivated by −OH and −H groups, which resulted in a low COF of 0.20. In the case of F−DLC,

the steady-state COF was reduced by an additional 30% to 0.14. As the sliding tests on H−DLC and F−DLC samples were done under the same environmental conditions, the effects of atmospheric humidity and Al oxidation on the COF should be comparable. The nanohardness values of transfer layers generated from F−DLC and H−DLC showed similar values (Section 3.3.3). Therefore, the observed reduction in the COF cannot be attributed to the hardness differences of the transfer layer. According to Figure 3.4, transfer of F atoms to an Al surface caused the formation of stable Al/diamond:F interfaces and the development of repulsive forces between these two F-passivated surfaces. It was suggested that, AlF_3 surfaces are likely to assume an F termination [71] rather than Al. Hence, the formation of AlF_3 would also contribute to the F passivation of the transfer layer. The interface atomic configurations responsible for attainment in low steady-state COF conditions are depicted in Figure 3.12c. Previous calculations by the authors have indicated that the forces developed between two F−DLC surfaces are more repulsive in nature than those that occur between the two H−DLC surfaces in contact [43]. Consequently, the repulsion between the charges reduced atomic attractions and hence lessened adhesion between two F-passivated surfaces.

Finally, it is pertinent to comment on the technological implications of the current results. In engineering components subjected to continuous sliding, such as a piston−cylinder bore assembly in aluminum internal combustion engines, the use of F−DLC−coated piston rings could be made feasible if a transfer layer incorporating F atoms is developed on the Al contact surface during continuous sliding motion. In this case, as both surfaces would be F passivated during sliding, the performance of the F−DLC coatings−by virtue of having a lower steady-state COF−might surpass that of the H−DLC piston ring coatings that are being considered for the same application. It follows that further evaluation of F−DLC coatings for the types of tribological applications in which these beneficial transfer layers could form during the sliding process is recommended, because more durable adhesion-resistant, low friction surfaces are likely to develop during sliding. On the other hand, the use of F−DLC coatings in applications where generation of transfer layers is unlikely cannot be recommended. Demanding machining applications such as deep hole drilling, metal tapping and also other machining operations carried out without the use of lubricants may not par-

ticularly benefit from the deposition of F−DLC coatings on the cutting tools. During Al−Si cast alloy machining−a process that is essential to the fabrication of powertrain components for use in vehicles−metal transfer to the tool surface is the principal problem causing drastic reduction in tool life. In this application, the contact time between the F−DLC-coated tool and the workpiece can be too short to establish an F−containing transfer layer on the machined Al surface, and the F−DLC-coated tool will face a fresh metal surface that is susceptible to Al adhesion and high friction.

3.5 Conclusions

Using first principles calculations, the atomic interactions at the Al/diamond:F interfaces were studied in order to provide insight into the tribological behavior of the technologically important Al and F−DLC coating system. For comparison, the same calculations and experiments were also conducted for Al and H−DLC. The predictions of these calculations, although excluding the effects of Al deformation, oxidation and hydration, when analyzed together with the results of sliding contact experiments between commercial purity Al and F−DLC coatings, provided insight into the mechanisms of the material transfer events that controlled the COFs of these coatings. The main conclusions arising from this work can be summarized as follows:

1. First-principles calculations using an interface model consisting of a diamond:F (111) and an Al (111) surfaces predicted that F atoms would transfer to the Al when the contact pressure at the interface reached 3.5 GPa. Higher contact pressures yielded more F transfer to Al, with all 4 F atoms on the diamond surface relocating to the Al surface when a pressure greater than 5.7 GPa was applied. No H transfer occurred from a diamond:H surface to Al when they were pressed together.

2. All F−transferred Al/diamond:F interfaces were more stable than the original Al/ diamond:F interface. ELF analyses showed that F effectively passivated both surfaces and a repulsive force was maintained between the F−transferred Al surface and the diamond surface.

3. The bond structure at the F−transferred Al surface predicted the formation of a stable AlF$_3$ compound at the Al surface. The presence of AlF$_3$ at the Al surface was experimentally confirmed when cross-sections of transfer layers that had formed on commercial purity Al samples placed in sliding contact with DLC containing 3 at.% F were examined by XPS and FIB HRTEM.

4. DLC coatings placed in sliding contact against Al generated an initially high COF due to wear and plastic deformation of the Al counterface. Once a carbonaceous transfer layer passivated by −H and −OH was established on the Al surface, a low steady-state COF of 0.20 was attained. F−containing DLC coatings produced a 30% lower COF of 0.14 as a consequence of F transfer to carbon layers and the resulting repulsion between two F−passivated surfaces.

5. The predictions of atomistic simulations at the interfaces, when analyzed in connection with the results of sliding experiments, provided a coherent atomistic model depicting the effect of fluorine on the material transfer mechanisms between metals and fluorinated carbon surfaces. Accordingly, for a fluorinated carbon surface put in sliding contact with a metallic counterface, a metal fluoride formation was expected to build on the metallic surface as a result of F transfer. The amount of F transfer would depend on the applied contact pressure. Following the F transfer, a low friction would arise due to repulsive interactions between the two F−passivated carbon surfaces.
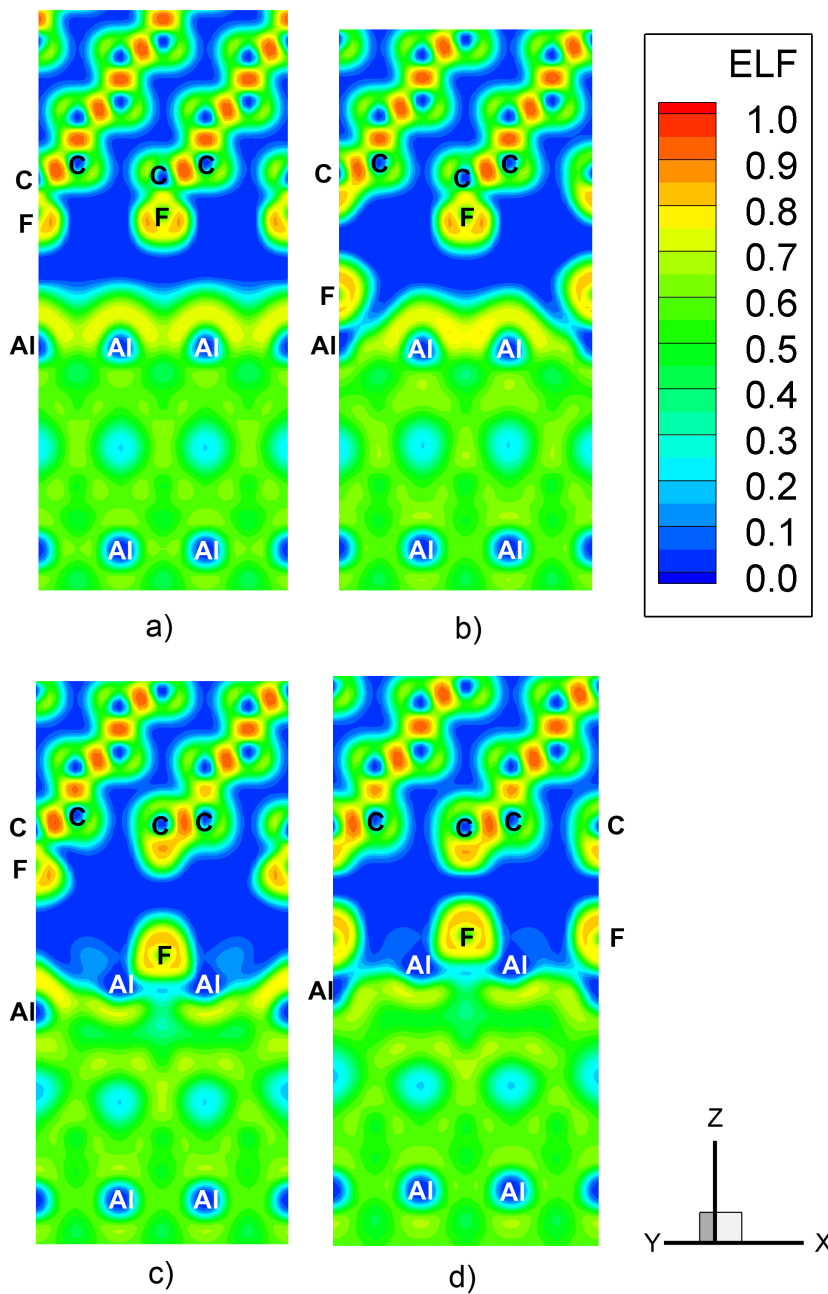
Figure 3.5: Electron localization function (ELF) plots of the equilibrium interface structure for the Al/diamond:F interfaces with (a) no transfer, (b) 1 F transfer, (c) 3 F transfer and (d) 4 F transfer.
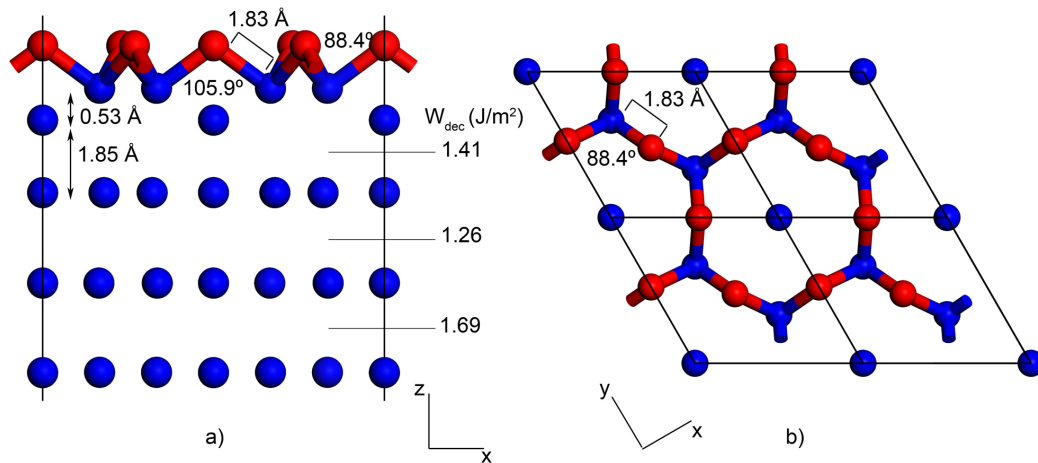
Figure 3.6: Reconstructed Al (111) surface after the transfer of 3 F atoms. (a) Side view that shows the two Al atoms that were shifted away from the top surface by a distance of 0.53 Å in the z−direction. The Al−F bond distance is 1.83 Å. The F−Al−F bond angle is 88.4 and the Al−F−Al bond angle is 105.9. (b) Top view, only the top layer of the Al surface is drawn to show that each shifted Al atom was bonded with 3 F atoms.
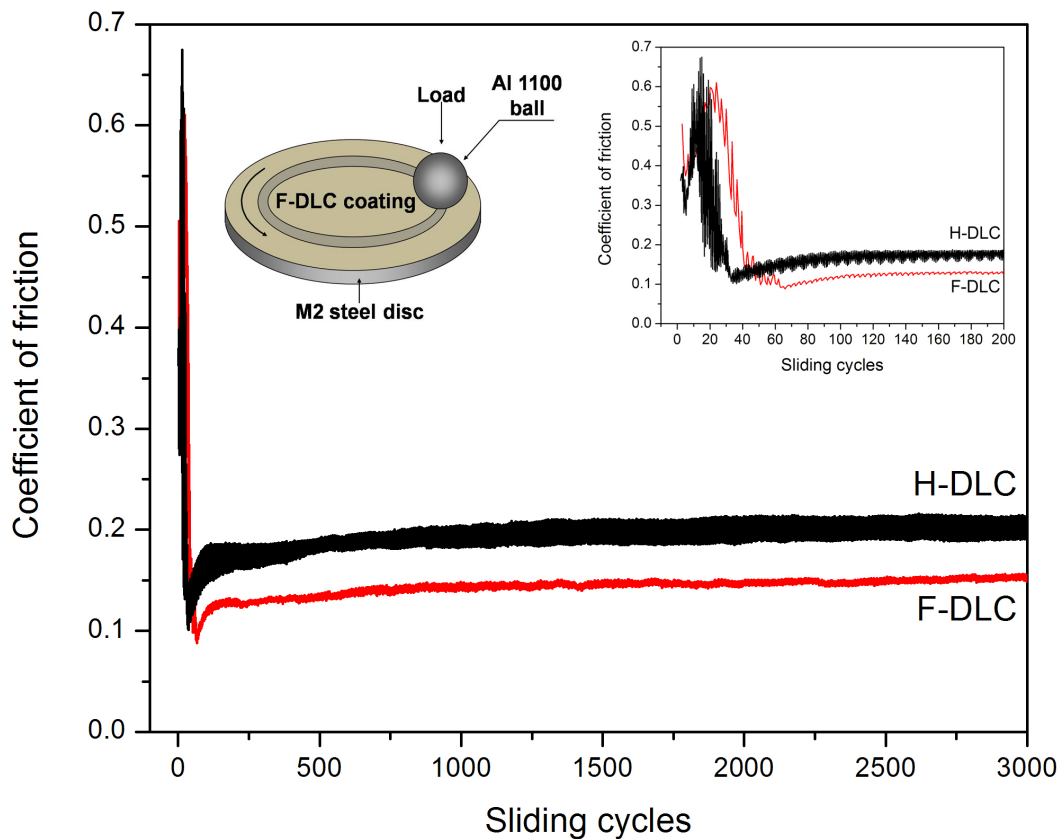
Figure 3.7: Variations of the F−DLC's and H−DLC's COFs with the sliding cycles. Tests were carried out against Al. A schematic of the test geometry and an enlarged view of the COF curves for the first 200 cycles are shown in the insets.
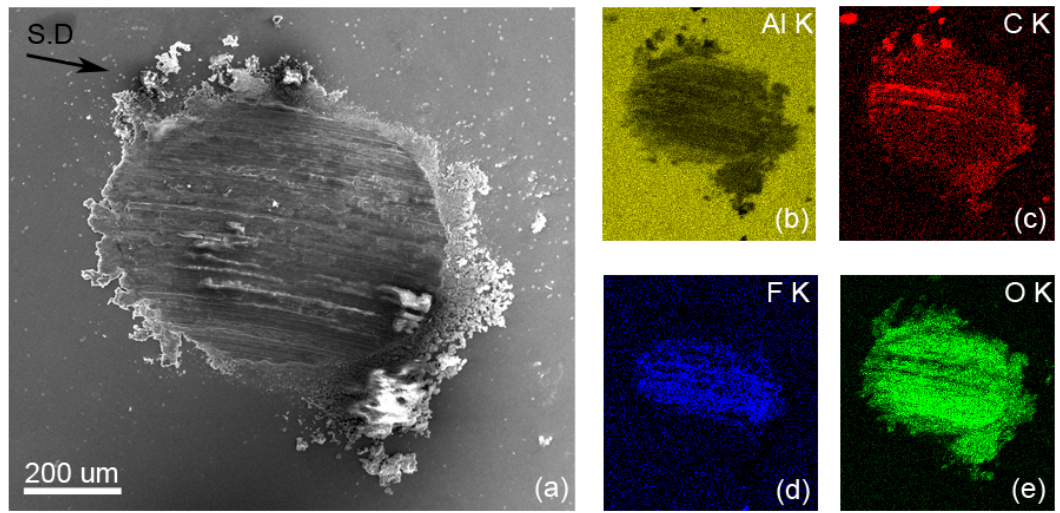
Figure 3.8: (a) Secondary electron image of the Al surface after the sliding test against an F−DLC coating with arrow indicating the sliding direction (SD). The elemental EDS maps taken from the whole area on (a) are shown for (b) Al, (c) C, (d) F and (e) O on the Al surface.
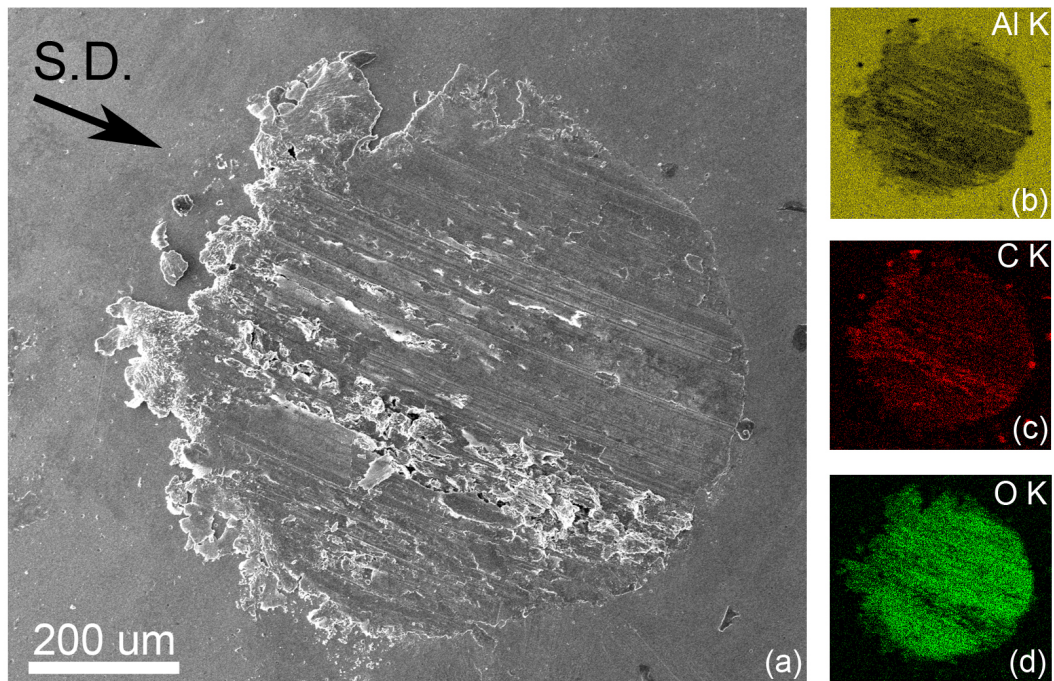
Figure 3.9: (a) Secondary electron image of Al ball surface after the sliding test against H−DLC coating, where the arrow shows the sliding direction (SD). The elemental EDS maps taken from the whole area on (a) are shown for (b) Al, (c) C, and (d) O on the Al surface.
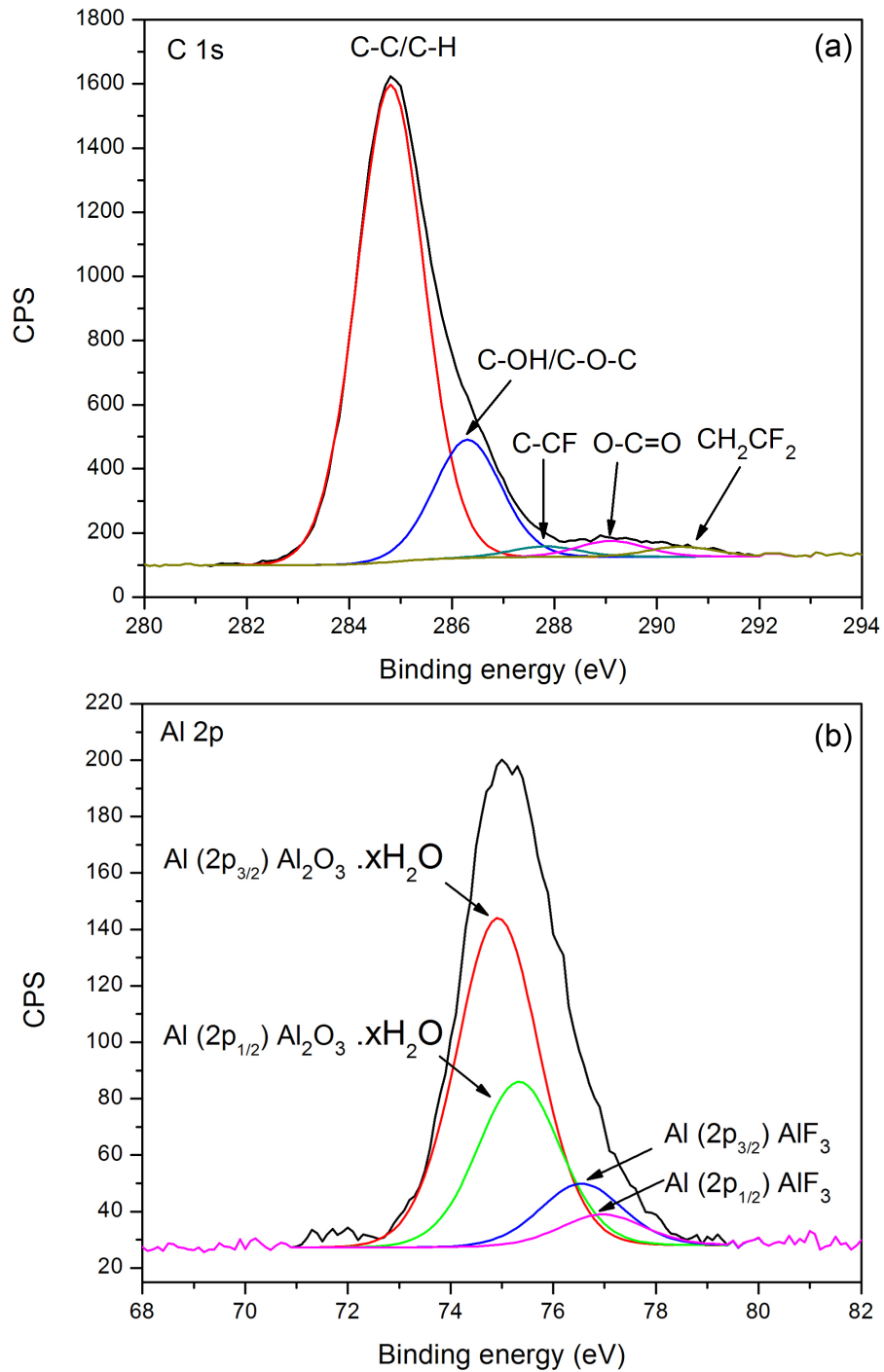
Figure 3.10: XPS spectra of transfer layer formed on Al pin after sliding against F−DLC: (a) the high-resolution spectra for the C 1s state and (b) the high-resolution spectra for the Al 2p states. In both figures the deconvoluted spectra show chemical states of elements.
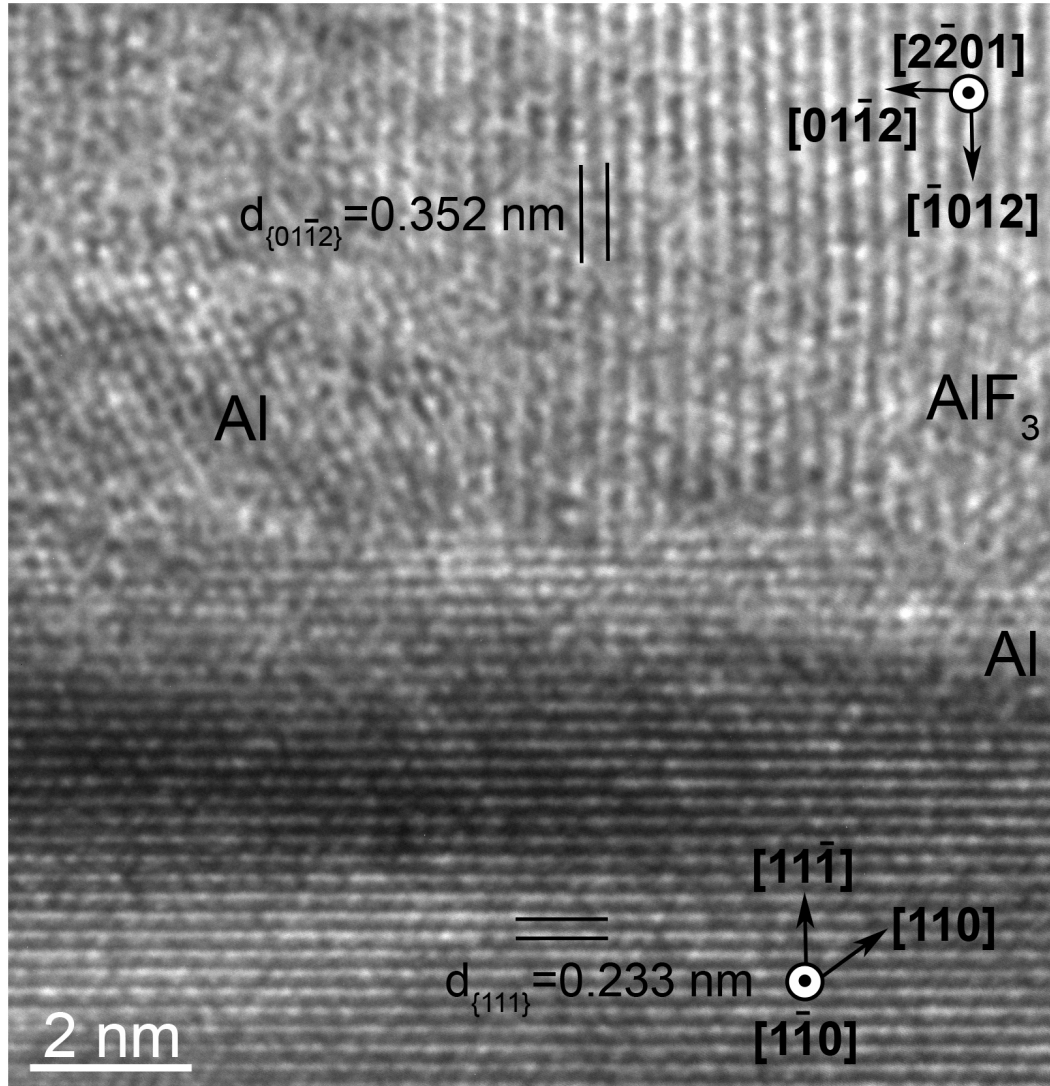
Figure 3.11: High-resolution transmission electron microscopy (HRTEM) image of $(111)_{Al} \parallel (01\bar{1}2)_{AlF_3}$ interface formed between AlF_3 in the transfer layer and the Al contact surface.
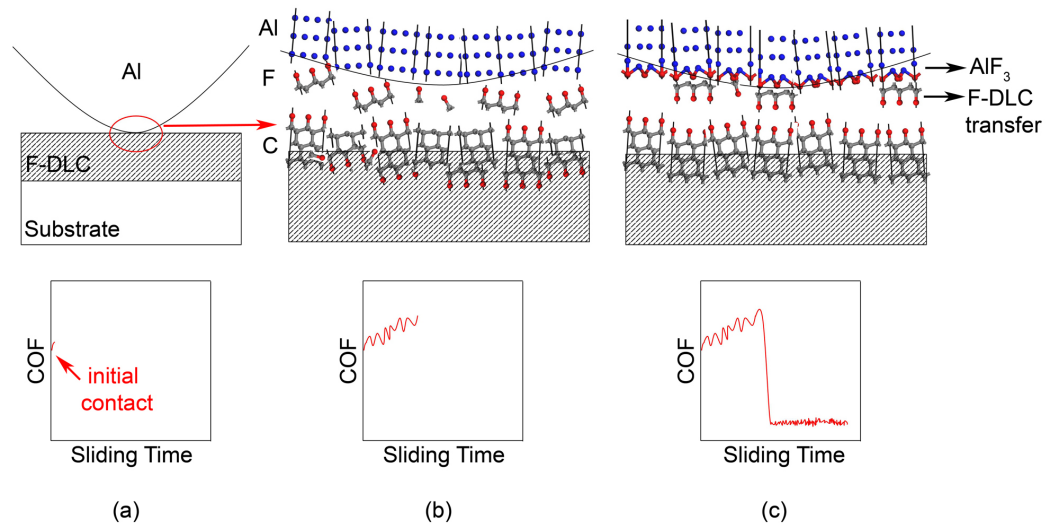
Figure 3.12: Schematic description of the evolution of the COF in relation to sliding time for F−DLC in contact with Al. (a) The initial contact between Al and F−DLC results in a static COF. (b) During the initial running-in period, F (and C) transfer from the DLC to the Al surface occurs. The COF increases due to the breaking of C−F bonds at the DLC surface and the formation of new Al−F bonds at the Al surface. (c) The transfer of F from DLC causes formation of AlF$_3$ at the Al surface and some C linked to F atoms also transfers to the Al surface. When all surface Al bonds are saturated with F, the final contact interface formed between two F-terminated surfaces results in a low steady-state COF. See text for their details.

Bibliography

[1] H. L. Coldwell, R. C. Dewes, D. K. Aspinwall, N. M. Renevier, and D. G. Teer. The use of soft/lubricating coatings when dry drilling BS L168 aluminium alloy. *Surface and Coatings Technology*, 177-178:716–726, 2004.

[2] E. Konca, Y. T. Cheng, A. M. Weiner, J. M. Dasch, A. Erdemir, and A. T. Alpas. Transfer of 319 Al alloy to titanium diboride and titanium nitride based (TiAlN, TiCN, TiN) coatings: Effects of sliding speed, temperature and environment. *Surface and Coatings Technology*, 200(7):2260–2270, 2005.

[3] E. Konca, Y. T. Cheng, A. M. Weiner, J. M. Dasch, and A. T. Alpas. Effect of test atmosphere on the tribological behaviour of the non-hydrogenated diamond-like carbon coatings against 319 aluminum alloy and tungsten carbide. *Surface and Coatings Technology*, 200(5-6):1783–1791, 2005.

[4] A. R. Riahi and A. T. Alpas. Adhesion of AA5182 aluminum sheet to DLC and TiN coatings at 25Â °C and 420Â °C. *Surface and Coatings Technology*, 202(4-7):1055–1061, 2007.

[5] A. Grill. Diamond-like carbon: State of the art. *Diamond and Related Materials*, 8(2-5):428–434, 1999.

[6] J. Robertson. Diamond-like amorphous carbon. *Materials Science and Engineering R*, 37(4-6):129–281, 2002.

[7] J. M. Dasch, C. C. Ang, C. A. Wong, Y. T. Cheng, A. M. Weiner, L. C. Lev, and E. Konca. A comparison of five categories of carbon-based tool coatings for dry drilling of aluminum. *Surface and Coatings Technology*, 200(9):2970–2977, 2006.

[8] S. Bhowmick and A. T. Alpas. The performance of hydrogenated and non-hydrogenated diamond-like carbon tool coatings during the dry drilling of 319 Al. *International Journal of Machine Tools and Manufacture*, 48(7-8):802–814, 2008.

[9] A. Erdemir and C. Donnet. Tribology of diamond-like carbon films: recent progress and future prospects. *Journal of Physics. D: Applied Physics*, 39(18):R311–R327, 2006.

[10] A. Erdemir, O. L. Eryilmaz, and G. Fenske. Synthesis of diamondlike carbon films with superlow friction and wear properties. *Journal of Vacuum Science and Technology A: Vacuum, Surfaces and Films*, 18(4 II):1987–1992, 25 October 1999 through 29 October 1999 2000.

[11] J. A. Heimberg, K. J. Wahl, I. L. Singer, and A. Erdemir. Superlow friction behavior of diamond-like carbon coatings: Time and speed effects. *Applied Physics Letters*, 78(17):2449–2451, 2001.

[12] C. Donnet and A. Grill. Friction control of diamond-like carbon coatings. *Surface and Coatings Technology*, 94-95:456–462, 1997.

[13] C. Donnet, J. Fontaine, A. Grill, and T. Le Mogne. The role of hydrogen on the friction mechanism of diamond-like carbon films. *Tribology Letters*, 9(3-4):137–142, 2001.

[14] A. Erdemir. The role of hydrogen in tribological properties of diamond-like carbon films. *Surface and Coatings Technology*, 146-147:292–297, 2001.

[15] H. I. Kim, J. R. Lince, O. L. Eryilmaz, and A. Erdemir. Environmental effects on the friction of hydrogenated DLC films. *Tribology Letters*, 21(1):51–56, 2006.

[16] J. Andersson, R. A. Erck, and A. Erdemir. Frictional behavior of diamondlike carbon films in vacuum and under varying water vapor pressure. *Surface and Coatings Technology*, 163-164:535–540, 2003.

[17] E. Konca, Y. T. Cheng, A. M. Weiner, J. M. Dasch, and A. T. Alpas. Vacuum tribological behavior of the non-hydrogenated diamond-like carbon coatings against aluminum: Effect of running-in in ambient air. *Wear*, 259(1-6):795–799, 2005.

[18] E. Konca, Y. T. Cheng, A. M. Weiner, J. M. Dasch, and A. T. Alpas. The role of hydrogen atmosphere on the tribological behavior of non-hydrogenated DLC coatings against aluminum. *Tribology Transactions*, 50(2):178–186, 2007.

[19] E. Konca, Y. T. Cheng, and A. T. Alpas. Dry sliding behaviour of non-hydrogenated DLC coatings against Al, Cu and Ti in ambient air and argon. *Diamond and Related Materials*, 15(4-8):939–943, 2006.

[20] Y. Qi, E. Konca, and A. T. Alpas. Atmospheric effects on the adhesion and friction between non-hydrogenated diamond-like carbon (DLC) coating and aluminum - a first principles investigation. *Surface Science*, 600(15):2955–2965, 2006.

[21] H. Guo, Y. Qi, and X. Li. Predicting the hydrogen pressure to achieve ultralow friction at diamond and diamondlike carbon surfaces from first principles. *Applied Physics Letters*, 92(24):241921, 2008.

[22] D. J. Siegel, Jr. L. G. Hector, and J. B. Adams. Adhesion, atomic structure, and bonding at the Al(111)/α-Al$_2$O$_3$ (0001) interface: A first principles study. *Physical Review B*, 65(8):085415, 2002.

[23] D. J. Siegel, Jr. L. G. Hector, and J. B. Adams. Adhesion, stability, and bonding at metal/metal-carbide interfaces: Al/WC. *Surface Science*, 498(3):321–336, 2002.

[24] D. J. Siegel, Jr. L. G. Hector, and J. B. Adams. First-principles study of metal-carbide/nitride adhesion: Al/VC vs. Al/VN. *Acta Materialia*, 50(3):619–631, 2002.

[25] N. Ooi, L. Hector, J. Adams, and D. Stanzione. First principles study of the aluminum-cubic boron nitride interface. *Journal of Adhesion*, 82(8):779–803, 2006.

[26] Yue Qi, Jr. L. G. Hector, N. Ooi, and J. B. Adams. A first principles study of adhesion and adhesive transfer at Al(111)/graphite(0001). *Surface Science*, 581(2-3):155–168, 05/01 2005.

[27] Yue Qi and L. G. Hector. Adhesion and adhesive transfer at aluminum/diamond interfaces: a first-principles study. *Physical Review B*, 69(23):235401, 06/15 2004.

[28] J. N. Israelachvili. *Intermolecular and Surface Forces*. Academic, San Diego, 2nd edition, 1992.

[29] H. Guo, Y. Qi, F. G. Sen, Gharam A. Abou, and A. T. Alpas. The effects of oxygen environment on the adhesion and friction of diamond and diamond-like carbon surfaces. page Submitted, 2012.

[30] Y. Morita, T. Shibata, T. Onodera, R. Sahnoun, M. Koyama, H. Tsubo, N. Hatakeyama, A. Endou, H. Takaba, M. Kubo, C. A. Del Carpio, and A. Miyamoto. Effect of surface termination on superlow friction of diamond film: A theoretical study. *Japanese Journal of Applied Physics*, 47(4):3032–3035, 2008.

[31] H. Ronkainen, J. Likonen, J. Koskinen, and S. Varjus. Effect of tribofilm formation on the tribological performance of hydrogenated carbon coatings. *Surface and Coatings Technology*, 79(1-3):87–94, 1996.

[32] R. Hauert. An overview on the tribological behavior of diamond-like carbon in technical and medical applications. *Tribology International*, 37(11-12 SPEC.ISS.):991–1003, 2004.

[33] A. Erdemir, C. Bindal, J. Pagan, and P. Wilbur. Characterization of transfer layers on steel surfaces sliding against diamond-like hydrocarbon films in dry nitrogen. *Surface and Coatings Technology*, 76-77(PART 2):559–563, 1995.

[34] C. Donnet. Recent progress on the tribology of doped diamond-like and carbon alloy coatings: A review. *Surface and Coatings Technology*, 100-101(1-3):180–186, 1998.

[35] M. Grischke, K. Bewilogua, K. Trojan, and H. Dimigen. Application-oriented modifications of deposition processes for diamond-like-carbon-based coatings. *Surface and Coatings Technology*, 74-75:739–745, 1995.

[36] J. Sanchez-Lopez and A. Fernandez. *Doping and alloying effects on DLC coatings*, pages 311–338. Tribology of Diamond-Like Carbon Films: Fundamentals and Applications. Springer, 2008.

[37] D. E. Patterson, R. H. Hauge, and J. L. Margrave. Fluorinated diamond films, slabs, and grit. In L. E. Pope, L. Fehrenbacher, and W. O. Winer, editors, *Materials Research Society Symposium Proceedings*, volume 140, pages 351–356, 1989.

[38] H. Touhara and F. Okino. Property control of carbon materials by fluorination. *Carbon*, 38(2):241–267, 2000.

[39] M. Hakovirta, X. M. He, and M. Nastasi. Optical properties of fluorinated diamond-like carbon films produced by pulsed glow discharge plasma immersion ion processing. *Journal of Applied Physics*, 88(3):1456–1459, 2000.

[40] K. P. Huang, P. Lin, and H. C. Shih. Structures and properties of fluorinated amorphous carbon films. *Journal of Applied Physics*, 96(1):354–360, 2004.

[41] G. Q. Yu, B. K. Tay, and Z. Sun. Fluorinated amorphous diamond-like carbon films deposited by plasma-enhanced chemical vapor deposition. *Surface and Coatings Technology*, 191(2-3):236–241, 2005.

[42] R. Prioli, L. G. Jacobsohn, M. E. H. Maia da Costa, and Jr. F. L. Freire. Nanotribological properties of amorphous carbon-fluorine films. *Tribology Letters*, 15(3):177–180, 2003.

[43] F. G. Sen, Y. Qi, and A. T. Alpas. Surface stability and electronic structure of hydrogen- and fluorine-terminated diamond surfaces: A first-principles investigation. *Journal of Materials Research*, 24(8):2461–2470, 2009.

[44] K. I. Nakamatsu, N. Yamada, K. Kanda, Y. Haruyama, and S. Matsui. Fluorinated diamond-like carbon coating as antisticking layer on nanoimprint mold. *Japanese journal of Applied Physics*, 45(33-36):L954–L956, 2006.

[45] M. Schvartzman and S. J. Wind. Plasma fluorination of diamond-like carbon surfaces: Mechanism and application to nanoimprint lithography. *Nanotechnology*, 20(14):145306, 2009.

[46] R. W. Fillman and R. R. Krchnavek. Ultrathin fluorinated diamondlike carbon coating for nanoimprint lithography imprinters. *Journal of Vacuum Science and Technology B*, 27(6):2869–2872, 2009.

[47] K. Enke, H. Dimigen, and H. Hübsch. Frictional properties of diamondlike carbon layers. *Applied Physics Letters*, 36(4):291–292, 1980.

[48] M. Ishihara, T. Kosaka, T. Nakamura, K. Tsugawa, M. Hasegawa, F. Kokai, and Y. Koga. Antibacterial activity of fluorine incorporated DLC films. *Diamond and Related Materials*, 15(4-8):1011–1014, 2006.

[49] M. Rubio-Roy, C. Corbella, E. Bertran, S. Portal, M. C. Polo, E. Pascual, and J. L. Andújar. Effects of environmental conditions on fluorinated diamond-like carbon tribology. *Diamond and Related Materials*, 18(5-8):923–926, 2009.

[50] W. Kohn and L. J. Sham. Self-consistent equations including exchange and correlation effects. *Physical review*, 140:A1133–A1138, 1965.

[51] J. P. Perdew, J. A. Chevary, S. H. Vosko, K. A. Jackson, M. R. Pederson, D. J. Singh, and C. Fiolhais. Atoms, molecules, solids, and surfaces: Applications of the generalized gradient approximation for exchange and correlation. *Physical Review B*, 46(11):6671–6687, 1992.

[52] G. Kresse and J. Hafner. Ab initio molecular-dynamics simulation of the liquid-metalamorphous- semiconductor transition in germanium. *Physical Review B*, 49(20):14251–14269, 1994.

[53] G. Kresse and J. Furthmüller. Efficiency of ab-initio total energy calculations for metals and semiconductors using a plane-wave basis set. *Computational Materials Science*, 6(1):15–50, 1996.

[54] J. Bandyopadhyay and K. P. Gupta. Low temperature lattice parameters of Al and Al-Zn alloys and Grüneisen parameter of Al. *Cryogenics*, 18(1):54–55, 1978.

[55] Katsuji Haruna, Hiroshi Maeta, Kazutoshi Ohashi, and Takuro Koike. Thermal expansion coefficient of synthetic diamond single crystal at low temperatures. *Japanese Journal of Applied Physics*, 31(8):2527–2529, 1992.

[56] S. Dag and S. Ciraci. Atomic scale study of superlow friction between hydrogenated diamond surfaces. *Physical Review B*, 70(24):241401(R), 2004.

[57] D. E. Jiang and E. A. Carter. Prediction of strong adhesion at the $MoSi_2$/Fe interface. *Acta Materialia*, 53(17):4489–4496, 2005.

[58] D. J. Siegel, Jr. L. G. Hector, and J. B. Adams. Ab initio study of Al-ceramic interfacial adhesion. *Physical Review B*, 67(9):921051, 2003.

[59] A. D. Becke and K. E. Edgecombe. A simple measure of electron localization in atomic and molecular systems. *The Journal of Chemical Physics*, 92(9):5397–5403, 1990.

[60] D. R. Lide. *CRC Handbook of Chemistry and Physics*. Taylor and Francis, Boca Raton, FL, 2007.

[61] P. Daniel, A. Bulou, M. Rousseau, J. Nouet, J. L. Fourquet, M. Leblanc, and R. Burriel. A study of the structural phase transitions in AlF_3: X-ray powder diffraction, differential scanning calorimetry (DSC) and Raman scattering investigations of the lattice dynamics and phonon spectrum. *Journal of Physics: Condensed Matter*, 2(26):5663–5677, 1990.

[62] X. Meng-Burany and A. T. Alpas. FIB and TEM studies of damage mechanisms in DLC coatings sliding against aluminum. *Thin Solid Films*, 516(2-4):325–335, 2007.

[63] G. Beamson and D. Briggs. *High Resolution XPS of Organic Polymers*. Wiley, 1992.

[64] A. Dilks and E. Kay. Plasma polymerization of ethylene and the series of fluoroethylenes: Plasma effluent mass spectrometry and ESCA studies. *Macromolecules*, 14(3):855–862, 1981.

[65] J. F. Moulder, W. F. Stickle, P. E. Sobol, and K. D. Bomben. *Handbook of X Ray Photoelectron Spectroscopy.* Physical Electronics, Chanhassen, MN, 1995.

[66] J. Ashley Taylor. XPS study of the oxidation of AlAs thin films grown by mbe. *Journal of Vacuum Science and Technology*, 20(3):751–755, 2 November 1981 through 6 November 1981 1982.

[67] James R. Lindsay, Harry J. Rose Jr., William E. Swartz Jr., Plato H. Watts Jr., and Kenneth A. Rayburn. X-ray photoelectron spectra of aluminum oxides: structural effects on the "chemical shift". *Applied Spectroscopy*, 27(1):1–5, 1973.

[68] C. D. Wagner, D. E. Passoja, H. F. Hillery, T. G. Kinisky, H. A. Six, W. T. Jansen, and J. A. Taylor. Auger and photoelectron line energy relationships in aluminum-oxygen and silicon-oxygen compounds. *Journal of Vacuum Science and Technology*, 21(4):933–944, 1982.

[69] I. Olefjord, H. J. Mathieu, and P. Marcus. Intercomparison of surface analysis of thin aluminium oxide films. *Surface and Interface Analysis*, 15(11):681–692, 1990.

[70] B. R. Strohmeier. Surface characterization of aluminum foil annealed in the presence of ammonium fluoborate. *Applied Surface Science*, 40(3):249–263, 1989.

[71] C. L. Bailey, S. Mukhopadhyay, A. Wander, B. G. Searle, and N. M. Harrison. Structure and stability of α-alf$_3$ surfaces. *Journal of Physical Chemistry C*, 113(12):4976–4983, 2009.

[72] S. Mukhopadhyay, C. L. Bailey, A. Wander, B. G. Searle, C. A. Muryn, S. L. M. Schroeder, R. Lindsay, N. Weiher, and N. M. Harrison. Stability of the AlF$_3$ (01 $\bar{1}$ 2) surface in H$_2$O and HF environments: An investigation using hybrid density functional theory and atomistic thermodynamics. *Surface Science*, 601(18):4433–4437, 2007.

[73] L. Pastewka, S. Moser, M. Moseler, B. Blug, S. Meier, T. Hollstein, and P. Gumbsch. The running-in of amorphous hydrocarbon tribocoatings: A comparison between experiment and molecular dynamics simulations. *International Journal of Materials Research*, 99(10):1136–1143, 2008.

[74] H. Ronkainen, J. Koskinen, J. Likonen, S. Varjus, and J. Vihersalo. Characterization of wear surfaces in dry sliding of steel and alumina on hydrogenated and hydrogen-free carbon films. *Diamond and Related Materials*, 3(11-12):1329–1336, 1994.

[75] Y. Liu, A. Erdemir, and E. I. Meletis. An investigation of the relationship between graphitization and frictional behavior of DLC coatings. *Surface and Coatings Technology*, 86-87(1 -3 pt 2):564–568, 22 April 1996 through 26 April 1996 1996.

[76] Y. Liu, A. Erdemir, and E. I. Meletis. A study of the wear mechanism of diamond-like carbon films. *Surface and Coatings Technology*, 82(1-2):48–56, 1996.

[77] F. P. Bowden and D. Tabor. *The friction and lubrication of solids.* Oxford University Press, New York, 1950.

[78] J. Fontaine, T. Le Mogne, J. L. Loubet, and M. Belin. Achieving superlow friction with hydrogenated amorphous carbon: Some key requirements. *Thin Solid Films*, 482(1-2):99–108, 2005.

Chapter 4

Low Friction and Environmentally Stable Diamond-like Carbon (DLC) Coatings Incorporating Silicon, Oxygen and Fluorine Sliding Against Aluminum

4.1 Introduction

Diamond-like carbon (DLC) coatings are used to achieve low friction in sliding components [1] such as gears, piston rings, dies, and tools. The adhesive transfer of aluminum to tool and die surfaces is a significant manufacturing problem for the machining and forming processes of components made of Al alloys. It was shown that DLC coatings consistently exhibited a very low coefficient of friction (COF) and reduced the adhesion much more effectively than the other coatings when tested against aluminum [2–13]. One drawback to the more widespread use of DLC coatings is that their tribological properties tend to vary widely with the environmental conditions. The extent of the environmental sensitivity of DLC coatings depends on the hydrogen content of the coating. Two grades of DLC coatings are

distinguished in this respect: hydrogenated DLC coatings with 40 at.% H (a-C:H) and non-hydrogenated DLC coatings with < 2 at.% H (a-C) [14–16]. The a-C:H coatings are known to exhibit low COF under a vacuum or inert atmosphere, whereas a-C films display high COF when tested under similar conditions [16]. Hydrogen termination of the dangling bonds of surface carbon atoms was shown to be responsible for the low COF (usually < 0.01) under these conditions [16–18]. When tested in an atmosphere with high relative humidity (RH > 50%), the COF of a-C:H increased, whereas the a-C showed low COF [1,14]. The surface passivation of $-OH$ groups, formed as a result of the dissociation of water molecules into $-H$ and $-OH$ at the carbon surface, was suggested to be responsible for the low COF encountered in the a-C coatings under ambient and high RH testing conditions [7,19]. Low friction in DLC coatings was also achieved by incorporating $2 - 35$ at.% F into the DLC structure [20–28] . A recent study has shown that when Al was placed in sliding contact against a 3 at.% a-C:H:F, F-passivated carbonaceous transfer layers on the Al surface were formed and a low COF of 0.14 was obtained. F-terminated carbon surfaces at the sliding contact interface (consisting of a-C:H:F and F-enriched transfer layers) were shown to exert repulsive forces to each other that were suggested to be responsible for the observed low COF between Al and the a-C:H:F [29–31]. It is important to maintain a low COF between Al and DLC when the atmospheric conditions during the service life of the coating change in tribological applications. Examples of these applications can be found in aerospace industry, the watch industry, and micro/nano-electromechanical systems.

It was reported that tribological properties that do not vary with atmospheric humidity could be achieved by the incorporation of Si ($3-20$ at.%) in the DLC structure [20–22,32–37]. The addition of Si in a-C:H was reported to be effective in decreasing the COF of this coating when tested against steel in ambient air (30% RH) from 0.2 to as low as 0.03 [21,34,37–40], depending on the Si concentration. An interesting observation was that the COF of a-C:H:Si remained low when the humidity in the test environment was changed in the wide range between 0 and 85% RH. Meanwhile, in a related set of observations, tests have shown that SiO_x containing DLC films (a-C:H:Si:O) exhibited COF < 0.1 against steel counterfaces [41]. In this case, also, the COF did not increase much with increasing the atmospheric humidity [40,42]. The low COF values of a-C:H:Si and a-C: H:Si:O coatings were attributed

to either the decrease in the surface energy [43] or the formation of a carbonaceous layer on the steel surface incorporating SiO_x groups [38, 44]. However, details of the mechanisms responsible for how the SiO_x groups facilitate the maintenance of a constant COF are yet to be clarified.

Although Si incorporation reduced humidity sensitivity of the tribological properties of DLC against ferrous materials, Si containing $(7 - 16$ at.%) DLC was not effective in preventing adhesion to the coating surface when placed in contact with aluminum. The latter point pertained to observations during aluminum forming where more aluminum adhesion to tool surfaces occurred in comparison to DLC coatings without Si [45, 46].

According to the above literature survey, it was proposed that a hybrid DLC coating that incorporates Si, O and F (a-C:H:Si:O:F) placed in sliding contact against aluminum could show low COF and minimize adhesion at the same time. The a-C:H:Si:O:F coating was tested to investigate whether this coating would show equally low COF both in ambient air and vacuum conditions. The principal purpose of the experiments and analyses was to rationalize the tribo-chemical mechanisms that led to environment independent low COF between a-C:H:Si:O:F and aluminum. The chemical and microstructural changes that occurred at the worn surfaces of aluminum and the a-C:H:Si:O:F coating, were determined using X-ray photoelectron spectroscopy (XPS), micro-Raman, cross-sectional focus ion beam (FIB) thinning and transmission electron microscopy (TEM). A model for the tribo-chemical mechanisms that are responsible for the observed friction behavior of a-C:H:Si:O:F coating is proposed.

4.2 Material and methods

4.2.1 Material properties

The DLC coatings designated as a-C:H:Si:O:F were deposited on 25.4 mm diameter M2 grade tool steel coupons with plasma enhanced chemical vapor deposition technique by Bekaert Advanced Coating Technologies, New York, USA. The chemical composition of the coating was determined using Rutherford backscattering spectroscopy (RBS), and the hydrogen content was determined using elastic recoil detection (ERD). The chemical com-

position of the a-C:H:Si:O:F coating is given in Table 4.1 and consists of 20 at.% Si, 12 at. F, 14 at.% O, 18 at.% H and the balance C. The thickness of the coating was measured as 2.3 ± 0.1 μm, based on the secondary electron image (SEI) of the cross-section given in Figure 4.1(a). The elemental map obtained using energy dispersive spectroscopy (EDS) from the same cross-sectional area is given in Figures 4.1(b)-(f) and shows that the F, Si and O are distributed homogeneously in the coating structure for the top 1.6 μm, whereas the region near the substrate was rich in Si, which was about 0.7 μm in thickness. Table 4.2 shows the properties of the coating including surface roughness, R_a, water contact angle, elastic modulus and hardness. The a-C:H:Si:O:F had a hardness of 8.8 ± 0.1 GPa, which was measured using a nanoindenter; the measured hardness value is in the lower range of hardness values reported for DLC coatings in the literature [47].

Table 4.1: Chemical composition of a-C:H:Si:O:F as determined by Rutherford backscattering spectroscopy (RBS) and elastic recoil detection (ERD) for H.

	H (at.%)	O (at.%)	F (at.%)	Si (at.%)	C (at.%)
a-C:H:Si:O:F	17 ± 2	14 ± 1	12 ± 1	20 ± 2	37 ± 3
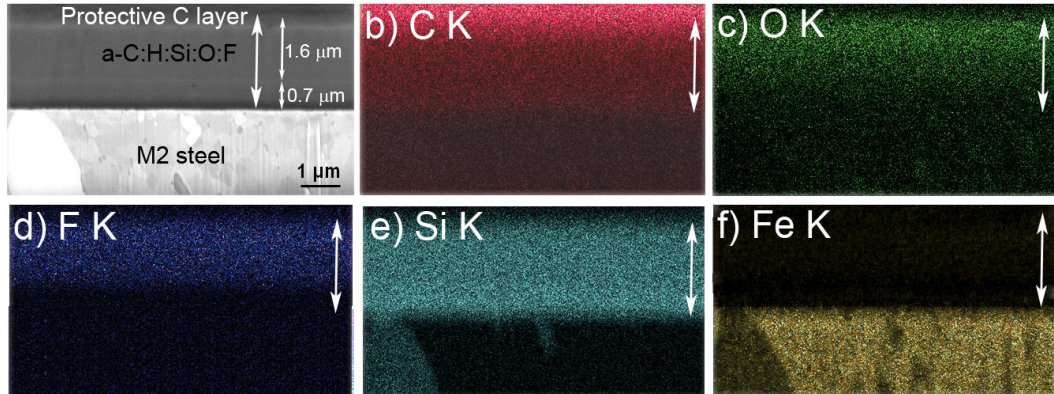
Figure 4.1: a) Secondary electron image (SEI) of the cross-section of a-C:H:Si:O:F coating and EDS elemental maps for b) C K, c) O K, d) F K, e) Si K and f) Fe K. The arrow shows the thickness of the coating on the M2 substrate. The layer (0.7 μm) near the M2 steel is rich in Si.

Commercial purity (cold forged) aluminum (1100) balls with a diameter of 6.35 mm (supplied by Alfa Aesar) were used in the sliding contact experiments. The surfaces of Al balls were electropolished in a 5% perchloric acid ($HClO_4$)–methanol solution at 20 V for 5 min to obtain a smooth surface. The surface roughness, R_a, of the polished Al balls,

Table 4.2: Properties of a-C:H:Si:O:F coating. The surface roughness of the coatings was measured on a 0.269 mm^2 area using a white light optical interferometer. Water contact angles were measured using the sessile-drop method. The hardness and elastic modulus were measured using a Hysitron nanoindenter.

	Thickness (μm)	Roughness (nm)	Water contact angle	Elastic modulus (GPa)	Hardness (GPa)
a-C:H:Si:OF	2.3 ± 0.1	30 ± 3	$91^{\text{o}} \pm 3$	77.2 ± 0.9	8.8 ± 0.1

measured using a white light optical surface profilometer (WYKO NT1100), was 50 ± 5 nm. The grain size of the Al was 9.5 ± 5.2 μm, and its Vickers hardness measured at a load of 10 g was 264.7 ± 18.7 MPa (26.9 ± 1.9 VHN).

4.2.2 Sliding contact experiments and surface analysis methods

The a-C:H:Si:O:F coated steel coupons were subjected to dry sliding contact tests against the Al 1100 balls using a ball-on-disk type vacuum tribometer (CSM, Switzerland) and the COF was recorded as a function of sliding cycles. The experiments were conducted in an ambient air atmosphere with a relative humidity (RH) of $39 \pm 3\%$ and in a vacuum atmosphere (6.5×10^{-3} Pa). The tests were done using constant loads of 1.0 and 5.0 N at a sliding speed of 0.12 m/s. During tests carried out in the vacuum atmosphere, the partial pressures of gasses (CO, CO_2, N_2, O_2, H_2, H_2O, SiF_4, SiH_4, turbo pump oil) inside the vacuum chamber were measured using a residual gas analyzer (RGA) (Hiden HMT100-RC) with a resolution of 10^{-11} Pa.

The transfer layers that were formed on the Al ball surfaces during the sliding contact experiments were analyzed with a JEOL JSM-5800LV scanning electron microscope (SEM) equipped with an EDS system. The chemical composition of the transfer layers was determined using an X-ray photoelectron spectroscopy (XPS) system (Kratos Axis Ultra) with an Al X-ray source (characteristic energy=1.4867 keV) and the charge correction was carried out using a carbon reference. The survey scans of the samples were conducted using a pass energy of 160 eV. High resolution XPS analyses were conducted on the same area using a pass energy of 20 eV. The micro-Raman studies of the unworn coating and the worn surfaces were carried out using a 20 mW He–Ne laser (632.8 nm excitation line) through the

50× objective lens of a Renishaw inVia Raman micro-spectrometer. The cross-sectional microstructures of the transfer layers that were formed on the Al contact surface were observed by transmission electron microscopy (TEM). These samples were sectioned using an H-bar focused-ion beam (FIB) milling technique, as described in Ref. [48]. The cross-sectional microstructures across the interface between the Al and the transfer layer on the samples prepared by this method were studied using a JEOL JEM-2100F field emission electron microscope.

4.3 Experimental results

4.3.1 Friction tests in ambient air and vacuum atmospheres

The variation of the COF of the a-C:H:Si:O:F coating tested against Al with the number of sliding cycles, for a total of 20×10^3 sliding cycles in ambient air and at a normal load of 5.0 N, is shown in Figure 4.2. The COF initially increased to a high value of 0.49 ± 0.07, fluctuated at this value for about 3×10^3 cycles (a running-in period), then decreased to a low value of 0.08 at 5×10^3 cycles following this running-in period and attained an average value of 0.06 ± 0.01 for the last 2×10^3 cycles. The contact surface of the Al ball and wear track formed on the a-C:H:Si:O:F coating are shown in Figure 4.3(a). The Al contact surface was covered with a carbonaceous layer (Figure 4.3(a)) that consisted of C, Si, O, Al and F according to the EDS analyses, and was thus consistent with material transfer from the worn surface of the a-C:H:Si:O:F coating. The secondary electron image (SEI) of the wear track formed on the surface of the a-C:H:Si:O:F coating is given in Figure 4.3(b). The EDS analyses of the wear track did not show evidence for Al transfer to the a-C:H:Si:O:F coating during sliding. The wear debris that was observed adjacent to both sides of the wear track consisted of particles that were composed of C, O, Si and F, similar to those detected in the transfer layer that was formed on the Al contact surface (Figure 4.3(a)).

The variation of the COF for the a-C:H:Si:O:F coating with the number of sliding cycles under an applied load of 1.0 N in ambient air is shown in Figure 4.4. The COF of the coating did not differ much from that tested at 5.0 N (Figure 4.2); initially a high COF of 0.39 ± 0.04 was observed for a running-in period of 20 cycles, which was followed by a
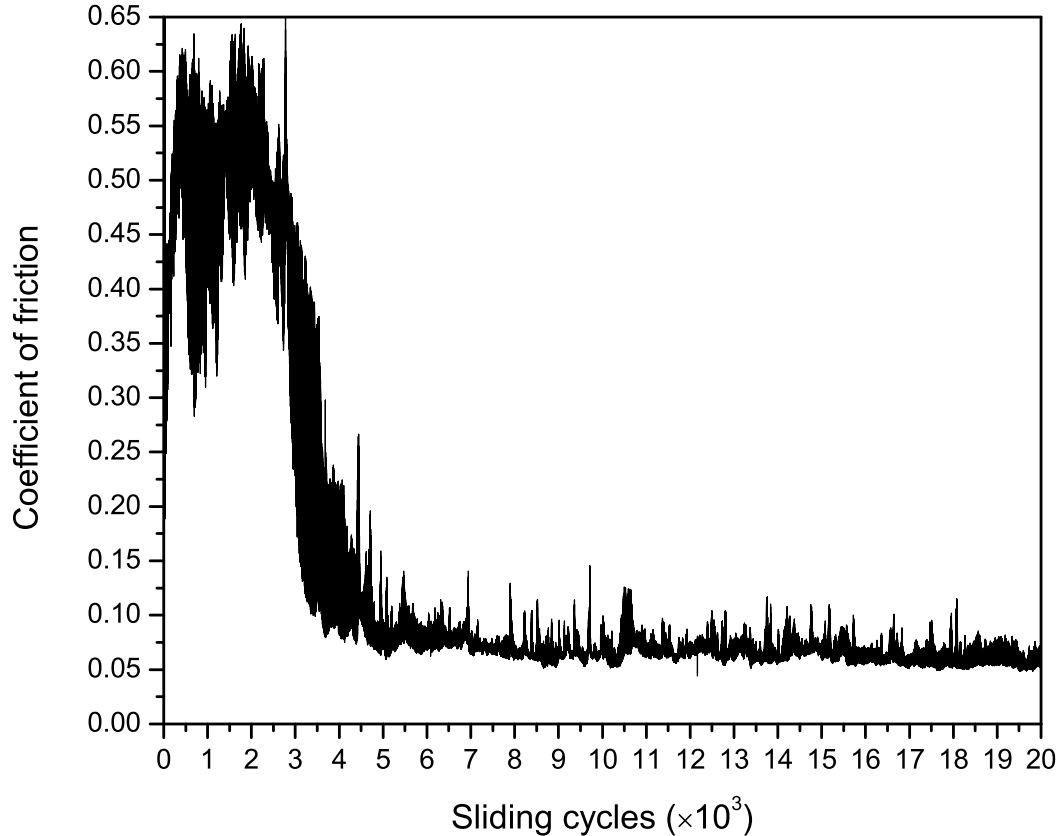
Figure 4.2: The variation of the coefficient of friction of a-C:H:Si:O:F coating with the number of cycles when tested against Al in ambient air at 5.0 N load.

decrease of COF to a steady state value of 0.08 ± 0.01 after 10^3 cycles. (Other experiments carried out at 1.0 and 5.0 N loads showed that the duration of the running-in period varied between 20 and 4000 cycles.) At all loads during the running-in period, transfer layers were formed on the Al surface consistent with previous observations [4, 5, 7, 8, 10, 16, 49]. Once these layers were established, a low steady-state COF regime was observed.

For the test conducted in the vacuum condition at 1.0 N, the COF of a-C:H:Si:O:F showed a similar behavior to the ambient air tests (Figure 4.4). The COF was 0.25 ± 0.05 in the initial running-in period after which the COF decreased and maintained a low steady-state COF value at 0.08 ± 0.01. Hence, the a-C:H:Si:O:F coating showed the same steady-state COF at 1.0 N load against Al when tested in either an ambient air or a vacuum atmosphere, but the concentration of compounds in transfer layers that formed on the Al surface were different. SEM and EDS surface analyses of the Al ball after sliding in ambient air revealed that this was covered with a Si-oxide rich carbonaceous transfer layer

129
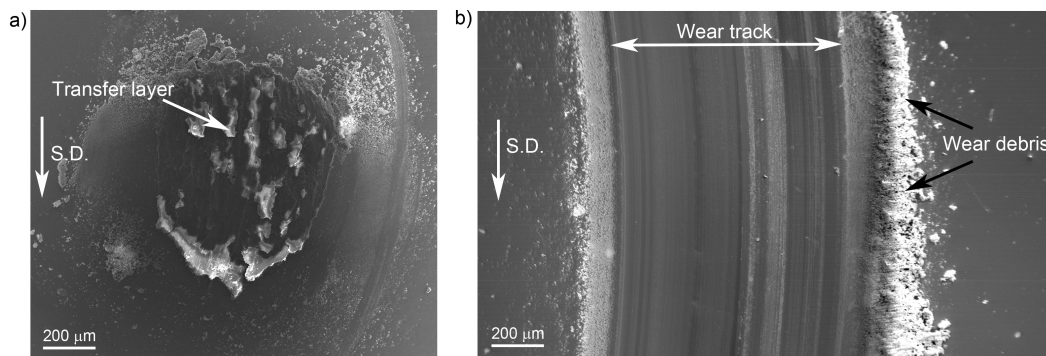
Figure 4.3: SEI of a) Al ball surface and b) the wear track formed on a-C:H:Si:O:F after sliding at 5.0 N in ambient air. The sliding direction (S.D.) is shown with an arrow.

incorporating small amounts of F, similar to that obtained with a load of 5.0 N in ambient air (Figure 4.3(a)). No adhered Al was observed on the wear track. On the other hand, SEM and EDS analyses of the transfer layers formed on the Al ball surface after sliding in the vacuum (Figure 4.5(a)) showed that the carbonaceous transfer layer formed was mainly incorporated with C and O as the principal elements with small amounts of Si and F. No adhered Al was observed on the wear track of the a-C:H: Si:O:F coating (Figure 4.5(b)). The width of the wear track formed in the vacuum was larger (400 ± 10 μm) than that formed in ambient air (127 ± 5 μm) at 1.0 N. XPS, micro-Raman, and cross-sectional TEM investigations were conducted for more detailed characterization of the microstructural and compositional changes that occurred in the transfer layers, and the results are presented in Section 4.3.2.

4.3.2 Characterization of composition and microstructure of transfer layers

4.3.2.1 X-ray photoelectron spectroscopy (XPS) analysis of transfer layers

Quantitative compositional analyses of transfer layers (at ambient atmosphere, 5.0 N) that were carried out using XPS (Figure 4.6(a)) were consistent with the EDS analyses and indicated that the transfer layer consisted of 43.7 at.% O, 21.1 at.% C, 16.6 at.% Si, 8.6 at.% F and 7.4 at.% Al. High resolution XPS spectra of the transfer layer that recorded the binding energies of C $1s$ (Figure 4.6(b)), Al $2p$ (Figure 4.6(c)), and Si $2p$ (Figure 4.6(d)) were also determined. The C $1s$ binding energies of 284.8, 286.3, 288.0 and 289.0 eV
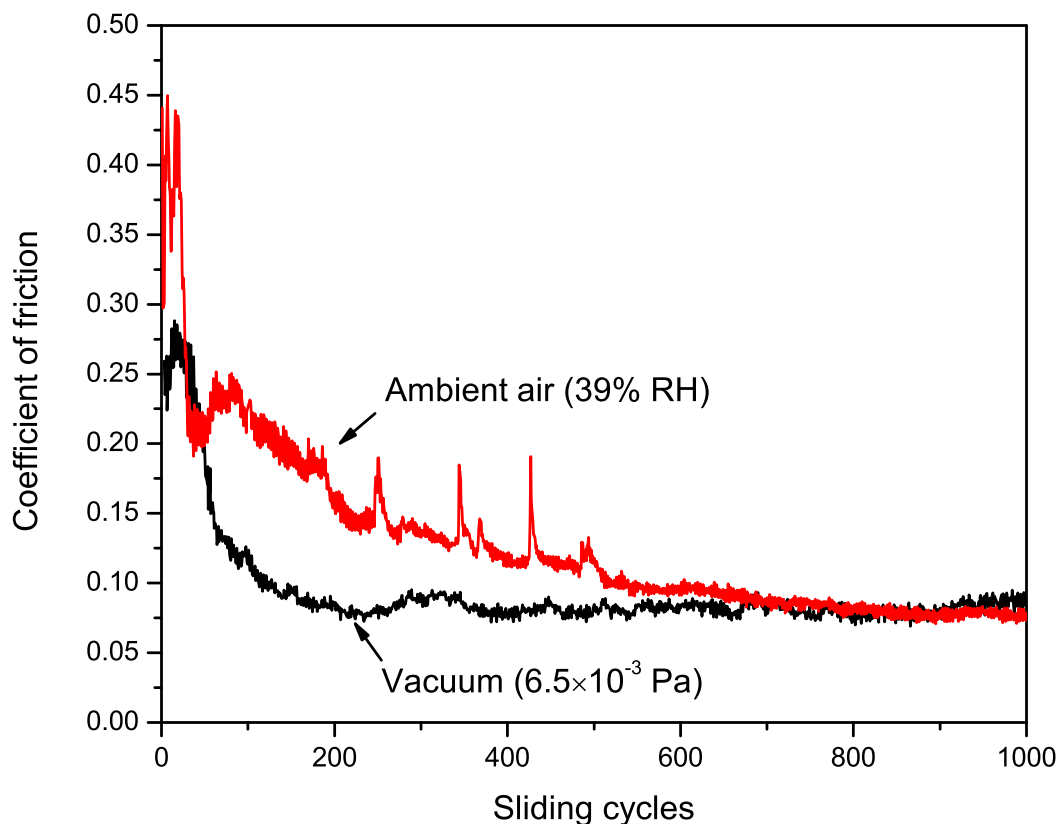
Figure 4.4: The variation of coefficient of friction of a-C:H:Si:O:F with the number of cycles when tested against Al under the vacuum atmosphere in comparison with the COF of the same system under the ambient atmosphere at 1.0 N load.

(Figure 4.6(b)) can be assigned to the $-C-C/-C-H$, $-C\text{-}OH/-C\text{-}O\text{-}C$, $-C-C-F$, and $-O-C=O$ bonding states, respectively [50–52]. By integrating the area of the decomposed peaks, the atomic ratio of $-C-C/-C-H$ was calculated as 85.3 at.% and the atomic ratio of $-C-OH/-C-O-C$ as 11.7 at.%. These results suggested that the carbon atoms in the transfer layers were terminated by -OH, $-H$, $-F$ and $-O$. For the Al $2p$ spectra shown in Figure 4.6(c), the binding energies of 73.6, 75.2 and 76.5 eV were assigned to Al, Al2O3 (xH_2O) and AlF_3, respectively [52–57]. The integral area of these decomposed peaks revealed that 54.8 at.% of Al was present in the form of AlF3, and the remaining Al atoms were either in the form of Al or Al_2O_3 (xH_2O). This suggests that the F in the coating transferred to the Al and formed AlF_3 on the Al surface. The binding energy of Si $2p$ spectra shown in Figure 4.6(d) deconvoluted to a single peak at 102.3 eV, which was assigned to the $Si-O-Si$ bonds [58–60] in the amorphous silicon oxide. This binding energy can also
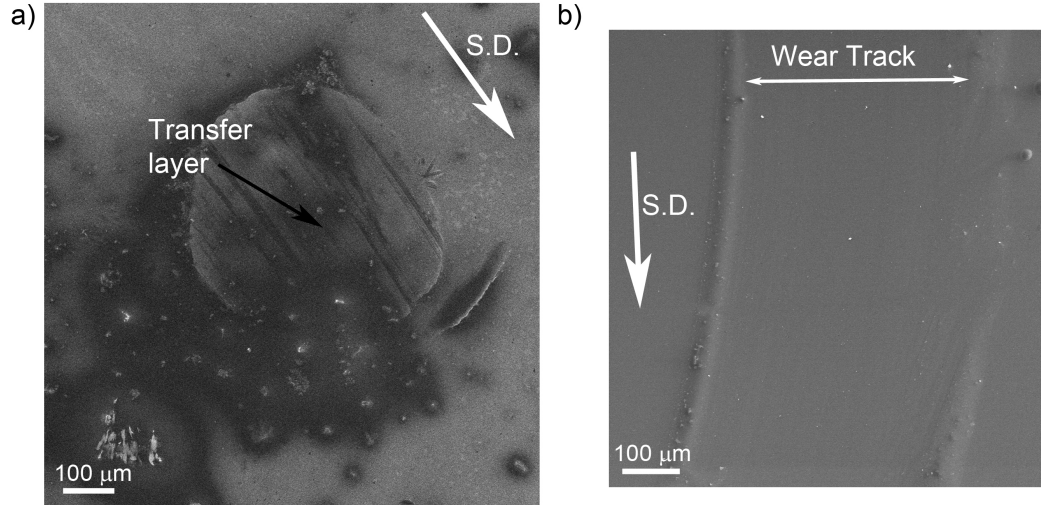
Figure 4.5: a) SEI of Al 1100 ball surface and b) the wear track formed on the a-C:H:Si:O:F coating after sliding test at 1.0 N load and under a vacuum atmosphere.

correspond to that of the Si-O$-$C bonds as reported in silicon containing polymers [59]. Therefore, the Si and O were found to form Si$-$O bonds similar to the amorphous silicon oxide and form a network in the a-C:H:Si:O:F coating. The transfer layers formed in the vacuum also revealed the presence of the same elements, but the amounts of the elements were different. These transfer layers were composed of 79.0 at.% C, 15.7 at.% O, 3.9 at.% Si, 0.9 at.% Al and 0.5 at.% F as determined by XPS. The high resolution XPS analyses of the C $1s$, Si $2p$ and Al $2p$ spectra showed analogous results presented in Figure 4.6(b)-(d).

4.3.2.2 Micro-Raman analysis of the wear tracks and transfer layers

The micro-Raman spectra of the a-C:H:Si:O:F DLC coating were obtained from both the unworn surface and the wear track formed in ambient air. In addition, Raman spectra of the transfer layer were taken. These are shown in Figure 4.7. The Raman spectra of the unworn DLC coating and the wear track did not differ significantly and both showed a broad peak between 1250 and 1650 cm^{-1}, which is a common feature of a-C coatings [61, 62]. On the other hand, the Raman spectra of the transfer layers that were generated on the Al surface showed noticeable peak shifts. Deconvolution of the Raman spectra into two Lorentzian functions indicated that the peaks centered at 1388 and 1583 cm^{-1} can be assigned to the D and G bands of the carbon, respectively. The peak shifts in the Raman spectra of
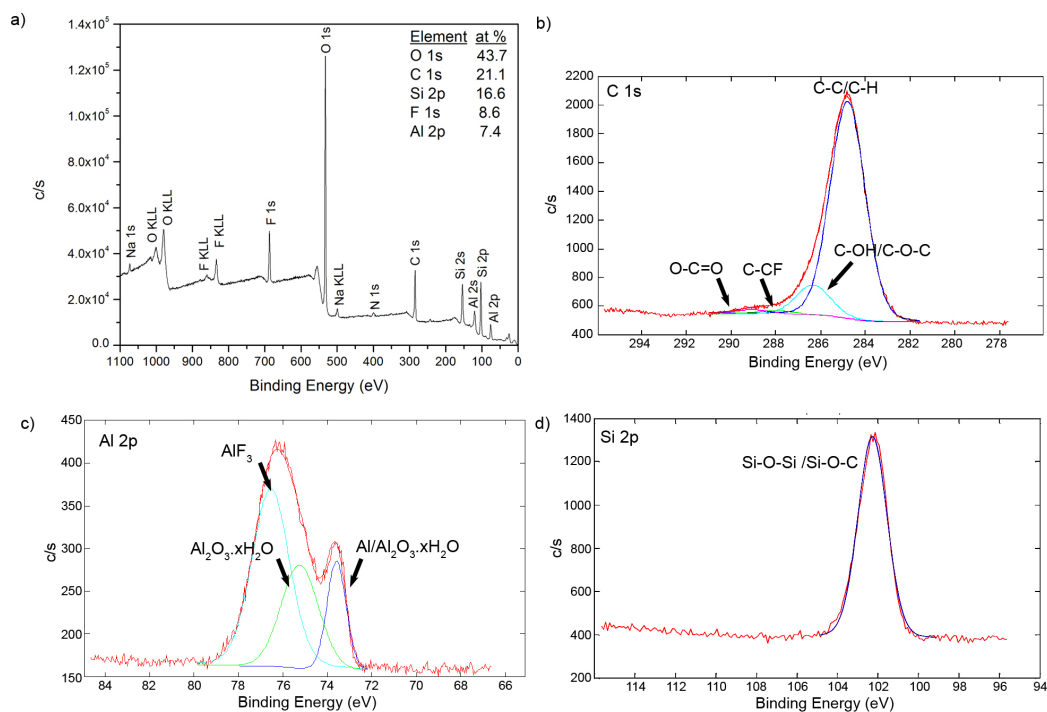
Figure 4.6: a) X-ray photoelectron spectroscopy (XPS) spectra of transfer layers that formed on Al during sliding against a-C:H:Si:O:F in ambient air at 5.0 N load. High resolution spectra for b) C 1s, c) Al 2p and d) Si 2p.

the transfer layer compared to the shift observed in the a-C:H:Si:O:F coating (Figure 4.7) indicated an increase in sp^2 content and, hence, likelihood of graphitization during sliding consistent with literature [40, 62].

4.3.2.3 Cross-sectional observation of transfer layers by focused-ion beam (FIB) and transmission electron microscopy (TEM)

Cross-sectional samples taken on a plane perpendicular to the interface between the transfer layer and the Al contact surface were prepared using FIB milling (see Section 4.2.2). The SEI showing the cross-sectional image of the transfer layer is presented in Figure 4.8(a), which indicates that a 3.9 ± 0.1 μm thick carbonaceous transfer layer was formed on the Al surface for the a-C:H:Si:O:F coating tested in ambient air under a 5.0 N load. EDS maps taken from the same section indicate the distribution of C, O, F and Si within the transfer layer, as shown in Figures 4.8(b)-(f). Accordingly, F had the highest concentration in locations adjacent to the Al surface (Figure 4.8(d)). On top of this region, the layer was
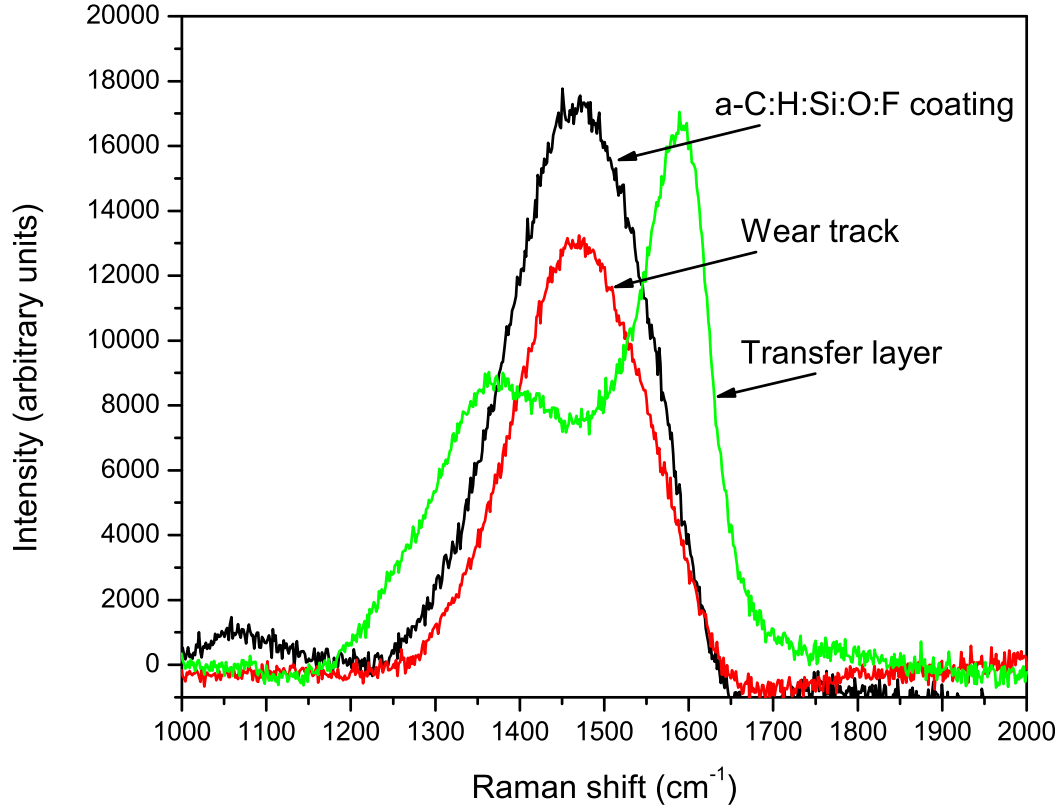
Figure 4.7: Raman spectra of unworn a-C:H:Si:O:F coating, the wear track, and the transfer layer that formed in ambient air at 5.0 N.

richer in C and incorporated Si, O, and F. This part of the layer appeared to be compact, yet exhibited through thickness cracks and cracks that extended parallel to the sliding direction. The topmost region of the transfer layer was rich in Si and O (Figure 4.8(e)) with lesser amounts of C and F concentrations compared to the inner sections of the transfer layer.

Figure 4.9(a) shows a TEM image of the same section of the transfer layer in Figure 4.8(a). The Al grains had an average size of 396.5 ± 131.1 nm and aspect ratio of 1.9 ± 0.9 and were elongated in the sliding direction, as a result of the plastic deformation that occurred during sliding. The details of microstructures of the three regions of the transfer layer noted in Figure 4.8(a) can be distinguished more clearly in Figure 4.9(a). The thin $(0.52 \pm 0.16$ μm) F-rich region near the Al/transfer layer interface – designated as "A" in Figure 4.9(a) – is shown in the high resolution TEM micrograph of Figure 4.9(b), which indicates that during sliding of Al against a-C:H:Si:O:F, the F reacted with Al and formed AlF$_3$ crystals with a d-spacing of 0.35 nm on the Al surface. Figure 4.9(b) also shows that
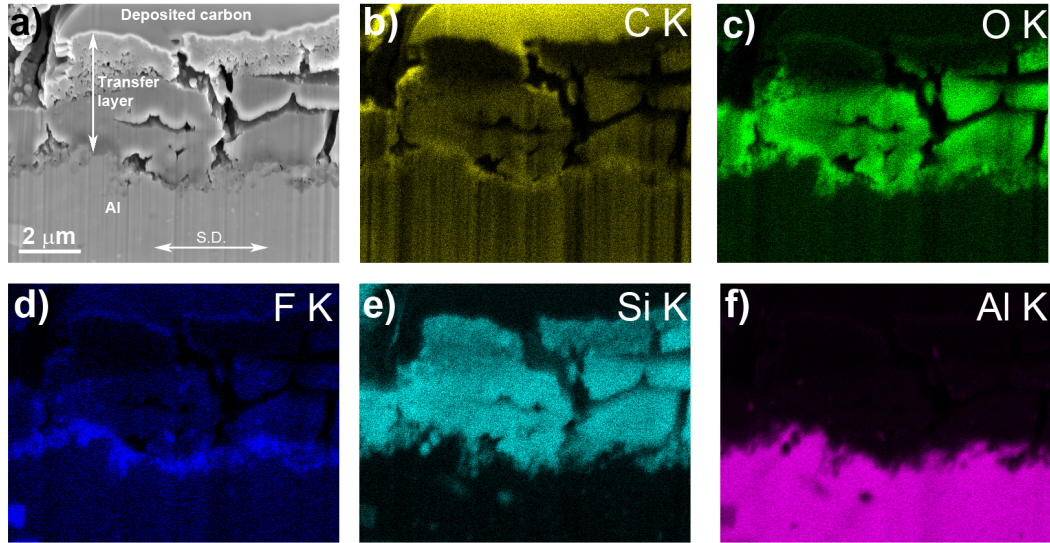
Figure 4.8: a) Secondary electron image (SEI) of the cross-section of the Al surface with the transfer layer formed during sliding contact. The elemental EDS maps are taken from the whole area shown in figure (a) are shown for b) C K, c) O K, d) F K, e) Si K and f) Al K.

the native oxide that naturally forms on Al surfaces was absent at the Al/transfer layer interface. The native Al_2O_3 layer was possibly removed during sliding, which allowed the nascent Al to react with the F atoms of the a-C:H:Si:O:F coating forming AlF_3. An HR TEM image of the transfer layer's mid-section ("B" in Figure 4.9(a)) shows Al nano-crystals with an average size of 2.8 ± 0.5 nm dispersed in an amorphous matrix (Figure 4.9(c)). The presence of these Al crystals in the transfer layer shows that during the running-in period (Fig. 2), the plastically deformed Al layers were detached from the aluminum's contact surface and mechanically mixed with the other elements of the transfer layer (C, F, Si and O). The presence of cracks parallel to the sliding direction suggests that the transfer layer would eventually become detached from the surface during sliding to form wear debris. The topmost part of the transfer layer in contact with the a-C:H:Si:O:F coating was richer both in Si and O compared to the rest of the layer and, as the HR TEM image (from "C" in Figure 4.9(a)) presented in Figure 4.9(d) indicates, it consisted of loosely packed nano and ultra-fine particles. The selected area diffraction pattern obtained from this region is shown in the inset of Figure 4.9(d), which is consistent with the amorphous structure of the transfer layer. A few diffraction spots were observed, which could be assigned to SiO_2 crystals with

the cristobalite structure in the $P4_12_12$ space group [63–65].

4.3.3 Ambient air to vacuum sliding contact tests

The transfer layers that were formed on the Al surface played an important role in establishing a low COF, as described in Sections 4.3.1 and 4.3.2. To elucidate the mechanisms that allowed the transfer layers to provide a low COF, changes in the chemistry of the transfer layers during sliding contact were determined by measuring the variations in the amount of gasses in the environment during the sliding test. For this purpose, the a-C:H:Si:O:F coating was first put in sliding contact against an Al ball in ambient air at a load of 1.0 N and the experiment continued until the transfer layers formed on the Al surface. A running-in period with a high COF occurred in sliding for 1×10^3 cycles and, as soon as the COF reduced to a steady-state value of 0.1, the environmental chamber surrounding the tribometer was evacuated while the sliding test was still running. Once a high vacuum of 2.5×10^{-3} Pa was reached (after 7.4×10^3 cycles), partial pressures of the residual gasses inside the chamber were measured, while the sliding contact experiment continued uninterrupted. The changes in the COF and the partial pressure of residual H_2O gas during the sliding test in ambient air to vacuum are shown in Figure 4.10. The results show that the COF increased from 0.1 to 0.3 during the initial purging period, but then reduced quickly to a very low value of 0.08 ± 0.01 at 6.88×10^3 sliding cycles and this COF value was maintained until the end of the test that lasted for 10×10^3 cycles.

An increase in the partial pressure of water vapor (H_2O) from 1.7×10^{-3} Pa to 2.0×10^{-3} Pa was recorded inside the chamber and this increase continued until the end of the sliding test, as shown in Figure 4.10. The H_2O partial pressure in the chamber slightly decreased to 1.9×10^{-3} Pa when the vacuum sliding test was stopped, which suggested that increase in the H_2O partial pressure was due to the tribo-chemical reactions that occurred during the sliding. There was also an increase in the partial pressures of H_2 and CO_2 during the test in the vacuum, while the concentrations of these gasses were two orders of magnitude lower than the partial pressure of H_2O observed. The partial pressures of other gasses that were recorded in the vacuum, namely SiF_4, SiH_4, turbo pump oil, CO, N_2 and O_2 were much lower (10^{-8}–10^{-6} Pa) and continuously decreased. The increase in the H_2O during sliding

in the vacuum may be interpreted as the H_2O becoming desorbed from the coating surface. To provide supporting evidence for the fact that the H_2O desorption that occurred during sliding was due to the wear of the a-C:H:Si:O:F coating, the same "*ambient air-to-vacuum test*" was repeated, but an a-C:H coating was used containing 29 at.% H against Al. For this tribological system, the COF decreased to 0.14 after a running-in period that lasted 3.9×10^3 cycles and the residual gas analyses showed a continuous decrease in the partial pressure of H_2O inside the vacuum chamber during sliding. This observation suggested that there was no desorption of H_2O molecules when Al was slid against a-C:H and that the H_2O desorption only occurred if the DLC coating contained Si and O.

4.3.4 Comparison with other DLC coatings

Previous sliding experimental studies $[5, 8, 16, 19, 30]$ supported by models based on first principles calculations established that $H-$, $OH-$ and $F-$passivation of the dangling carbon bonds at contact surfaces is an important requirement for the generation of low COF values between aluminum and DLC coatings. Thus, formation of carbon rich transfer layers on aluminum and also passivation of these transfer layers are both essential for attainment of a low COF. A comparison of the COF of the a-C:H:Si:O:F coating with the a-C, a-C:H and a-C: H:F coatings is provided in Figure 4.11. The COF exhibited by the a-C:H: Si:O:F coating when tested against Al in either ambient air or vacuum was lower and more stable compared to the COF observed for the other coatings. The a:C coating showed a high COF of 0.55 in the vacuum. The high COF is accompanied by a high amount of Al adhesion to the DLC surface, and no carbonaceous transfer layers were formed $[5, 8]$. Repulsive forces between H-passivated $[16, 18, 19, 66]$, F-passivated $[29, 30]$ and OH-passivated $[19]$ DLC or diamond surfaces and their carbonaceous counterfaces were computed using first principles calculations. The effect of OH-passivation was noted as being particularly important because trace amounts of H_2O molecules in the environment (3×10^{-3} Pa) were found to be sufficient for OH-passivation of the dangling carbon bonds $[67]$. The feasibility of H_2O molecules in the environment dissociating into –H and –OH groups when placed at the close proximity of the carbon atoms on diamond surface has been shown by Qi et al. $[19, 67]$. The effectiveness of OH-passivation of an a-C coating in reducing the COF after the generation of passivated

carbon transfer layers in ambient air was demonstrated by Konca et al. [8]. When the OH-passivated carbon layers were formed under the a-C/Al systems running under the ambient conditions, the coating maintained the low COF in the vacuum until these layers were consumed [8].

4.4 Discussion

The a-C:H:Si:O:F showed an interesting tribological behavior by displaying a very low and stable steady state COF of 0.08 both in ambient and vacuum atmospheres against Al. The low COF was preceded by a high COF running-in period that corresponded to the formation of carbonaceous transfer layers on the aluminum contact surface. This section focuses on the interpretation and rationalization of the low COF values observed, by considering the tribo-chemical mechanisms that operate at the contacting interfaces. Possible reasons why the same mechanisms would operate in both ambient and vacuum conditions are also discussed. For the discussion of OH-passivation in a-C:H:Si:O:F coatings, the roles of silicon and oxygen should be considered together. Then, the role of fluorine is discussed on the surface passivation.

4.4.1 The roles of silicon and oxygen

The low friction achieved with Si and SiO_x containing DLC was commonly attributed to the formation of SiO_2-containing transfer layers on the counterfaces [38, 40, 42, 44], but the mechanisms responsible for the low COF were not clarified. In this work, similar transfer layers were observed (Figure 4.9). The top portions of the layers were rich in Si and it is conceivable that the Si and O atoms present in the a-C: H:Si:O:F coating likely formed silica, SiO_2 or silicate structures in the layer. The silicate structure, $[SiO_4]^{-4}$ for which two Si were connected by a bridging O atom such that $Si-O-Si$ bonds seen in the XPS spectra of Figure 4.6(d), is the basic unit of both crystalline and amorphous forms of silica. It is well known that $Si-O-Si$ bonds are susceptible to attack by the H_2O molecules when the silica is placed under stress − a phenomenon known as stress corrosion cracking or static fatigue [68, 69]. The physical mechanism of stress corrosion involves the H_2O molecule −

aligning the lone pair of its oxygen molecules with the unoccupied electron orbitals of the Si atoms in the stressed Si$-$O$-$Si chain [68–70]. Concurrently, a bond forms between the H of the water molecule and the bridging O atom. It was proposed that this mechanism results in the breaking of the Si$-$O$-$Si bond, which is replaced by two Si$-$OH bonds. This hydration mechanism is shown below in Eq. 4.1 and schematically depicted in Fig. 12:

$$\text{-Si} - \text{O} - \text{Si} - + \text{H}_2\text{O} = -\text{Si} - \text{OH} + \text{-Si} - \text{OH} \qquad (4.1)$$
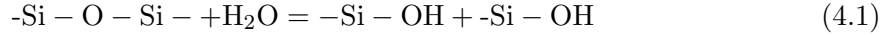
The proposed hydration mechanism would occur during sliding at the surface of the a-C:H:Si:O:F coating surface, as well as within the transfer layer (Figure 4.9(d)). Ambient air-to-vacuum sliding contact experiments (Figure 4.10) provided evidence for the presence of adsorbed H_2O molecules at the contact interfaces.

The hydration reaction shown in Eq. 4.1 is necessary, but not a sufficient mechanism to achieve the low COF in a-C:H:Si:O:F coating. This was shown by performing experiments during which a silicate glass (namely an amorphous SiO_2 plate with a structure known to consist of interconnected $[SiO_4]^{-4}$ units) was put into sliding contact against the same Al counterface under 5.0 N load and a sliding speed of 0.12 m/s, i.e. the same condition used to test the a-C:H:Si:O:F coating (Figure 4.1). A high COF of 0.65 was obtained for silicate glass in ambient air and when the experiment was repeated, while the silicate glass was submerged in water, an even higher COF of 0.90 was measured. (A COF of 0.63 was obtained when a plate of pure silicon was tested in ambient air.) Thus, neither Si nor the SiO_2 exhibited the low steady-state COF of a-C:H:Si:O:F run against Al. These results are consistent with results reported in the literature that indicated the COF between Si and SiO_2 pairs ranged between 0.2 and 0.4 [71]. Therefore, it can be argued that in order to achieve the low COF, Si and O must be present within the amorphous carbon network.

The nano-sized fragments rich in Si and O that were formed on the top section of the transfer layer (Figure 4.8) can be interpreted as evidence for the fracture of the layer, due to stress corrosion (Figure 4.9(d)). These loosely-packed, nano-sized, hydrated fragments may facilitate shearing of the solid core of the transfer layer against the coating surface, and thus might contribute to the low COF.

4.4.2 The role of fluorine

Fluorine is another contributor to the low COF in the a-C:H:Si:O:F coating. As reported in the literature [30], incorporation of F in the DLC coating reduced the friction against Al and, hence, F would take part in the establishment of very low COF of the a-C:H:Si:O:F coating compared to a-C and a-C:H coatings, as shown in Figure 4.11. The a-C:H:F tested against Al showed low COF due to formation of two F-passivated carbon surfaces at the sliding contact interface [29, 30]. The formation of AlF_3 compound in the transfer layer – near the aluminum interface – was observed by XPS and high resolution TEM studies conducted by the authors in an a:C:H:F coating [30]. Consistent with the observations in a-C:H:F, the a-C:H:Si:O:F coating had also an F-rich film within the transfer layers on Al (Figure 4.8(d)). The presence of AlF_3 was detected near the aluminum side of the transfer layer (Figure 4.9(b)). The transfer of fluorine to the Al surface and AlF_3 compound could facilitate transfer layer formation.

4.4.3 The tribo-chemical mechanisms for low coefficient of friction in ambient air

The suggested mechanisms of the low COF attained during sliding a-C:H:Si:O:F and Al are summarized in the schematic diagrams, shown in Figure 4.13(a). Accordingly, when a-C:H:Si:O:F was placed in contact with Al, the F was conceivably the first component to transfer to the Al contact surface. The reaction between Al and F formed AlF_3, resulting in an F-rich layer on the Al surface. On top of this region, a carbonaceous layer incorporating Si, O and F was formed. This layer appears to be compact and contained Al nano-crystals (Figure 4.13(a)). Thus, Al surface that was subjected to severe plastic deformation [48] became detached and the fragments were mechanically mixed with the carbonaceous transfer layers. The topmost region of the transfer layer consisted of a loosely packed particulate structure that was formed when the adsorbed H_2O molecules caused fracture of the $-Si-O-Si-$ bond in the amorphous (graphitized) carbon network (Figure 4.13(a)). As discussed above, the $OH-$ hydration and passivation of carbon and $[SiO_4]^{-4}$ groups on the surface, and the easy shearing of nano-sized $Si-O$ and C appeared to operate

together leading to a low COF in ambient air, as in Figure 4.13(b).

4.4.4   The low coefficient of friction in the vacuum

An important observation was that a-C:H:Si:O:F showed the same low COF when tested within a vacuum atmosphere. The environmental stability of the COF made this particular coating unique among the DLC coatings (Figure 4.11). The mechanism of the low COF of this coating in vacuum can be discussed considering the fact that when the a-C:H: Si:O:F was subjected to sliding in the vacuum, the transfer layer showed evidence of passivation by $-H$, $-F$ and $-OH$ groups. It was previously shown in [72] that in a-SiC:H thin films loaded in tension and placed in testing environments of different relative humidity values, the crack growth velocity was insensitive to the humidity level even when the humidity in the surrounding atmosphere was reduced to very low levels of 0.1%. The model developed in [72] revealed that the change in the strain energy release rate with the partial pressure of H_2O was constant and, as such, an infinitesimal amount of atmospheric H_2O was sufficient to break the Si-O bonds. Figure 4.10 shows that H_2O molecules that were desorbed during the sliding test conducted in vacuum with a partial pressure of about 10^{-3} Pa, which were sufficient for the mechanism shown in Eq. 4.1 to be activated and thus allowed the tribological mechanisms, shown in Figure 4.13, to operate under the vacuum atmosphere.

In summary, a-C:H:Si:O:F coating is of value for engineering applications where a low COF is required for the extended service life, during which the atmospheric conditions may change considerably. The low and stable COF of this coating can be useful in applications where very low humidity is present, such as in lithium-ion battery manufacturing and aerospace tribology.

4.5   Conclusions

Sliding contact experiments between a-C:H:Si:O:F and 1100 Al were carried out in ambient air and vacuum atmospheres. The microstructure and chemical changes that occurred at the contact surfaces and within the transfer layer generated during sliding were investigated. The following conclusions were reached:

1. The a-C:H:Si:O:F exhibited a low COF of 0.08 against Al in an ambient air, as well as a vacuum atmosphere, following a running-in period during which carbonaceous transfer layers containing fluorine and silicon oxide formed on the Al surface.

2. The low friction achieved with a-C:H:Si:O:F coating can be attributed to the operation of passivation and hydration mechanisms during sliding. It is suggested that the hydration of the $-Si-O-Si-$ chains in the coating and transfer layers resulted in the formation of two OH-passivated surfaces at the contact interface that led to low COF.

3. The hydration of $Si-O-Si$ chains is suggested to be responsible for the formation of easily sheared nano-sized a-C:Si:O fragments at the contact interface, passivated by –OH.

4. The fluorine in the a-C:H:Si:O:F coating transferred to the Al and formed AlF_3 on the Al surface. The fluorine and hydrogen appeared to have provided additional passivation of the carbon surfaces and contributed to the reduction of COF observed to levels below those for a-C, a-C:H and a-C:H:F coatings.

5. The fact that low friction was also obtained in vacuum indicated that a very small amount of water vapor (10^{-3} Pa) in the environment may be sufficient to allow the hydration and OH-passivation mechanisms to be effective.
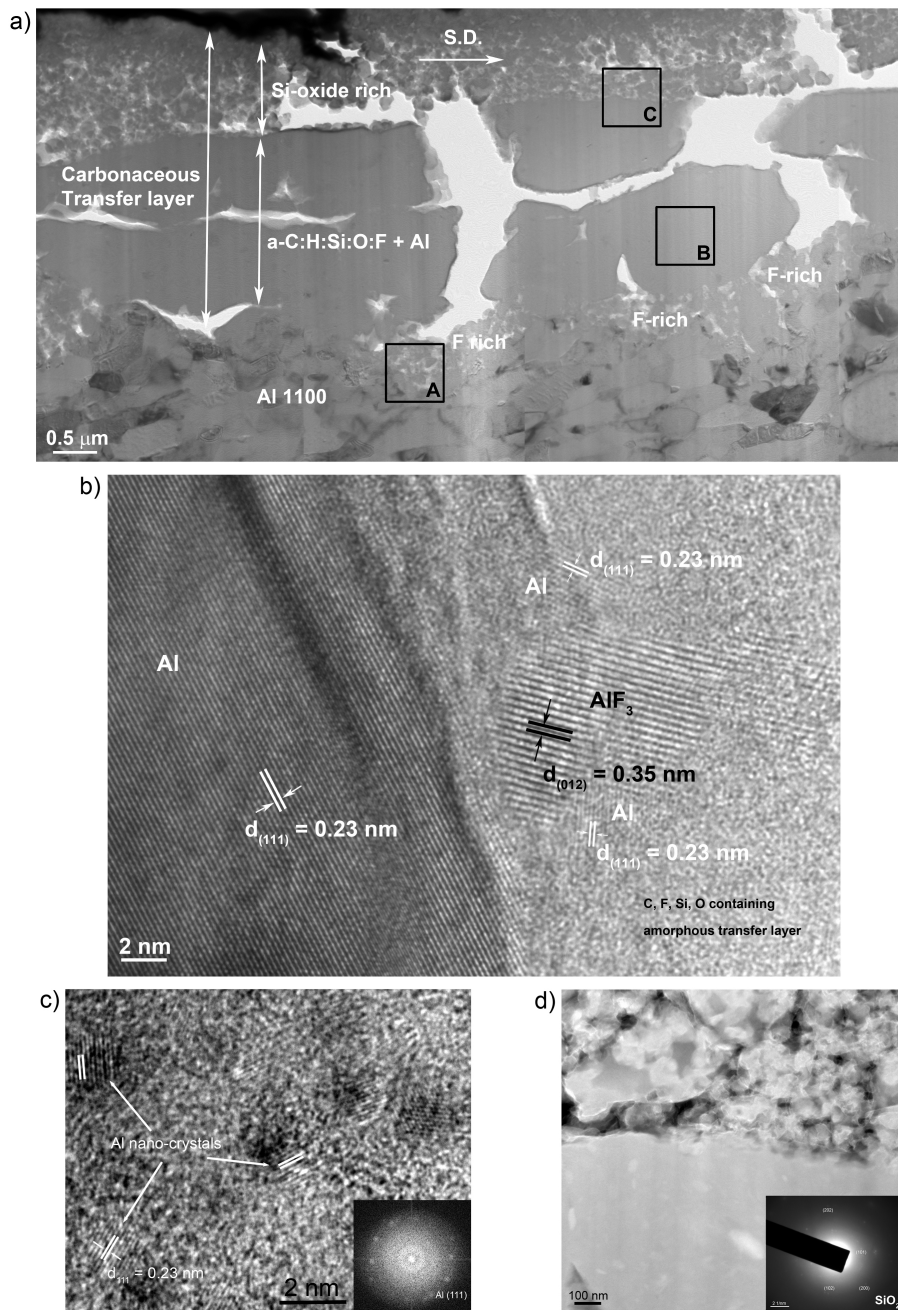
Figure 4.9: a) Bright field cross-sectional transmission electron microscope (TEM) image of the transfer layer formed on the Al surface. b) High resolution TEM (HR TEM) image obtained from the region labeled as "A" in (a). c) HR TEM image obtained from the region labeled as "B" in (a). Inset shows the diffraction pattern obtained by fast Fourier transformation (FFT) of the image. d) HR TEM image of the transfer layer obtained from the region labeled as "C" in (a). Inset shows the selected area diffraction pattern of the same area.
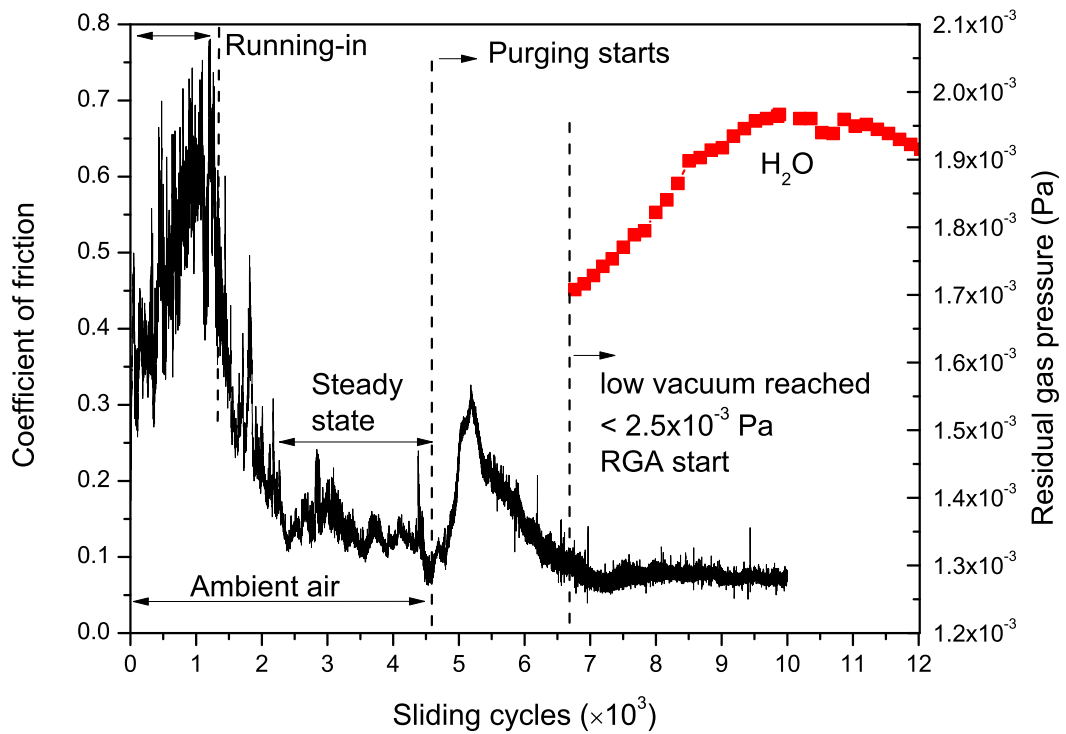
Figure 4.10: The variation of the COF of a-C:H:Si:O:F when the test atmosphere changed from ambient air to that of vacuum at 1.0 N. The partial pressure of the H_2O in the vacuum chamber recorded during the sliding test is plotted.
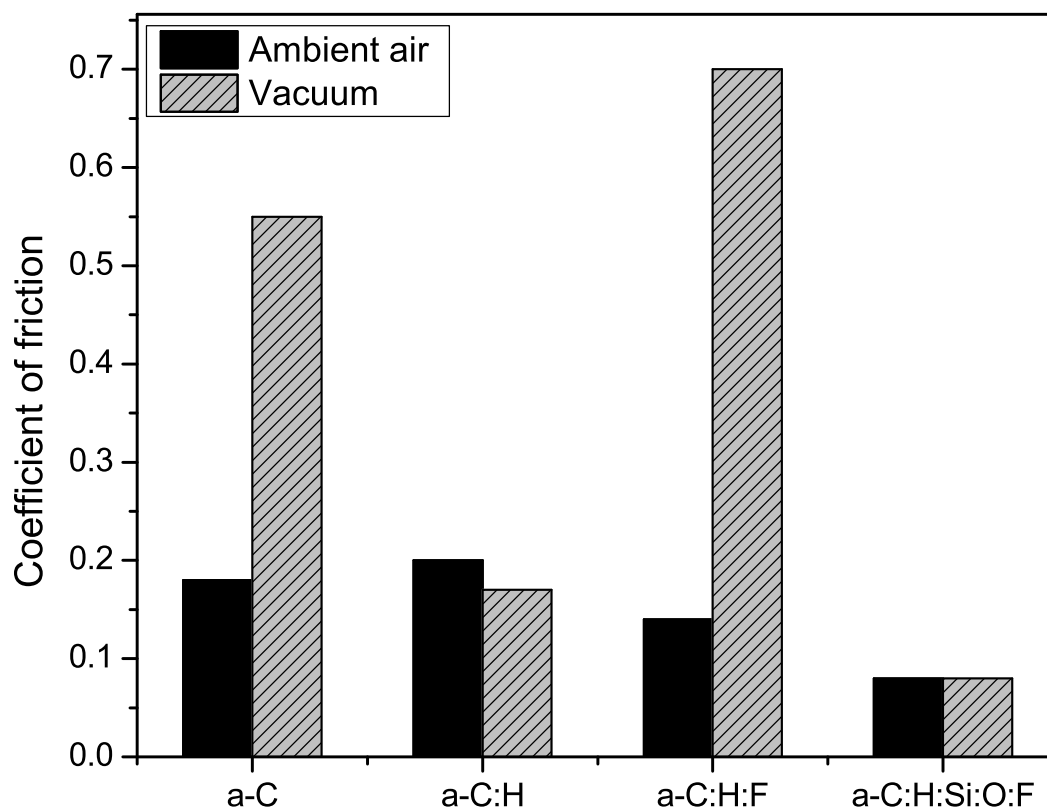
Figure 4.11: The steady state COF data of a-C:H:Si:O:F compared to a-C, a-C:H (29 at.% H) and a-C:H:F (26 at.% H, 3 at.% F) coatings [4, 7] against Al under ambient air and vacuum atmospheres. All tests were performed using the same ball-on-disk tribometer at 5.0 N.
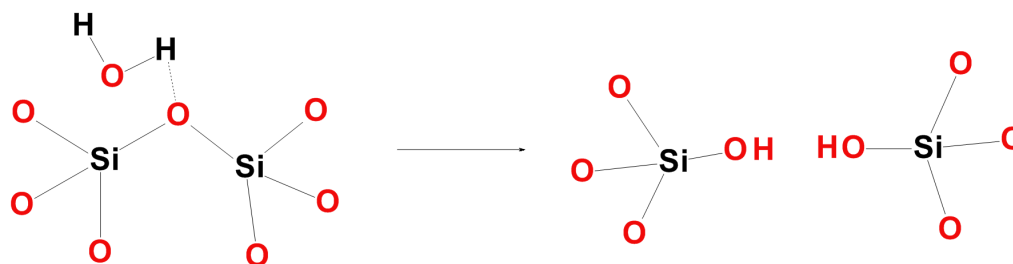
Figure 4.12: Schematic diagram showing the $[SiO_4]^{-4}$ tetrahedral groups (connected by $-Si-O-Si-$ bridging oxygen bonds) that are attacked by H_2O molecules breaking the $Si-O$ bonds and passivating the surface by $-OH$.
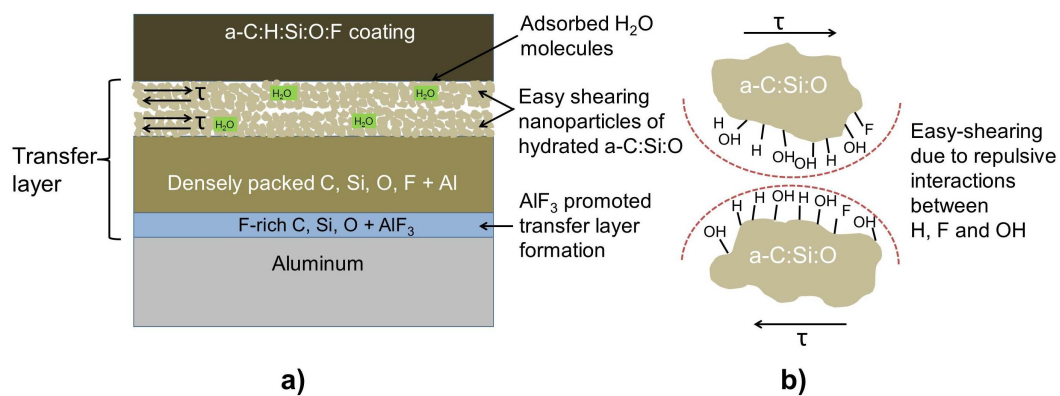
Figure 4.13: Schematic diagrams showing the mechanisms responsible for the low friction of a-C:H:Si:O:F. a) Formation of F-rich carbonaceous transfer layer containing AlF_3 and a densely packed amorphous layer containing C, Si, O, F and nanocrystalline Al. The topmost part of the layer had loosely packed, nano-sized, fragments (C, Si and O) passivated by $-OH$. b) The easy shearing mechanism between the passivated fragments and development of repulsive forces between these passivated groups.

Bibliography

[1] A. Erdemir and C. Donnet. Tribology of diamond-like carbon films: recent progress and future prospects. *Journal of Physics. D: Applied Physics*, 39(18):R311–R327, 2006.

[2] S. Bhowmick and A. T. Alpas. The performance of hydrogenated and non-hydrogenated diamond-like carbon tool coatings during the dry drilling of 319 Al. *International Journal of Machine Tools and Manufacture*, 48(7-8):802–814, 2008.

[3] S. Bhowmick and A. T. Alpas. Minimum quantity lubrication drilling of aluminium-silicon alloys in water using diamond-like carbon coated drills. *International Journal of Machine Tools and Manufacture*, 48(12-13):1429–1443, 2008.

[4] E. Konca, Y. T. Cheng, and A. T. Alpas. Dry sliding behaviour of non-hydrogenated DLC coatings against Al, Cu and Ti in ambient air and argon. *Diamond and Related Materials*, 15(4-8):939–943, 2006.

[5] E. Konca, Y. T. Cheng, A. M. Weiner, J. M. Dasch, and A. T. Alpas. The role of hydrogen atmosphere on the tribological behavior of non-hydrogenated DLC coatings against aluminum. *Tribology Transactions*, 50(2):178–186, 2007.

[6] E. Konca, Y. T. Cheng, A. M. Weiner, J. M. Dasch, and A. T. Alpas. Elevated temperature tribological behavior of non-hydrogenated diamond-like carbon coatings against 319 aluminum alloy. *Surface and Coatings Technology*, 200(12-13):3996–4005, 2006.

[7] E. Konca, Y. T. Cheng, A. M. Weiner, J. M. Dasch, and A. T. Alpas. Effect of test atmosphere on the tribological behaviour of the non-hydrogenated diamond-like

carbon coatings against 319 aluminum alloy and tungsten carbide. *Surface and Coatings Technology*, 200(5-6):1783–1791, 2005.

[8] E. Konca, Y. T. Cheng, A. M. Weiner, J. M. Dasch, and A. T. Alpas. Vacuum tribological behavior of the non-hydrogenated diamond-like carbon coatings against aluminum: Effect of running-in in ambient air. *Wear*, 259(1-6):795–799, 2005.

[9] J. M. Dasch, C. C. Ang, C. A. Wong, Y. T. Cheng, A. M. Weiner, L. C. Lev, and E. Konca. A comparison of five categories of carbon-based tool coatings for dry drilling of aluminum. *Surface and Coatings Technology*, 200(9):2970–2977, 2006.

[10] A. Abou Gharam, M. J. Lukitsch, Y. Qi, and A. T. Alpas. Role of oxygen and humidity on the tribo-chemical behaviour of non-hydrogenated diamond-like carbon coatings. *Wear*, 271(9-10):2157–2163, 2011.

[11] A. Abou Gharam, M. J. Lukitsch, M. P. Balogh, N. Irish, and A. T. Alpas. High temperature tribological behavior of W-DLC against aluminum. *Surface and Coatings Technology*, 206(7):1905–1912, 2011.

[12] A. Abou Gharam, M. J. Lukitsch, M. P. Balogh, and A. T. Alpas. High temperature tribological behaviour of carbon based (B_4C and DLC) coatings in sliding contact with aluminum. *Thin Solid Films*, 519(5):1611–1617, 2010.

[13] H. L. Coldwell, R. C. Dewes, D. K. Aspinwall, N. M. Renevier, and D. G. Teer. The use of soft/lubricating coatings when dry drilling BS L168 aluminium alloy. *Surface and Coatings Technology*, 177-178:716–726, 2004.

[14] A. Grill. Diamond-like carbon: State of the art. *Diamond and Related Materials*, 8(2-5):428–434, 1999.

[15] J. Andersson, R. A. Erck, and A. Erdemir. Frictional behavior of diamondlike carbon films in vacuum and under varying water vapor pressure. *Surface and Coatings Technology*, 163-164:535–540, 2003.

[16] A. Erdemir. The role of hydrogen in tribological properties of diamond-like carbon films. *Surface and Coatings Technology*, 146-147:292–297, 2001.

[17] C. Donnet, J. Fontaine, A. Grill, and T. Le Mogne. The role of hydrogen on the friction mechanism of diamond-like carbon films. *Tribology Letters*, 9(3-4):137–142, 2001.

[18] Yue Qi and L. G. Hector. Adhesion and adhesive transfer at aluminum/diamond interfaces: a first-principles study. *Physical Review B*, 69(23):235401, 06/15 2004.

[19] Y. Qi, E. Konca, and A. T. Alpas. Atmospheric effects on the adhesion and friction between non-hydrogenated diamond-like carbon (DLC) coating and aluminum - a first principles investigation. *Surface Science*, 600(15):2955–2965, 2006.

[20] C. Donnet. Recent progress on the tribology of doped diamond-like and carbon alloy coatings: A review. *Surface and Coatings Technology*, 100-101(1-3):180–186, 1998.

[21] M. Grischke, K. Bewilogua, K. Trojan, and H. Dimigen. Application-oriented modifications of deposition processes for diamond-like-carbon-based coatings. *Surface and Coatings Technology*, 74-75:739–745, 1995.

[22] J. Sanchez-Lopez and A. Fernandez. *Doping and alloying effects on DLC coatings*, pages 311–338. Tribology of Diamond-Like Carbon Films: Fundamentals and Applications. Springer, 2008.

[23] D. E. Patterson, R. H. Hauge, and J. L. Margrave. Fluorinated diamond films, slabs, and grit. In L. E. Pope, L. Fehrenbacher, and W. O. Winer, editors, *Materials Research Society Symposium Proceedings*, volume 140, pages 351–356, 1989.

[24] H. Touhara and F. Okino. Property control of carbon materials by fluorination. *Carbon*, 38(2):241–267, 2000.

[25] M. Hakovirta, X. M. He, and M. Nastasi. Optical properties of fluorinated diamond-like carbon films produced by pulsed glow discharge plasma immersion ion processing. *Journal of Applied Physics*, 88(3):1456–1459, 2000.

[26] K. P. Huang, P. Lin, and H. C. Shih. Structures and properties of fluorinated amorphous carbon films. *Journal of Applied Physics*, 96(1):354–360, 2004.

[27] G. Q. Yu, B. K. Tay, and Z. Sun. Fluorinated amorphous diamond-like carbon films deposited by plasma-enhanced chemical vapor deposition. *Surface and Coatings Technology*, 191(2-3):236–241, 2005.

[28] R. Prioli, L. G. Jacobsohn, M. E. H. Maia da Costa, and Jr. F. L. Freire. Nanotribological properties of amorphous carbon-fluorine films. *Tribology Letters*, 15(3):177–180, 2003.

[29] F. G. Sen, Y. Qi, and A. T. Alpas. Surface stability and electronic structure of hydrogen- and fluorine-terminated diamond surfaces: A first-principles investigation. *Journal of Materials Research*, 24(8):2461–2470, 2009.

[30] F. G. Sen, Y. Qi, and A. T. Alpas. Material transfer mechanisms between aluminum and fluorinated carbon interfaces. *Acta Materialia*, 59:2601–2614, 2011.

[31] M. Ishihara, T. Kosaka, T. Nakamura, K. Tsugawa, M. Hasegawa, F. Kokai, and Y. Koga. Antibacterial activity of fluorine incorporated DLC films. *Diamond and Related Materials*, 15(4-8):1011–1014, 2006.

[32] A. K. Gangopadhyay, P. A. Willermet, M. A. Tamor, and W. C. Vassell. Amorphous hydrogenated carbon films for tribological applications I. Development of moisture insensitive films having reduced compressive stress. *Tribology International*, 30(1):9–18, 1997.

[33] R. Gilmore and R. Hauert. Comparative study of the tribological moisture sensitivity of Si-free and Si-containing diamond-like carbon films. *Surface and Coatings Technology*, 133-134:437–442, 2000.

[34] R. Gilmore and R. Hauert. Control of the tribological moisture sensitivity of diamond-like carbon films by alloying with F, Ti or Si. *Thin Solid Films*, 398-399:199–204, 30 April 2001 through 30 May 2001 2001.

[35] K. Oguri and T. Arai. Tribological properties and characterization of diamond-like carbon coatings with silicon prepared by plasma-assisted chemical vapour deposition. *Surface and Coatings Technology*, 47(1-3):710–721, 1991.

[36] J. Meneve, R. Jacobs, L. Eersels, J. Smeets, and E. Dekempeneer. Friction and wear behaviour of amorphous hydrogenated $Si_{1-x}C_x$ films. *Surface and Coatings Technology*, 62(1-3):577–582, 1993.

[37] T. Hioki, Y. Itoh, A. Itoh, S. Hibi, and J. Kawamoto. Tribology of carbonaceous films formed by ion-beam- assisted deposition of organic material. *Surface and Coatings Technology*, 46(2):233–243, 1991.

[38] M. G. Kim, K. R. Lee, and K. Y. Eun. Tribological behavior of silicon-incorporated diamond-like carbon films. *Surface and Coatings Technology*, 112(1-3):204–209, 1999.

[39] S. Miyake, R. Kaneko, Y. Kikuya, and I. Sugimoto. Micro-tribological studies on fluorinated carbon films. *Journal of Tribology-Transactions of the ASME*, 113(2):384–389, 1991.

[40] T. W. Scharf, J. A. Ohlhausen, D. R. Tallant, and S. V. Prasad. Mechanisms of friction in diamondlike nanocomposite coatings. *Journal of Applied Physics*, 101(6):063521, 2007.

[41] Šarūnas MeŠkinis and Asta Tamulevičienĕ. Structure, properties and applications of diamond like nanocomposite (SiO_x containing DLC) films: A review. *Materials Science*, 17(4):358–370, 2011.

[42] D. Neerinck, P. Persoone, M. Sercu, A. Goel, C. Venkatraman, D. Kester, C. Halter, P. Swab, and D. Bray. Diamond-like nanocomposite coatings for low-wear and low-friction applications in humid environments. *Thin Solid Films*, 317(1-2):402–404, 1998.

[43] M. Grischke, A. Hieke, F. Morgenweck, and H. Dimigen. Variation of the wettability of DLC-coatings by network modification using silicon and oxygen. *Diamond and Related Materials*, 7(2-5):454–458, 1998.

[44] W. J. Wu, T. M. Pai, and M. H. Hon. Wear behavior of silicon-containing diamond-like carbon coatings. *Diamond and Related Materials*, 7(10):1478–1484, 1998.

[45] M. Murakawa and S. Takeuchi. Evaluation of tribological properties of DLC films used in sheet forming of aluminum sheet. *Surface and Coatings Technology*, 163-164:561–565, 2003.

[46] A. Wank, G. Reisel, and B. Wielage. Behavior of DLC coatings in lubricant free cold massive forming of aluminum. *Surface and Coatings Technology*, 201(3-4):822–827, 2006.

[47] J. Robertson. Diamond-like amorphous carbon. *Materials Science and Engineering R*, 37(4-6):129–281, 2002.

[48] X. Meng-Burany and A. T. Alpas. FIB and TEM studies of damage mechanisms in DLC coatings sliding against aluminum. *Thin Solid Films*, 516(2-4):325–335, 2007.

[49] A. Erdemir, C. Bindal, J. Pagan, and P. Wilbur. Characterization of transfer layers on steel surfaces sliding against diamond-like hydrocarbon films in dry nitrogen. *Surface and Coatings Technology*, 76-77(PART 2):559–563, 1995.

[50] G. Beamson and D. Briggs. *High Resolution XPS of Organic Polymers*. Wiley, 1992.

[51] A. Dilks and E. Kay. Plasma polymerization of ethylene and the series of fluoroethylenes: Plasma effluent mass spectrometry and esca studies. *Macromolecules*, 14(3):855–862, 1981.

[52] J. F. Moulder, W. F. Stickle, P. E. Sobol, and K. D. Bomben. *Handbook of X Ray Photoelectron Spectroscopy*. Physical Electronics, Chanhassen, MN, 1995.

[53] J. Ashley Taylor. XPS study of the oxidation of AlAs thin films grown by mbe. *Journal of Vacuum Science and Technology*, 20(3):751–755, 2 November 1981 through 6 November 1981 1982.

[54] James R. Lindsay, Harry J. Rose Jr., William E. Swartz Jr., Plato H. Watts Jr., and Kenneth A. Rayburn. X-ray photoelectron spectra of aluminum oxides: structural effects on the "chemical shift". *Applied Spectroscopy*, 27(1):1–5, 1973.

[55] C. D. Wagner, D. E. Passoja, H. F. Hillery, T. G. Kinisky, H. A. Six, W. T. Jansen, and J. A. Taylor. Auger and photoelectron line energy relationships in aluminum-oxygen and silicon-oxygen compounds. *Journal of Vacuum Science and Technology*, 21(4):933–944, 1982.

[56] I. Olefjord, H. J. Mathieu, and P. Marcus. Intercomparison of surface analysis of thin aluminium oxide films. *Surface and Interface Analysis*, 15(11):681–692, 1990.

[57] B. R. Strohmeier. Surface characterization of aluminum foil annealed in the presence of ammonium fluoborate. *Applied Surface Science*, 40(3):249–263, 1989.

[58] M. Anwar, C. A. Hogarth, and R. Bulpett. An XPS study of amorphous MoO_3/SiO films deposited by co-evaporation. *Journal of Materials Science*, 25(3):1784–1788, 1990.

[59] P. Laoharojanaphand, T. J. Lin, and J. O. Stoffer. Glow discharge polymerization of reactive functional silanes on poly(methyl methacrylate). *Journal of Applied Polymer Science*, 40(3-4):369–384, 1990.

[60] W. A. M. Aarnink, A. Weishaupt, and A. van Silfhout. Angle-resolved x-ray photo-electron spectroscopy (ARXPS) and a modified levenberg-marquardt fit procedure: a new combination for modeling thin layers. *Applied Surface Science*, 45(1):37–48, 1990.

[61] D. R. Tallant, J. E. Parmeter, M. P. Siegal, and R. L. Simpson. The thermal stability of diamond-like carbon. *Diamond and Related Materials*, 4(3):191–199, 1995.

[62] A. C. Ferrari and J. Robertson. Interpretation of raman spectra of disordered and amorphous carbon. *Physical Review B*, 61(20):14095–14107, 2000.

[63] W. A. Dollase. Reinvestigation of the structure of low cristobalite. *Zeitschrift für Kristallographie*, 121:369–377, 1965.

[64] D. R. Peacor. High-temperature single-crystal study of the cristobalite inversion. *Zeitschrift für Kristallographie*, 138:274–298, 1973.

[65] J. J. Pluth, J. V. Smith, and Jr. J. Faber. Crystal structure of low cristobalite at 10, 293, and 473 K: Variation of framework geometry with temperature. *Journal of Applied Physics*, 57(4):1045–1049, 1985.

[66] S. Dag and S. Ciraci. Atomic scale study of superlow friction between hydrogenated diamond surfaces. *Physical Review B*, 70(24):241401(R), 2004.

[67] H. Guo and Y. Qi. Environmental conditions to achieve low adhesion and low friction on diamond surfaces. *Modelling and Simulation in Materials Science and Engineering*, 18(3):034008, 2010.

[68] A. J. Moulson and J. P. Roberts. Entry of water into silica glass. *Nature*, 182(4629):200–201, 1958.

[69] S. M. Wiederhorn. Influence of water vapor on crack propagation in soda-lime glass. *J.Am.Ceram.Soc.*, 50(8):407–414, 1967.

[70] T. A. Michalske and S. W. Freiman. A molecular interpretation of stress corrosion in silica. *Nature*, 295(5849):511–512, 1982.

[71] S. Venkatesan and B. Bhushan. The sliding friction and wear behavior of single-crystal, polycrystalline and oxidized silicon. *Wear*, 171(1-2):25–32, 1994.

[72] Y. Matsuda, S. W. King, J. Bielefeld, J. Xu, and R. H. Dauskardt. Fracture properties of hydrogenated amorphous silicon carbide thin films. *Acta Materialia*, 60(2):682–691, 2012.

Chapter 5

Oxidation Induced Softening in Al Nanowires

Nanowires (NWs), have significant potential to be used in a broad range of new applications including flexible electronics, nano-electromechanical systems (NEMS), and nano devices [1–5]. Understanding the mechanical properties of NWs is important in order to improve the functionality and reliability of these devices. However, the elastic modulus of NWs, even though is one of their most fundamental mechanical property, has neither accurately reported nor consistently interpreted in the literature. Contrary to the general observation that "smaller is stronger," the Young's moduli (E) of NWs have been reported to increase [1, 6–9], or decrease [7, 9, 10], with the decreasing NW diameter or become less sensitive to it [7]. The reasons for these variations have been discussed in terms of surface stresses, atmospheric contamination, and the presence of the native oxide layers on the NW surfaces [1, 6–12].

Park et al. [12] reviewed recent studies on the size dependence of the E of NWs and indicated that one of the main discrepancies between the computational and experimental studies arose because the role of the native oxides that form on metal surfaces was neglected in the computational studies [6,12]. Limited experimental data suggests that the oxidation of tungsten NWs would increase its Young's modulus [7], whereas for silicon NWs an oxidation induced Young's modulus reduction was reported [7, 13, 14]. The effect of oxidation on the

155

mechanical properties should become more prominent for metallic NWs that have high affinity for oxygen such as Al, Mg, and Ti. For instance, Al can rapidly form an oxide layer even in ultra-high vacuum, i.e., at surface exposures to as low as 10^{-8} Torr sec O_2 [15, 16]. However, experimental determination of the E of the native oxide phase generated on the surface of metallic NW, separately from the overall or "composite" E of the NW, is extremely difficult. Molecular dynamics (MD) simulations have been widely used to simulate the deformation mechanisms of NWs, yet; so far these studies were limited to the pure metals for which empirical potentials are available [8, 17–20]. The current study demonstrates that the formation of a native oxide layer would lead to a reduction in the Young's modulus of the aluminum (Al) NWs.

MD simulations of the oxidation process of the Al-NW were carried out using a reactive force field (ReaxFF) method. The ReaxFF was implemented to capture the charge transfer during an oxidation reaction. Briefly, the ReaxFF [21,22] determines the atomic charge with the electron equilibration method [23], sets up the bond order based on atomic distances, and then computes bond, columbic, over coordination, and non-bond (van der Waals like) terms of the total energy. Previously reported ReaxFF Al/O configuration [24] was tailored for the Al-O system studied here and a pure Al structure as well as various Al_xO_y gas phases where the Al atoms assumed different oxidation states (including over-oxidized AlO_2 clusters) were considered and integrated with the ReaxFF nitramine description [25]. A ReaxFF force field input file, which can be used with the standalone ReaxFF program and LAMMPS [26], has been provided as supplementary material (ffield.reax) [27]. ReaxFF captures both the metallic and the partially ionic bonds for Al/Al_2O_3 interfaces, and also predicts the non-wetting to wetting transition of liquid Al on α-Al_2O_3 surface at high temperature [24]. All calculations were carried out using the LAMMPS code [26], and the atomic charges were updated at every MD time step of 0.5 fs. The model consisted of 10.2 nm-long [001] oriented Al-NWs with three different diagonal lengths (assumed as the diameter) of 3.2, 4.0, and 5.6 nm with an octagonal cross-section consisting of {100} and {110} crystallographic facets. For preparation for mechanical testing, a system consisting of Al-NW surrounded by oxygen molecules in a gaseous atmosphere was equilibrated until a stable oxide layer was formed on the surface [28]. The oxidized Al-NWs prepared in this

way were subjected to tensile deformation under a vacuum environment. All simulations were carried out at the homologous room temperature that corresponds to $0.3T_m$ for Al, where T_m is the melting temperature of Al estimated as 600 K for the pure bulk Al by ReaxFF.

As soon as the pure Al-NW was exposed to O_2, the oxidation process started instantaneously. The rate of the oxidation process was determined by computing the numbers of Al and O atoms inside the oxide phase as a function of the simulation time. Figure 5.1(a) shows the oxidation rate for the NW with a 4.0 nm initial diameter. Atomic charge values (Q) were used to distinguish between the atoms that participated in the oxidation reaction. Typical snapshots of the oxidation process are shown in Figure 5.1 as insets. Initially, both Al atoms in the NW and the O_2 molecules in the environment had neutral charges (0.0), as shown in Figure 5.1(b). The formation of an oxide shell around the metallic Al-NW that consisted of Al atoms with a charge of $\sim +1.5$ and O atoms with a charge of ~ -1.0 can be seen in Figures 5.1(c), 5.1(d) and 5.1(e) that show the stages of the oxidation process at 5, 25, and 50 ps MD time, respectively. The number of atoms in the oxide phase increased rapidly during the initial 25 ps and then started to slow down, i.e., the oxidation process followed the typical diffusion-limited passivation layer formation kinetics [29–31]. According to Figure 5.1(a), the oxygen uptake rate dropped from 9.2×10^3 g s^{-1} cm^{-2} at 5 ps to 3.0×10^1 g s^{-1} cm^{-2} at 50 ps. For MD times beyond 25 ps, the numbers of Al and O atoms showed little change until the end of the simulation at 50 ps as depicted in Figures 5.1(d) and 5.1(e), indicating that the oxide passivated the Al surface effectively and the effect of further oxidation was not significant on the oxide's structural and bonding properties. Although the calculated oxidation rate was much higher than the experimentally determined rates [12], the applied strain rate in MD simulations was higher too, so that the ratio of strain rate to the oxidation rate ($\sim 10^{5-7}$) was comparable to the ratio of experimental rates (which is also 10^{5-7}).

The average oxide thickness (t_{oxide}) was calculated as ~ 1.0 nm. The exact values of t_{oxide} are given in Table 5.1 for Al-NWs with different initial thicknesses. The oxide shell had a unique bond structure, density, and stoichiometry that did not depend significantly on the initial Al-NW diameter. Thus, the structures and the properties of the oxide that was formed
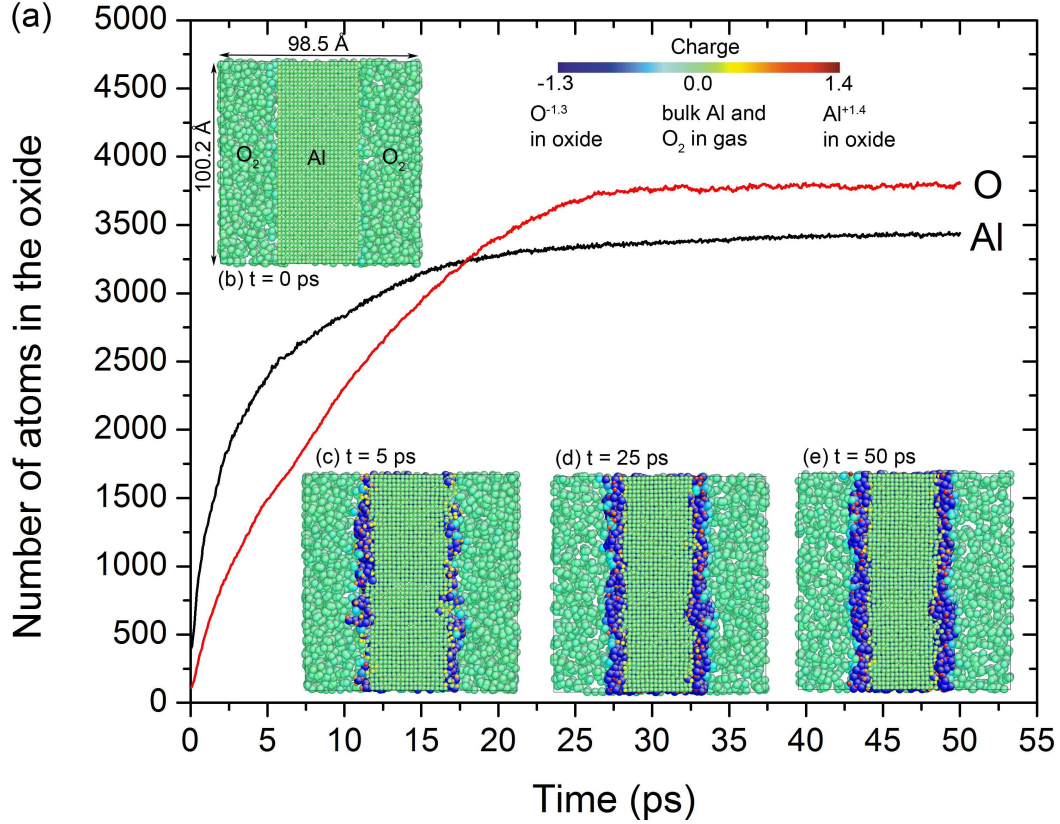
Figure 5.1: The variation of oxidation rate of Al-NW with MD time and the formation of a passive oxide layer at (a) $t = 0$ ps, (b) $t = 5$ ps, (c) $t = 25$ ps, and (d) $t = 50$ ps. The atoms are color coded according to their charges (Q) such that Al atoms with $Q > 0.1$ and O atoms with $Q < -0.1$ are considered to belong to the oxide film. The numbers of O and Al atoms in the oxide phase are determined as a function of time based on their atomic charges.

on the initially 4.0 nm thick Al-NW are the representative of all oxidized Al-NWs. The basic structural units of the oxide consisted of a mixture of [AlO$_4$] and [OAl$_4$] tetrahedra that were inter-connected either by corner-sharing (75%) or edge-sharing (25%). The oxide had a short range order and consisted of 3440 Al and 3805 O atoms forming the chemical formula of AlO$_{1.1}$. Oxygen-deficient structure of the amorphous oxides was previously reported for Al oxides formed on NiAl [32]. Based on the radial distribution function (RDF), $g(r)$ [33], the average Al-O bond length was estimated as $1.8 - 1.9$ Å. The Al-Al bond length was 3.2 Å and that of the O-O was 3.1 Å. On average, Al atoms were coordinated to 2.8 O atoms and O to 2.6 Al atoms, consistent with the O/Al ratio of 1.1. The atomic density of the oxidized NW was calculated on the radial sections starting from the NW's center. The

core of the NW consisting only of Al had a density of $\rho = 2.68$ g/cm^3. The AlO$_x$ density varied through the thickness with $\rho = 2.35$ g/cm^3 closer to Al/AlO$_x$ interface increasing to $\rho = 2.78$ g/cm^3 at the mid-section of the oxide shell then reducing again to $\rho = 2.35$ g/cm^3 near the outer surface. The average oxide density was similar to the experimental values of $2.70 - 2.80$ g/cm^3 for bulk amorphous oxides [34–36]. The Al-O bond structure compared well with the neutron diffraction data obtained for the amorphous oxide with a density of 2.8 g/cm^3 produced by anodic oxidation of Al foils [36, 37]. Overall, ReaxFF predicted the atomic structural changes that occurred during the Al oxidation process and the oxide's bond structure compared very well with the results of previous computational and experimental findings [31, 38].

The Al-NWs whose surfaces were covered with an oxide phase were then subjected to tensile deformation simulations at a strain rate of 0.05% ps^{-1} (5×10^8 s^{-1}). The tensile strain was applied along the [001] direction of the Al crystal at constant increments of 0.5% and at each strain increment the structure was allowed to relax for 10 ps using NVT ensemble. The stress generated during the deformation was calculated using Clausius virial theorem [33], which was corrected by the true volume of the NWs and the engineering stress-strain curves were obtained for each NW. Representative stress-strain curves of Al-NW with a diameter of 4.0 nm before (Al) and after oxidation (Al + AlO$_x$ shell) are shown in Figure 5.2(a). The figure also shows the stress-strain response of the oxide shell (AlO$_x$ shell) tested without Al-NW core. All three structures, (Al-NW), (AlO$_x$ shell), and (Al + AlO$_x$ shell) showed a linear stress-strain relationship up to 6% strain.

While the elastic deformation of Al crystals occurred by reversible stretching of the bonds, the amorphous oxide shell exhibited a viscoelastic deformation mechanism as observed in other amorphous oxides that undergo irreversible diffusional flow of the atoms [39, 40]. The stress-strain curves of both the Al-NW and the oxide covered NWs structures showed a linear increase up to the yield point (9% of strain), where dislocation nucleation occurred in Al crystal, and was immediately followed by a drop in the stress as a result of dislocation motion inside the NWs. The Young's moduli were calculated by a linear fitting of the stress-strain curves up to 5% strain as indicated in Figure 2(a) and the results are tabulated in Table 5.1. For the oxidized Al-NWs with 6.84, 5.07, and 4.22 nm diameters

($d_{Al+oxide}$), the computed $E_{Al+oxide}$ values were 46.62, 38.53, and 35.36 GPa, respectively. These values are at least 30% lower than the Young's modulus of the pure Al-NWs calculated in vacuum with initial diameters of 3.2, 4.0, and 5.6, which have E_{Al} values of 58.00, 61.19, and 64.14 GPa, respectively. The values in turn are in agreement with the experimentally determined values ($E_{Al} = 61 - 69$ GPa (Refs. [41] and [42])) for bulk Al single crystal samples. Therefore, the reduction of E in the oxidized Al-NWs was due to softening induced by the oxide shell. To compute the Young's modulus of the oxide shell separate from the Al-NW, the metallic Al atoms (with $Q < 0.1$) at the center of the NW were removed. It was found that the amorphous oxide shell had an unexpectedly low Young's modulus of 25.50 GPa.

Table 5.1: Young's modulus (E) data for Al-NWs with different diameters and oxide layers. The initial diameter of Al-NW before oxidation is (d_{Al}), the diameter of Al-NW with an oxide shell is ($d_{Al+oxide}$), and the thickness of the oxide is (t_{oxide}). The calculated values of the density of the oxide (ρ), O/Al atomic ratio (x) for the oxide, and Young's modulus of the oxide shell (E_{oxide}) are tabulated for three different d_{Al}.

System	d_{Al} (nm)	$d_{Al+oxide}$ (nm)	t_{oxide} (nm)	ρ (g/cm^3)	x	E (GPa)	E_{oxide} (GPa)
Al core + oxide shell	3.20	4.22	0.98	2.73	1.05	35.36	25.87
Al core + oxide shell	4.00	5.07	0.92	2.78	1.11	38.53	25.50
Al core + oxide shell	5.60	6.84	1.06	2.74	1.12	46.62	26.90
Al-NW	3.20	...	...	...	0.00	58.00	...
Al-NW	4.00	...	...	...	0.00	61.19	...
Al-NW	5.60	...	...	...	0.00	64.14	...
Al (100) (Exp.)	Bulk	...	...	...	...	61 [42]	...
Al polycrystalline (Exp.)	Bulk	...	...	...	...	69 [41]	...

The low Young's modulus of oxidized Al-NWs may appear counter-intuitive, considering that the crystalline $\alpha-Al_2O_3$ has much higher Young's modulus than that of the pure Al. Computations made using ReaxFF predicted the Young's modulus of bulk crystalline Al_2O_3 as 401 GPa (Ref. [24]), whereas the amorphous form of bulk Al_2O_3 (a-Al_2O_3) had a lower modulus in the range of $89.19 - 135.36$ GPa— both of which compared well with the experimental values of $366 - 410$ GPa (Ref. [43]) for the crystalline Al_2O_3 and $95 - 110$ GPa (Refs. [35, 44, 45]) for its amorphous counterpart. Accordingly, the factors that can result in the observed low Young's modulus of the oxidized Al-NWs were investigated in more detail. By comparing properties of amorphous-AlO_x (a-AlO_x) phase configured in

different geometrical shapes including bulk, wire, and shell type structures, it was revealed that the stoichiometry (i.e., O/Al atomic ratios, x), bond structure, and density (ρ) of the oxide phase all contributed to the unexpectedly low E of the native oxide shell. In addition, the fast surface diffusion during deformation at the nano-scale also contributed to the same. These amorphous structures were generated by quenching (rather than by oxidation) an a-AlO$_x$ melt from 5000 K to 200 K to obtain 5.0 nm in diameter solid oxides with different densities and shapes. The calculated Young's moduli of resulting a-AlO$_x$ structures are listed in Table 5.2 that shows that $E_{AlO_{1.5}}$ = 268.28 GPa of the bulk oxide structure was higher than $E_{AlO_{1.5}}$ = 114.28 GPa for the wire structure both with the same ρ = 4 : 0 g/cm^3. This observation suggests that a large surface to volume ratio in NWs facilitates the deformation of the nano-sized amorphous oxides. For a shell with the same size, but with two free surfaces, a slightly lower E_{AlO_x} was observed for all x and ρ values considered. When the density of the a-AlO$_{1.5}$ shell was reduced from 4.0 to 2.8 g/cm^3, the $E_{AlO_{1.5}}$ decreased from 103.21 to 81.36 GPa. At the same density of 2.8 g/cm^3, the reduction of the O/Al ratio from 1.5 to 1.1, further decreased the Young's modulus to 57.50 GPa. The $E_{AlO_{1.1}}$ (57.50 GPa) estimated for the shell (with ρ = 2.8 g/cm^3) was still higher than the E of the native oxide shell (25.50 GPa) formed during the oxidation process, because in a-AlO$_{1.1}$ shell both Al-O had higher coordination (each Al was coordinated to 3.8 O and each O to 3.5 Al) compared the Al-O coordination in the native oxide shell for which the coordination numbers were 2.8 and 2.6, respectively. The Young's modulus for the native oxide of Al (or a very thin a-Al$_2$O$_3$ with a thickness of 1 nm) has not been reported in the literature due to experimental limitations at this scale. In a recent study [46], micro-pillar compression experiments conducted on anodic aluminum oxide reported a low Young's modulus of $31 - 46$ GPa, which is within the same range as the computed values in this work.

The lower Young's modulus of the oxide on Al-NW compared to those observed for the bulk structures infers a size dependence of the oxidized Al-NWs ($E_{Al+oxide}$) to the initial Al diameter (d_{Al}). The value of $E_{Al+oxide}$ can be estimated using the rule of mixtures (RoM) such that a "composite" modulus can be obtained similar to composites with a core-shell structure subjected to a tensile deformation under plane strain condition. The Al-NW can
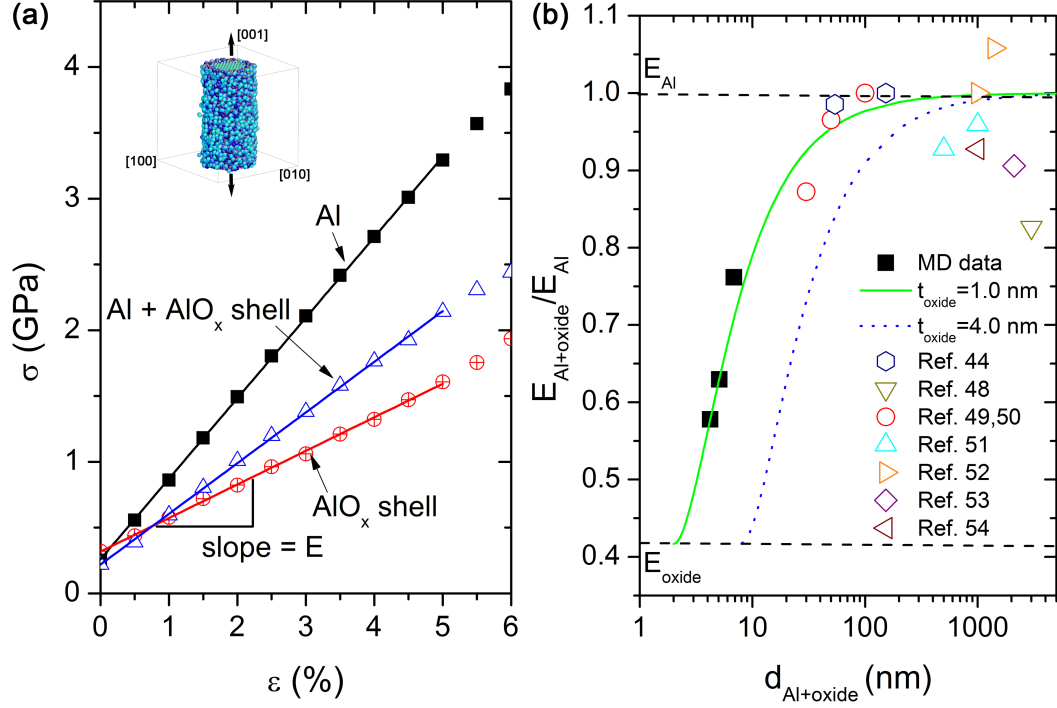
Figure 5.2: (a) Engineering stress-strain ($\sigma - \varepsilon$) response of pure Al-NW with a diameter of 4.0 nm, the oxidized Al-NW (Al + AlO$_x$ shell) and AlO$_x$ shell which was tested without the Al-NW core. The inset shows the Al + AlO$_x$ shell along the [001] of a NW deformed in vacuum. The initial $0\% - 5\%$ strain region was fitted to a straight line ($R^2 > 0.9995$) and the Young's modulus of each structure was calculated from the slope of the straight line. (b) Size dependence of the Young's modulus of oxidized Al-NW. Solid symbols are from MD simulations (Table 5.1) and open symbols are from experimental data reported in the literature. The curves were computed assuming that the oxide layer thickness was either 1.0 nm or 4.0 nm. The diameter of NWs and thickness of thin films represent the sizes of the structures in Refs. [44, 47–53].

be assumed to have a cylindrical shape with $r_{Al+oxide}$ being the radius of the oxidized Al-NW, r_{Al} the radius of the Al core and with a shell thickness of t_{oxide}. Thus, according to RoM

$$E_{Al+oxide} = E_{Al}\left(\frac{r_{Al}}{r_{Al+oxide}}\right)^2 + E_{oxide}\left[1 - \left(\frac{r_{Al}}{r_{Al+oxide}}\right)^2\right] \qquad (5.1)$$

As $r_{Al} = r_{Al+oxide} - t_{oxide}$ and $r_{Al+oxide} = \frac{d_{Al+oxide}}{2}$, then Eq. 5.1 can be re-written as

$$E_{Al+oxide} = E_{Al}\left[1 - \frac{2t_{oxide}}{d_{Al+oxide}}\right]^2 + E_{oxide}\left[1 - \left(1 - \frac{2t_{oxide}}{d_{Al+oxide}}\right)^2\right] \qquad (5.2)$$

The normalized values for $E_{Al+oxide}$ with respect to the computed Young's modulus of

162

Table 5.2: Young's modulus (E) data of 5.0 nm diameter amorphous aluminum oxides (a-AlO_x) with different shapes, O/Al atomic ratio (x), and density (ρ), computed from the tensile deformation in vacuum conditions. The properties of bulk structures were computed using the periodic boundary conditions. The shell structures had an outer diameter of 5.0 nm with a thickness of 1.0 nm (i.e., inner diameter of 3.0 nm). The data from earlier experimental and ReaxFF studies on bulk aluminum oxides are also listed.

Oxide systems	Shape	ρ (g/cm^3)	E (GPa)
a-$AlO_{1.1}$ native	Shell	2.78	25.50
a-$AlO_{1.5}$	Bulk	4.00	268.28
a-$AlO_{1.5}$	Wire	4.00	114.28
a-$AlO_{1.5}$	Shell	4.00	103.21
a-$AlO_{1.5}$	Bulk	2.80	135.36
a-$AlO_{1.5}$	Wire	2.80	83.45
a-$AlO_{1.5}$	Shell	2.80	81.36
a-$AlO_{1.1}$	Bulk	2.80	89.19
a-$AlO_{1.1}$	Wire	2.80	57.71
a-$AlO_{1.1}$	Shell	2.80	57.50
$\alpha-Al_2O_3$ (ReaxFF)	Bulk	3.95	401
$\alpha-Al_2O_3$ (Exp.)	Bulk	3.95	$366 - 410$
a-Al_2O_3 (Exp.)	Bulk	$2.20 - 3.30$	$95 - 110$

pure Al-NW ($E_0 = 61.19$ GPa) are plotted in Figure 5.2(b) as a function of the size of the oxidized Al-NW, $d_{Al+oxide}$. The two t_{oxide} values of 1.0 and 4.0 nm represent the lowest and the highest possible oxide thicknesses that can form on Al surfaces [31,38,54]. Figure 5.2(b) indicates that the normalized $E_{Al+oxide}$ values listed in Table 5.1 matched well with those predicted by Eq. 5.2 for $t_{oxide} = 1.0$ nm and $E_{oxide} = 25.50$ GPa. According to Figure 5.2(b) for both $t_{oxide} = 1.0$ and 4.0 nm, E increased linearly with $d_{Al+oxide}$ for small diameters. For larger $d_{Al+oxide}$ values the increase was less and eventually $E_{Al+oxide}$ values converged to E_{Al}. Considering $t_{oxide} = 1.0$, the linear increase of $E_{Al+oxide}$ occurred for $d_{Al+oxide} \leq 10$ nm, and for $d_{Al+oxide} > 100$ nm it was noted that $E_{Al+oxide} \approx E_{Al}$. In summary, for Al-NWs with diameters less than 100 nm, a decrease in the Young's modulus of up to 50% can be expected due to the effect of native oxide covering their surface. The amount of the decrease depended on the oxide thickness on the NWs. For $t_{oxide}/d_{Al+oxide} > 0.05$, the Young's modulus decreased linearly with decreasing $d_{Al+oxide}$.

The dependence of $E_{Al+oxide}$ to the Al-NW size found in this study can also serve to explain several discrepancies in the Young's moduli observed for nano-sized Al films and pillars. In these experiments, the Al-NWs should have inevitably a native oxide, and hence

the reported modulus values can be considered equivalent to $E_{Al+oxide}$. The experimentally measured Young's moduli of Al thin films [44,47–53] are plotted in Figure 5.2(b) after normalizing them with respect to experimentally measured $E_{Al} = 69$ GPa. In four independent experiments [44,48–51], $E_{Al+oxide}$ were reported to decrease with decreasing Al film thickness (t_{Al}) and the decrease in $E_{Al+oxide}$ was significant for $t_{Al} < 100$ nm [48,49,55]. For $t_{Al} > 100$ nm, the reported $E_{Al+oxide}$ were within 5% of the bulk Young's modulus of Al [44,50,51,53]. For $2 - 3$ μm thick Al films produced by evaporation [52], a slightly lower Young's modulus of $57.0 - 62.5$ GPa was reported. Nano-sized Al films were reported to have a very low Young's modulus between 25 and 40 GPa [45,56,57]. The reported variations can be due to the microstructural changes during the thin film production. Alternative explanations to the observation of low modulus of nano-sized Al thin films were suggested in literature. For example, it was suggested that [58] if the surface waviness of the oxide was within the same range as the oxide thickness, the Young's modulus of the Al-oxide film could be lower than bulk Al. The results of the current investigation revealed that if the native oxide on the Al surface had a very low Young's modulus, due to its amorphous structure, then a reduction in the Young's modulus of nano-sized Al should be expected. The low Young's modulus of the oxide can be attributed to the low Al-O coordination in the amorphous structure and also the low density of the oxide. In previous experimental and computational studies, reviewed by Park et al. [12], the lower atomic coordination at the interfaces and free surfaces of NWs were shown to reduce the Young's modulus of NWs. According to the current observations, the density of the native oxide near the Al/AlO_x interface (and at the outer surface) was lower than the mid-section of the oxide layer. This implies a lower Al-O coordination at the Al/AlO_x interface and the outer oxide surface that would result to a reduction in the Young's modulus.

In summary, an oxidation-induced reduction of the Young's modulus of Al-NWs was demonstrated. The Al-NWs with diameters of $3.20 - 5.60$ nm were found to form a 1.0 nm thick amorphous surface oxide film with a Young's modulus of as low as 25.50 GPa. The oxide film had an oxygen-deficient structure with a low Al-O coordination, which was the possible cause for the oxide film to be much softer than the pure Al-NW. The "composite" Young's modulus of the oxidized Al-NWs decreased with decreasing the initial Al-NW di-

ameter. The oxidation induced softening effect vanished for Al structures whose thicknesses exceeded 100 nm.

Bibliography

[1] M. D. Uchic, D. M. Dimiduk, J. N. Florando, and W. D. Nix. Sample dimensions influence strength and crystal plasticity. *Science*, 305(5686):986–989, 2004.

[2] Y. Kondo and K. Takayanagi. Gold nanobridge stabilized by surface structure. *Physical Review Letters*, 79(18):3455–3458, 1997.

[3] Y. Kondo and K. Takayanagi. Synthesis and characterization of helical multi-shell gold nanowires. *Science*, 289(5479):606–608, 2000.

[4] Z. L. Wang and J. Song. Piezoelectric nanogenerators based on zinc oxide nanowire arrays. *Science*, 312(5771):242–246, 2006.

[5] X. Wang, J. Song, J. Liu, and L. W. Zhong. Direct-current nanogenerator driven by ultrasonic waves. *Science*, 316(5821):102–105, 2007.

[6] M. T. McDowell, A. M. Leach, and K. Gall. On the elastic modulus of metallic nanowires. *Nano Letters*, 8(11):3613–3618, 2008.

[7] C. C Röhlig, M. Niebelschütz, K. Brueckner, K. Tonisch, O. Ambacher, and V. Cimalla. Elastic properties of nanowires. *Physica Status Solidi B*, 247(10):2557–2570, 2010.

[8] J. Diao, K. Gall, and M. L. Dunn. Atomistic simulation of the structure and elastic properties of gold nanowires. *Journal of the Mechanics and Physics of Solids*, 52(9):1935–1962, 2004.

[9] H. Liang, M. Upmanyu, and H. Huang. Size-dependent elasticity of nanowires: Nonlinear effects. *Physical Review B*, 71(24):241403(R), 2005.

[10] G. Y. Jing, H. L. Duan, X. M. Sun, Z. S. Zhang, J. Xu, Y. D. Li, J. X. Wang, and D. P. Yu. Surface effects on elastic properties of silver nanowires: Contact atomic-force microscopy. *Physical Review B*, 73(23):235409, 2006.

[11] R. E. Miller and V. B. Shenoy. Size-dependent elastic properties of nanosized structural elements. *Nanotechnology*, 11(3):139–147, 2000.

[12] Harold S Park, Wei Cai, Horacio D Espinosa, and Hanchen Huang. Mechanics of crystalline nanowires. *MRS Bulletin*, 34(03):178–183, 2009.

[13] Z. L. Wang, Z. R. Dai, R. P. Gao, Z. G. Bai, and J. L. Gole. Side-by-side silicon carbide-silica biaxial nanowires: Synthesis, structure, and mechanical properties. *Applied Physics Letters*, 77(21):3349–3351, 2000.

[14] M. J. Gordon, T. Baron, F. Dhalluin, P. Gentile, and P. Ferret. Size effects in mechanical deformation and fracture of cantilevered silicon nanowires. *Nano Letters*, 9(2):525–529, 2009.

[15] R. Z. Bachrach, S. A. Flodstrom, R. S. Bauer, S. B. M. Hastrom, and D. J. Chadi. Surface resonances and the oxidation of single-crystal aluminum. *Journal of Vacuum Science and Technology*, 15(2):488–493, 1978.

[16] A. Bianconi, R. Z. Bachrach, and S. A. Flodström. Oxygen chemisorption on Al: Unoccupied extrinsic surface resonances and site-structure determination by surface soft-x-ray absorption. *Physical Review B*, 19(8):3879–3888, 1979.

[17] J. Diao, K. Gall, and M. L. Dunn. Surface-stress-induced phase transformation in metal nanowires. *Nature Materials*, 2(10):656–660, 2003.

[18] H. Ikeda, Y. Qi, T. Çagin, K. Samwer, W. L. Johnson, and III W. A. Goddard. Strain rate induced amorphization in metallic nanowires. *Physical Review Letters*, 82(14):2900–2903, 1999.

[19] H. S. Park, K. Gall, and J. A. Zimmerman. Deformation of FCC nanowires by twinning and slip. *Journal of the Mechanics and Physics of Solids*, 54(9):1862–1881, 2006.

[20] E. Z. Da Silva, A. J. R. Da Silva, and A. Fazzio. How do gold nanowires break? *Physical Review Letters*, 87(25):256102/1–256102/4, 2001.

[21] A. C. T. Van Duin, S. Dasgupta, F. Lorant, and III W. A. Goddard. Reaxff: A reactive force field for hydrocarbons. *Journal of Physical Chemistry A*, 105(41):9396–9409, 2001.

[22] K. Chenoweth, A. C. T. Van Duin, and III W. A. Goddard. Reaxff reactive force field for molecular dynamics simulations of hydrocarbon oxidation. *Journal of Physical Chemistry A*, 112(5):1040–1053, 2008.

[23] W. J. Mortier, S. K. Ghosh, and S. Shankar. Electronegativity equalization method for the calculation of atomic charges in molecules. *Journal of the American Chemical Society*, 108(15):4315–4320, 1986.

[24] Qing Zhang, T. Cagin, A. van Duin, W. A. Goddard, Yue Qi, and L. G. Hector. Adhesion and nonwetting-wetting transition in the Al/α-Al$_2$O$_3$ interface. *Physical Review B*, 69(4):045423, 01/15 2004.

[25] Alejandro Strachan, Edward M. Kober, Adri C.T. van Duin, Jonas Oxgaard, and William A. Goddard III. Thermal decomposition of RDX from reactive molecular dynamics. *The Journal of Chemical Physics*, 122:054502, 2005.

[26] S. Plimpton. Fast parallel algorithms for short-range molecular dynamics. *Journal of Computational Physics*, 117(1):1–19, 1995.

[27] F.G. Sen, Y. Qi, A.C.T. van Duin, and A.T. Alpas. Oxidation induced softening in Al nanowires. *Applied Physics Letters*, 102:051912, 2013.

[28] *The oxidation process was simulated in a reasonable MD time with the use of a high O_2 pressure, considering that the use of a high O_2 pressure was not expected to alter the final oxide properties based on Al oxidation experiments. When the pure Al-NWs were exposed to O_2 gas at 188 atm (with 4×10^3 O_2 molecules in the $\tilde{1}0 \times 10 \times 10$ nm^3 simulation cell), the oxidation process started instantaneously at 200 K. For the 3.2 nm diameter NW, the oxidation simulation was carried out for 150 ps to reach a passive*

oxide layer, but shorter MD simulation time of 50 *ps was sufficient to form a passive*
oxide layer for NWs with diameters> 4.0 *nm.*

[29] E. A. Gulbransen and W. S. Wysong. Thin oxide films on aluminum. *Journal of Physical Chemistry*, 51(5):1087–1103, 1947.

[30] Wm H. Krueger and S. R. Pollack. The initial oxidation of aluminum thin films at room temperature. *Surface Science*, 30(2):263–279, 1972.

[31] C. E. Aumann, G. L. Skofronick, and J. A. Martin. Oxidation behavior of aluminum nanopowders. *Journal of Vacuum Science and Technology B: Microelectronics and Nanometer Structures*, 13(3):1178–1183, 24 October 1994 through 28 October 1994 1995.

[32] G. Kresse, M. Schmid, E. Napetschnig, M. Shishkin, L. Köhler, and P. Varga. Structure of the ultrathin aluminum oxide film on NiAl(110). *Science*, 308(5727):1440–1442, 2005.

[33] M. P. Allen and L. J. Tildesley. *Computer Simulation of Liquids*. Oxford University Press, New York, 1987.

[34] C. Landron, L. Hennet, T. E. Jenkins, G. N. Greaves, J. P. Coutures, and A. K. Soper. Liquid alumina: Detailed atomic coordination determined from neutron diffraction data using empirical potential structure refinement. *Physical Review Letters*, 86(21):4839–4842, 2001.

[35] B. S. Berry and W. C. Pritchet. Elasticity and density of amorphous aluminum oxide. *Journal of Non-Crystalline Solids*, 18(2):285–288, 1975.

[36] R. Kniep, P. Lamparter, and S. Steeb. Structure of anodic oxide coatings on aluminum. *Angew. Chem. Adv. Mater.*, 101:975–977, 1989.

[37] P. Lamparter and R. Kniep. Structure of amorphous Al2O3. *Physica B*, 234-236:405–406, 1997.

[38] M. A. Trunov, S. M. Umbrajkar, M. Schoenitz, J. T. Mang, and E. L. Dreizin. Oxidation and melting of aluminum nanopowders. *Journal of Physical Chemistry B*, 110(26):13094–13099, 2006.

[39] C Gauthier, J-M Pelletier, Q Wang, and JJ Blandin. Viscoelastic and viscoplastic properties of bulk metallic glasses: Comparison with oxide glasses and amorphous polymers. *Journal of Non-Crystalline Solids*, 345:469–472, 2004.

[40] Christopher A Schuh, Todd C Hufnagel, and Upadrasta Ramamurty. Mechanical behavior of amorphous alloys. *Acta Materialia*, 55(12):4067–4109, 2007.

[41] W. F. Gale and T. C. Totemeier. *Smithells Metals Reference Book*. Elsevier Butterworth-Heinemann, Burlington, U.S.A., 8th edition, 2004.

[42] G. N. Kamm and G. A. Alers. Low-temperature elastic moduli of aluminum. *Journal of Applied Physics*, 35(2):327–330, 1964.

[43] W. Martienssen and H. Warlimont. *Springer Handbook of Condensed Matter and Materials Data*. Springer Handbook of Condensed Matter and Materials Data. Springer, Berlin Heidelberg, 2005.

[44] G. T. Mearini and R. W. Hoffman. Tensile properties of aluminum/alumina multi-layered thin films. *Journal of Electronic Materials*, 22(6):623–629, 1993.

[45] R. W. Hoffman. Nanomechanics of thin films: Emphasis: Tensile properties. *Mater. Res. Soc. Symp. Proc.*, 130:295–306, 1989.

[46] K. Y. Ng, Y. Lin, and A. H. W. Ngan. Compression of micron-sized pillars of anodic aluminium oxide nano-honeycomb. *Journal of the Mechanics and Physics of Solids*, 59(2):251–264, 2011.

[47] H. Huang and F. Spaepen. Tensile testing of free-standing Cu, Ag and Al thin films and Ag/Cu multilayers. *Acta Materialia*, 48(12):3261–3269, 2000.

[48] M. A. Haque and M. T. A Saif. Mechanical behavior of $30 - 50$ nm thick aluminum films under uniaxial tension. *Scripta Materialia*, 47(12):863–867, 2002.

[49] M. A. Haque and M. T. A. Saif. Application of MEMS force sensors for in situ mechanical characterization of nano-scale thin films in SEM and TEM. *Sensors and Actuators, A: Physical*, 97-98:239–245, 10 June 2001 through 14 June 2001 2002.

[50] Y. C. Cheng, C. J. Tong, and M. T. Lin. Measurement of static and dynamic mechanical behavior of micro and nano-scale thin metal films: Using micro-cantilever beam deflection. *Microsystem Technologies*, 17(4):721–730, 2011.

[51] A. Reddy, H. Kahn, and A. H. Heuer. A MEMS-based evaluation of the mechanical properties of metallic thin films. *Journal of Microelectromechanical Systems*, 16(3):650–658, 2007.

[52] J. Gaspar, M. E. Schmidt, J. Held, and O. Paul. Wafer-scale microtensile testing of thin films. *Journal of Microelectromechanical Systems*, 18(5):1062–1076, 2009.

[53] C. T. Rosenmayer, F. R. Brotzen, and J. Gale. Mechanical testing of thin films. *Mater. Res. Soc. Symp. Proc.*, 130:77–86, 1989.

[54] T. J. Campbell, G. Aral, S. Ogata, R. K. Kalia, A. Nakano, and P. Vashishta. Oxidation of aluminum nanoclusters. *Physical Review B*, 71(20):205413, 2005.

[55] C.H. Hamilton and A.K. Ghosh, editors. *Metals Handbook Volume 14*. ASM International, Metals Park, Ohio, 1988.

[56] D. Heinen, H. G. Bohn, and W. Schilling. On the mechanical strength of free-standing and substrate-bonded Al thin films. *Journal of Applied Physics*, 77(8):3742–3745, 1995.

[57] D. T. Read, Y. W. Cheng, R. R. Keller, and J. D. McColskey. Tensile properties of free-standing aluminum thin films. *Scripta Materialia*, 45(5):583–589, 2001.

[58] M. T. A. Saif, S. Zhang, A. Haque, and K. J. Hsia. Effect of native Al_2O_3 on the elastic response of nanoscale al films. *Acta Materialia*, 50(11):2779–2786, 2002.

Chapter 6

Plastic Deformation of Aluminum in O$_2$ Environment

The chemical environment is known to affect the mechanical properties that depend on the surface structure of materials, but its effect on bulk mechanical properties of materials, such as the elastic modulus, strength and plasticity, is generally disregarded. Yet, at the nano-scale, the chemical environment can drastically alter the mechanical properties of materials due to the increase in the surface-to-volume ratio. The emergence of nanowires [1–4] as potential elements in electronic, optic and nano-electromechanical devices due to their exciting properties created a pronounced interest in the nano-mechanical properties materials, however, their performance in different environments even in an oxidizing environment that present in ambient air is still unknown. The understanding of mechanics of nanowires is not only important for small devices, but also in mechanical processing of bulk materials, especially metals that are affine to oxygen such as Al, oxidation can result in the formation of nanowires that can have a profound effect on surface properties. For instance, Al forms a $4 - 5$ nm thick amorphous oxide film on its surface even at high vacuum conditions [5, 6] and in hot forming processes that are used to manufacture automotive parts at relatively high temperatures (> 400 °C), surprisingly, this oxide elongated superplastically to form nanowires on Al surface as a result of dynamic oxidation [7–10]. In these processes Al sheet is usually pressed against steel tool surfaces as demonstrated in Figure 6.1(a), but the sur-

172
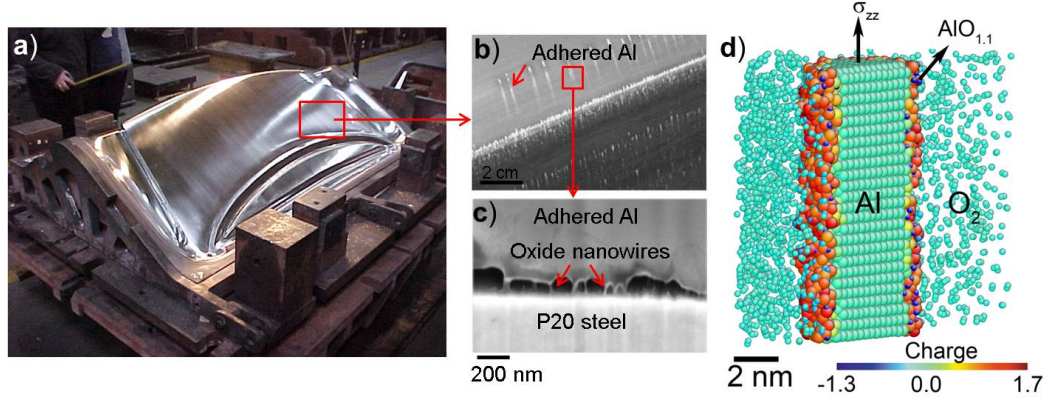
Figure 6.1: Nanowire formation in bulk aluminum forming processes. a) The outer surface of a die made of P20 steel used to produce a trunk of a car. b) Secondary electron image of adhered Al particles on the die surface after forming about 300 parts. c) Higher magnification microstructure of the focused-ion beam (FIB) cross-section of the interface formed between the steel tool surface and the adhered aluminum. d) The (100) cross-section of the nanowire model used to simulate deformation and oxidation of aluminum at the nano-scale. Aluminum nanowires were placed in an oxygen environment until a 1 nm thick amorphous oxide ($AlO_{1.1}$) formed on the nanowire surface. During oxidation process electronic charge transferred from Al to O atoms that resulted in positively charged $Al^{+1.5}$ and $O^{-1.0}$ ions in the oxide layer and as a result, core-shell nanowire structure with metallic Al core and oxide shell was obtained. Subsequently, oxidized aluminum nanowires were subjected to tensile deformation in O_2 atmosphere in the [001] direction.

face quality suffers due to the Al build up on the tool surface (Figure 6.1(b)) due to adhesive interactions at the Al/tool steel interface [11]. The cross-sectional analysis of the adhered Al pieces on tool surface indicated formation of stretched nanowires at the Al/tool steel interface as shown in Figure 6.1(c), which were identified to be Al,Mg oxide nanowires using transmission electron microscopy (TEM) [8]. The superplastic oxide nanowires increased the amount of Al adhesion to tool surfaces and were detrimental to efficiency of forming process. Therefore, understanding the effect of oxidation on the Al deformation is not only important at the nano-scale but also essential to control the surfaces of materials in bulk forming applications affecting product quality and productivity at large industrial scales (at the macro-scale).

The mechanical behaviour of a material under an applied load can be extremely different at the nano-scale compared to its bulk counterpart in such a way that at the nano-scale, either "*smaller is stronger*" [4, 12–16] or "*smaller is superplastic*" [17–19] or "*smaller is softer*" [20] behaviour can be observed. For instance, most bulk metals are known to deform

plastically with the motion of mobile dislocations, which require relatively small Peierls-Nabarro forces so that bulk metals generally yield at stresses in the order of megapascals (alloys $50 - 500$ MPa). At nano-scale, in-situ transmission electron microscopy (TEM) experiments [21, 22] and molecular dynamics (MD) studies [23–27] showed that plasticity is controlled by the nucleation and escape of dislocations from the free surfaces that require much higher stresses. In contrast, bulk amorphous solids are known to deform by the viscoplastic mechanism, which provides very limited plasticity in ambient temperature conditions. However, at the nano-scale these materials became superplastic when elongated and even formed atomic thick chains at the fracture surface due to the fast surface diffusion [17, 18]. These fore-mentioned studies aimed to reveal the nano-scale deformation mechanisms only focused on pure materials and generally disregarded the effect of oxidation, which can significantly alter the surface structure of the material, hence the nano-scale deformation mechanisms.

The study of oxidation and deformation, simultaneously at the nano-scale is still a big challenge due to the experimental limitations. Atomistic simulations based on MD served to explain many nano-scale mechanical properties of pure metals; however, the inclusion of oxidation necessitates modeling the charge transfer between oxide atoms in addition to correct prediction of interactions between metallic atoms. Here, we report the first study that considers the effect of surface oxidation on the deformation characteristics of an aluminum single crystal nanowire using MD with a reactive force field (ReaxFF) [28–30]. We first oxidized an Al nanowire (see Ref. [20]) and subsequently, an amorphous oxide film was formed on its surface which resulted in a core-shell structure consisting of Al core and oxide shell as shown in Figure 6.1(d). The oxidized Al nanowire was then subjected to tensile elongation in an oxygen and vacuum environment at three different strain rates, namely 0.05% ps^{-1} (5×10^8 s^{-1}), 0.5% ps^{-1} (5×10^9 s^{-1}) and 5.0% ps^{-1} (5×10^{10} s^{-1}). The significant changes in the deformation mechanisms of Al core and the covering amorphous oxide shell in O_2 environment were reported separately.

The stress-strain diagrams obtained at the lowest strain rate of 0.05% ps^{-1} as shown in Figure 6.2(a) indicates that O_2 atmosphere drastically increased the ductility of Al nanowires. For the pure Al nanowire, when the applied strain exceeded the elastic limit

($\varepsilon_y = 0.090$) in vacuum, a sudden drop in the stress was observed which followed a little plastic deformation ($\varepsilon = 0.100 - 0.120$) and finally Al fractured in a quasi-brittle characteristic at $\varepsilon = 0.120$, with a clean fracture plane and no indication of necking as shown in Figure 6.2(b). The behaviour shown here is similar to the previous MD studies for deformation of Al nanowires [23, 31]. The presence of a ≈ 1 nm thick amorphous oxide layer on the Al surface lowered the elastic limit of Al to $\varepsilon_y = 0.065$ and increased the plasticity of the nanowire in both vacuum and O_2 (Figure 6.2(a)). In vacuum, the atomic structure given in Figure 6.2(c), shows that the nano-sized amorphous oxide layer interestingly exhibited a higher plasticity than Al and its bulk counterparts and formed atomic thick Al-O chains at the fracture surface. In O_2, the stress-strain curve (Figure 6.2(a)) did not show any significant indication of drop in the stress with the applied strain for the maximum strain of 0.800. The atomic structure of this nanowire given in Figure 6.2(d) shows that the Al in the core of the nanowire fractured at a higher $\varepsilon = 0.260$, but the amorphous oxide shell could sustain very high strain values without showing any sign of necking or fracture up to a strain of 0.600 as exhibiting a superplastic deformation behaviour.

Figure 6.2(a) shows that the strain rate did not have a significant effect on the plasticity of pure and oxidized Al nanowires, when deformed in vacuum. However, the superplasticity of the amorphous oxide in O_2 decreased with the increasing strain rate and at the highest strain rate of 5.0% ps^{-1}, the stress-strain behavior in O_2 was same as the stress-strain response in vacuum. Therefore, as superplasticity observed in the amorphous oxide was strain rate dependent, the oxidation rate needed to be comparable to the deformation rate to maintain the superplastic behavior. Consequently, O_2 supply enhanced the plasticity of both the metallic Al and the amorphous oxide, and the different mechanisms contributed to the increased ductility is presented in the following sections.

The deformation mechanisms of Al were investigated in detail by considering the stacking faults in the crystal using centro-symmetry parameter (CSP) [32, 33]. Figure 6.3(a) shows that when pure Al was elongated in vacuum, the yielding occurred by the nucleation of Shockley partial dislocations from the energetically favourable [34] edges on the surface, namely at the intersection of (100) and (110) facets indicated at the nanowire surface, which caused a large drop in the stress in Figure 6.2(a). The two partial dislocations propagated
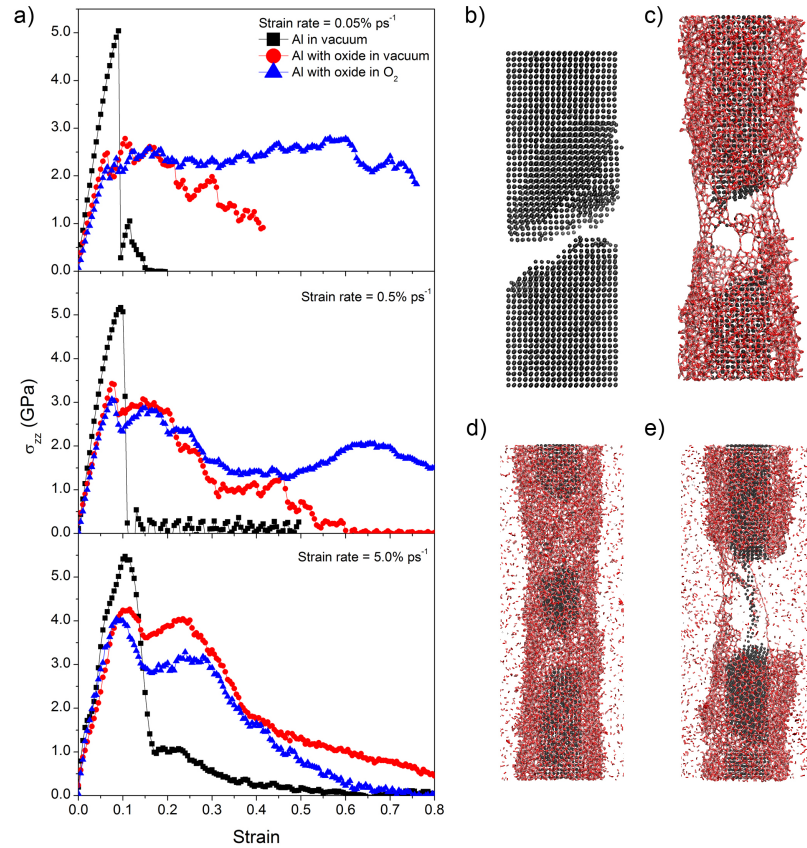
Figure 6.2: Deformation of aluminum nanowires in O_2 and vacuum environments at different strain rates. a) The comparison between the stress-strain diagrams of pure aluminum deformed in vacuum, oxidized aluminum deformed in vacuum and oxidized aluminum deformed O_2 environments at different strain rates. b) The atomic structure of the pure aluminum nanowire deformed in vacuum at the strain rate of 0.05% ps^{-1}. The snapshot taken at the strain of $\varepsilon = 0.20$ showing the brittle fracture of aluminum. c) The atomic structure of the oxidized aluminum nanowire deformed in vacuum at the strain rate of 0.05% ps^{-1}. The snapshot was taken at $\varepsilon = 0.40$, showing the fractured aluminum in the core and plastically deformed oxide at the surface that formed atomic thick Al-O-Al-O chains at the fracture surface. d) The atomic structure of the oxidized aluminum nanowire deformed in O_2 at the strain rate of 0.05% ps^{-1}. The snapshot taken at $\varepsilon = 0.60$ showing that aluminum core region was fractured, and the oxide deformed superplastically without indication of a fracture. e) The atomic structure of the oxidized aluminum nanowire deformed in O_2 at the strain rate of 5.0% ps^{-1}. The snapshot taken at $\varepsilon = 0.80$ showing that the deformation characteristics in O_2 was similar to the (c) when strain rate was increased.

in $\{111\} \langle 11\bar{2} \rangle$ slip systems, traveled through the crystal and exited from the opposite side of the nanowire surface leaving a stacking fault inside the nanowire as shown in Figure 6.3(a). The Al crystal fractured before nucleation of new dislocations, and the necking of Al immediately occurred along with the formation of a stacking fault.

When Al nanowire with an oxide layer on its surface was deformed in vacuum, –in contrast to pure Al– the yielding of the Al initiated by the nucleation of Shockley partial dislocations from the Al/AlO_x interface as shown in Figure 6.3(b). Due to the amorphous nature of the oxide, the Al/AlO_x interface provided defect sites, which facilitated dislocation nucleation so that Al had a lower yield point and showed enhanced plasticity, in comparison to pure Al nanowire, but the strain at the fracture was similar to pure Al. A significant enhancement in the plasticity was observed when Al with oxide deformed in the O_2 environment. Although, the yield strain was same ($\varepsilon_y = 0.065$) and the yielding initiated by the nucleation of Shockley partial dislocations from the Al/AlOx interface, upon increasing strain, stacking faults formed not only one but at two distinct regions within the nanowire (Figure 6.3(c)). Moreover, a drastic increase in the number of dislocation nucleation and escape events in O_2 atmosphere was observed as shown by the increased number of stacking faults in the Al at $\varepsilon = 0.160$ in Figure 6.3(d). As the dislocation activity increased considerably, a much higher number of dislocation-dislocation interactions took place inside the Al crystal. Figure 6.3(d) shows that at two different regions, two stacking faults met at an angle of 70.5^o and each formed Lomer-Cottrell locks. Lomer-Cottrell obstacle formation observed here was reported in the previous MD studies of nanocrystalline Al deformation [35].

As shown in Figure 6.3 the strength is controlled by the ease of dislocation nucleation occurred in pure Al free surface, but at the interfaces in pure Al with the oxide shell. The stress required for dislocation nucleation under constant temperature (T) and strain rate ($\dot{\varepsilon}$) is given as [34]

$$\sigma = \frac{Q^*}{\hat{\Omega}} - \frac{k_B T}{\hat{\Omega}} ln \frac{k_B T N \nu_0}{E \dot{\varepsilon} \hat{\Omega}} \tag{6.1}$$

where the term $\frac{Q^*}{\hat{\Omega}}$ corresponds to nucleation stress at 0 K, in which Q^* is the activation energy barrier for dislocation nucleation in the absence of stress and $\hat{\Omega}$ is the activation volume. k_B is the Boltzmann constant, N is the number of nucleation sites, ν_0 is the
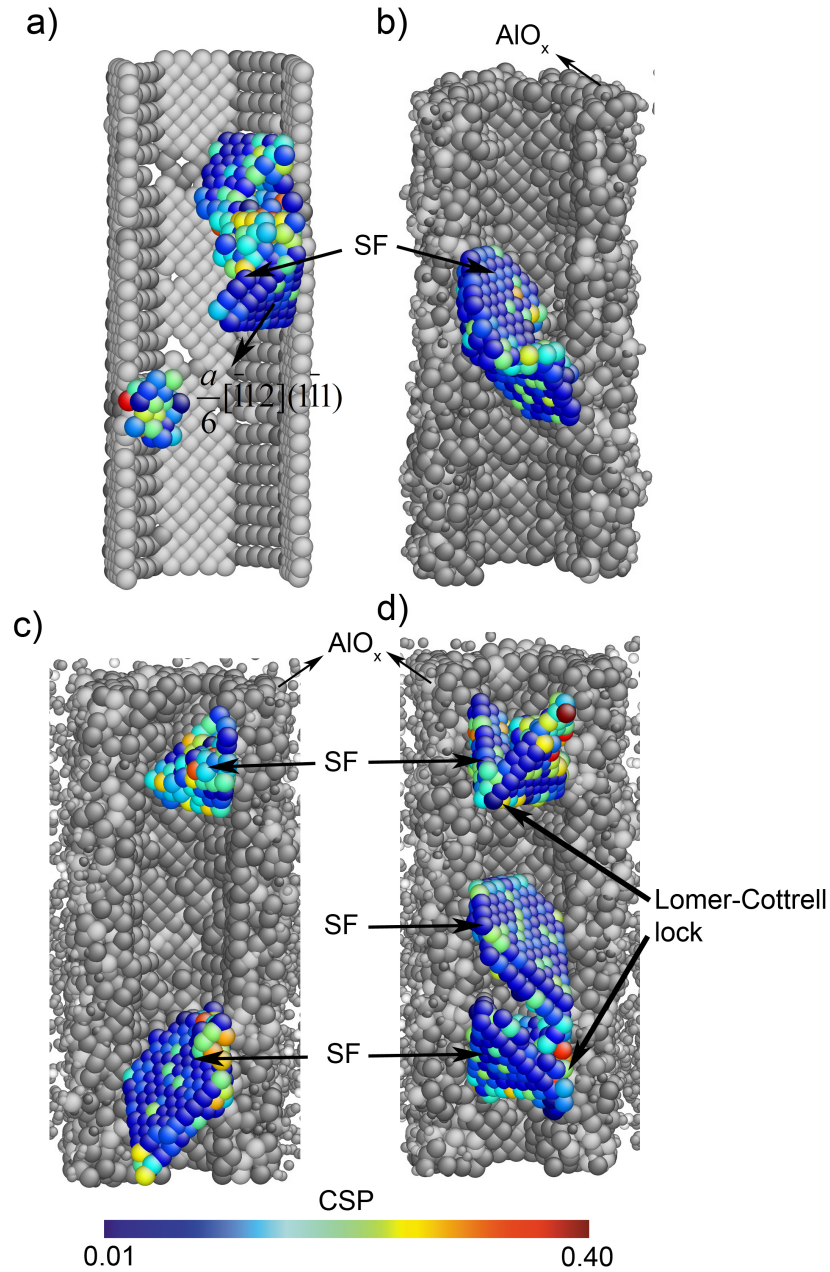
Figure 6.3: Stacking faults (SFs) in aluminum when deformed in oxygen and vacuum at the strain rate of 0.05% ps^{-1}. a) The SFs in the aluminum when deformed in vacuum at the yield point of $\varepsilon = 0.090$. b) The SFs in oxidized aluminum nanowire deformed in vacuum at the yield point of $\varepsilon = 0.065$. c) The SFs in oxidized aluminum nanowire deformed in O_2 at the yield point of $\varepsilon = 0.065$. e) The SFs in the oxidized aluminum deformed in O_2 at $\varepsilon = 0.160$, which indicates Lomer-Cottrell lock formation due to enhanced dislocation activity. The stacking faults are visualized with the use of centro-symmetry parameter (CSP), while the CSP value of 0.04 corresponds to the stacking faults in Al FCC lattice.

atomic vibrational frequency and E is the Young's modulus. When Al was covered with an oxide shell the stress required for dislocation nucleation from Al/AlO$_x$ interface was lower than the stress required for dislocation nucleation from the pure Al surface. The irregular structure of the Al/AlO$_x$ interface decreased the activation energy barrier (Q^*) in Eq. 6.1 and also provided more nucleation sites for dislocations (N) – both lead to a decrease in the nucleation stress. In O$_2$ environment, the number of dislocation nucleation events was increased due to an additional increase in the number of available N. Therefore, Al covered with oxide had a lower stress for dislocation nucleation and showed increased number of dislocation nucleation events during the plastic deformation; hence Al with oxide underwent an extended plastic deformation compared to pure Al.

Although the dislocation nucleation controlled yield strength in the deformation of nanoscale Al with or without oxide, no new ones could form by the time they escaped, resulting in the Al crystal free of dislocations [21, 22, 36–38]. Dislocations that are approaching to the free surfaces eliminated from the crystal due to the image forces acting on them, described as the escape of dislocations [39]. The escape of dislocations at the Al/AlO$_x$ interface could only be possible if the oxide layer had a lower shear modulus than the aluminum [39, 40] and our recent work has shown that the oxide shell had much lower Young's modulus (25.5 GPa) compared to Al (61.9 GPa) [20]. The image forces on a dislocation at the vicinity of an Al free surface and in Al near the Al/AlO$_x$ interface were estimated using the relation $F = \frac{R\mu_B b^2}{4\pi r}$ [40] as -0.045 N/m and -0.154 N/m, respectively (see Methods section for details). These calculations showed that the presence of an amorphous oxide layer on Al surface decreased the image force on a dislocation by 3 times making the escape more difficult, and hence enhancing the ductility of Al covered by an oxide shell (Figure 6.2). Nevertheless, the image force had still a negative value indicating that the Al/AlO$_x$ interface would still exert attractive force on the dislocations. These results explained the observations of dislocation escape events during deformation of single crystal Al inside TEM [21], although the Al had an oxide layer on the surface.

The amorphous AlO$_x$ film on the Al surface deformed by viscoplastic mechanism (Figure 6.2) [41–43], and showed a superplastic behavior in an O$_2$ atmosphere at low strain rate. Figure 6.4(a) shows that when placed in an O$_2$ atmosphere, the number of Al in the oxide

increased linearly due to continuous oxidation with the applied strain and at the lowest strain rate (0.05% ps^{-1}) the O/Al ratio in the oxide increased from 1.1 to 1.2 at 0.750 strain. At higher strain rates the change in the number of Al in the oxide in O_2 is similar to that in vacuum and the nanowire did not exhibit a superplastic behaviour. The change in the number of rings with the applied strain of $\Delta\varepsilon = 0.400$ in vacuum and O_2 given in Figure 6.4(b) shows that in vacuum, the number of rings with large members (16, 18, 20) increased, and the smaller rings with 4 members decreased. On the other hand, in O_2 no formation of large rings was identified, instead, number of rings with 4 members increased. The formation of large rings in vacuum was also evident in the deformed atomic structures of the oxide given in Figures 6.4(c)-(l). In vacuum (Figure 6.4c), rings were opened from the weak homopolar O-O bonds and with the applied plastic strain, rings grew at the expense of smaller rings and formed large voids in the structure as shown in Figure 6.4(d)-(e), in accordance with the free volume theory. The voids in the structure further grew with the applied strain (Figure 6.4(f)) and eventually formed Al-O-Al atomic thick chains (Figure 6.4(g)) that elongated infinitely at the fracture surface as shown in Figure 6.2(c).

In O_2 (Figure 6.4(h)), Al-O bonds were also broken during deformation (Figure 6.4(i)), but diffused O_2 molecules became attached to the broken Al-O chains and the freshly formed O-O homopolar bonds (Figure 6.4(j)). These weak bonds were later broken and the O atoms with unsaturated bonds attached to nearby Al atoms with the applied strain (Figure 6.4k) and prevented the further fracture of Al-O bonds. As a result, no large rings in the structure were formed in O_2, and the oxide maintained its structure owing to "*healing*" by O_2 (Figure 6.4l). The repair mechanisms had a significant benefit as the low initial O/Al ratio -oxygen deficiency- in the native oxide also eased the oxide to be reactive to the oxygen with the applied strain contributed to the superplasticity of the oxide. The O_2 diffusion also increased the Al coordination number and, hence the number of AlO_4 tetrahedra in the oxide inferring that during deformation in O_2 the short range order increased and O diffusion resulted in crystallization of the amorphous oxide, while in vacuum the Al coordination did not indicate any significant change.

This work clearly demonstrated that the nano-sized native oxide of Al significantly enhances the plasticity of Al nanowires. In O_2, not only the dislocation activity in the Al
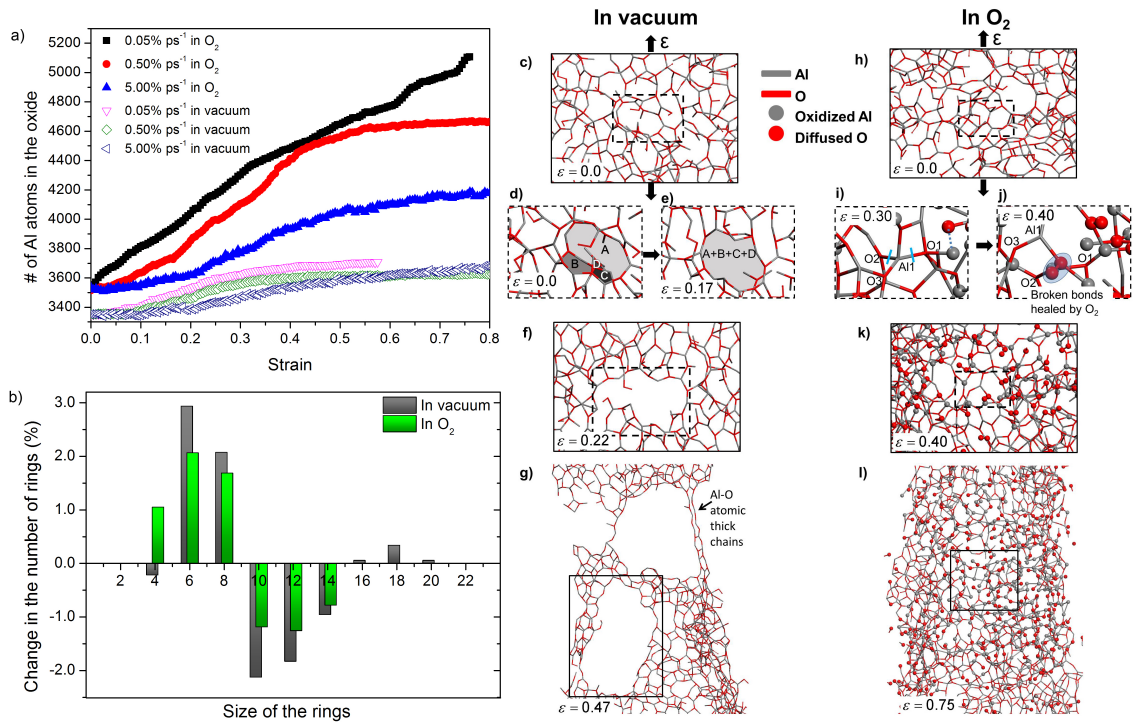
Figure 6.4: Deformation mechanisms of the amorphous oxide in vacuum and O_2. (a) The change in the number of Al atoms in the oxide upon deformation at different strain rates. (b) the change in the ring size distribution with $\Delta\varepsilon = 0.400$, when Al was deformed in vacuum and O_2. (c)-(g)The atomic structural changes in the amorphous AlO_x deformed in vacuum and (h)-(l) deformed in O_2 environment. In vacuum, (d)-(e) shows the evolution of the voids upon applied strain in vacuum due to Al-O bond breaking and formation of larger rings as expense of smaller rings. (f)-(g) Upon further deformation up to $\varepsilon = 0.470$, voids grew and the oxide formed Al-O atomic thick chains at the fracture surface. In O_2, (i)-(j) shows that O_2 atoms diffused in the oxide structure upon applied strain and attached the broken Al-O chains that caused a healing effect and allowed superplastic deformation in O_2 by suppressing void formation ((k)-(l)). c) Change in the number of Al atoms in the amorphous oxide when deformed in O_2 and vacuum at different strain rates.

crystal increased but also the oxide shell showed superplasticity. Observation of Al-O rings and also Al-O atomic thick chains at the fracture surface suggested that one- and two-dimensional oxide structures can be produced by subjecting the oxide to tensile deformation and the properties of these structures can be tailored in O_2 environment. These results at the nano-scale also advised that the adhesion problems in bulk Al forming due to super-plastic deformation of the oxide can be controlled either by preventing oxygen from the environment or the amorphous oxide bonds can be saturated with excess oxygen to break-down the oxide's plasticity. Consequently, one can tailor the atmospheric conditions to alter the mechanical properties of materials at the nano-scale and these properties can essentially change the bulk mechanical response of materials.

Methods

A reactive force field, namely ReaxFF was used in molecular dynamics simulations as implemented [44] in the LAMMPS [30] to study the oxidation and deformation of aluminum simultaneously. In ReaxFF, the total energy of the system is defined to be composed of bond, Coulomb, over-coordination and van der Waals energies and in the Coulomb energy calculation part the charge on each atom was determined in every molecular dynamics step with the electron equilibration method [45]. All MD calculations were carried out at constant temperature of $T = 200$ K using Nose-Hoover thermostat [46, 47]. The effect of oxidation on the deformation of aluminum using MD simulations was investigated in two steps. First, a 4.0 nm diameter and 10.2 nm long aluminum nanowire was constructed with a faceted cross-section composed of {100} and {110} surfaces consisting of 8500 Al atoms. The Al nanowire was periodic in the [001] direction and placed in a box containing 4000 O_2 molecules with a density of 188 times more than the ambient conditions. At the end of a 50 ps oxidation, a 0.9 nm thick amorphous oxide layer passivated the Al nanowire surface with a stoichiometry of $AlO_{1.1}$.

In deformation simulations tensile strain was applied in the [001] direction at increments of 0.5% and at each strain increment the structure was allowed to relax. The strain rate was changed by using different relaxing times between consecutive strain increments. The strain

was applied until the nanowire fractured. The virial theorem was used to obtain engineering stress-strain curve in the [001] direction. To visualize the stacking faults in aluminum, the definition of centro-symmetry parameter [32] as implemented in ATOMEYE [33] program was used. Plastic deformation in the amorphous AlO_x was revealed by the investigation of the changes in the Al-O bond structure and the calculation of the statistical shortest path rings [48] as implemented in the R.I.N.G.S. code [49].

The calculation of the image force per unit length between a screw dislocation with a burgers vector, b, that is located inside crystal B and its nearest image that is located in crystal A was defined by Koehler [40] as

$$F = \frac{R\mu_B b^2}{4\pi r} \tag{6.2}$$

where $R = \frac{\mu_A - \mu_B}{\mu_A + \mu_B}$, μ_A and μ_B are the modulus of rigidity of metals A and B, respectively, and r is the distance between the dislocation and its nearest image. This formulation was used to calculate the maximum image force when $r = 2b$ that acted on a partial dislocation with a Burger's vector of $b = \frac{a}{6}\left[11\bar{2}\right]$ that is located in the Al crystal with a lattice parameter of $a = 4.05$ Å and close to the Al/AlO_x interface. In our system $\mu_A = \mu_{AlO_x}$ and $\mu_B = \mu_{Al}$, and we estimated the modulus of rigidity of Al and AlO_x from the calculated Young's modulus (E) using $\mu = \frac{E}{2(1+\nu)}$. Here, we assumed the Poisson ratio (ν) of Al as 0.3 and Poisson ratio of the AlO_x as 0.15.

Bibliography

[1] H. Ohnishi, Y. Kondo, and K. Takayanagi. Quantized conductance through individual rows of suspended gold atoms. *Nature*, 395(6704):780–783, 1998.

[2] Y. Kondo and K. Takayanagi. Gold nanobridge stabilized by surface structure. *Physical Review Letters*, 79(18):3455–3458, 1997.

[3] Y. Kondo and K. Takayanagi. Synthesis and characterization of helical multi-shell gold nanowires. *Science*, 289(5479):606–608, 2000.

[4] M. D. Uchic, D. M. Dimiduk, J. N. Florando, and W. D. Nix. Sample dimensions influence strength and crystal plasticity. *Science*, 305(5686):986–989, 2004.

[5] F. Jona. Preparation and properties of clean surfaces of aluminum. *Journal of Physics and Chemistry of Solids*, 28:2155–2158, 1967.

[6] Wm H. Krueger and S. R. Pollack. The initial oxidation of aluminum thin films at room temperature. *Surface Science*, 30(2):263–279, 1972.

[7] J. K. Chang, E. M. Taleff, P. E. Krajewski, and J. R. Ciulik. Effects of atmosphere in filament formation on a superplastically deformed aluminum-magnesium alloy. *Scripta Materialia*, 60:459–462, 2009.

[8] S. Das, A. R. Riahi, X. Meng-Burany, A. T. Morales, and A. T. Alpas. High temperature deformation and fracture of tribo-layers on the surface of AA5083 sheet aluminum-magnesium alloy. *Materials Science and Engineering A*, 531:76–83, 2012.

[9] S. Das, A. T. Morales, A. R. Riahi, X. Meng-Burany, and A. T. Alpas. Role of plastic deformation on elevated temperature tribological behavior of an Al-Mg alloy (AA5083):

A friction mapping approach. *Metallurgical and Materials Transactions A*, 42(8):2384–2401, 2011.

[10] M. G. Zelin. On micro-superplasticity. *Acta Materialia*, 45(9):3533–3542, 1997.

[11] P. E. Krajewski and A. T. Morales. Tribological issues during quick plastic forming. *Journal of Materials Engineering and Performance*, 13(6):700–709, 2004.

[12] S. S. Brenner. Tensile strength of whiskers. *Journal of Applied Physics*, 27(12):1484–1491, 1956.

[13] S. S. Brenner. Plastic deformation of copper and silver whiskers. *Journal of Applied Physics*, 28(9):1023–1026, 1957.

[14] B. Wu, A. Heidelberg, and J. J. Boland. Mechanical properties of ultrahigh-strength gold nanowires. *Nature Materials*, 4(7):525–529, 2005.

[15] J. R. Greer, W. C. Oliver, and W. D. Nix. Size dependence of mechanical properties of gold at the micron scale in the absence of strain gradients. *Acta Materialia*, 53(6):1821–1830, 2005.

[16] M. D. Uchic, P. A. Shade, and D. M. Dimiduk. Plasticity of micrometer-scale single crystals in compression. *Annual Review of Materials Research*, 39:361–386, 2009.

[17] J.H. Luo, F.F. Wu, J.Y. Huang, J.Q. Wang, and S.X. Mao. Superelongation and atomic chain formation in nanosized metallic glass. *Physical Review Letters*, 104:215503, 2010.

[18] N. W. Moore, J. Luo, J. Y. Huang, S. X. Mao, and J. E. Houston. Superplastic nanowires pulled from the surface of common salt. *Nano Letters*, 9(6):2295–2299, 2009.

[19] H. Guo, P.F. Yan, Y.B. Wang, J. Tan, Z.F. Zhang, M.L. Sui, and E. Ma. Tensile ductility and necking of metallic glass. *Nature Materials*, 6:735–739, 2007.

[20] F.G. Sen, Y. Qi, A.C.T. van Duin, and A.T. Alpas. Oxidation induced softening in Al nanowires. *Applied Physics Letters*, 102:051912, 2013.

[21] S. H. Oh, M. Legros, D. Kiener, and G. Dehm. In situ observation of dislocation nucleation and escape in a submicrometre aluminium single crystal. *Nature Materials*, 8(2):95–100, 2009.

[22] H. Zheng, A. Cao, C. R. Weinberger, J. Y. Huang, K. Du, J. Wang, Y. Ma, Y. Xia, and S. X. Mao. Discrete plasticity in sub-10-nm-sized gold crystals. *Nature Communications*, 1:144, 2010.

[23] H. S. Park, K. Gall, and J. A. Zimmerman. Deformation of FCC nanowires by twinning and slip. *Journal of the Mechanics and Physics of Solids*, 54(9):1862–1881, 2006.

[24] K. Gall, J. Diao, and M. L. Dunn. The strength of gold nanowires. *Nano Letters*, 4(12):2431–2436, 2004.

[25] C. R. Weinberger and W. Cai. Surface-controlled dislocation multiplication in metal micropillars. *Proceedings of the National Academy of Sciences of the United States of America*, 105(38):14304–14307, 2008.

[26] E. Rabkin and D. J. Srolovitz. Onset of plasticity in gold nanopillar compression. *Nano Letters*, 7(1):101–107, 2007.

[27] J. Diao, K. Gall, M. L. Dunn, and J. A. Zimmerman. Atomistic simulations of the yielding of gold nanowires. *Acta Materialia*, 54(3):643–653, 2006.

[28] A. C. T. Van Duin, S. Dasgupta, F. Lorant, and III W. A. Goddard. ReaxFF: A reactive force field for hydrocarbons. *Journal of Physical Chemistry A*, 105(41):9396–9409, 2001.

[29] Q. Zhang, T. Çağin, A. Van Duin, III W. A. Goddard, Y. Qi, and L. G. Hector Jr. Adhesion and nonwetting-wetting transition in the Al/α-Al$_2$O$_3$ interface. *Physical Review B*, 69(4):454231, 2004.

[30] S. Plimpton. Fast parallel algorithms for short-range molecular dynamics. *Journal of Computational Physics*, 117(1):1–19, 1995.

[31] L. Pastor-Abia, M. J. Caturla, E. Sanfabián, G. Chiappe, and E. Louis. Abnormal stress drop at the yield point of aluminum nanowires: A molecular dynamics study. *Physical Review B*, 83(16):165441, 2011.

[32] C. L. Kelchner, S. J. Plimpton, and J. C. Hamilton. Dislocation nucleation and defect structure during surface indentation. *Physical Review B*, 58(17):11085–11088, 1998.

[33] J. Li. Atomeye: An efficient atomistic configuration viewer. *Modelling and Simulation in Materials Science and Engineering*, 11(2):173–177, 2003.

[34] T. Zhu, J. Li, A. Samanta, A. Leach, and K. Gall. Temperature and strain-rate dependence of surface dislocation nucleation. *Physical Review Letters*, 100(2):25502, 2008.

[35] V. Yamakov, D. Wolf, S.R. Phillpot, A.K. Mukherjee, and H. Gleiter. Dislocation processes in the deformation of nanocrystalline aluminium by molecular-dynamics simulation. *Nature Materials*, 1:45–49, 2002.

[36] J. R. Greer and W. D. Nix. Nanoscale gold pillars strengthened through dislocation starvation. *Physical Review B*, 73(24):245410, 2006.

[37] K. Sieradzki, A. Rinaldi, C. Friesen, and P. Peralta. Length scales in crystal plasticity. *Acta Materialia*, 54(17):4533–4538, 2006.

[38] Z. W. Shan, R. K. Mishra, S. A. Syed Asif, O. L. Warren, and A. M. Minor. Mechanical annealing and source-limited deformation in submicrometre- diameter nicrystals. *Nature Materials*, 7(2):115–119, 2008.

[39] J. Weertman and J. R. Weertman. *Elementary Dislocation Theory*. Oxford University Press, New York, 1992.

[40] J. S. Koehler. Attempt to design a strong solid. *Physical Review B*, 2(2):547–551, 1970.

[41] F. Spaepen. A microscopic mechanism for steady state inhomogeneous flow in metallic glasses. *Acta Metallurgica*, 25(4):407–415, 1977.

[42] A. S. Argon. Plastic deformation in metallic glasses. *Acta Metallurgica*, 27(1):47–58, 1979.

[43] M. L. Falk and J. S. Langer. Dynamics of viscoplastic deformation in amorphous solids. *Physical Review E*, 57(6):7192–7205, 1998.

[44] K. Chenoweth, A.C.T. van Duin, P. Persson, M.J. Cheng, J. Oxgaard, and W.A. Goddard Iii. Development and application of a ReaxFF reactive force field for oxidative dehydrogenation on vanadium oxide catalysts. *Journal of Physical Chemistry C*, 112(37):14645, 2008.

[45] W. J. Mortier, S. K. Ghosh, and S. Shankar. Electronegativity equalization method for the calculation of atomic charges in molecules. *Journal of the American Chemical Society*, 108(15):4315–4320, 1986.

[46] S. Noseé. A unified formulation of the constant temperature molecular dynamics methods. *Journal of Chemical Physics*, 81:511–519, 1984.

[47] W.G. Hoover. Canonical dynamics: Equilibrium phase-space distributions. *Physical Review A*, 31:1695–1697, 1985.

[48] L. Guttman. Ring structure of the crystalline and amorphous forms of silicon dioxide. *Journal of Non-Crystalline Solids*, 116(2-3):145–147, 1990.

[49] S. Le Roux and P. Jund. Ring statistics analysis of topological networks: New approach and application to amorphous ges_2 and sio_2 systems. *Computational Materials Science*, 49(1):70–83, 2010.

Chapter 7

Anchoring Platinum on Graphene using Metallic Adatoms: A First Principles Investigation

7.1 Introduction

Recently discovered carbon structures, namely carbon nanotubes (CNT), and graphene provide excellent mechanical, electrical and optical properties [1–4]. Graphene−a two-dimensional, single atomic layer of carbon−is the building block of many advanced carbon structures, while a CNT is a rolled graphene structure. There has been ample research in the literature on tuning the chemical and physical properties (electronic, magnetic, optical) of graphene using dopants that are incorporated at its surface [5–13]. In certain applications, graphene is used in contact with a metal surface, highlighting the difficulty of selecting a suitable dopant that effectively enhances the metal−carbon interfacial strength without causing any deterioration to its physical and mechanical properties. According to first principles calculations, contact between graphene and transition metals like Co, Ni, Pd and Ti can alter the graphene's band structure significantly due to a charge transfer at the metal graphene interface. However, metals such as Al, Ag, Cu, Au and Pt showed very weak interactions with graphene to the extent that they had no significant effect on the graphene band

structure [7, 14–19]. Other important applications that feature an interface between noble metals and graphene include electrochemical systems, in which the graphene is considered a support material for the electrocatalysts used in fuel cells and batteries because of its high chemical stability and conductivity [20]. The performance of catalysts used in direct methanol fuel cells (DMFCs), and proton exchange membrane fuel cells (PEMFCs) [21], along with the catalysts used in lithium−air batteries [22–24], all benefit from the strong adhesion between the catalysts (e.g., Pt) and the carbon support [25]. The Pt catalysts used in these applications are deposited on carbon surfaces in the form of nanoparticles. Strong adhesion between the Pt and the carbon is necessary to improve the performance of the electrocatalyst. Finding elements that enhance the anchorage of Pt nanoparticles to the graphene surface is an important goal, but a systematic study for determining which materials would increase the interfacial strength between Pt and graphene has not been presented in the literature thus far.

An increase in the interface strength between Pt and graphene can be achieved by modifying the Pt, the graphene, or both surfaces. Experimental studies reported [26–31] that alloying the Pt with transition metals such as Co [32], Ni [33], Fe [34], Cr [35], Mo [36] and other metals or metal oxides [37–39] increased the interfacial strength between the Pt and the carbon. According to a first principles study, the Ru-alloying of a Pt surface increased the Pt/C interface strength via strong interaction between Ru and carbon [14]. However, modifying the Pt surface potentially decreases the catalytic performance of the Pt. Moreover, the surface composition of Pt alloys is hard to control due to the segregation of the Pt to the surface [40, 41].

Pt typically binds very strongly to metals that have strong interaction with carbon [42]. Consequently, we propose to modify the carbon surface using the metallic elements featured in this study. Modifying the carbon surface with these metallic elements may enhance the adhesion between the Pt and the carbon without changing the catalytic properties of the Pt [30]. So far there have been no systematic studies that compare the effects of different metals on the Pt/C interface strength. It was reported that increasing sites on the carbon surface and the surface basicity of carbon enhanced the binding sites for Pt [43]. The functionalization of the carbon support by S, N and P improved in the binding of carbon to

190

Pt and N doping additionally improved the catalytic activity of the Pt particles [44]. The use of carbon nanotubes (CNTs) [45, 46] and graphene [47] as support materials provided even stronger binding with Pt particles [48]. The Pt particles favored attachment at N-rich sites in N-doped CNT [49] and B-doped carbon [50, 51]. However, modifying the carbon surface with S, N, P or organic molecules may not sufficiently improve the electron conductivity between the carbon support and the Pt catalyst, which is important to the electrochemical performance. Therefore, the modification of the carbon surface by metallic elements studied here could be more effective with a simultaneous focus on the improvement of the interface strength and the conductivity.

Accordingly, in this study a graphene surface was systematically modified with metallic elements and the effects that these elements had on the Pt/C interface strength were investigated using first principles calculations. These calculations were proven to be accurate when applied to the investigation of metal−carbon interfaces [52–55]. The metals considered included all fourth-row transition metals (TMs): Sc, Ti, V, Cr, Mn, Fe, Co, Ni, Cu and Zn; fifth-row TM elements: Zr, Nb, Mo, Ru and Rh; sixth-row TM elements: Ta, W, Re, Os and Ir with Au as a noble metal. Simple metallic elements such as Li, Na, Mg and Al were also considered. The changes in the interfacial strength resulting from the presence of these metals were determined by computing the work of separation.

7.2   Computational methodology

Pt (111) and a single sheet of graphite (0001) were used to represent the interface properties between Pt and graphene. This was consistent with high resolution transmission electron microscopy studies that showed the formation of an interface between Pt(111) and graphite (0001) basal planes (graphene) [56, 57]. Van der Waals interactions between graphite planes cannot be computed accurately by DFT. The lattice parameter between the graphite layers, c, cannot be predicted by generalized gradient approximation (GGA), but can be predicted rather accurately by local density approximation (LDA) [53]. Because new covalent or ionic bonding would be formed by the introduction of adsorbed atoms to the interface, the much weaker interactions between the graphite layers were not expected to affect the comparisons

made between different metal adatoms; therefore, the use of a single layer of graphite with GGA was a suitable method for studying the metal adsorption on the graphite surface. In fact, the in-planar lattice distance computed with the GGA was in good agreement with the experimentally found value of $a = 2 : 46$ Å [58].

Prior to interface calculations, the possible atomic sites that the adatoms may be located at the interface were determined by studying the adsorption of metals on graphite (0001) and Pt (111). The metallic adatoms studied were adsorbed on top, hollow and bridge sites on a 2×2 graphene surface with an edge length of 4.92 Å as shown in Figure 7.1(a). A 15 Å vacuum was employed in the $z-$direction to eliminate attractive forces between the periodic images. The adsorption energies (E^{ads}) of adatoms on graphene surface were calculated as follows:

$$E^{ads} = E_{\text{graphene}} + E_{\text{M}} - E_{\text{graphene+M}} \qquad (7.1)$$

where $E_{\text{graphene+M}}$ is the total energy of the graphene with adatom and E_{graphene} is the total energy of graphene. E_{M} is the total energy of a single adatom calculated in a cubic box with lattice dimension of 15 Å . The E^{ads} of metals at 'top', 'fcc', and 'hcp' sites on the Pt (111) surface as shown in Figure 7.1(b) were also calculated using the same method.

Interfaces between the Pt (111) and the metal-adsorbed graphene were constructed by matching six layers of a Pt (111) surface (each layer containing three atoms) with a 2×2 graphene (0001) surface containing eight carbon atoms. The interface model and interface registry used are shown in Figure 7.2. The Pt $[\bar{1}2\bar{1}]$ direction was aligned with the $[01\bar{1}0]$ direction of the graphene so that an interface geometry consisting of $(111)[\bar{1}2\bar{1}]_{\text{Pt}} \parallel (0001)[01\bar{1}0]_{\text{C}}$ was created as seen in Figure 7.2(a). This particular interface geometry between Pt and graphene had the lowest energy, which was consistent with the previous DFT studies [7]. The calculated edge dimension of the Pt (111) slab was 4.87 Å. As the graphene 2×2 surface had an edge dimension of 4.92 Å, this configuration resulted in a lattice mismatch of about 1%, suggesting that the misfit dislocations could be ignored. Two different interface registries were considered when a metal adatom at the interface was introduced,

while keeping the metal atom on the hollow site at the graphene surface. The Pt surface was moved in such a way that, for the first registry, the metal adatom was located on the 'top' adsorption site of the Pt (111) (Figure 7.2(a)) and for the second, the metal adatom was located on the 'fcc' adsorption site of the Pt (111) (Figure 7.2(b)). These configurations were deemed appropriate, because most metals preferred to locate at the hollow site on the graphene (see section 3.1). A 15 Å vacuum was used in the $z-$direction to prevent the effects of periodic images, for which the initial separation between the Pt surface and the adatom was 2.0 Å (Figure 7.2(c)). The interface structures were relaxed according to atomic positions, while maintaining constant cell dimensions.

The strength of each Pt/graphene interface with an adatom was determined by calculating the work of separation (W_{sep}), which is defined as the energy required to reversibly separate an interface into two free surfaces [59]. In the presence of an adatom, the interface could be separated into two distinct surfaces by breaking the bond between the Pt and the metal adatom (Pt$-$M), or by breaking the bond between the carbon and the metal adatom (C$-$M). The strength of the interface was computed for both cases by considering the atomic arrangements shown in Figure 7.2(c). The W_{sep} for breaking the Pt$-$M bond ($W_{sep}^{\text{Pt}-\text{M}}$) and W_{sep} for breaking the C$-$M bond ($W_{sep}^{\text{C}-\text{M}}$) are defined as follows:

$$W_{sep}^{\text{Pt}-\text{M}} = \frac{1}{A} \left[E_{\text{Pt}} + E_{\text{graphene+M}} - E_{\text{Pt/graphene+M}} \right] \tag{7.2}$$

$$W_{sep}^{\text{C}-\text{M}} = \frac{1}{A} \left[E_{\text{graphene}} + E_{\text{Pt+M}} - E_{\text{Pt/graphene+M}} \right] \tag{7.3}$$

where E_{Pt}, $E_{\text{Pt+M}}$ and E_{graphene}, $E_{\text{graphene+M}}$ are the total energies of the relaxed six layer Pt (111) slab with and without an adatom and the relaxed graphene (0001) surface with and without an adatom respectively, and $E_{\text{Pt/graphene+M}}$ is the total energy of the relaxed interface.

All calculations were based on DFT, where the ground state structures and energies were obtained by solving the single particle Kohn$-$Sham [60] equation with a plane wave basis set. A projector-augmented wave (PAW) method was used with exchange correlation energy approximated in the generalized gradient approximation (GGA) [61] to DFT, as

implemented in the Vienna ab initio simulation package (VASP) [62,63]. Calculations were carried out by PAW−PBE [64,65] potentials, supplied by VASP. All calculations were carried out considering the spin polarization. The total energies were obtained by relaxing the system according to atomic positions and minimizing the Hellman−Feynman forces using a conjugate gradient method. In all calculations, an energy convergence to $1 - 2$ meV was obtained using a $10 \times 10 \times 1$ grid of Γ−centered k−points and a plane wave cutoff energy of 500 eV. The electronic degrees of freedom for structures were converged to 10^{-5} eV/cell and Hellman−Feynman forces were relaxed to less than 0.05 eV Å^{-1}. Atomic relaxations were carried out using Methfessel–Paxton [66] smearing with a width of $\sigma = 0.05$ eV and the final total energy was calculated using tetrahedron method with Blöchl corrections [67].

7.3   Results and discussion

7.3.1   Surface binding

The calculated E^{ads} of metals on the graphene surface are given in Table 7.1. All metals preferred the 'hollow' site on the graphene surface with the exception of Mg, Cu and Re which preferred the 'bridge' site. The E^{ads} of metals on graphene were in good agreement with previous DFT calculations for the studied metals [68,69]. The E_{ads} of metals on the Pt (111) surface were found to be the lowest for 'fcc' and 'hcp' sites and are provided in Table 7.1 for comparison. It should be noted that the differences between the E^{ads} for 'fcc' and 'hcp' sites were very close (less than 0.05 eV/atom), as observed in previous first principles calculations [70]. The E^{ads} of the metal atom on the Pt surface was in the range of 1.8–8.4 eV/atom−$3 - 4$ times higher than the E^{ads} on graphene (in the range of $0.1 - 2.9$ eV/atom). The E^{ads} of early transition metals such as Sc, Ti, V, Zr, Nb and Ta were found to be the highest, and these elements also showed the strongest binding for both graphite (0001) and Pt (111) surfaces. The E^{ads} decreased while going from left to right (e.g. E^{ads} of Ni is lower than Sc) in the periodic table and increased while going from top to bottom (e.g. E^{ads} of Zr is higher than Ti).

Table 7.1: Adsorption energies (E^{ads}) of adatoms on the graphite (0001) and Pt (111) surfaces at the lowest energy surface site.

	Graphite (0001)		Pt (111)	
Adatom	Site	E^{ads}(eV)	Site	E^{ads}(eV)
Li	Hollow	0.86	hcp	3.09
Na	Hollow	0.60	hcp	2.40
Mg	Bridge	0.13	hcp	2.81
Al	Hollow	0.92	hcp	4.86
Sc	Hollow	1.99	hcp	6.38
Ti	Hollow	1.89	hcp	6.60
V	Hollow	1.37	fcc	5.24
Cr	Hollow	0.26	hcp	3.34
Mn	Hollow	0.23	hcp	3.90
Fe	Hollow	0.73	fcc	4.27
Co	Hollow	1.17	fcc	3.99
Ni	Hollow	1.41	fcc	3.97
Cu	Bridge	0.26	fcc	3.12
Zn	Hollow	0.04	hcp	1.82
Zr	Hollow	2.89	hcp	7.83
Nb	Hollow	1.96	fcc	6.68
Mo	Hollow	0.49	fcc	4.53
Ru	Hollow	1.86	fcc	3.80
Rh	Hollow	1.66	fcc	4.11
Ta	Hollow	2.49	fcc	8.42
W	Hollow	1.34	fcc	6.23
Re	Bridge	0.01	fcc	4.87
Os	Hollow	1.26	fcc	5.16
Ir	Hollow	1.34	fcc	4.80
Au	Hollow	0.16	fcc	2.70

7.3.2   Interfacial strength

Stronger adsorption of the metal adatom on either graphene or Pt surfaces does not guarantee better bridging ability for the metallic atom sandwiched at the Pt and graphene interface. The bonding of the metal atom at the interface will be affected by both the Pt and graphene surfaces, so the adsorption energies do not provide a correct estimate of interfacial strength. To determine the interfacial strength of the adatom-modified Pt/graphene interface, the $W_{sep}^{\mathrm{Pt-M}}$ and the $W_{sep}^{\mathrm{C-M}}$ were calculated for both interface registries as shown in Figures 7.2(a) and (b). For all metals, the interface registry where the metal adatom located at the 'fcc' site on Pt (111) (Figure 7.2(b)) resulted in the lowest total energy. The $W_{sep}^{\mathrm{Pt-M}}$

values for the registry where the adatom was on the Pt 'fcc' site were about $25\%-30\%$ larger than the $W_{sep}^{\text{Pt}-\text{M}}$ values for the registry where the adatom was on the Pt 'top' site (Figure 7.2(a)). Therefore, the W_{sep} values presented in Figure 7.3 pertain to those corresponding to Figure 7.2(b). The W_{sep} values are plotted according to the sequence of the atomic number of elements.

The W_{sep} for the unmodified Pt/graphene interface was calculated as 0.009 J m^{-2}, which is very low. With metal adatom modification at the graphene surface, almost all the W_{sep} are higher than 0.009 J m^{-2}, with the exception of Al, Au and Zn modification, for which $W_{sep}^{\text{C}-\text{M}} < 0.01$ J m^{-2}. Early TM elements such as Sc, Ti, Zr, Nb and Ta along with Re and W, formed the strongest bond with Pt. For all of these adatoms, $W_{sep}^{\text{Pt}-\text{M}} \geq 3.5$ J m^{-2}. Figure 7.3, however, reveals that a higher energy is required to break the Pt$-$M bond compared to the C$-$M bond. Consequently, the interface is expected to break at the C$-$M bond, inferring that this C$-$M interface plays a more important role than the Pt$-$M bond in controlling the overall interface strength. Figure 7.3 shows that transition metals such as Ti and Cr formed stronger C$-$M bonds than light metals such as Li and Al. The $W_{sep}^{\text{C}-\text{M}}$ increased slightly with the increase in atomic size among transition metals, because $W_{sep}^{\text{C}-\text{M}}$ of the elements increases with the row number in the periodic table. For example, $W_{sep}^{\text{C}-\text{Os}} > W_{sep}^{\text{C}-\text{Ru}} > W_{sep}^{\text{C}-\text{Fe}}$. The $W_{sep}^{\text{C}-\text{M}}$ increased when going from left to right and top to bottom in the periodic table. The fourth-row TM elements had a $W_{sep}^{\text{C}-\text{M}}$ that differed by only 0.03 J m^{-2} and showed similar interfacial strength with the exception of Mn, Fe and Cu for which $W_{sep}^{\text{C}-\text{M}}$ were 0.2 J m^{-2} less than the other elements. For each row in the periodic table Ir, Os, Re, Ru, Rh and Re showed the highest $W_{sep}^{\text{C}-\text{M}}$ with values exceeding 0.5 J m^{-2}$-$identifying them as the most promising elements for strengthening the Pt/graphene interface. In contrast, Al, Zn and Au did not bind to carbon, so they were not considered suitable for enhancing the Pt/graphene interfacial strength. Al exchanged all of its electrons with Pt, resulting in a very weak bond with graphene. Given that Au and Zn had fully occupied d orbitals, they provided very weak binding to both Pt and graphene. Early TM elements were found to form very strong bonds with Pt, but for the configuration shown in Figure 7.2(c), i.e., located between the carbon and Pt, their bond with carbon weakened relative to other elements. These elements are not as beneficial as middle TM

elements, or group VIII elements for anchoring Pt to carbon.

The strength of the C−M bond at the interface was different from the binding strength of adatoms when simply adsorbed on graphene. In the case of adsorption, the early TM elements showed much stronger binding to carbon than middle or late TM elements, but at the interface the group VIII TM elements showed stronger binding to carbon than early TM. The adsorption energy of Zr, for instance, was higher than Ru on the graphene surface (2.89 for Zr and 1.86 for Ru eV/atom, respectively). When these elements were inserted into the interface, the Ru exhibited a stronger C−M bond with $W_{sep}^{\mathrm{C-M}} = 0.71$ J m^{-2}, while for Zr $W_{sep}^{\mathrm{C-M}} = 0.59$ J m^{-2}. Therefore, in the presence of Pt the carbon−metal bond characteristics have been altered. Consequently, the nature of the bond between metal and carbon is analyzed in more detail in Section 7.3.3.

7.3.3 Electronic structure at the Pt/graphene interface

The adatom inserted at the Pt/graphene interface was found to increase both $W_{sep}^{\mathrm{Pt-M}}$ and $W_{sep}^{\mathrm{C-M}}$ and the overall interface strength was found to be dependent on the $W_{sep}^{\mathrm{C-M}}$. To assess why some elements more effectively increased the $W_{sep}^{\mathrm{C-M}}$, the changes in the bond structure of the interface were analyzed. When the adatom was inserted into the Pt/graphene interface, the adatom resulted in the movement of carbon atoms from their original positions in the graphene structure and the graphene surface was distorted which could affect the $W_{sep}^{\mathrm{C-M}}$ values due to the change in C−M bond characteristics. The distortion of the graphene surface at the Pt/graphene interface in the presence of metal adatoms was analyzed in relation to the changes in the bond angles and relative movements of carbon atoms in the out-of-plane direction. At interface structures, the metal adatoms were not found to create a substantial distortion on graphene and the highest distortion was caused by the elements Re, Mo,W and Os −for which the distortion of the six-carbon-ring in the out-of-plane direction was in the range of $0.015 − 0.022$ Å. The interfacial strength increase that results from metal adatoms cannot be attributed to the change in hybridization type of the carbon atoms from sp^2 to sp^3 due to distortion which was observed in the previous first principles calculations for metal adatom adsorption studies on graphene [68]. Instead, the characteristic electronic structure of the metal adatom plays a more important role in

197

the interfacial bond strength. The electronic structure of the interfaces were analyzed by considering the charge density transfer, electron localization function (ELF) and projected density of the states (PDOS).

In order to determine the total amount of charge transfer at the Pt/graphene interface, Bader charge analysis [71, 72] was carried out. Bader charges, Z_i, for each atom i, were calculated and the total charge transfer to Pt (ΔZ^{Pt}) and graphene (ΔZ^{C}) were determined using the following:

$$\Delta Z^{\mathrm{Pt}} = \sum_i^{n_{\mathrm{Pt}}} (Z_i)_{\mathrm{interface}} - \sum_i^{n_{\mathrm{Pt}}} (Z_i)_{\mathrm{Pt}\ (111)} \tag{7.4}$$

$$\Delta Z^{\mathrm{C}} = \sum_i^{n_{\mathrm{C}}} (Z_i)_{\mathrm{interface}} - \sum_i^{n_{\mathrm{C}}} (Z_i)_{\mathrm{graphene}\ (0001)} \tag{7.5}$$

where $(Z_i)_{\mathrm{interface}}$ is the charge of atom i in the interface, $(Z_i)_{\mathrm{Pt}\ (111)}$ is the charge of atom i in the individual Pt (111) slab, $(Z_i)_{\mathrm{graphene}\ (0001)}$ is the charge of atom i in the individual graphene (0001) surface and n_{Pt} and n_{C} are the number of Pt and C atoms in the system, respectively. It was found that the charge donation from the adatom to both the Pt and the graphene occurred in all of the different adatoms.

7.3.3.1   Analysis of M−Pt bonding

ELF analysis revealed that Pt and metal adatoms form metallic bonds, as expected. The cohesion between metals was found to be proportional to the charge transfer between the two metals and the interatomic charge density [42, 73]. Therefore, a larger amount of charge transfer from the adatom to the Pt is expected to increase $W_{sep}^{\mathrm{Pt-M}}$. Thus, to interpret the results $W_{sep}^{\mathrm{Pt-M}}$ was plotted against the amount of charge transfer from the adatom to the Pt as shown in Figure 7.4. Figure 7.4(a) shows that for each row, the $W_{sep}^{\mathrm{Pt-M}}$ monotonically increased with the total amount of charge transfer from the adatom to the Pt. Among the elements considered, Zr, Ti, Sc, W, Nb, Re and Mo donated the highest amount of charge to the Pt, resulting in the highest $W_{sep}^{\mathrm{Pt-M}}$. In the adsorption energy calculations (Table 7.1), it was found that these transition metals also formed strong bonds with the Pt. It was shown that [42, 73], for a pure metal, the surface energy, γ_s, was proportional to the

interatomic electron density while n_{WS} was the average electron density at the boundary of the Wigner–Seitz cell, as can be written in equation 7.6

$$\gamma_s \propto \Delta H^{vap}/V_m^{2/3} \propto n_{\text{WS}} \qquad (7.6)$$

where the ΔH^{vap} is the heat of vaporization at $T = 0$ K and V_m is the atomic volume. Following this approach, we considered the interatomic density at the boundary of the Wigner–Seitz cell of Pt/M enhanced by the charge transfer from the adatom to Pt, ΔZ^{Pt}, and the atomic volume of the metallic atom was related to the bond distance between the M atom and the Pt surface, $d_{\text{Pt–M}}$. Thus,

$$W_{sep}^{\text{Pt–M}} \propto \left(n_{\text{WS}} + \Delta Z^{\text{Pt}} \right)/d_{\text{Pt–M}}^2 \qquad (7.7)$$

Figure 7.4(b) shows this relationship. $W_{sep}^{\text{Pt–M}}$ correlates with the tabulated n_{WS} values for pure metals [42], the computed charge transfer and the interface structure for almost all of the metal adatoms we computed. In Figure 7.4(b) all data points were fitted to a straight line (dashed line) for an equation in the form of $W_{sep}^{\text{Pt–M}} = 2.66 \left(n_{\text{WS}} + \Delta Z^{\text{Pt}} \right)/d_{\text{Pt–M}}^2 + 1.01$. The Pt–M bond strength was found to increase with the charge density of the adatoms and the amount of charge transfer due to metallic bonding.

7.3.3.2   Analysis of M–graphene bonding

The bonding characteristics between metal atoms and the carbon atom at the nearest neighboring distance to the metal adatom was investigated by calculating the PDOS for each atom in the simulation cell. The C–M bonding was expected to have a covalent character, hence the covalent radii [74] of elements as the Wigner–Seitz radius were used, with the exception of C, for which a radius of 1.03 Å was used. The PDOS of carbon atoms in the modified Pt/graphene interfaces were then compared with the carbon PDOS obtained from the pure Pt/graphene interface, as shown in Figure 7.5(a). Although pure graphene has zero band gap energy [20], Figure 7.5(a) shows that at the Fermi level (E_{F}), a small peak appeared due to hybridization between the Pt and graphene surfaces [75]. Metals with similar electronegativities showed similarities in their electronic structures at the interface. The early

transition metals (e.g., Sc, Ti, Zr, Nb and Ta) and the middle transition metals (e.g., Co, Ni, Ru, Rh, Re, Os and Ir) had similar PDOS characteristics among each group. Ti-, Zr-, Co- and Ru-modified Pt/graphene interface PDOS were selected to represent the changes in the PDOS with different transition metal groups in the periodic table.

The spin up (spin down is symmetric to spin up) PDOS of Ti and the carbon atom located at the nearest neighboring distance is shown in Figure 7.5(b). This figure shows that the d states of Ti hybridize with the carbon p states around energies $4.0 - 5.0$ eV below E_{F}, revealed the formation of a covalent bond between Ti and carbon. The s states of Ti appeared around 2.5 eV below E_{F}, but there were not a considerable number of available p states of carbon at those energy levels to suggest that the contribution of s states of Ti to bonding with carbon is minimal. In addition, the Ti atom's PDOS shows that the number of occupied d states decreased considerably, which was due to the large amount of charge transfer from Ti d orbitals to both Pt and carbon. Other early transition metal atoms (Sc, Zr, Nb and Ta) also formed covalent bonds with carbon. There was a charge transfer to both carbon and Pt while in the case of Ta, Zr and Sc the charge transfers from the d orbitals were more prominent.

The spin up PDOS for Co is plotted in Figure 7.5(c). This figure shows that the d states of the Co atom lay around 4.0 eV below E_{F} and were hybridized with the p states of carbon, similar to Ti. Additionally, there were hybridized Co sd and C p states at energy levels in the range of 2.5 eV below E_{F}, an indication of additional bond formation between Co and carbon near the Fermi level. Another difference of Co PDOS compared to Ti was the near disappearance of the s states, indicating that in Co the charge transfer occurred mainly from the s orbitals and that the remaining s states around the 2.5 eV range below E_{F} were all hybridized with the p orbitals of carbon. Those p states of carbon were not existent in the case of Ti. Therefore, the C−Co bond had a more prominent covalent character than the C−Ti bond. The elements in the fifth and sixth rows also had similar PDOS characteristics in the same group, but they resulted in a larger $W_{sep}^{\mathrm{C-M}}$.

The stronger C−M bond in the cases of other middle transition elements like Ir, Os, Ru and Rh can be explained by the additional hybridization of metal s states in addition to d and carbon p states that occurred at energy levels lower than 2.5 eV below E_{F} (Figure

7.5(d)). In contrast, the early TM elements in the fifth row showed characteristics that were similar to those of Ti, but with more charge transfer. The PDOS of carbon and Zr in the Pt/graphene interface as given in Figure 7.5(e) shows similar PDOS to that found in Figure 7.5(b), which shows a substantial depletion in the number of Zr atom's d states below E_F−implying more charge transfer and a C−M bond with a higher ionic character. Overall, PDOS analysis showed that metals bonded with carbon through a mixed ionic and covalent bonding, but for early transition metals such as Ti and Zr ionic bonding was more prominent with a large amount of charge transfer from the adatom to the carbon. The bonds between carbon and the middle transition metals, however, showed more covalent character with more hybridized states of carbon and adatom. In addition, the metals in the fifth and sixth rows of the periodic table showed additional hybridized states with carbon that further increased the C−M bond strength.

To better understand the charge distribution at the interface, the charge transfers at the interfaces were calculated by subtracting the electronic densities of individually calculated graphene, Pt and adatoms from the total interface electronic density. Figure 7.6 compares the charge density differences for the Pt/graphene interface without anchoring atoms (Figure 7.6(a)) and with anchoring atoms Ti (Figure 7.6(b)), Co (Figure 7.6(c)), Zr (Figure 7.6(d)), Ru (Figure 7.6(e)), and Ir (Figure 7.6(e)). The featureless charge density plot of Pt on graphene further confirmed that there was no interaction between graphene and Pt, resulting in very weak interface strength. When an anchoring atom was present at the interface, a substantial amount of charge was depleted from the anchoring element and accumulated in the regions between the anchoring element and the Pt and graphene, as can be seen in Figures 7.6(b) and (c) for Ti and Co. The C−M bond display different characteristics among elements. Figure 7.6(b) shows the charge accumulation to the π orbitals of carbon, an indication that the C−Ti bond had an ionic character. The amount of charge transfer to the Pt was higher than the amount of charge transfer to the carbon. In the case of Co, Figure 7.6(c) shows that the charge transfer occurred to the π orbitals of carbon and also at the center of the C−Co bond. The orbitals of C atoms were bent in such a way that the σ bonds of C interacted with Co, suggesting the formation of a more covalent bond between C and Co compared to Ti, which is in agreement with the PDOS analysis presented in

Figure 7.5. As opposed to Ti, the amount of charge accumulation from Co to C and Pt was equally distributed between Pt and C. A similar distinction was also observed for the other metals belonging to the same row of the periodic table with Figure 7.6(d) showing how Zr donated more charge to the Pt surface than the graphene surface much like the charge density difference plot in the case of Ti insertion. In contrast, Figure 7.6(e) shows that Ru donated its electrons evenly between Pt and C and that the orbitals of the C atoms were rotated to form strong σ bonds with Ru. Figure 7.6(f) reveals similar changes in the charge density upon Ir insertion, which resulted in the largest $W_{sep}^{\text{C–M}}$. This confirms that the interfacial strength increase with metal adatoms cannot be attributed to the change in the hybridization type of the carbon atoms from sp^2 to sp^3 due to the distortion of the graphene plane, as suggested by Chan et al [68]. Instead, the bonding nature of graphene was altered by the distortion of the carbon's σ and π orbitals.

The bonding analysis presented above clearly indicates that for the C–M interface, the large amount of charge transfer from the adatom to carbon did not always give rise to a large $W_{sep}^{\text{C–M}}$. The $W_{sep}^{\text{C–M}}$ depended on the covalent or ionic nature of the M–graphene bond, whereas the metallic bond formed between M and Pt where the $W_{sep}^{\text{Pt–M}}$ monotonically increased with ΔZ^{Pt}. Figure 7.7(a) plots $W_{sep}^{\text{C–M}}$ and the charge transfer from metal adatom to graphene, ΔZ^C. Co, for instance, donated a charge of 0.31 to carbon and 0.33 to Pt. On the other hand, Ti donated a charge of 0.51 to carbon and 1.53 to Pt. While Ti donated more charge to carbon than Co, Co exhibited a similar $W_{sep}^{\text{C–M}}$ compared to Ti. Hence, $W_{sep}^{\text{C–M}}$ did not correlate with the charge transfer from metal to carbon.

The charge density difference analysis showed (Figure 7.6) that the group VIII elements (Co, Ni, Ru, Rh, Os and Ir) donated their charges more equally to Pt and graphene. Consequently, the strength of the C–M bond was assumed to depend on the adatom's capability to exchange/share its electrons equally between the two sides of the interface (Pt and graphene)–a capability that can be named as the anchoring ability of an adatom between the Pt and the carbon. Here, the anchoring ability of an adatom is defined as the ratio of the charge donated from the adatom to the graphene, over the charge donated to the Pt, $\Delta Z^C/\Delta Z^{Pt}$, as shown in Figure 7.7(b). This figure shows that the elements that provided larger $W_{sep}^{\text{C–M}}$ values donated more electronic charge to graphene compared to Pt,

such that for Co this ratio was 0.93, but for Ti it was 0.33. Similarly, fifth-row TM elements Ru and Rh donated their electrons equally to Pt and graphene, resulting in higher $W_{sep}^{\text{C-M}}$ values than Zr and Nb. Figure 7.7(b) illustrates that, for values of $\Delta Z^C / \Delta Z^{Pt} \geq 1.0$, the adatom preferred to exchange its electrons with carbon rather than with Pt. Among all the metals considered, this ratio was the highest (1.41) for Ir—showing that Ir prefers to exchange its electrons with carbon rather than Pt, which results in the largest $W_{sep}^{\text{C-M}}$, and thus Ir is highly effective for anchoring Pt to graphite, as are Re, Ru, Os and Rh.

7.3.4 Technological implications

The effect of different metal adatoms on the improvement of the Pt/graphene interface strength was investigated systematically by comparing their effect on interfacial bond strength and interface electronic structure. The C−M bond in the Pt/graphene interface was weaker than the Pt−M bond (Figure 7.3), suggesting that the interface would break from the C−M bond. Most of the adatoms (excluding Al, Au and Zn) were found to enhance the Pt/graphene interface strength, while some metals caused a more prominent increase in the $W_{sep}^{\text{C-M}}$. Therefore, it is expected that the presence of metals at the Pt/graphene interfaces found in fuel cells will help anchor the Pt particles, yielding more resistance against Pt migration on the carbon surface. The observations made in fuel cell experiments [34] suggesting that alloying the Pt decreased the particle agglomeration can be explained by these results. The relationship between $W_{sep}^{\text{C-M}}$ values and the bridging ability of an adatom at the interface can be used to select a suitable metal for anchoring Pt nanoparticles in fuel cell catalysts, and hence provide a design method for more durable fuel cells.

The PDOS of carbon atoms (Figure 7.5) showed that in the presence of certain metals (Ti, Co, Zr and Ru) the band gap of graphene disappeared and graphene was metalized, resulting in a better conduction between the Pt catalyst and the carbon and more efficient fuel cell operation. While carbon black is generally used to support Pt particles in fuel cells, this study considered applying metallic adatoms to a perfect graphene surface, whereas vacancies and defects would locate on the carbon's surface. It was reported that edge and defect sites on the carbon surfaces had stronger interactions with Pt [76, 77] compared to basal planes. However, a metal that can improve the strength of the weaker Pt–graphite

basal surface interaction can also improve the interaction between the graphite edge and defect sites as well as the overall adhesion between Pt and C. Recent DFT calculations, however, have shown that transition metal atoms bonded more strongly to graphene in the presence of vacancies [6], so the presence of defects on carbon are not expected to oppose the results of this work.

The coverage of adatoms on the graphene surface can affect the work of separation of adatoms on the graphene surface as reported in the literature [78–80]. The Zr/C coverage that corresponds to a ratio of 0.375, with two adatoms located at the 'top' site and one adatom at the 'hollow' site on the graphene surface, was found to be most stable configuration for Zr/C [78]. In an earlier study [81] a coverage of 0.375 was adopted for selected metals namely Ti, Cr and Au that provided low, intermediate and high work of separation values at the M/graphene interface. The following order was maintained for both 0.125 or 0.375 M/C coverage ratios; $W_{sep}^{C-Ti} > W_{sep}^{C-Cr} > W_{sep}^{C-Au}$ and $W_{sep}^{Pt-Ti} > W_{sep}^{Pt-Cr} > W_{sep}^{Pt-Au}$. Therefore, the use of a single adatom on a graphene surface with coverage ratio of 0.125 is reasonable and this selection facilitated comparison of W_{sep}^{C-M} and W_{sep}^{Pt-M} values between the 25 elements considered in this work. Pursuant to this first round of screening work, the effect of coverage ratio can be considered for the promising adatoms suggested here in future studies.

In summary, it was predicted that if carbon surfaces could be modified by metals, the Pt nanoparticles would bind more strongly to carbon. A recent study showed that Pt adhesion to various carbon surfaces is enhanced after coating the carbon surfaces with Ti and Cr [81]. The modification of carbon structures by various metals [82–85] or the functionalization of the carbon structures [86–88] has been investigated in the literature to improve the physical and chemical properties of carbon structures. Metallic modifications were reported to alter the electronic and catalytic properties of carbon structures in several computational studies [89]. This study predicted that the interface strength between Pt and graphene would be enhanced by a metallic modification of the carbon surface, and that the most efficient metals for this purpose would be the Ir, Os, Ru, Rh and Re. Because graphene is the building block of many carbon structures, these metallic elements can be very effective in bridging the Pt and carbon structures in applications that involve contacts

between Pt and carbon, in addition to fuel cells. The results presented in this work can also be used to improve interfacial strength between other metals and graphene that typically show very weak binding similar to Pt, such as Cu, Ag, Pd and Au [17].

7.4 Conclusions

The strengthening of the Pt–graphene interface was studied using first principles calculations by inserting metallic adatoms between graphene and Pt. We considered 25 different metallic atoms (Sc, Ti, V, Cr, Mn, Fe, Co, Ni, Cu, Zn, Zr, Nb, Mo, Ru, Rh, Ta, W, Re, Os, Ir, Au, Li, Na, Mg and Al) and the effect of each of these adatoms on the work of separation of Pt−adatom and graphene−adatom bonds was calculated. It was concluded that:

1. Modification of the graphene surface with metal adatoms improved the Pt−graphene interfacial strength, with the exception of Al, Zn and Au. Transition metals with unfilled d orbitals, including Ni, Co, Sc, V, Cr, Ti, Rh, Ru, Nb, Zr, W, Mo, Ta, Re, Ir and Os increased the Pt/graphene interfacial strength from 0.009 J m^{-2} to above 0.5 J m^{-2}.

2. The metal adatom-modified Pt−graphene interface tended to break at the graphene-adatom bond rather than at the Pt-adatom bond. The latter bond had a metallic character, and its strength increased with the amount of charge transferred from the adatom to the Pt.

3. Early transition metals (Sc, Ti, V, Zr, Nb and Ta) formed strong bonds with graphene and Pt (111) surfaces when they were adsorbed at these surfaces. When their behavior as adatoms at the Pt/graphene interface was considered, however, it was observed that the graphene−adatom bond became weakened as shown by the adatom's stronger tendency to bond with Pt.

4. The graphene−adatom bond was mostly covalent and its strength was related to the distribution of charge donated from metal adatoms to the Pt and graphene surfaces. The extent of charge distribution determined an adatom's bridging ability between Pt and graphene. The work of separation of the carbon−adatom bond was proportional

to the ratio of the charge transferred from the adatom to the carbon over the charge transferred to the platinum. For Ir, Os, Ru, Rh and Re this ratio was about 1.0, making these elements the most effective adatoms for anchoring Pt to graphene.

5. The density of states analysis showed that the incorporation of metal adatoms at the Pt/graphene interface resulted in the metallization of the graphene surface and, hence, was expected to enhance the electronic conductivity between Pt and graphene. These results provide insight into the modification of the graphene surface to enhance its bonding with Pt or with other metals for applications in fuel cells and optical and electronic devices.
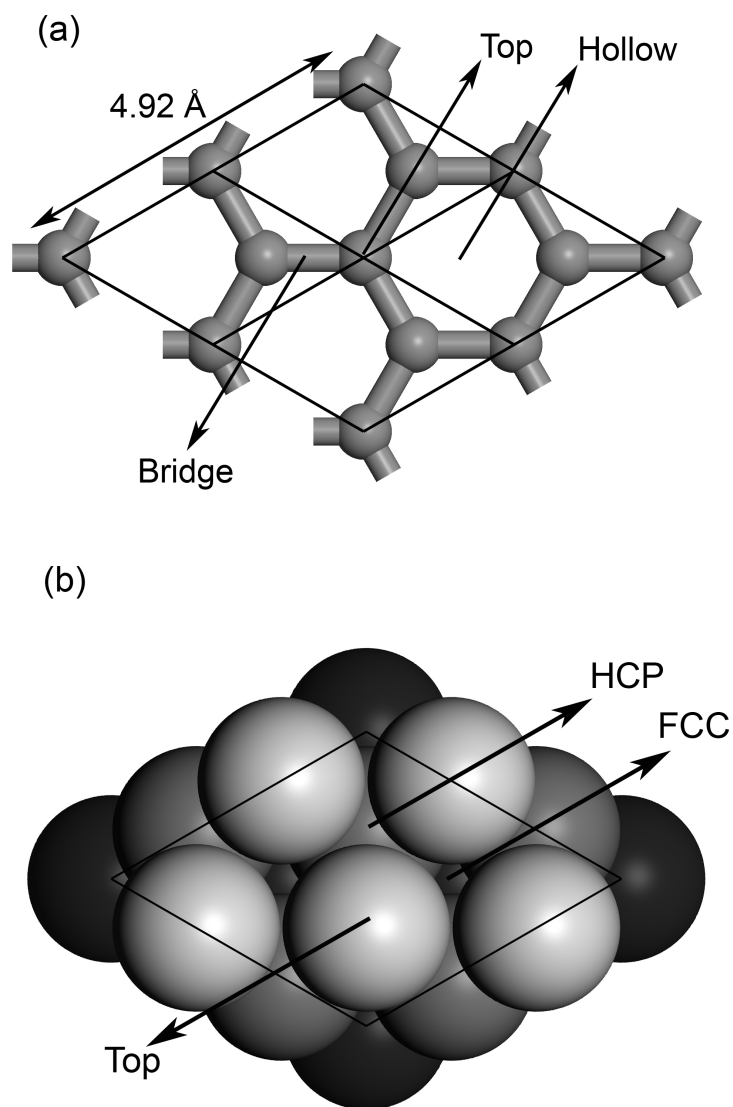
Figure 7.1: (a) Graphite (0001) 2×2 surface showing three adsorption sites: top, bridge and hollow. (b) Pt (111) surface showing the three adsorption sites: top, fcc and hcp.
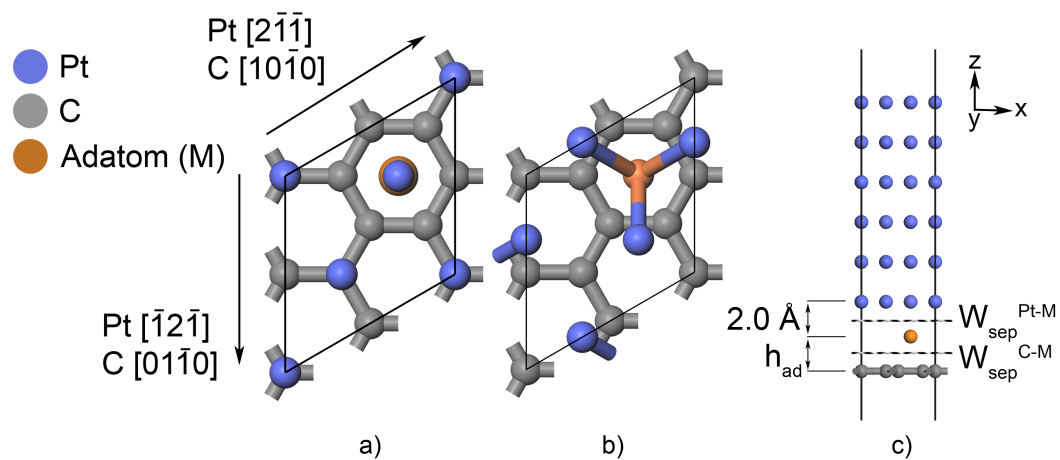
Figure 7.2: Pt/graphene interface model: interface registry for adatom (a) below Pt top position, (b) below Pt fcc position and (c) slab model used in calculations.
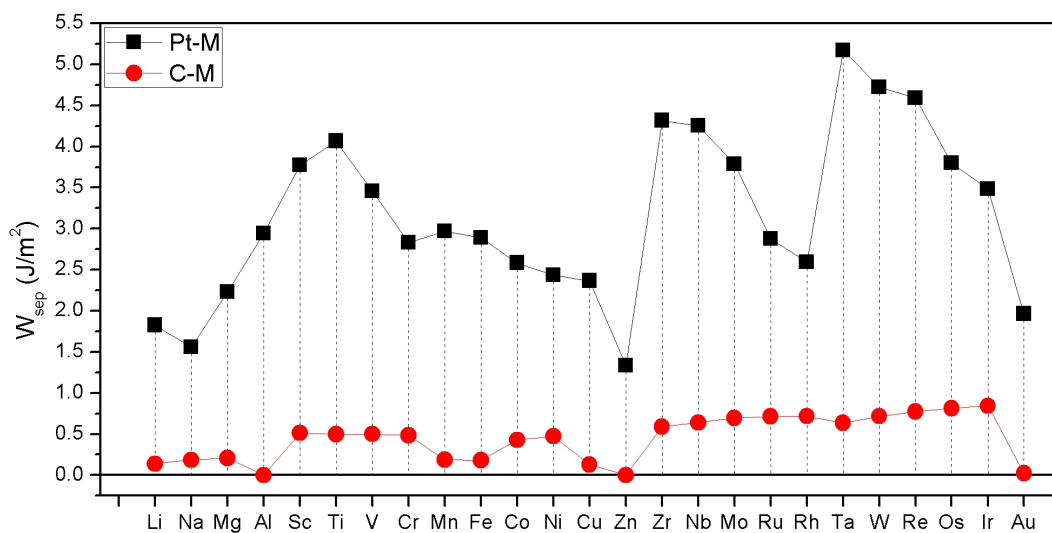
Figure 7.3: Work of separation for breaking Pt/graphene interface from Pt−adatom (Pt−M) bond and breaking the interface from the carbon−adatom (C−M) bond.

Figure 7.4: (a) The relationship between the work of separation for Pt−M bond with the associated charge transfer from metals at Pt/graphene interface to the Pt surface (dotted lines added for guidance). (b) The relationship between the work of separation for Pt−M bond and the charge density at the Wigner−Seitz radius for the adatoms added with the charge transfer to Pt.
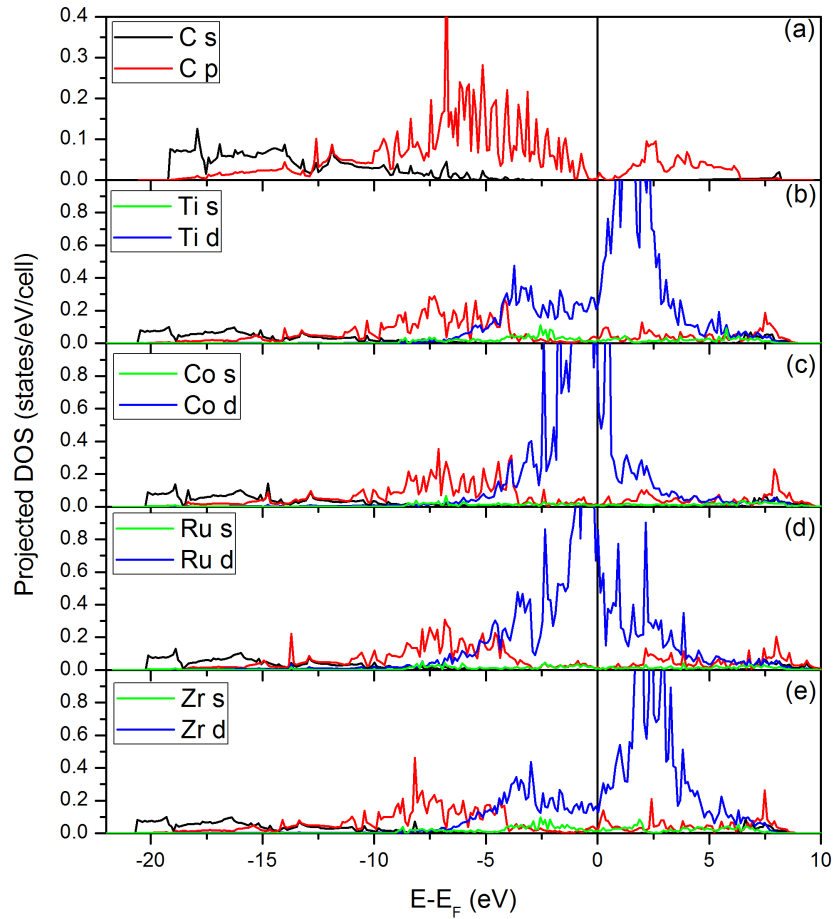
Figure 7.5: Partial DOS of carbon and adatoms at the Pt/graphene interface (a) without anchoring atoms and (b)−(e) with the anchoring atoms (b) Ti, (c) Co, (d) Ru and (e) Zr. The C s and p states are shown in black and red lines in all of the figures. The metal s and d states are shown in green and blue lines for the corresponding adatom as depicted in (b)−(e).
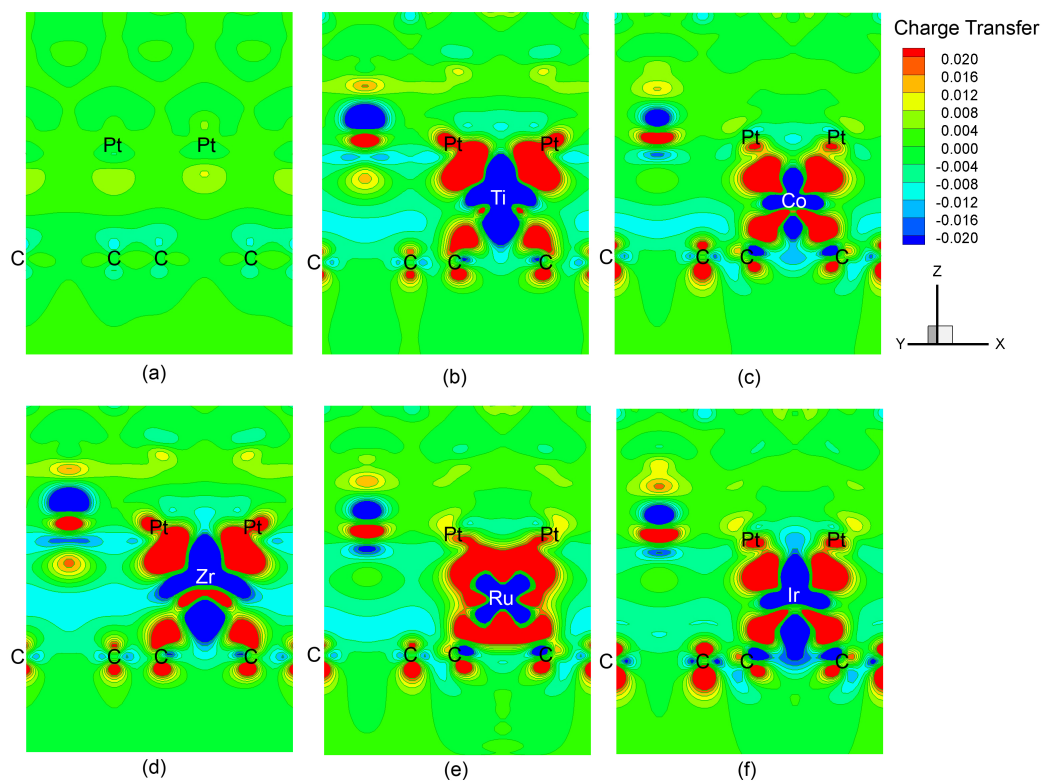
Figure 7.6: Charge density difference plots of (a) the Pt/graphene interface and the Pt/graphene interface with anchoring atoms (b) Ti, (c) Co, (d) Zr, (e) Ru and (f) Ir. Slices were taken from the longer diagonal of the interface. Positive values show the charge accumulated regions and negative values show charge depleted regions. The labels for C and metals shows the exact atomic positions while the Pt labels only show the positions of Pt atoms in the $z-$direction because the Pt atoms were not lying on the diagonal of the simulation cell.
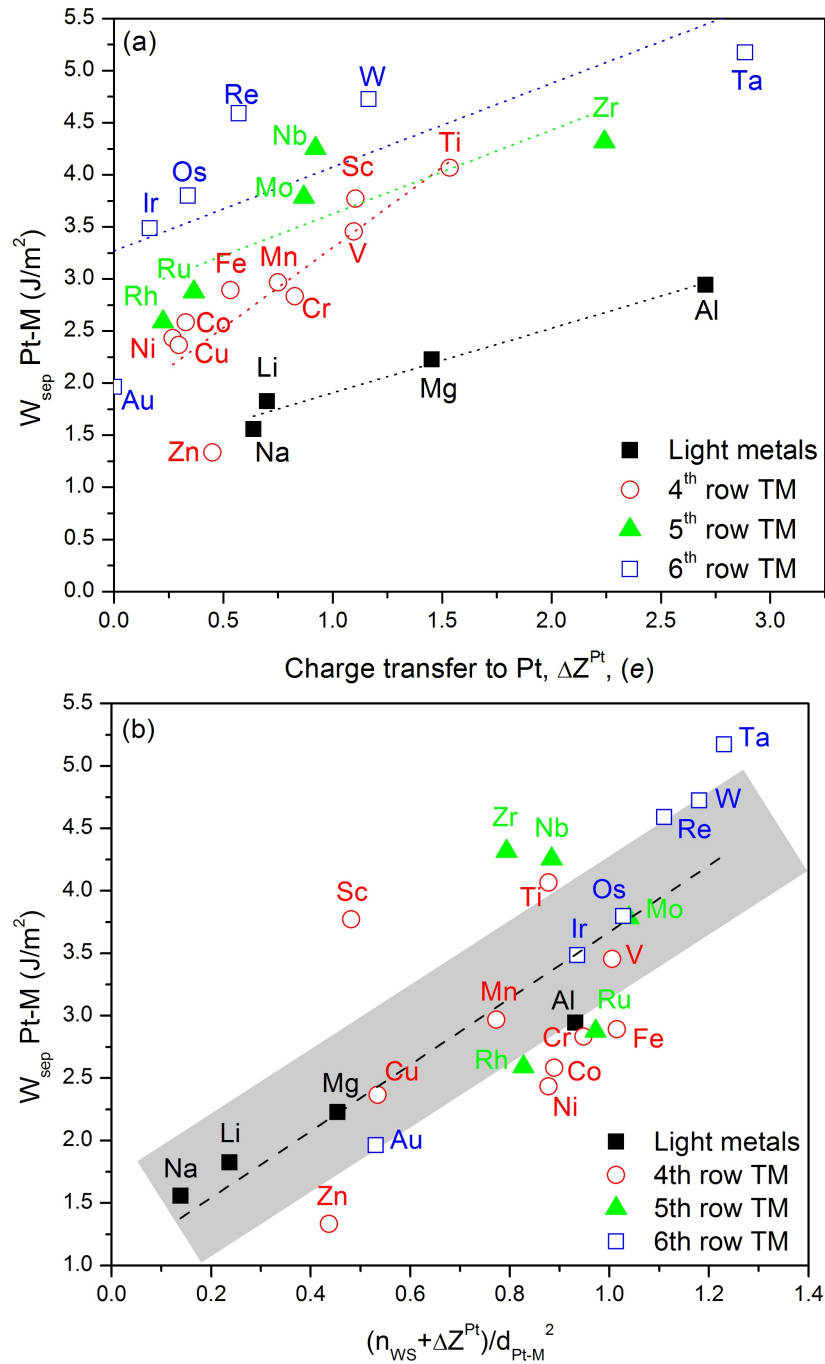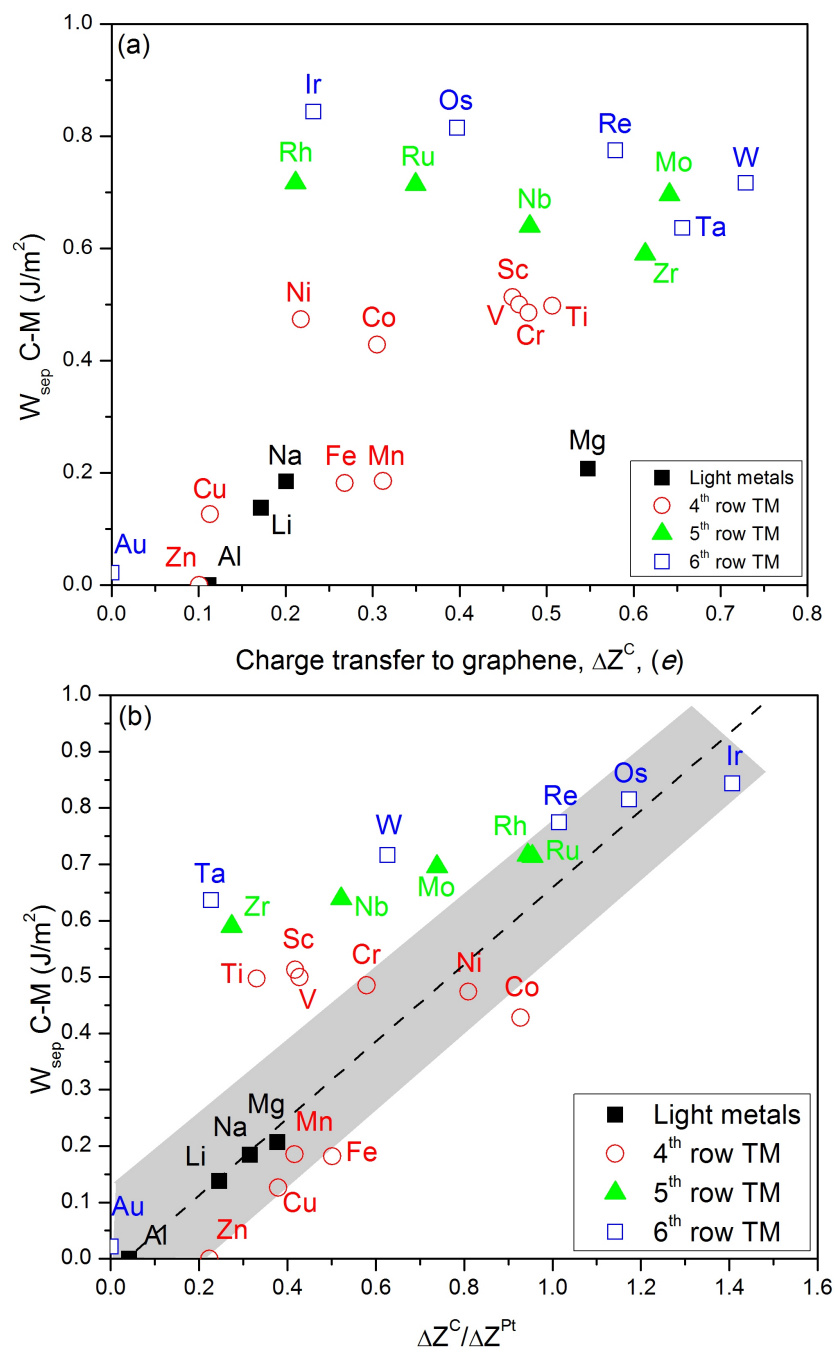
Figure 7.7: (a) The relationship between the work of separation for C−M bond with the associated charge transfer from metals at the Pt/graphene interface to the graphene surface. (b) The relationship between the work of separation for C−M bond with the associated charge transfer ratio 'charge transfer to C/charge transfer to Pt' at the Pt/graphene interface (dashed line added for guidance).

Bibliography

[1] H. W. Kroto, J. R. Heath, S. C. O'Brien, R. F. Curl, and R. E. Smalley. C60: Buckminsterfullerene. *Nature*, 318(6042):162–163, 1985.

[2] K. S. Novoselov, D. Jiang, F. Schedin, T. J. Booth, V. V. Khotkevich, S. V. Morozov, and A. K. Geim. Two-dimensional atomic crystals. *Proceedings of the National Academy of Sciences of the United States of America*, 102(30):10451–10453, 2005.

[3] K. S. Novoselov, A. K. Geim, S. V. Morozov, D. Jiang, Y. Zhang, S. V. Dubonos, I. V. Grigorieva, and A. A. Firsov. Electric field in atomically thin carbon films. *Science*, 306(5696):666–669, 2004.

[4] S. Iijima. Helical microtubules of graphitic carbon. *Nature*, 354(6348):56–58, 1991.

[5] N. Gorjizadeh, A. A. Farajian, K. Esfarjani, and Y. Kawazoe. Spin and band-gap engineering in doped graphene nanoribbons. *Physical Review B*, 78(15):155427, 2008.

[6] A. V. Krasheninnikov, P. O. Lehtinen, A. S. Foster, P. Pyykkö, and R. M. Nieminen. Embedding transition-metal atoms in graphene: Structure, bonding, and magnetism. *Physical Review Letters*, 102(12):126807, 2009.

[7] G. Giovannetti, P. A. Khomyakov, G. Brocks, V. M. Karpan, J. Van Den Brink, and P. J. Kelly. Doping graphene with metal contacts. *Physical Review Letters*, 101(2):026803, 2008.

[8] O. Leenaerts, B. Partoens, and F. M. Peeters. Adsorption of H_2O, NH_3, CO, NO_2, and NO on graphene: A first-principles study. *Physical Review B*, 77(12):125416, 2008.

[9] L. Liu, S. Ryu, M. R. Tomasik, E. Stolyarova, N. Jung, M. S. Hybertsen, M. L. Steiger-
wald, L. E. Brus, and G. W. Flynn. Graphene oxidation: Thickness-dependent etching
and strong chemical doping. *Nano Letters*, 8(7):1965–1970, 2008.

[10] T. O. Wehling, K. S. Novoselov, S. V. Morozov, E. E. Vdovin, M. I. Katsnelson, A. K.
Geim, and A. I. Lichtenstein. Molecular doping of graphene. *Nano Letters*, 8(1):173–
177, 2008.

[11] A. L. M. Reddy, A. Srivastava, S. R. Gowda, H. Gullapalli, M. Dubey, and P. M.
Ajayan. Synthesis of nitrogen-doped graphene films for lithium battery application.
ACS Nano, 4(11):6337–6342, 2010.

[12] R. A. Nistor, D. M. Newns, and G. J. Martyna. The role of chemistry in graphene
doping for carbon-based electronics. *ACS Nano*, 5(4):3096–3103, 2011.

[13] F. Schedin, A. K. Geim, S. V. Morozov, E. W. Hill, P. Blake, M. I. Katsnelson, and
K. S. Novoselov. Detection of individual gas molecules adsorbed on graphene. *Nature
Materials*, 6(9):652–655, 2007.

[14] Y. Okamoto. Density-functional calculations of graphene interfaces with Pt(111) and
Pt(111)/RuML surfaces. *Chemical Physics Letters*, 407(4-6):354–357, 2005.

[15] A. B. Preobrajenski, M. L. Ng, A. S. Vinogradov, and N. Mårtensson. Control-
ling graphene corrugation on lattice-mismatched substrates. *Physical Review B*,
78(7):073401, 2008.

[16] K. Okazaki-Maeda, T. Akita, S. Tanaka, and M. Kohyama. First-principles calculations
of M_{10}/graphene (M = Au, Pt) systems - atomic structures and hydrogen adsorption.
Materials Transactions, 49(11):2441–2444, 2008.

[17] P. A. Khomyakov, G. Giovannetti, P. C. Rusu, G. Brocks, J. Van Den Brink, and P. J.
Kelly. First-principles study of the interaction and charge transfer between graphene
and metals. *Physical Review B*, 79(19):195425, 2009.

[18] C. K. Acharya and C. H. Turner. CO oxidation with Pt(111) supported on pure and
boron-doped carbon: A DFT investigation. *Surface Science*, 602(23):3595–3602, 2008.

[19] P. Sutter, J. T. Sadowski, and E. Sutter. Graphene on Pt(111): Growth and substrate interaction. *Physical Review B*, 80(24):245411, 2009.

[20] A. K. Geim and K. S. Novoselov. The rise of graphene. *Nature Materials*, 6(3):183–191, 2007.

[21] G. Hooger. *Fuel Cell Technology Handbook*. CRC Press, Boca Raton, 2003.

[22] A. Débart, J. Bao, G. Armstrong, and P. G. Bruce. An O_2 cathode for rechargeable lithium batteries: The effect of a catalyst. *Journal of Power Sources*, 174(2):1177–1182, 2007.

[23] Y. C. Lu, H. A. Gasteiger, M. C. Parent, V. Chiloyan, and Y. Shao-Horn. The influence of catalysts on discharge and charge voltages of rechargeable li-oxygen batteries. *Electrochemical and Solid-State Letters*, 13(6):A72, 2010.

[24] M. F. Mathias, R. Makharia, H. A. Gasteiger, J. J. Conley, T. J. Fuller, C. J. Gittleman, S. S. Kocha, D. P. Miller, C. K. Mittelsteadt, T. Xie, S. G. Van, and P. T. Yu. Two fuel cell cars in every garage? *Electrochemical Society Interface*, 14(3):24–35, 2005.

[25] Mahlon S. Wilson, Fernando H. Garzon, Kurt E. Sickafus, and Shimshon Gottesfeld. Surface area loss of supported platinum in polymer electrolyte fuel cells. *Journal of the Electrochemical Society*, 140(10):2872–2877, 1993.

[26] F. A. De Bruijn, V. A. T. Dam, and G. J. M. Janssen. Review: Durability and degradation issues of pem fuel cell components. *Fuel Cells*, 8(1):3–22, 2008.

[27] R. Borup, J. Meyers, B. Pivovar, Y. S. Kim, R. Mukundan, N. Garland, D. Myers, M. Wilson, F. Garzon, D. Wood, P. Zelenay, K. More, K. Stroh, T. Zawodzinski, J. Boncella, J. E. McGrath, M. Inaba, K. Miyatake, M. Hori, K. Ota, Z. Ogumi, S. Miyata, A. Nishikata, Z. Siroma, Y. Uchimoto, K. Yasuda, K. I Kimijima, and N. Iwashita. Scientific aspects of polymer electrolyte fuel cell durability and degradation. *Chemical Reviews*, 107(10):3904–3951, 2007.

[28] J. Wu, X. Z. Yuan, J. J. Martin, H. Wang, J. Zhang, J. Shen, S. Wu, and W. Merida. A review of pem fuel cell durability: Degradation mechanisms and mitigation strategies. *Journal of Power Sources*, 184(1):104–119, 2008.

[29] Y. Shao, G. Yin, and Y. Gao. Understanding and approaches for the durability issues of Pt-based catalysts for PEM fuel cell. *Journal of Power Sources*, 171(2):558–566, 2007.

[30] X. Yu and S. Ye. Recent advances in activity and durability enhancement of Pt/C catalytic cathode in PEMFC. part ii: Degradation mechanism and durability enhancement of carbon supported platinum catalyst. *Journal of Power Sources*, 172(1):145–154, 2007.

[31] E. Antolini, J. R. C. Salgado, and E. R. Gonzalez. The stability of Pt-M (M = first row transition metal) alloy catalysts and its effect on the activity in low temperature fuel cells. a literature review and tests on a Pt-Co catalyst. *Journal of Power Sources*, 160(2 SPEC. ISS.):957–968, 2006.

[32] H. R. Colón-Mercado and B. N. Popov. Stability of platinum based alloy cathode catalysts in PEM fuel cells. *Journal of Power Sources*, 155(2):253–263, 2006.

[33] H. R. Colón-Mercado, H. Kim, and B. N. Popov. Durability study of Pt_3Ni_1 catalysts as cathode in PEM fuel cells. *Electrochemistry Communications*, 6(8):795–799, 2004.

[34] Z. Wei, H. Guo, and Z. Tang. Heat treatment of carbon-based powders carrying platinum alloy catalysts for oxygen reduction: Influence on corrosion resistance and particle size. *Journal of Power Sources*, 62(2):233–236, 1996.

[35] S. Mukerjee and S. Srinivasan. Enhanced electrocatalysis of oxygen reduction on platinum alloys in proton exchange membrane fuel cells. *Journal of Electroanalytical Chemistry*, 357(1-2):201–224, 1993.

[36] S. Mukerjee, R. C. Urian, S. J. Lee, E. A. Ticianelli, and J. McBreen. Electrocatalysis of CO tolerance by carbon-supported PtMo electrocatalysts in PEMFCs. *Journal of the Electrochemical Society*, 151(7):A1094–A1103, 2004.

[37] J. Zhang, K. Sasaki, E. Sutter, and R. R. Adzic. Stabilization of platinum oxygen-reduction electrocatalysts using gold clusters. *Science*, 315(5809):220–222, 2007.

[38] L. Protsailo and A. Haug. Alternative catalysts for PEM FCs: Performance and durability at normal and high temperature operations. In *208th Meeting of The Electrochemical Society*, volume MA2005-02, 2005.

[39] G. Liu, H. Zhang, Y. Zhai, Y. Zhang, D. Xu, and Z. g Shao. Pt_4ZrO_2/C cathode catalyst for improved durability in high temperature PEMFC based on H_3PO_4 doped PBI. *Electrochemistry Communications*, 9(1):135–141, 2007.

[40] J. Greeley and M. Mavrikakis. Alloy catalysts designed from first principles. *Nature Materials*, 3(11):810–815, 2004.

[41] V. R. Stamenkovic, B. Fowler, B. S. Mun, G. Wang, P. N. Ross, C. A. Lucas, and N. M. Markovic. Improved oxygen reduction activity on $Pt_3Ni(111)$ via increased surface site availability. *Science*, 315(5811):493–497, 2007.

[42] F. R. De Boer, R. Boom, W. C. M. Mattens, A. R. Miedema, and A. K. Niessen. *Cohesion in Metals Transition Metal Alloys*. North-Holland, Amsterdam, 1988.

[43] F. Coloma, A. Sepúlveda-Escribano, J. L. G. Fierro, and F. Rodríguez-Reinoso. Preparation of platinum supported on pregraphitized carbon blacks. *Langmuir*, 10(3):750–755, 1994.

[44] S. C. Roy, A. W. Harding, A. E. Russell, and K. M. Thomas. Spectroelectrochemical study of the role played by carbon functionality in fuel cell electrodes. *Journal of the Electrochemical Society*, 144(7):2323–2328, 1997.

[45] D. J. Guo and H. L. Li. High dispersion and electrocatalytic properties of Pt nanoparticles on SWNT bundles. *Journal of Electroanalytical Chemistry*, 573(1):197–202, 2004.

[46] Y. Shao, G. Yin, Y. Gao, and P. Shi. Durability study of Pt/C and Pt/CNTs catalysts under simulated PEM fuel cell conditions. *Journal of the Electrochemical Society*, 153(6):A1093–A1097, 2006.

[47] E. Yoo, T. Okata, T. Akita, M. Kohyama, J. Nakamura, and I. Honma. Enhanced electrocatalytic activity of Pt subnanoclusters on graphene nanosheet surface. *Nano Letters*, 9(6):2255–2259, 2009.

[48] W. Q. Deng, Y. Matsuda, and III W. A. Goddard. Bifunctional anchors connecting carbon nanotubes to metal electrodes for improved nanoelectronics. *Journal of the American Chemical Society*, 129(32):9834–9835, 2007.

[49] X. Lepró, E. Terrés, Y. Vega-Cantú, F. J. Rodríguez-Macías, H. Muramatsu, Y. A. Kim, T. Hayahsi, M. Endo, M. Torres R., and M. Terrones. Efficient anchorage of Pt clusters on N-doped carbon nanotubes and their catalytic activity. *Chemical Physics Letters*, 463(1-3):124–129, 2008.

[50] C. K. Acharya and C. Heath Turner. Stabilization of platinum clusters by substitutional boron dopants in carbon supports. *Journal of Physical Chemistry B*, 110(36):17706–17710, 2006.

[51] C. K. Acharya, W. Li, Z. Liu, G. Kwon, C. Heath Turner, A. M. Lane, D. Nikles, T. Klein, and M. Weaver. Effect of boron doping in the carbon support on platinum nanoparticles and carbon corrosion. *Journal of Power Sources*, 192(2):324–329, 2009.

[52] Yue Qi and L. G. Hector. Adhesion and adhesive transfer at aluminum/diamond interfaces: a first-principles study. *Physical Review B*, 69(23):235401, 06/15 2004.

[53] Yue Qi, Jr. L. G. Hector, N. Ooi, and J. B. Adams. A first principles study of adhesion and adhesive transfer at Al(111)/graphite(0001). *Surface Science*, 581(2-3):155–168, 05/01 2005.

[54] Y. Qi, E. Konca, and A. T. Alpas. Atmospheric effects on the adhesion and friction between non-hydrogenated diamond-like carbon (DLC) coating and aluminum - a first principles investigation. *Surface Science*, 600(15):2955–2965, 2006.

[55] F. G. Sen, Y. Qi, and A. T. Alpas. Material transfer mechanisms between aluminum and fluorinated carbon interfaces. *Acta Materialia*, 59:2601–2614, 2011.

[56] Y. Zhang, M. L. Toebes, A. D. Van Eerden, W. E. O'Grady, K. P. De Jong, and D. C. Koningsberger. Metal particle size and structure of the metal-support interface of carbon-supported platinum catalysts as determined with EXAFS spectroscopy. *Journal of Physical Chemistry B*, 108(48):18509–18519, 2004.

[57] J. T. Chou and K. Sasaki. Microstructural analysis of catalyst/catalyst support interfaces of pefc electrocatalysts. *Solid State Ionics*, 179(27-32):1405–1408, 2008.

[58] P. Trucano and R. Chen. Structure of graphite by neutron diffraction. *Nature*, 258(5531):136–137, 1975.

[59] J. N. Israelachvili. *Intermolecular and Surface Forces*. Academic, San Diego, 2nd edition, 1992.

[60] W. Kohn and L. J. Sham. Self-consistent equations including exchange and correlation effects. *Physical review*, 140:A1133–A1138, 1965.

[61] J. P. Perdew, J. A. Chevary, S. H. Vosko, K. A. Jackson, M. R. Pederson, D. J. Singh, and C. Fiolhais. Atoms, molecules, solids, and surfaces: Applications of the generalized gradient approximation for exchange and correlation. *Physical Review B*, 46(11):6671–6687, 1992.

[62] G. Kresse and J. Hafner. Ab initio molecular-dynamics simulation of the liquid-metalamorphous- semiconductor transition in germanium. *Physical Review B*, 49(20):14251–14269, 1994.

[63] G. Kresse and J. Furthmüller. Efficiency of ab-initio total energy calculations for metals and semiconductors using a plane-wave basis set. *Computational Materials Science*, 6(1):15–50, 1996.

[64] P. E. Blöchl. Projector augmented-wave method. *Physical Review B*, 50(24):17953–17979, 1994.

[65] G. Kresse and D. Joubert. From ultrasoft pseudopotentials to the projector augmented-wave method. *Physical Review B*, 59(3):1758–1775, 1999.

[66] M. Methfessel and A. T. Paxton. High-precision sampling for brillouin-zone integration in metals. *Physical Review B*, 40(6):3616–3621, 1989.

[67] P. E. Blöchl, O. Jepsen, and O. K. Andersen. Improved tetrahedron method for brillouin-zone integrations. *Physical Review B*, 49(23):16223–16233, 1994.

[68] K. T. Chan, J. B. Neaton, and M. L. Cohen. First-principles study of metal adatom adsorption on graphene. *Physical Review B*, 77(23):235430, 2008.

[69] H. Sevinçli, M. Topsakal, E. Durgun, and S. Ciraci. Electronic and magnetic properties of 3d transition-metal atom adsorbed graphene and graphene nanoribbons. *Physical Review B*, 77(19):195434, 2008.

[70] I. Pašti and S. Mentus. First principles study of adsorption of metals on Pt(111) surface. *Journal of Alloys and Compounds*, 497(1-2):38–45, 2010.

[71] R. F. W. Bader. Atoms in molecules. *Accounts of Chemical Research*, 18(1):9–15, 1985.

[72] G. Henkelman, A. Arnaldsson, and H. Jónsson. A fast and robust algorithm for bader decomposition of charge density. *Computational Materials Science*, 36(3):354–360, 2006.

[73] A. R. Miedema, P. F. de Châtel, and F. R. de Boer. Cohesion in alloys - fundamentals of a semi-empirical model. *Physica B+C*, 100(1):1–28, 1980.

[74] B. Cordero, V. Gómez, A. E. Platero-Prats, M. Revés, J. Echeverría, E. Cremades, F. Barragán, and S. Alvarez. Covalent radii revisited. *Dalton Transactions*, 21:2832–2838, 2008.

[75] T. Kondo, Y. Iwasaki, Y. Honma, Y. Takagi, S. Okada, and J. Nakamura. Formation of nonbonding electronic states of graphite due to Pt-C hybridization. *Physical Review B*, 80(23):233408, 12/15 2009.

[76] C. F. Sanz-Navarro, P. O. Åstrand, D. Chen, M. Rønning, A. C. T. Van Duin, T. Jacob, and III W. A. Goddard. Molecular dynamics simulations of the interactions between

platinum clusters and carbon platelets. *Journal of Physical Chemistry A*, 112(7):1392–1402, 2008.

[77] I. Kvande, J. Zhu, T. J. Zhao, N. Hammer, M. Rønning, S. Raaen, J. C. Walmsley, and D. Chen. Importance of oxygen-free edge and defect sites for the immobilization of colloidal Pt oxide particles with implications for the preparation of CNF-supported catalysts. *Journal of Physical Chemistry C*, 114(4):1752–1762, 2010.

[78] Y. Sanchez-Paisal, D. Sanchez-Portal, and A. Ayuela. Ab initio calculations of zirconium adsorption and diffusion on graphene. *Physical Review B*, 80(4):045428, 2009.

[79] E. Loginova, N. C. Bartelt, P. J. Feibelmarr, and K. F. McCarty. Factors influencing graphene growth on metal surfaces. *New Journal of Physics*, 11:063046, 2009.

[80] K. H. Jin, S. M. Choi, and S. H. Jhi. Crossover in the adsorption properties of alkali metals on graphene. *Physical Review B*, 82(3):033414, 2010.

[81] M. Shafiei, A. R. Riahi, F. G. Sen, and A. T. Alpas. Improvement of platinum adhesion to carbon surfaces using PVD coatings. *Surface and Coatings Technology*, 205(2):306–311, 2010.

[82] A. Thess, R. Lee, P. Nikolaev, H. Dai, P. Petit, J. Robert, C. Xu, Y. H. Lee, S. G. Kim, A. G. Rinzler, D. T. Colbert, G. E. Scuseria, D. TomÃ¡nek, J. E. Fischer, and R. E. Smalley. Crystalline ropes of metallic carbon nanotubes. *Science*, 273(5274):483–487, 1996.

[83] A. F. Hebard, M. J. Rosseinsky, R. C. Haddon, D. W. Murphy, S. H. Glarum, T. T. M. Palstra, A. P. Ramirez, and A. R. Kortan. Superconductivity at 18 K in potassium-doped C60. *Nature*, 350(6319):600–601, 1991.

[84] A. M. Rao, P. C. Eklund, S. Bandow, A. Thess, and R. E. Smalley. Evidence for charge transfer in doped carbon nanotube bundles from raman scattering. *Nature*, 388(6639):257–259, 1997.

[85] R. S. Lee, H. J. Kim, J. E. Fischer, A. Thess, and R. E. Smalley. Conductivity enhancement in single-walled carbon nanotube bundles doped with K and Br. *Nature*, 388(6639):255–257, 1997.

[86] Y. P. Sun, K. Fu, Y. Lin, and W. Huang. Functionalized carbon nanotubes: Properties and applications. *Accounts of Chemical Research*, 35(12):1096–1104, 2002.

[87] A. Hirsch. Functionalization of single-walled carbon nanotubes. *Angewandte Chemie - International Edition*, 41(11):1853–1859, 2002.

[88] S. S. Wong, E. Joselevich, A. T. Woolley, C. L. Cheung, and C. M. Lieber. Covalently functionalized nanotubes as nanometresized probes in chemistry and biology. *Nature*, 394(6688):52–55, 1998.

[89] S. R. Stoyanov, A. V. Titov, and P. Král. Transition metal and nitrogen doped carbon nanostructures. *Coordination Chemistry Reviews*, 253(23-24):2852–2871, 2009.

Chapter 8

General Summary and Conclusions

Automotive components that are made of lightweight and energy efficient materials that are used in contact with other components experience adhesion problems at the interface between these materials during their operation, as well as during their manufacturing processes. The objective of this study was to use synergistically combined computational and experimental methods to address these adhesion problems in order to increase the efficiency and durability of automotive components, as well as to increase the efficiency of their manufacturing processes and the quality of the resulting products. Specifically, carbon based coatings and carbonaceous tribolayers, that show a low amount of friction and adhesion against Al components, were investigated as model materials, and as interfaces for fundamental studies. Accordingly, new adhesion mechanisms were revealed (Chapters 2, 3, and 4) that provided new insights into the development of low friction and/or adhesion resistant surfaces. As was shown in the main body of this dissertation, the adhesion phenomenon in lightweight Al alloy manufacturing processes manifests itself in different ways depending on the operating atmosphere and temperature. The adhesion of Al to tool surfaces can be mitigated by the use of diamond-like carbon (DLC) coatings on the tools for applications at room temperature (and to a certain extent at moderately high temperatures), but at elevated temperatures, such as those occurring in hot forming processes, most DLC coatings is not effective. In order to mitigate the Al adhesion to tool surfaces at high temperatures, the oxidation and deformation of aluminum surfaces and tribolayer formation were examined (Chapters 5 and 6), and oxidation was revealed to cause superplasticity in the oxide and

enhance the adhesion of Al at high temperatures, as in machining and hot forming processes. In the case of fuel cell technology, adhesion has to be considered to be an advantage rather than an impediment. For efficient catalyst retention in particular, the adhesion between the Pt catalyst and the carbon support needs to be strengthened, which is critical in enhancing the long term durability of fuel cells (as examined in Chapter 7). All of these technologically important adhesion problems with lightweight and energy materials originate from the fundamental atomic interactions that take place at the contact interfaces. In this dissertation, a common methodology was followed in order to examine the origins of these problems, which consisted of a detailed study of material transfer events using atomistic simulation methods and carefully designed tribological experiments. Material and surface characterization methods served to elucidate the microstructural and chemical changes that occur at the contact interfaces. Interfacial microstructural properties, tribolayers, material transfer events, and compound formation processes were determined by using cross-sectional SEM/EDS, FIB-TEM, and XPS methods. Carefully designed tribological experiments were carried out measuring the interfacial mechanical properties, namely friction and adhesion propensity, as a function of the applied load, environment (oxidizing, vacuum etc.) and temperature. The atomistic models of the surfaces and interfaces were constructed to capture any possible chemical changes that could be observed in these experiments, with the use of proper approximations. This methodology (combining atomistic simulations and experiments) contributed to the depiction of the atomistic and microstructural aspects of the adhesion mechanisms in different problems. The overall impacts of this work are summarized in the following sections:

8.1 Adhesion mitigating DLC coatings for Al manufacturing

For the use of DLC coatings in manufacturing and sliding contact applications against Al alloys, the required adhesion mitigating and low friction properties were often achieved following the formation of carbonaceous transfer layers on the Al counterfaces. The new insights gained by this study involve a demonstration of the fact that the passivation of these transfer layers played a critically important role in achieving low friction properties,

in such a way that the carbon layer that was not passivated by -H, -OH, or -F was not effective in reducing friction. The observations that showed the importance of passivation were revealed by conducting sliding contact experiments on Al that was rubbed against an a-C:H:F coated disk, successfully replicating the adhesion conditions of real sliding and manufacturing applications. Material modeling techniques, particularly the use of first principles calculations based on density functional theory (DFT), elucidated the adhesion mechanisms. In this way the effect of the incorporation of F, Si, and O on the adhesion mitigating properties of DLC coatings against Al was investigated. The most important results arising from these studies are as follows:

The bonding structure and stability of the F–incorporated DLC surfaces studied using DFT calculations on an F–terminated diamond (111) surface showed that strong C–F ionic bonds at the diamond surface were formed. This effect was stronger than the effect in a-C:H because of the more effective surface coverage of the large F atoms when compared to H. By building a surface phase diagram, it was shown that the F–terminated diamond surface was more stable in a larger phase space than the H termination. When the F–terminated diamond (111) surface was put in contact with the Al (111) surface, F atoms transferred to the Al surface in increasing quantities with an increase in the contact pressure, and this F transfer led to the formation of a stable AlF_3 compound at the Al surface. The presence of AlF_3 was confirmed by XPS and the cross-sectional FIB-TEM analyses of the transfer layers formed on the Al counterface that was placed in sliding contact against the a-C:H:F (containing 3 at.% F and 26 at.% H). The steady-state COF of the a-C:H:F coating was 0.14, which was 30% lower than the a-C:H coating. The generation of larger repulsive forces between two F–passivated surfaces, when compared to two H–passivated surfaces, was shown to be responsible for the low COF between the Al and F–incorporated DLC. As a result, the F–incorporated DLC is better suited for Al sliding applications than the a-C:H after the formation of stable transfer layers on Al counterface.

When a 20 at.% Si and 14 at.% O incorporated DLC coating containing 12 at.% F, and 18 at.% H (a-C:H:Si:O:F) was tested against Al in ambient air (39% relative humidity) and vacuum (6.5×10^{-3} Pa) atmosphere, a low steady state COF of 0.08 under both testing atmospheres was observed. Carbonaceous transfer layers incorporating F, Si, and O

225

compounds were formed on the Al, with an AlF_3 compound concentrated adjacent to the Al surface. The top surfaces of the carbonaceous transfer layers that were in contact with the a-C:H:Si:O:F coating were rich in Si and O, and consisted of loosely-packed nano-sized fragments. The hydration of the $Si-O-Si$ chains in the coating and transfer layers resulted in the formation of two OH–passivated surfaces with repulsive forces at the contact interface, and together with H- and F- passivation led to a lower COF than the a-C, a-C:H, and a-C:H:F. As a result, the a-C:H:Si:O:F coating showed promise for use in applications where a stable friction coefficient is desired, with varying humidity conditions, such as in battery manufacturing and sliding applications in aerospace.

In conclusion, the chemistry of the contact interface can be altered by the incorporation of alloying elements of the DLC structure to control the friction properties and adhesion behaviour of DLC coatings against Al. The impact of these results can be listed as:

- A transfer layer must form on the Al counterface so that repulsive forces are generated between the –F, –H, and –OH groups at the contact interface, and lead to a low COF in sliding automotive components such as the piston rings in engines.

- The presence of F in the DLC structure eased transfer layer formation on the Al counterface by forming a compound during sliding, and the presence of SiO_x groups reduced the humidity dependence of the DLC's friction coefficient against Al.

- The formation of transfer layers in manufacturing applications is not desirable. In these applications the Al surface comes into contact with the tool surface for a very short period of time, and this is not long enough for the formation of a stable transfer layer. In addition, for every contact between the Al and DLC, a transfer of materials from the DLC to Al will occur, and the coating will be worn out gradually during the manufacturing process. For manufacturing applications, it is desirable to use a coating that does not interact with Al, such that the DLC surface should be H- and OH-passivated, but not F-passivated.

- The SiO_x incorporated DLC can be useful for sliding applications in aerospace or lithium-ion battery manufacturing, where a low friction is required for extended service life, during which the atmospheric conditions may change considerably.

8.2 Adhesion in hot forming processes due to oxidation

In the high temperature forming of Al alloy sheets, oxide fibers formed on the Al surface as a result of Al and Mg oxidation play an important role in the adhesion to tool surfaces. Molecular dynamics simulations with ReaxFF were undertaken in order to study the deformation of Al nanowires subjected to a tensile load in an O_2 environment. The 1.0 nm native amorphous oxide shell formed around the Al nanowires had a 60% lower Young's modulus than the Al, due to low density and low Al-O coordination (Chapter 5). In O_2, the oxide shell showed superplastic deformation characteristics were attributed to the diffusion of oxygen in the amorphous network that healed the broken Al-O bonds during the applied strain. These superplastic deformation characteristics of the amorphous oxide predicted in O_2 environmental conditions were surprising. A viscous flow mechanism successfully interpreted the deformation characteristics of the oxide, and explained the observation of superplastically elongated oxide fibers using cross-sectional FIB methods, on the Al surface during the hot forming processes in the O_2 containing ambient air atmosphere. The oxide shell significantly altered the deformation characteristics of Al by providing additional nucleation sites for dislocations that decreased the Al yield strength. In the O_2 atmosphere, the number of mobile dislocations contributing to dislocation glide increased, and consequently, the plastic work prior to fracture the Al (toughness) increased.

The transfer of Al to the tool material surfaces in hot forming applications under ambient air, for the complex Al/tool interface system (Fe/FeO/AlO$_x$/Al), can be represented, as shown in Figure 8.1, the interface separated from the Al immediately below the contact surface. The delamination of aluminum under large strains, at certain critical depths below the sliding surface, was previously studied [1], and it was determined that the maximum damage would not occur at the surface, but at a location that is determined by the competition between the hydrostatic pressure that suppresses the damage, and the flow stress that enhances void growth. The elevated temperature separation may also include grain boundary sliding and cavitation. Figure 6.1(c) shows that the oxide nanowires formed at the contact interface serve to attach the separated Al fragments to the tool surface. The fibers were found to be formed as a result of superplastic deformation due to dynamic ox-

idation. At the Al chip/tool interfaces, the metal/oxide and oxide/oxide interfaces were relatively stronger than the Al and the oxide strength, so that the material transfer direction was decided by the competition between the energy required to fracture the Al (W_{dec}^{Al}) and the energy required to fracture the oxide nano-fiber ($W_f^{AlO_x}$). The $W_f^{AlO_x}$ of the fibers, as shown in Chapter 6, is dependent on the deformation or strain rate ($\dot{\varepsilon}$) and the oxidation rate ($\dot{N}_O$), namely the number of oxygen atoms reacted with Al at unit surface area per unit time. The oxidation rate is a function of O_2 partial pressure (P_{O_2}) and temperature, (T), i.e. $\dot{N}_O = \dot{N}(P_{O_2}, T)$, where the the oxidation rate can be expressed in terms of temperature (T), activation energy (Q), and number of available sites for oxidation (N_O^0) as

$$\dot{N}_O = N_O^0 \exp\left(-\frac{Q}{kT}\right) \tag{8.1}$$

The strain rate can also be expressed in terms of stress (σ), T, and Q using the creep equation as

$$\dot{\varepsilon} = A\sigma^n \exp\left(-\frac{Q}{kT}\right) \tag{8.2}$$

where $n = 1$ for the viscous flow can be used for the amorphous oxide deformation. According to the stress-strain data presented in Figure 6.2 it can be written that

$$W_f^{AlO_x} \propto \frac{\dot{N}(P_{O_2}, T)}{\dot{\varepsilon}} \tag{8.3}$$

Using Equations 8.1 and 8.2, a critical strain rate for a particular oxidation rate that results in the superplasticity of the oxide can be estimated. Using the stress-strain data in Figure 6.2, the work of fracture for pure Al deformed in a vacuum was estimated as $W_f^{Al} = 0.3$ J/m^3. On the other hand, and the Al deformed in O_2 had an approximately 6 times higher work of fracture $W_f^{AlO_x} = 1.75$ J/m^3 for the maximum strain of 0.75, in which the oxide did not fracture. Consequently, as depicted in Figure 8.2, in inert atmospheres, Al fractures in a quasi-brittle way and a minimal Al transfer to the tool surface is expected. Conversely, in O_2 atmospheres, the superplastic oxides adhered to the tool steel surface, and due to the very high work of fracture, the oxides elongated at the interface. This does not result in the fracture of the oxide, but instead a chunk of Al will fracture from the bulk,
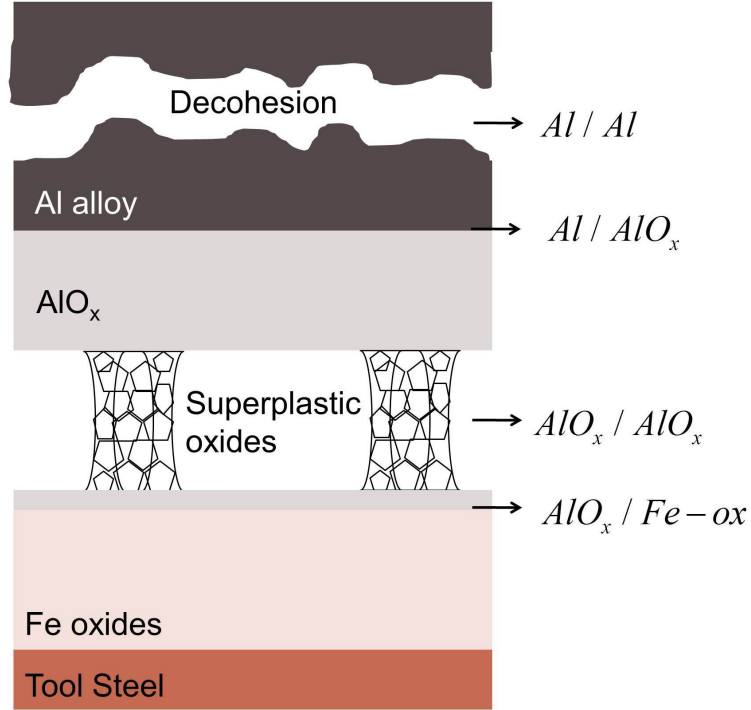
Figure 8.1: The Al/tool interface structure observed in the Al hot forming process showing the decohesion occurring in the bulk Al, and the AlO_x nanowires elongated at the interface that did not fracture due superplastic deformation mechanisms.

and a significant amount of Al will be transferred to the tool surface.

To minimize the adhesion of Al fragments, it is desirable to prevent the superplastic oxide fiber formation. For a particular strain rate used in the forming process, the oxide fibers formed as a result of exposure of nascent Al to oxygen so that superplasticity of the AlO_x can be decreased by decreasing the rate of oxidation (such as in using an inert atmosphere).

Alternatively, since the oxide shows superplasticity due to its viscous flow, the Young-Dupré equation [2] can be used to define the W_{sep} at the AlO_x/tool interface, which is given as

$$W_{sep} = \gamma_L(1 + \cos\theta) \tag{8.4}$$

where γ_L is the surface tension of the AlO_x, and θ is the contact angle between the AlO_x and the tool surface. Equation 8.4 dictates that the W_{sep} at the AlO_x/tool interface can be decreased by increasing the contact angle between the AlO_x and the tool surface. This

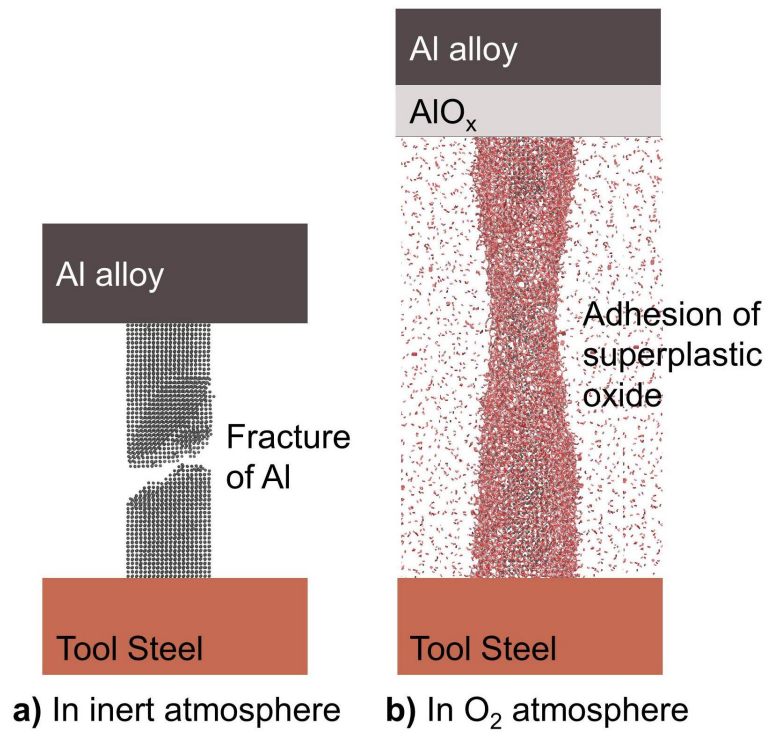**a)** In inert atmosphere   **b)** In O$_2$ atmosphere

Figure 8.2: The Al chip/tool interface in (a) an inert atmosphere featuring easily fractured Al nanowires and in (b) an O$_2$ atmosphere that had superplastically elongated oxide nanowires resulting in the adhesion of large Al fragments to the tool surface.

can be achieved by the application of nano-patterns, such as replicating the surface pattern of lotus leaves on tool surfaces [3] that will form nano-scale protuberances on the surface that entrap a high fraction of air beneath the water droplets, creating a water contact angle more than 150$^\text{o}$. Otherwise, application of a coating that will show lesser interfacial tension against the AlO$_x$ at hot forming temperature conditions can also decrease the adhesion.

The impact of these results to the industrial problem can be listed as:

- Oxidation enhances the plasticity of Al and its oxide, which results in an increase in the formability of Al. It was revealed that oxidation caused the formation of more than 75% elongated oxide fibers during the applied strain that was observed on Al sheets in the manufacturing process. In O$_2$, the oxide showed a superplastic deformation mechanism due to continuous oxygen diffusion, and formed Al-O atomically thick chains at the fracture surface, which is akin to viscous flow.

- The native oxide of the Al nanowire was revealed to be less stiff, but also more ductile than the single crystal Al due to its low density and oxygen deficient structure. The oxide layer provided additional nucleation sites that contributed to an increase in ductility. But the image forces provided by the thin amorphous layer were still low letting some dislocations to escape from the oxide surface.

- The oxygen deficient structure of the oxide nanowire and the presence of unsaturated Al bonds led the oxide to be more chemically reactive when compared to its stoichiometric counterparts, and increased its adhesion tendency. The oxide was tougher than the single crystal Al, and as a result, the fracture of the oxide is not expected to occur in manufacturing processes, but the material transfer of Al does occur at the tool surfaces.

- To reduce adhesion due to oxidation in Al manufacturing processes, it is suggested that the process be carried out in an inert environment that will prevent the superplastic deformation of the oxides, and decrease the toughness of the oxide so that it will fracture easily. The presence of a pure Al nano-fiber is preferred at the contact interface since it provides the lowest toughness.

8.3 Adhesion problem in electro-catalyst of fuel cells

To prevent loss of performance, and increase the long-term durability of fuel cells, the adhesion of Pt catalysts on carbon surfaces needs to be enhanced. First principles calculations based on spin-polarized DFT were used to identify metallic adatoms that strengthen the weak Pt (111)/graphene interface (with a low work of separation of 0.009 J/m^2), when the adatom was placed between the Pt (111) and the graphene. The overall Pt (111)/graphene interface strength, and therefore, the anchoring effect of the adatom, were controlled by the C–adatom bond strength since the C–adatom bond was weaker than the Pt–adatom bond for each of the 25 elements considered. The suitable adatoms were identified according to their ability to distribute charges between the graphene and Pt surfaces, i.e. their anchoring ability. Ir, Os, Ru, Rh, and Re were found to share electrons strongly with the graphene, which made these elements the most effective adatoms for anchoring Pt to graphene. The technological impacts of this study can be listed as:

- It was predicted that if the carbon surfaces could be modified by metals, the Pt nanoparticles would bind more strongly to the carbon, and that the most efficient metals for this purpose are Ir, Os, Ru, Rh, and Re. The surface modification of the carbon supports with these metals is expected to increase the durability and performance of fuel cells.

- Graphene is the building block of many carbon structures, and metallic elements can be very effective in bridging Pt and other carbon structures in applications that involve contacts between Pt and carbon (in addition to fuel cells). This work can be used to identify possible metallic modifications and to improve interfacial strength between the graphene and metals that typically show very weak binding (similar to Pt), such as Cu, Ag, Pd, and Au.

8.4 General conclusions and final remarks

For all of the different adhesion problems presented in this dissertation, the initial problem was industrial scale, in which the products of concern had dimensions of more than few

centimeters, however, we scaled the problem down to the atomistic level by identifying the most fundamental factors that contributed to this industrial problem of lightweight and energy materials technologies. The passivation of DLC surfaces with –H, –F or –OH groups, which is achieved either by the incorporation of these molecular groups into the DLC structure during the deposition process, or by absorption from the atmosphere, can mitigate aluminum adhesion with the same desirable result of obtaining low friction. The surface properties of aluminum during deformation are shown to be affected by oxidation, in which both the mechanical properties of the native oxide on the aluminum, and as well as the deformation characteristics of the aluminum at the subsurface, were modified during a dynamic oxidation process that explained the adhesion property changes of aluminum occurring at high temperature forming applications. On the other side of adhesion spectra, where adhesion is most desirable in a (potential) automotive component, the incorporation of metallic adatoms on carbon surfaces was shown to enhance the weak adhesion between Pt and carbon, which is an important performance and durability problem in PEMFCs. The applications of the problems treated in this dissertation are pervasive. The study of adhesion related problems with a combined atomistic and microstructural perspective provided insight into the design of atomically engineered surfaces, which will enable the more efficient production and development of materials, not only in automotive industry, but also in other applications that rely on the surface properties of materials.

8.5 Future work

The adhesion problems of different automotive applications can be further studied in many ways. For Al components in sliding applications, the DLC coatings shown to provide exceptional friction characteristics, and the tribological properties of these coatings, can be further improved by studying different alloying elements to enable these coatings to be operable at extreme conditions, such as at high temperatures and variable atmospheric humidity. The beneficial tribological properties of DLC were attained (mostly) after the formation of transfer layers on the counterfaces, and these transfer layers can have very complex structures as shown in this dissertation. However, for manufacturing processes, the transfer layer forma-

tion should be imminent and efficient such that the transfer layer should form at the initial contact with a very thin structure that blocks the adhesive interactions between Al and the dangling carbon bonds. In future studies, the mechanisms of transfer layer formation can be studied by atomistic simulations and tribological experiments. Additionally, computational material designs of different alloying elements (to DLC) and possible atmospheric compounds that can ease transfer layer formation can be carried out.

For hot forming applications, the adhesion occurring due to oxidation was studied in single crystal Al nanowires. In a large scale, Al has a polycrystalline structure, and some of its alloys (e.g. Al-Mg alloys) deform superplastically by grain boundary sliding mechanisms at hot forming temperatures. For the polycrystalline Al structure, the oxidation can have a more prominent affect, since the grain boundaries will act as diffusion pathways for oxygen atoms. The native oxide was found to be very soft and can act as a fluid layer between Al grains, drastically changing the overall deformation characteristics of Al, and therefore, its fracture and adhesion behaviour. In future studies it is suggested to carry out MD simulations to investigate the effect of oxidation on the deformation of polycrystalline Al. To mitigate adhesion it is suggested to carry out hot forming experiments at inert atmospheres, as well as varying oxidizing atmospheres, which can potentially decrease the plasticity of the oxide. Alternatively, the application of high temperature resistant coatings and the nano-patterning of tool surfaces can be studied to investigate the decrease in the adhesion of Al.

For the fuel cell problem, we identified many metallic adatoms that can be incorporated onto the graphene surface to enhance the Pt-carbon adhesion. The experimental validation of these systems can be carried out in the next step of research. Different carbon surfaces that are used in fuel cells as a catalyst support can be modified with the selected metallic elements (Ir, Rh, Ru, Os, and Re), and the performance and durability of the electro-catalyst on that new support can be experimentally tested for fuel cell conditions.

Bibliography

[1] J. Zhang and A.T. Alpas. Delamination wear in ductile materials containing second phase particles. *Materials Science and Engineering A*, 160:25–35, 1993.

[2] A.H. Cottrell. *The Mechanical Properties of Matter*. John Wiley and Sons Inc., U.S.A., 1964.

[3] M. Shafiei and A.T. Alpas. Nanocrystalline nickel films with lotus leaf texture for superhydrophobic and low friction surfaces. *Applied Surface Science*, 256:710–719, 2009.

Appendix A

Atomistic Simulation Methods

In recent years materials modeling, in the broad sense of theory and simulation in integration with experiments, has emerged as a field of research with unique capabilities, as such the growing computational power enabled the use of simulation methods to solve wide range of physical, chemical and biological problems in life [1]. It is necessary to handle the problems in different length scales of materials such that the simulation models and the experimental techniques complement to investigate materials processes across nano to macro length and time scales. In general five different regions can be identified in the materials length scale where materials phenomena are studied as illustrated in Figure A.1. These five regions can be referred to as quantum mechanics (QM), molecular dynamics (MD) with reactive charge transfer (ReaxFF), non-reactive MD or Monte-Carlo (MC), mesoscale and continuum. At the smallest scale, the electronic structure of materials are studied using the theories of quantum mechanics such as density functional theory (DFT). These calculations are the most accurate to calculate properties of materials, but computationally very expensive that only systems with few hundreds of atoms can be studied. At the larger scale atomic level simulations that involve hybrid QM-MD methods such as reactive MD methods (ReaxFF) that can take charge transfer processes into account, while calculating the materials processes in which systems with few thousands of atoms can be simulated in a reasonable time. In atomic level MD simulations, an empirical/semi-empirical interatomic potential functions are used to describe the atomic interaction while ignoring the electronic interactions. In MD simulations, one can study systems with more than 10^6 atoms with

the current computational power. Above atomic level, mesoscale simulations that study the microstructure of materials exist such as phase-field or finite element methods. At the largest extend continuum level methods such as computational fluid dynamics are used.
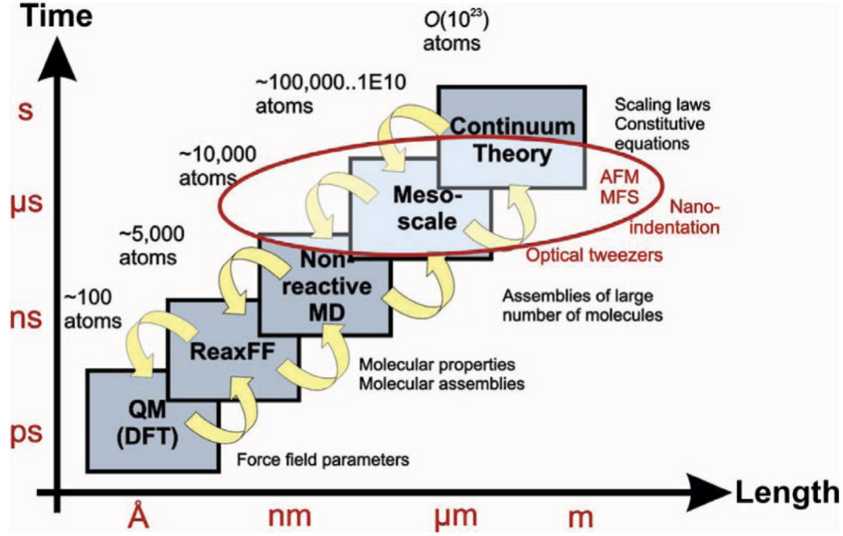

Figure A.1: Schematic of the concept of hierarchical multiscale modeling. Hierarchical coupling of different computational tools can be used to traverse throughout a wide range of length and time scales. Such methods provide a fundamental insight into materials phenomena across various time and length scales. Handshaking between different methods enables one to transport information from one scale to another. Experimental techniques such as atomic force microscopy (AFM), molecular force spectroscopy (MFS), nanoindentation, or optical tweezers now overlap into atomistic and molecular approaches, enabling direct comparison of experiment and simulation [2].

The modeling adhesion requires very accurate description of the bonding properties at materials interfaces that the atomistic simulations at QM and QM-MD hybrid simulations are the most suitable. In the present studies we have used DFT based methods to calculation adhesion strength and reactive MD (ReaxFF) methods to calculate the mechanical properties in oxidizing environments. In this chapter, a brief detail of these methods will be given.

A.1 First principles calculations based on density functional theory (DFT)

A.1.1 Method description

One of the most profound scientific advancements of the twentieth century was probably the discovery and development of the quantum mechanics [3]. The theories in the quantum mechanics describe the interactions between electrons and the atomic nuclei accurately as supported by experiments that these theories can be used to solve many physical phenomena in chemistry, physics, biology and materials science at the atomic scale. In all atomistic simulations one of the most fundamental quantity to calculate is the change in the total energy of the system with the change in the atomic positions, which needs solutions or approximations to QM equations. In order to locate an atom, it is required to locate the positions of nucleus and electrons of the atom. It is known that electron are more than 1800 times lighter in mass than the nucleus, so that electrons respond to the changes in the surrounding more rapidly than the nucleus. As a result, according to Born-Oppenheimer approximation [4] the physical problem can be solved separately for the nucleus and electrons as two individual mathematical problems. The lowest energy state, E, is known as the ground state of the electrons can be expressed as a function of the positions of M nuclei at positions $R_1, ..., R_M$ as $E(R_1, ..., R_M)$.

The change in the energy of the quantum system is defined with the well-known time-independent, non-relativistic Schrodinger equation which has the simplest form of

$$H\psi = E\psi \qquad (A.1)$$

where H is the Hamiltonian operator and the wavefunction ψ is a function of all the electronic r_i and ionic R_i coordinates i.e. $\psi = \psi(r_1, ..., r_N : R_1, ..., R_M)$. When multiple electrons interact with multiple nuclei the Eq. A.1 can be written in more complete form as

$$H\psi = \left[\hat{T} + \hat{V} + \hat{U}\right]\psi = \left[\frac{\hbar^2}{2m_e}\sum_{i=1}^{N}\nabla_i^2 + \sum_{i=1}^{N}V(r_i) + \sum_{i=1}^{N}\sum_{j<i}U(r_i, r_j)\right]\psi = E\psi \quad \text{(A.2)}$$

where $\hbar$ is the Planck's constant and m_e is the electron mass. The three terms in the brackets in Eq. A.2 define, the kinetic energy of each electron ($\hat{T}$), electron-ion interactions ($\hat{V}$) and electron-electron interactions ($\hat{U}$), in order. The solution of this equation gives the total energy E and the wavefunction ψ from which all physical quantities can be derived. There are several approaches to the solution of this problem based on non-interacting single-particle wavefunction (Hartree-Fock [5]) or charge density (density functional theory (DFT) [6, 7]).

The wavefunction for any particular set of coordinates cannot be directly observed, but the probability of N electrons are at a particular set of coordinates can be measured. In DFT, one close value to the probability, which is the electron density of electrons at a particular position, $n(r)$ is estimated. Hohenberg and Kohn [6] theorem stated that the ground state energy from Schrodinger's equation is a unique functional of the electron density, i.e. $E = E[n(r)]$. Accordingly, it can be written as

$$E[n(r)] = \hat{T}[n(r)] + \hat{U}[n(r)] + \int V_{ion}(r)n(r)dr \quad \text{(A.3)}$$

When Kohn-Sham ansatz is used, the many body kinetic energy, $T[n(r)]$, and electron-electron, $U[n(r)]$, terms of Eq. A.3 can be replaced by the kinetic energy of a set of non-interacting electrons, coulomb interaction between the electron and itself, E_H and an additional term exchange correlation energy, E_{XC}, which is the sum of all remaining many-body contributions to the total energy:

$$E[n(r)] = \frac{-\hbar^2}{2m_e}\nabla^2 + \int V_{ion}(r)n(r)dr + E_H[n(r)] + E_{XC}[n(r)] \quad \text{(A.4)}$$

where

$$E_H[n(r)] = \frac{1}{2}\int \frac{n(r)n(r')}{|r - r'|}drdr' \quad \text{(A.5)}$$

239

$$n(r) = \sum_{i=1}^{N} |\psi_i(r)|^2 \tag{A.6}$$

Here, E_{XC} term does not have an exact functional form but several approximations were carried out in the literature. When a constant electron density at all points is assumed, the local density is used to define the approximate exchange-correlation functional, which is called, local density approximation (LDA). A better approach than LDA used the local electron density and the local gradient in the electron density, defined as the generalized gradient approximation (GGA). There are two common GGA functionals to calculate solid properties are Perdew-Wang (PW91) [8,9] and Perdew-Burke-Ernzernhof (PBE) [10].

The Kohn-Sham equations given in Eq. A.4 requires electron density value to calculate the E_H term and it is not possible to calculate it analytically. Instead these equations are solved iteratively by a self-consistent method. First, an initial trial $n(r)$ is defined. Then, the Kohn-Sham equations are solved using the trial $n(r)$ to find the single-particle wavefunctions, $\psi_i(r)$. Then the electron density, $n_{KS}(r)$ is calculated using the wavefunctions and if $n(r) = n_{KS}(r)$ then the ground-state electron density is achieved. If $n(r) \neq n_{KS}(r)$, the electron density is updated somehow and the calculations start over. The details of the electron density calculations can be found elsewhere [3,11,12].

The most important outcome of the first principles calculations carried out in this study was to gather information about the bonding nature between materials. There were several different methods that were used in this study to classify chemical bonds such as charge density difference, density of states (DOS), Bader charge analysis, and electron localization function (ELF). The definitions of these methods are given in the following sections.

A.1.2 Chemical bonding analysis methods

A.1.2.1 Charge density difference

The charge density $n(r)$ is a measure of the probability of an electron being present at a specific location and calculated on a grid according to Eq. A.6. $n(r)$ is generally visualized as 3-dimensional iso-surfaces or 2-dimensional contour slices . $n(r)$ can give information about where the atoms are localized in the system of interest and is a very useful quantity

240

to understand the bonding between atoms. However, for systems where there is a large variation in the $n(r)$, it is hard to classify the bonding scheme between atoms. Therefore, a more practical, charge density difference, $\triangle n(r)$, between the total charge density of the system and the charge density of the individual atoms is calculated as given in Eq. A.7.

$$\triangle n(r) = n(r) - \sum_i n_i^{atom}(r) \tag{A.7}$$

where $n_i^{atom}(r)$ is the charge density calculated for an individual atom, i, in the same system using the same grid used to calculate the total charge density, $n(r)$. $\triangle n(r)$ gives information about the charge transfer in the system where positive values represent charge accumulated regions and negative values represent charge depleted regions.

A.1.2.2 Electron localization function (ELF)

Electron localization function (ELF) is a more rigorous way to classify chemical bonds based on the Pauli-exclusion principle [13, 14]. ELF is a measure of the probability of finding an electron in the neighborhood space of a reference electron located at a given point and with the same spin. ELF is defined for a spin density matrix of $\rho(r)$ as [13]

$$\text{ELF}(r) = \frac{1}{1 + \left(\frac{D(r)}{D_h(r)}\right)^2} \tag{A.8}$$

$$D(r) = \sum |\nabla\psi_i(r)|^2 - \frac{1}{4}\left|\frac{\nabla\rho(r)}{\rho(r)}\right|^2 \tag{A.9}$$

$$D_h(r) = \frac{3}{5}(6\pi^2)^{2/3}\rho^{5/3}(r) \tag{A.10}$$

In Eq. A.8 and A.9 $D(r)$ is the Pauli excess kinetic energy density, which is the difference between the kinetic energy density of the Kohn-Sham system of electrons and that of a system of non-interacting bosons of the same density. $D_h(r)$ is the kinetic energy density of a homogeneous electron gas with the same local density. The ELF calculated with Eq. A.8 is a dimensionless localization index having values in the range 0-1. ELF $= 1$ corresponds to perfect localization and indicates a covalent bonding, and ELF $= 0.5$ corresponds to

241

electron-gas-like probability, which indicates metallic bonding. For ELF < 0.5, the chemical bonding is undefined. ELF is particularly useful to distinguish metallic and covalent bonding in the system of interest and used to categorize the chemical bonds at the metal-carbon interfaces [14–19] in this study.

A.1.2.3 Bader charge analysis

There are different methods to partition the electron density to define the charges on individual atoms separately from the total system. Bader charge analysis [20, 21] creates a Bader volume around each atom according to so called zero flux surfaces on which the charge density has a minimum perpendicular to the surface. The total charge enclosed in this Bader volume is a good approximation to the total electronic charge of an atom. We have employed Bader charge analysis to monitor the charge transfer events in the interface systems studied and useful information about the characteristics of a chemical bond was acquired.

A.1.2.4 Density of states

One of the primary quantities used to describe the electronic state of a material is the electronic density of states (DOS), which describes the number of states that are available to be occupied by electrons at each energy level per interval of energy. The DOS, $\rho(E)$, is defined as [12]

$$\rho(E) = \frac{1}{N_k} \sum_{i,k} \delta(\varepsilon_{i,k} - E) = \frac{\Omega_{cell}}{(2\pi)^d} \int_{BZ} dk \delta(\varepsilon_{i,k} - E) \tag{A.11}$$

where $\varepsilon_{i,k}$ is the energy of an electron. The DOS can determine the overlap or hybridization of states from different atoms and it is useful to distinguish metallic or covalent type bonding. The DOS can be decomposed by dividing the space into atom-centered spheres to count the number of states per energy that was projected onto selected atoms and also the angular-momentum-dependent (partial DOS/PDOS) contributions can be calculated to determine the s,p,d, etc. nature of a particular atom. The DOS gives also information about the band structure of a system which enables to predict what can happen when an
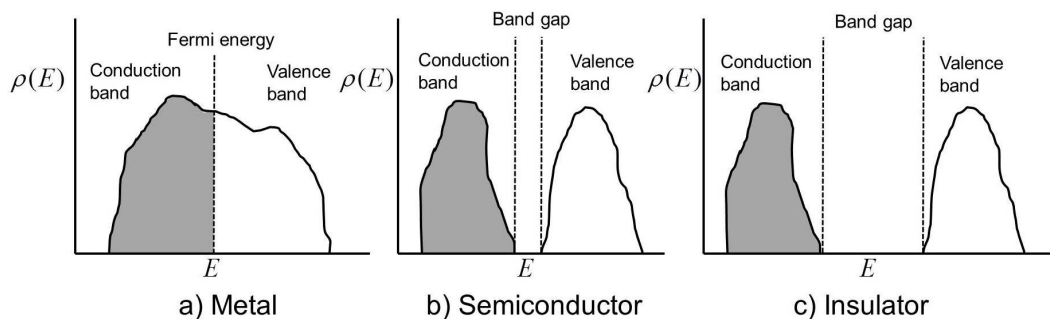
Figure A.2: Typical density of states (DOS) of a (a) metal, (b) semiconductor and (c) insulator. The shaded areas indicate the occupied energy levels.

electric field is applied to the material. DFT can accurately predicts the existence of a band gap, but fails to calculate the band gap value correctly. Typical DOS plots for a metal, semiconductor and insulator relative to Fermi level are given in Figure A.2. The Fermi level of metals lie inside at least one band with energetically available states that each electron can occupy, and hence for metals conduction and valence bands are overlapping (Figure A.2(a)). For semi-conductors (Figure A.2(a)) and insulators (Figure A.2(a)) there is an energy difference between electron occupied energy levels and empty energy levels (band gap). For insulators this band gap is very large that it is very hard to excite an electron to move to the conduction band. On the other hand, the band gap of semiconductors is small enough that even a small increase in temperature can promote electrons to transfer to the conduction band.

A.2   Reactive molecular dynamics simulations

A.2.1   Method Description

First principles methods based on DFT is very accurate for prediction of many physical properties of materials, but it has limitations in the number of atoms it can be studied. The current computational power does not allow simulation of systems more than containing few hundred atoms using methods based on quantum mechanics. To overcome the limitations in the system size empirical/semi-empirical force fields (FFs) were developed that regard the nucleus and the electrons of an atom as a single identity. The functional form of FFs

often have a theoretical basis, but the parameters are fit to predict experimentally known quantities (lattice parameters, bond lengths, heat of vaporization, etc.) or results of DFT calculations in a reasonable accuracy [22]. These force field The empirical FFs allow simulation of more than 10^6 atoms in classical MD simulations, but for systems involving chemical reactions, classical MD simulations lacks in accuracy due to the static bond definitions and exclusion of charge transfer processes. The classical force fields are also not transferable such that they were developed only for specific systems such as AMBER [23] for proteins, CHARMM [24] and CVFF [25] for organic molecules, and embedded atom model (EAM) for metallic systems [26, 27].

There has been mixed quantum mechanics/molecular mechanics (QM/MM) methods developed in literature [28] to study larger systems by applying QM methods in the reactive regions, and simulating the rest of the system using MM methods. The QM/MM methods also has some difficulties in coupling QM and MM methods and also requires knowledge of the reactive regions in the system before setting up the simulations so that these methods were not widely used. Another approach to connect QM and MD simulations were pursued by defining a bond order term in the force field that dynamically updates the bonding properties between atoms during the evolution of the system in simulation which allows to simulate the reactions accurately in the system referred as reactive molecular dynamics (RMD) [29]. There are several RMD force fields available in the literature such as reactive empirical bond order (REBO) [30], AIREBO [31], RMDff [32], adiabatic RMD method (ARMD) [33], empirical valence bond (EVB) model [34], and other bond order potentials are available as reviewed by Farah et. al [29]. ReaxFF was reported to show more accurate results compared to REBO for hydrocarbons. In addition, ReaxFF was further developed to study Si-O [35], nitramine [36], Mg-H [37], Al-O [38], Pt-C [39], V-O [40], and Li-C [41] systems. In this study, we have used ReaxFF for Al-O system [38] to study Al oxidation and predicted mechanical properties of Al nanowires in an oxygen environment, which was reported to predict Al/Al_2O_3 wetting/non-wetting properties very well.

In classical MD, the time-evolution of a system is simulated in consideration of finite pressure and temperature based on solving the Newton's equation of motion. During MD simulations the force, F, exerted between atoms due to the force field is calculated and the

244

atomic coordinates (x_i) were updated according to Eq. A.12.

$$F = -\frac{\partial E_{system}}{\partial x_i} = m_i \frac{\mathrm{d}^2 x_i(t)}{\mathrm{d}t^2} \tag{A.12}$$

In Eq. A.12, E_{system} is the potential energy function or the force field function that describes the atomic interactions. The atomic positions of each atom are updated according to Eq. A.12 at each time step using an iterative numerical method and the position of atoms are corrected according to periodic boundary conditions (PBC).

In ReaxFF, E_{system} is partitioned into several contributions as given in Eq. A.13.

$$E_{system} = E_{bond} + E_{over-coordination} + E_{under-coordination} +$$

$$E_{valence-angle} + E_{penalty} + E_{torsion} +$$

$$E_{conjugation} + E_{vdWaals} + E_{Coulomb} \tag{A.13}$$

The calculation of each term in Eq. A.13 is given in [42]. ReaxFF employs a bond length/bond order relationship to ensure a smooth transition from non-bonded to single, double and triple bonded systems and bond orders are updated at every MD time step. The non-bonded interactions (Coulomb and van der Waals) are calculated between every atom. In this equation $E_{Coulomb}$ term take into account the interactions due to the charges on each atom. The atomic charges are calculated using the Electron Equilibration Method (EEM) [43, 44] at every MD time step. ReaxFF requires usage of smaller time step of less than 0.5 fs for temperatures between $0 - 1500$ K to ensure energy conservation.

MD simulations can be carried out at different ensembles defined in the statistical mechanics such as constant number of atoms (N), volume (V) and energy (E), i.e. NVE ensemble, or constant temperature (NVT), or constant temperature and pressure (NPT) [45]. The methods to constrain the desired quantities in MD simulations are described in Ref. [45]. At the end of simulation the desired properties with respect to time are calculated by averaging over all atoms in the system. There are numerous MD programs developed in the literature, which are available to researchers. Some of the commonly used MD programs can

be named as LAMMPS [46], CHARMm [24], GROMACS [47], AMBER [48], GULP [49], Materials Studio (Acclerys Inc.).

In this study, we have used LAMMPS for our simulations which is a very robust MD code, and the ReaxFF was implemented in it with linear scaling parallelization. In our MD simulations in order to understand the mechanical properties and bond structures we evaluated several properties of the simulated systems such as temperature, stress, radial distribution function, centro-symmetry parameter (CSP), and rings statistics.

A.2.2 Analysis of MD simulations

A.2.2.1 Temperature

Temperature, T, is calculated from the instantaneous kinetic energy of atoms, $K(t)$, using the equipartition theorem as

$$T(t) = \frac{2K(t)}{N_f k_B} \tag{A.14}$$

where N_f is the degree of freedom, which is $3N$ for three-dimensional simulations and k_B is the Boltzmann constant. The instantaneous kinetic energy is given by

$$K(t) = \frac{1}{2} \sum_{i=1}^{N} m_i [v_i(t)^2] \tag{A.15}$$

where $\vec{v_i}(t)$ is the instantaneous velocity of an atom, i, at time t.

A.2.2.2 Pressure (Stress)

The pressure or stress, σ, of the system of atoms is calculated using the Clausius virial theorem and its 6 components for xx, yy, zz, xy, xz, yz directions are given as

$$\sigma_{ij} = \frac{\sum_k^N m_k v_{ki} v_{kj}}{V} + \frac{\sum_k^N R_{ki} F_{kj}}{V} \tag{A.16}$$

where V is the volume of the system, i and $j = x$, y, z.

A.2.2.3 Radial distribution function

Radial distribution function, $g(r)$, is a measure for characterization of the local structure of a material. This function gives the probability of finding an atom at a distance r apart from a given reference atoms. The $g(r)$, usually normalized relative to the probability expected for a completely random distribution at the same density [45] and given in Eq. A.17.

$$g(r) = \frac{V}{N^2} \left\langle \sum_i \sum_{j \neq i} \delta(R - R_{ij}) \right\rangle \qquad (A.17)$$

A.2.2.4 Centro-symmetry parameter

Centro-symmetry parameter (CSP) is defined [50] for a group of atoms to characterize the disorder around an atom such that it can be used to understand whether the atom belong to a perfect lattice, a local defect (dislocation or a stacking fault), or at a surface. It can be effective only for centro-symmetric structures such as FCC and BCC lattices. CSP is implemented in ATOMEYE [51] program as in Eq. A.18.

$$CSP = \frac{\sum_{i=1}^{\alpha} |R_i + R_{i+\alpha}|}{2 \sum_{i=1}^{2\alpha} |R_i|^2} \qquad (A.18)$$

where α is the number of centro-symmetric neighbours of an atom. For an FCC lattice at an intrinsic stacking fault CSP has a dimensionless value of 0.042. For perfect crystals $CSP < 0.01$.

Bibliography

[1] S. Yip. *Handbook of materials modeling*. Springer, Dordrecht, The Netherlands, 2005.

[2] Markus J. Buehler and Theodor Ackbarow. Fracture mechanics of protein materials. *Materials Today*, 10(9):46–58, 2007.

[3] D. Sholl and J.A. Steckel. *Density functional theory: a practical introduction*. John Wiley and Sons Inc., New Jersey, 2009.

[4] M. Born and R. Oppenheimer. Zur quantentheorie der molekeln. *Annalen der Physik*, 84(20):457–484, 1927.

[5] A. Szabo and N.S. Ostlund. *Modern quantum chemistry: introduction to advanced electronic structure theory*. Dover Publications, Mineola, New York, 1996.

[6] P. Hohenberg and W. Kohn. Inhomogeneous electron gas. *Physical Review*, 136(3B):B864–B871, 1964.

[7] W. Kohn and L. J. Sham. Self-consistent equations including exchange and correlation effects. *Physical review*, 140:A1133–A1138, 1965.

[8] J.P. Perdew. *Unified Theory of Exchange and Correlation Beyond the Local Density Approximation*, pages 11–20. Electronic Structure of Solids '91. Akademie Verlag, Berlin, 1991.

[9] J. P. Perdew, J. A. Chevary, S. H. Vosko, K. A. Jackson, M. R. Pederson, D. J. Singh, and C. Fiolhais. Atoms, molecules, solids, and surfaces: Applications of the generalized gradient approximation for exchange and correlation. *Physical Review B*, 46(11):6671–6687, 1992.

[10] J.P. Perdew, K. Burke, and M. Ernzerhof. Generalized gradient approximation made simple. *Physical Review Letters*, 77(18):3865–3868, 1996.

[11] M.C. Payne, M.P. Teter, D.C. Allan, T.A. Arias, and J.D. Joannopoulos. Iterative minimization techniques for ab initio total-energy calculations: molecular dynamics and conjugate gradients. *Reviews of Modern Physics*, 64(4):1045–1097, 1992.

[12] R.M. Martin. *Electronic structure: basic theory and practical methods*. Cambridge University Press, United Kingdom, 2004.

[13] A. D. Becke and K. E. Edgecombe. A simple measure of electron localization in atomic and molecular systems. *The Journal of Chemical Physics*, 92(9):5397–5403, 1990.

[14] B. Silvi and A. Savin. Classification of chemical bonds based on topological analysis of electron localization functions. *Nature*, 371:683–686, 1994.

[15] Andreas Savin, Ove Jepsen, Jürgen Flad, Ole Krough Andersen, Heinzwerner Preuss, and Hans Georg von Schnering. Electron localization in solid-state structures of the elements: the diamond structure. *Angewandte Chemie International Edition in English*, 31(2):187–188, 1992.

[16] D. J. Siegel, Jr. L. G. Hector, and J. B. Adams. First-principles study of metal-carbide/nitride adhesion: Al/VC vs. Al/VN. *Acta Materialia*, 50(3):619–631, 2002.

[17] J. B. Adams, Jr. L. G. Hector, D. J. Siegel, H. Yu, and J. Zhong. Metal/ceramic interfaces: A microscopic analysis. *Surface and Interface Analysis*, 31:637–658, 2001.

[18] D. J. Siegel, Jr. L. G. Hector, and J. B. Adams. Ab initio study of Al-ceramic interfacial adhesion. *Physical Review B*, 67(9):921051, 2003.

[19] D. J. Siegel, Jr. L. G. Hector, and J. B. Adams. Adhesion, stability, and bonding at metal/metal-carbide interfaces: Al/WC. *Surface Science*, 498(3):321–336, 2002.

[20] R. F. W. Bader. Atoms in molecules. *Accounts of Chemical Research*, 18(1):9–15, 1985.

[21] G. Henkelman, A. Arnaldsson, and H. Jónsson. A fast and robust algorithm for Bader decomposition of charge density. *Computational Materials Science*, 36(3):354–360, 2006.

[22] C.A. Becker. Atomistic simulations for engineering: potentials and challenges. In *Models, Databases, and Simulation Tools Needed for the Realization of Integrated Computational Materials Engineering: Proceedings of the Symposium Held at Materials Science & Technology 2010, October 18-20, 2010 Houston, Texas, USA*, page 91. ASM International, 2011.

[23] Scott J. Weiner, Peter A. Kollman, David A. Case, U. Chandra Singh, Caterina Ghio, Guliano Alagona, Salvatore Profeta, and Paul Weiner. A new force field for molecular mechanical simulation of nucleic acids and proteins. *Journal of the American Chemical Society*, 106(3):765–784, 1984.

[24] Bernard R. Brooks, Robert E. Bruccoleri, Barry D. Olafson, David J. States, S. Swaminathan, and Martin Karplus. CHARMM: A program for macromolecular energy, minimization, and dynamics calculations. *Journal of Computational Chemistry*, 4(2):187–217, 1983.

[25] P. Dauber-Osguthorpe, V.A. Roberts, D.J. Osguthorpe, J. Wolff, M. Genest, and A.T. Hagler. Structure and energetics of ligand binding to proteins: Escherichia coli dihydrofolate reductase-trimethoprim, a drug-receptor system. *Proteins: Structure, Function, and Bioinformatics*, 4(1):31–47, 1988.

[26] M.S. Daw and M.I. Baskes. Embedded-atom method: Derivation and application to impurities, surfaces, and other defects in metals. *Physical Review B*, 29(12):6443–6453, 1984.

[27] S.M. Foiles, M.I. Baskes, and M.S. Daw. Embedded-atom-method functions for the fcc metals Cu, Ag, Au, Ni, Pd, Pt, and their alloys. *Physical Review B*, 33(12):7983–7991, 1986.

[28] R.A. Friesner. Ab initio quantum chemistry: Methodology and applications. *Proceedings of the National Academy of Sciences*, 102(19):6648–6653, 2005.

[29] K. Farah, F. Müller-Plathe, and M.C. Böhm. Classical reactive molecular dynamics implementations: State of the art. *ChemPhysChem*, 13(5):1127–1151, 2012.

[30] D.W. Brenner, O.A. Shenderova, J.A Harrison, S.J. Stuart, B. Ni, and S.B. Sinnott. A second-generation reactive empirical bond order (REBO) potential energy expression for hydrocarbons. *Journal of Physics: Condensed Matter*, 14(4):783–802, 2002.

[31] S.J. Stuart, A.B. Tutein, and J.A Harrison. A reactive potential for hydrocarbons with intermolecular interactions. *The Journal of Chemical Physics*, 112:6472–6486, 2000.

[32] Marc R. Nyden, Glenn P. Forney, and James E.Brown. Molecular modeling of polymer flammability: application to the design of flame-resistant polyethylene. *Macromolecules*, 25(6):1658–1666, 1992.

[33] M. Meuwly, O.M. Becker, R. Stote, and M. Karplus. NO rebinding to myoglobin: a reactive molecular dynamics study. *Biophysical chemistry*, 98(1):183–207, 2002.

[34] Arieh Warshel and Robert M. Weiss. An empirical valence bond approach for comparing reactions in solutions and in enzymes. *Journal of the American Chemical Society*, 102(20):6218–6226, 1980.

[35] Adri C. T. van Duin, Alejandro Strachan, Shannon Stewman, Qingsong Zhang, Xin Xu, and William A. Goddard. ReaxFF$_{SiO}$ reactive force field for silicon and silicon oxide systems. *Journal of Physical Chemistry A*, 107(19):3803–3811, 2003.

[36] Alejandro Strachan, Adri C. T. van Duin, Debashis Chakraborty, Siddharth Dasgupta, and William A. Goddard. Shock waves in high-energy materials: The initial chemical events in nitramine RDX. *Physical Review Letters*, 91:098301, 2003.

[37] S. Cheung, W.Q. Deng, A.C.T. van Duin, and III W.A. Goddard. ReaxFF$_{MgH}$ reactive force field for magnesium hydride systems. *The Journal of Physical Chemistry A*, 109(5):851–859, 2005.

[38] Qing Zhang, T. Cagin, A. van Duin, W. A. Goddard, Yue Qi, and L. G. Hector. Adhesion and nonwetting-wetting transition in the Al/α-Al$_2$O$_3$ interface. *Physical Review B*, 69(4):045423, 01/15 2004.

[39] C. F. Sanz-Navarro, P. O. Åstrand, D. Chen, M. Rønning, A. C. T. Van Duin, T. Jacob, and III W. A. Goddard. Molecular dynamics simulations of the interactions between platinum clusters and carbon platelets. *Journal of Physical Chemistry A*, 112(7):1392–1402, 2008.

[40] K. Chenoweth, A.C.T. van Duin, P. Persson, M.J. Cheng, J. Oxgaard, and III W.A. Goddard. Development and application of a ReaxFF reactive force field for oxidative dehydrogenation on vanadium oxide catalysts. *Journal of Physical Chemistry C*, 112(37):14645, 2008.

[41] S.S. Han, A.C.T. van Duin, III W.A. Goddard, and H.M. Lee. Optimization and application of lithium parameters for the reactive force field, ReaxFF. *Journal of Physical Chemistry A*, 109(20):4575–4582, 2005.

[42] A. C. T. Van Duin, S. Dasgupta, F. Lorant, and III W. A. Goddard. ReaxFF: A reactive force field for hydrocarbons. *Journal of Physical Chemistry A*, 105(41):9396–9409, 2001.

[43] Wilfried J. Mortier, Swapan K. Ghosh, and S. Shankar. Electronegativity-equalization method for the calculation of atomic charges in molecules. *Journal of the American Chemical Society*, 108(15):4315–4320, 1986.

[44] Geert O. A. Janssens, Bart G. Baekelandt, Helge Toufar, Wilfried J. Mortier, and Robert A. Schoonheydt. Comparison of cluster and infinite crystal calculations on zeolites with the electronegativity equalization method (EEM). *Journal of Physical Chemistry*, 99(10):3251–3258, 1995.

[45] M. P. Allen and L. J. Tildesley. *Computer Simulation of Liquids.* Oxford University Press, New York, 1987.

[46] S. Plimpton. Fast parallel algorithms for short-range molecular dynamics. *Journal of Computational Physics*, 117(1):1–19, 1995.

[47] H.J.C. Berendsen, D. van der Spoel, and R. van Drunen. Gromacs: a message-passing parallel molecular dynamics implementation. *Computer Physics Communications*, 91(1):43–56, 1995.

[48] David A. Case, Thomas E. Cheatham, Tom Darden, Holger Gohlke, Ray Luo, Kenneth M. Merz, Alexey Onufriev, Carlos Simmerling, Bing Wang, and Robert J. Woods. The Amber biomolecular simulation programs. *Journal of Computational Chemistry*, 26(16):1668–1688, 2005.

[49] J.D. Gale. Gulp: A computer program for the symmetry-adapted simulation of solids. *Journal of the Chemical Society, Faraday Transactions*, 93(4):629–637, 1997.

[50] C. L. Kelchner, S. J. Plimpton, and J. C. Hamilton. Dislocation nucleation and defect structure during surface indentation. *Physical Review B*, 58(17):11085–11088, 1998.

[51] J. Li. AtomEye: An efficient atomistic configuration viewer. *Modelling and Simulation in Materials Science and Engineering*, 11(2):173–177, 2003.

Appendix B

Copyright Releases from Publications

Chapter 2 Surface stability and electronic structure of hydrogen- and fluorine-terminated diamond surfaces: A first principles investigation

This is a License Agreement between Fatih Sen ("You") and Cambridge University Press ("Cambridge University Press") provided by Copyright Clearance Center ("CCC"). The license consists of your order details, the terms and conditions provided by Cambridge University Press, and the payment terms and conditions.

All payments must be made in full to CCC. For payment instructions, please see information listed at the bottom of this form.

License Number	3120060241951
License date	Apr 01, 2013
Licensed content publisher	Cambridge University Press
Licensed content publication	Journal of Materials Research
Licensed content title	Surface stability and electronic structure of hydrogen- and fluorine-terminated diamond surfaces: A first-principles investigation
Licensed content author	Fatih G. Sen, Yue Qi and Ahmet T. Alpas
Licensed content date	Aug 1, 2009
Volume number	24
Issue number	08
Start page	2461
End page	2470
Type of Use	Dissertation/Thesis
Requestor type	Author
Portion	Full article
Author of this Cambridge University Press article	Yes
Author / editor of the new work	Yes
Order reference number	
Territory for reuse	World
Title of your thesis / dissertation	Atomistic Simulations to Micro-Mechanisms of Adhesion in Automotive Applications
Expected completion date	Jun 2013
Estimated size(pages)	300
Billing Type	Invoice
Billing address	Materials Engineering, MAME

University of Windsor

Windsor, ON N9B 3P4

Canada

Total   0.00 USD

Terms and Conditions

Terms and Conditions are not available at this time.

Chapter 3 Material transfer mechanisms between aluminum and fluorinated carbon interfaces

Supplier	Elsevier Limited The Boulevard,Langford Lane Kidlington,Oxford,OX5 1GB,UK
Registered Company Number	1982084
Customer name	Fatih Sen
Customer address	Materials Engineering, MAME Windsor, ON N9B 3P4
License number	3120060642229
License date	Apr 01, 2013
Licensed content publisher	Elsevier
Licensed content publication	Acta Materialia
Licensed content title	Material transfer mechanisms between aluminum and fluorinated carbon interfaces
Licensed content author	F.G. Sen,Y. Qi,A.T. Alpas
Licensed content date	April 2011
Licensed content volume number	59
Licensed content issue number	7
Number of pages	14
Start Page	2601
End Page	2614
Type of Use	reuse in a thesis/dissertation
Intended publisher of new work	other
Portion	full article
Format	both print and electronic
Are you the author of this Elsevier article?	Yes

Will you be translating?	No
Order reference number	
Title of your thesis/dissertation	Atomistic Simulations to Micro-Mechanisms of Adhesion in Automotive Applications
Expected completion date	Jun 2013
Estimated size (number of pages)	300
Elsevier VAT number	GB 494 6272 12
Permissions price	0.00 USD
VAT/Local Sales Tax	0.0 USD / 0.0 GBP
Total	0.00 USD
Terms and Conditions	

INTRODUCTION

1. The publisher for this copyrighted material is Elsevier. By clicking "accept" in connection with completing this licensing transaction, you agree that the following terms and conditions apply to this transaction (along with the Billing and Payment terms and conditions established by Copyright Clearance Center, Inc. ("CCC"), at the time that you opened your Rightslink account and that are available at any time at http://myaccount.copyright.com).

GENERAL TERMS

2. Elsevier hereby grants you permission to reproduce the aforementioned material subject to the terms and conditions indicated.

3. Acknowledgement: If any part of the material to be used (for example, figures) has appeared in our publication with credit or acknowledgement to another source, permission must also be sought from that source. If such permission is not obtained then that material may not be included in your publication/copies. Suitable acknowledgement to the source must be made, either as a footnote or in a reference list at the end of your publication, as follows:

"Reprinted from Publication title, Vol /edition number, Author(s), Title of article / title of chapter, Pages No., Copyright (Year), with permission from Elsevier [OR APPLICABLE SOCIETY COPYRIGHT OWNER]." Also Lancet special credit - "Reprinted from The Lancet, Vol. number, Author(s), Title of article, Pages No., Copyright (Year), with permission from Elsevier."

4. Reproduction of this material is confined to the purpose and/or media for which permission is hereby given.

5. Altering/Modifying Material: Not Permitted. However figures and illustrations may be altered/adapted minimally to serve your work. Any other abbreviations, additions, deletions and/or any other alterations shall be made only with prior written authorization of Elsevier Ltd. (Please contact Elsevier at permissions@elsevier.com)

6. If the permission fee for the requested use of our material is waived in this instance, please be advised that your future requests for Elsevier materials may attract a fee.

7. Reservation of Rights: Publisher reserves all rights not specifically granted in the combination of (i) the license details provided by you and accepted in the course of this licensing transaction, (ii) these terms and conditions and (iii) CCC's Billing and Payment terms and conditions.

8. License Contingent Upon Payment: While you may exercise the rights licensed immediately upon issuance of the license at the end of the licensing process for the transaction, provided that you have disclosed complete and accurate details of your proposed use, no license is finally effective unless and until full payment is received from you (either by publisher or by CCC) as provided in CCC's Billing and Payment terms and conditions. If full payment is not received on a timely basis, then any license preliminarily granted shall be deemed automatically revoked and shall be void as if never granted. Further, in the event that you breach any of these terms and conditions or any of CCC's Billing and Payment terms and conditions, the license is automatically revoked and shall be void as if never granted. Use of materials as described in a revoked license, as well as any use of the materials beyond the scope of an unrevoked license, may constitute copyright infringement and publisher reserves the right to take any and all action to protect its copyright in the materials.

9. Warranties: Publisher makes no representations or warranties with respect to the licensed material.

10. Indemnity: You hereby indemnify and agree to hold harmless publisher and CCC, and their respective officers, directors, employees and agents, from and against any and all claims arising out of your use of the licensed material other than as specifically authorized pursuant to this license.

11. No Transfer of License: This license is personal to you and may not be sublicensed, assigned, or transferred by you to any other person without publisher's written permission.

12. No Amendment Except in Writing: This license may not be amended except in a writing signed by both parties (or, in the case of publisher, by CCC on publisher's behalf).

13. Objection to Contrary Terms: Publisher hereby objects to any terms contained in any purchase order, acknowledgment, check endorsement or other writing prepared by you, which terms are inconsistent with these terms and conditions or CCC's Billing and Payment terms and conditions. These terms and conditions, together with CCC's Billing and Payment terms and conditions (which are incorporated herein), comprise the entire agreement between you and publisher (and CCC) concerning this licensing transaction. In the event of any conflict between your obligations established by these terms and conditions and those established by CCC's Billing and Payment terms and conditions, these terms and conditions shall control.

14. Revocation: Elsevier or Copyright Clearance Center may deny the permissions described in this License at their sole discretion, for any reason or no reason, with a full refund payable to you. Notice of such denial will be made using the contact information provided by you. Failure to receive such notice will not alter or invalidate the denial. In no event will Elsevier or Copyright Clearance Center be responsible or liable for any costs, expenses or damage incurred by you as a result of a denial of your permission request, other than a refund of the amount(s) paid by you to Elsevier and/or Copyright Clearance Center for denied permissions.

LIMITED LICENSE

The following terms and conditions apply only to specific license types:

15. **Translation**: This permission is granted for non-exclusive world **English** rights only unless your license was granted for translation rights. If you licensed translation rights you may only translate this content into the languages you requested. A professional translator must perform all translations and reproduce the content word for word preserving the integrity of the article. If this license is to re-use 1 or 2 figures then permission is granted for non-exclusive world rights in all languages.

16. **Website**: The following terms and conditions apply to electronic reserve and author websites:
Electronic reserve: If licensed material is to be posted to website, the web site is to be password-protected and made available only to bona fide students registered on a relevant course if:
This license was made in connection with a course,
This permission is granted for 1 year only. You may obtain a license for future website posting,
All content posted to the web site must maintain the copyright information line on the bottom of each image,
A hyper-text must be included to the Homepage of the journal from which you are licensing at http://www.sciencedirect.com/science/journal/xxxxx or the Elsevier homepage for books at http://www.elsevier.com , and
Central Storage: This license does not include permission for a scanned version of the material to be stored in a central repository such as that provided by Heron/XanEdu.

17. **Author website** for journals with the following additional clauses:

All content posted to the web site must maintain the copyright information line on the bottom of each image, and the permission granted is limited to the personal version of your paper. You are not allowed to download and post the published electronic version of your article (whether PDF or HTML, proof or final version), nor may you scan the printed edition to create an electronic version. A hyper-text must be included to the Homepage of the journal from which you are licensing at http://www.sciencedirect.com/science/journal/xxxxx . As part of our normal production process, you will receive an e-mail notice when your article appears on Elsevier's online service ScienceDirect (www.sciencedirect.com). That e-mail will include the article's Digital Object Identifier (DOI). This number provides the electronic link to the published article and should be included in the posting of your personal version. We ask that you wait until you receive this e-mail and have the DOI to do any posting.

Central Storage: This license does not include permission for a scanned version of the material to be stored in a central repository such as that provided by Heron/XanEdu.

18. **Author website** for books with the following additional clauses:
Authors are permitted to place a brief summary of their work online only.
A hyper-text must be included to the Elsevier homepage at http://www.elsevier.com . All content posted to the web site must maintain the copyright information line on the bottom of each image. You are not allowed to download and post the published electronic version of your chapter, nor may you scan the printed edition to create an electronic version.

Central Storage: This license does not include permission for a scanned version of the material to be stored in a central repository such as that provided by Heron/XanEdu.

19. **Website** (regular and for author): A hyper-text must be included to the Homepage of the journal from which you are licensing at http://www.sciencedirect.com/science/journal/xxxxx. or for books to the Elsevier homepage at http://www.elsevier.com

20. **Thesis/Dissertation**: If your license is for use in a thesis/dissertation your thesis may be submitted to your institution in either print or electronic form. Should your thesis be published commercially, please reapply for permission. These requirements include permission for the Library and Archives of Canada to supply single copies, on demand, of the complete thesis and include permission for UMI to supply single copies, on demand, of the complete thesis. Should your thesis be published commercially, please reapply for permission.

21. **Other Conditions**:

v1.6

Chapter 4 Low friction and environmentally stable diamond-like carbon (DLC) coatings incorporating silicon, oxygen and fluorine sliding against aluminum

Supplier	Elsevier Limited The Boulevard,Langford Lane Kidlington,Oxford,OX5 1GB,UK
Registered Company Number	1982084
Customer name	Fatih Sen
Customer address	Materials Engineering, MAME
	Windsor, ON N9B 3P4
License number	3120060798057
License date	Apr 01, 2013
Licensed content publisher	Elsevier
Licensed content publication	Surface and Coatings Technology
Licensed content title	Low friction and environmentally stable diamond-like carbon (DLC) coatings incorporating silicon, oxygen and fluorine sliding against aluminum
Licensed content author	F.G. Sen,X. Meng-Burany,M.J. Lukitsch,Y. Qi,A.T. Alpas
Licensed content date	25 January 2013
Licensed content volume number	215
Licensed content issue number	
Number of pages	10
Start Page	340
End Page	349
Type of Use	reuse in a thesis/dissertation
Intended publisher of new work	other
Portion	full article
Format	both print and electronic
Are you the author of this	Yes

6. If the permission fee for the requested use of our material is waived in this instance, please be advised that your future requests for Elsevier materials may attract a fee.

7. Reservation of Rights: Publisher reserves all rights not specifically granted in the combination of (i) the license details provided by you and accepted in the course of this licensing transaction, (ii) these terms and conditions and (iii) CCC's Billing and Payment terms and conditions.

8. License Contingent Upon Payment: While you may exercise the rights licensed immediately upon issuance of the license at the end of the licensing process for the transaction, provided that you have disclosed complete and accurate details of your proposed use, no license is finally effective unless and until full payment is received from you (either by publisher or by CCC) as provided in CCC's Billing and Payment terms and conditions. If full payment is not received on a timely basis, then any license preliminarily granted shall be deemed automatically revoked and shall be void as if never granted. Further, in the event that you breach any of these terms and conditions or any of CCC's Billing and Payment terms and conditions, the license is automatically revoked and shall be void as if never granted. Use of materials as described in a revoked license, as well as any use of the materials beyond the scope of an unrevoked license, may constitute copyright infringement and publisher reserves the right to take any and all action to protect its copyright in the materials.

9. Warranties: Publisher makes no representations or warranties with respect to the licensed material.

10. Indemnity: You hereby indemnify and agree to hold harmless publisher and CCC, and their respective officers, directors, employees and agents, from and against any and all claims arising out of your use of the licensed material other than as specifically authorized pursuant to this license.

11. No Transfer of License: This license is personal to you and may not be sublicensed, assigned, or transferred by you to any other person without publisher's written permission.

12. No Amendment Except in Writing: This license may not be amended except in a writing signed by both parties (or, in the case of publisher, by CCC on publisher's behalf).

13. Objection to Contrary Terms: Publisher hereby objects to any terms contained in any purchase order, acknowledgment, check endorsement or other writing prepared by you, which terms are inconsistent with these terms and conditions or CCC's Billing and Payment terms and conditions. These terms and conditions, together with CCC's Billing and Payment terms and conditions (which are incorporated herein), comprise the entire agreement between you and publisher (and CCC) concerning this licensing transaction. In the event of any conflict between your obligations established by these terms and conditions and those established by CCC's Billing and Payment terms and conditions, these terms and conditions shall control.

14. Revocation: Elsevier or Copyright Clearance Center may deny the permissions described in this License at their sole discretion, for any reason or no reason, with a full refund payable to you. Notice of such denial will be made using the contact information provided by you. Failure to receive such notice will not alter or invalidate the denial. In no event will Elsevier or Copyright Clearance Center be responsible or liable for any costs, expenses or damage incurred by you as a result of a denial of your permission request, other than a refund of the amount(s) paid by you to

Elsevier and/or Copyright Clearance Center for denied permissions.

LIMITED LICENSE

The following terms and conditions apply only to specific license types:

15. **Translation**: This permission is granted for non-exclusive world **English** rights only unless your license was granted for translation rights. If you licensed translation rights you may only translate this content into the languages you requested. A professional translator must perform all translations and reproduce the content word for word preserving the integrity of the article. If this license is to re-use 1 or 2 figures then permission is granted for non-exclusive world rights in all languages.

16. **Website**: The following terms and conditions apply to electronic reserve and author websites:
Electronic reserve: If licensed material is to be posted to website, the web site is to be password-protected and made available only to bona fide students registered on a relevant course if:
This license was made in connection with a course,
This permission is granted for 1 year only. You may obtain a license for future website posting,
All content posted to the web site must maintain the copyright information line on the bottom of each image,
A hyper-text must be included to the Homepage of the journal from which you are licensing at http://www.sciencedirect.com/science/journal/xxxxx or the Elsevier homepage for books at http://www.elsevier.com , and
Central Storage: This license does not include permission for a scanned version of the material to be stored in a central repository such as that provided by Heron/XanEdu.

17. **Author website** for journals with the following additional clauses:

All content posted to the web site must maintain the copyright information line on the bottom of each image, and the permission granted is limited to the personal version of your paper. You are not allowed to download and post the published electronic version of your article (whether PDF or HTML, proof or final version), nor may you scan the printed edition to create an electronic version. A hyper-text must be included to the Homepage of the journal from which you are licensing at http://www.sciencedirect.com/science/journal/xxxxx . As part of our normal production process, you will receive an e-mail notice when your article appears on Elsevier's online service ScienceDirect (www.sciencedirect.com). That e-mail will include the article's Digital Object Identifier (DOI). This number provides the electronic link to the published article and should be included in the posting of your personal version. We ask that you wait until you receive this e-mail and have the DOI to do any posting.

Central Storage: This license does not include permission for a scanned version of the material to be stored in a central repository such as that provided by Heron/XanEdu.

18. **Author website** for books with the following additional clauses:
Authors are permitted to place a brief summary of their work online only.
A hyper-text must be included to the Elsevier homepage at http://www.elsevier.com . All content

posted to the web site must maintain the copyright information line on the bottom of each image. You are not allowed to download and post the published electronic version of your chapter, nor may you scan the printed edition to create an electronic version.

Central Storage: This license does not include permission for a scanned version of the material to be stored in a central repository such as that provided by Heron/XanEdu.

19. **Website** (regular and for author): A hyper-text must be included to the Homepage of the journal from which you are licensing at http://www.sciencedirect.com/science/journal/xxxxx. or for books to the Elsevier homepage at http://www.elsevier.com

20. **Thesis/Dissertation**: If your license is for use in a thesis/dissertation your thesis may be submitted to your institution in either print or electronic form. Should your thesis be published commercially, please reapply for permission. These requirements include permission for the Library and Archives of Canada to supply single copies, on demand, of the complete thesis and include permission for UMI to supply single copies, on demand, of the complete thesis. Should your thesis be published commercially, please reapply for permission.

21. **Other Conditions**:

Chapter 5 Oxidation induced softening in Al nanowires

License Number	3120060942337
Order Date	Apr 01, 2013
Publisher	American Institute of Physics
Publication	Applied Physics Letters
Article Title	Oxidation induced softening in Al nanowires
Author	Fatih G. Sen, Yue Qi, Adri C. T. van Duin, Ahmet T. Alpas et al.
Online Publication Date	Feb 7, 2013
Volume number	102
Issue number	5
Type of Use	Thesis/Dissertation
Requestor type	Author (original article)
Format	Print and electronic
Portion	Excerpt (> 800 words)
Will you be translating?	No
Title of your thesis / dissertation	Atomistic Simulations to Micro-Mechanisms of Adhesion in Automotive Applications
Expected completion date	Jun 2013
Estimated size (number of pages)	300
Total	0.00 USD

does not hold copyright.

3. You may not alter or modify the Material in any manner. You may translate the Material into another language only if you have licensed translation rights. You may not use the Material for promotional purposes. AIP reserves all rights not specifically granted herein.

4. The foregoing license shall not take effect unless and until AIP or its agent, Copyright Clearance Center, receives the Payment in accordance with Copyright Clearance Center Billing and Payment Terms and Conditions, which are incorporated herein by reference.

5. AIP or the Copyright Clearance Center may, within two business days of granting this license, revoke the license for any reason whatsoever, with a full refund payable to you. Should you violate the terms of this license at any time, AIP, American Institute of Physics, or Copyright Clearance Center may revoke the license with no refund to you. Notice of such revocation will be made using the contact information provided by you. Failure to receive such notice will not nullify the revocation.

6. AIP makes no representations or warranties with respect to the Material. You agree to indemnify and hold harmless AIP, American Institute of Physics, and their officers, directors, employees or agents from and against any and all claims arising out of your use of the Material other than as specifically authorized herein.

7. The permission granted herein is personal to you and is not transferable or assignable without the prior written permission of AIP. This license may not be amended except in a writing signed by the party to be charged.

8. If purchase orders, acknowledgments or check endorsements are issued on any forms containing terms and conditions which are inconsistent with these provisions, such inconsistent terms and conditions shall be of no force and effect. This document, including the CCC Billing and Payment Terms and Conditions, shall be the entire agreement between the parties relating to the subject matter hereof.

This Agreement shall be governed by and construed in accordance with the laws of the State of New York. Both parties hereby submit to the jurisdiction of the courts of New York County for purposes of resolving any disputes that may arise hereunder.

VITA AUCTORIS

Name: Fatih Gurcag Sen

Birth place and year: Ankara, Turkey, 1981

EDUCATION

Ph. D. Engineering Materials, University of Windsor, 2007-2013

M.Sc. Metallurgical and Materials Engineering, Middle East Technical University, 2003-2006

B.Sc. Metallurgical and Materials Engineering, Middle East Technical University, 1999-2003

REFEREED JOURNAL ARTICLES

1. F.G. Sen, Y. Qi, A.C.T. Van Duin, A.T. Alpas, "Oxidation induced softening in Al nanowires", *Applied Physics Letters* 102 (2013) 051912.

2. F.G. Sen, X. Meng-Burany, M. Lukitsch, Y. Qi, A.T. Alpas, "Low friction and environmentally stable diamond-like carbon (DLC) coatings incorporating Si and F sliding against aluminum", *Surface and Coatings Technology* 215 (2013) 340.

3. F.G. Sen, Y. Qi, A.T. Alpas, "Tribology of fluorinated diamond-like carbon coatings: first principles calculations and sliding experiments", *Lubrication Science*, 25 (2012) 111.

4. F.G. Sen, Y. Qi, A.T. Alpas, "Anchoring Pt on graphene using metallic adatoms: A first principles investigation", *Journal of Physics Condensed Matter* 24 (2012) 225003. Featured as "IOP Select".

5. F.G. Sen, Y. Qi, A.T. Alpas, "Material transfer mechanisms between aluminum and fluorinated carbon interfaces", *Acta Materialia*, 59 (2011) 2601.

6. M. Shafiei, A.R. Riahi, F.G. Sen, A.T. Alpas, "Improvement of platinum adhesion to carbon surfaces using PVD coatings", *Surface and Coatings Technology* 205 (2010) 306.

7. F.G. Sen, Y. Qi, A.T. Alpas, "Surface stability and electronic structure of hydrogen and fluorine terminated diamond surfaces: a first principles investigation", *Journal of Materials Research* 24 (2009) 2461, Featured as "Outstanding Symposium Paper".

8. F.G. Sen, M. K. Aydinol, "Atomistic simulation of self-diffusion in Al and Al Alloys under electromigration conditions", *Journal of Applied Physics*, 104 (2008) 073510.

9. F.G. Sen, M.K. Aydinol, "Non-Equilibrium Molecular Dynamics Simulation of Electromigration in Aluminum Based Metallic Interconnects", *Turkish Journal of Engineering and Environmental Sciences*, 30 (2006) 387.

CONFERENCE PROCEEDINGS AND PRESENTATIONS

1. F.G. Sen, X. Meng-Burany, M. Lukitsch, Y. Qi, A.T. Alpas, "Friction and adhesion of Si and F incorporating diamond-like-carbon (DLC) coatings sliding against aluminum", *39th International Conference on Metallurgical Coatings and Thin Films (ICMCTF-2012)*, San Diego, CA (2012).

2. F.G. Sen, Y.Qi, A.C.T van Duin, A.T. Alpas, "Deformation of Al nanowires in an oxygen environment" *Materials Research Society Fall 2011 Meeting*, Boston, MA (2011).

3. F.G. Sen, Y.Qi, A.T. Alpas, "Tribology of fluorinated diamond-like carbon coatings", *6th Symposium on Functional Coatings and Surface Engineering (FCSE-2011)*, Montreal, QC (2011).

4. F.G. Sen, Y.Qi, A.T. Alpas, "Anchoring platinum on graphene using metallic adatoms", *American Physical Society March 2011 Meeting*, Dallas, TX (2011).

5. F.G. Sen, Y.Qi, A.T. Alpas, "Tribology of fluorinated diamond-like carbon coatings: first principles calculations and sliding experiments", *First International Brazilian Conference on Tribology TriboBr-2010*, Rio de Janeiro (2010).

6. F.G. Sen, Y. Qi, A.T. Alpas, "Improvement of the Pt/graphene interface adhesion by metallic adatoms for fuel cell applications", *Materials Research Society Fall 2009 Meeting*, Boston, MA (2009).

7. F. G. Sen, Y. Qi, A.T. Alpas, "Adhesion and Friction between Fluorinated Diamond-like Carbon Coatings and Aluminum", EUROMAT 2009, Glasgow, UK (2009).

8. F.G. Sen, Y. Qi, A.T. Alpas, "Surface stability and electronic structure of hydrogen and fluorine terminated diamond surfaces: a first principles investigation", *Materials Research Society Fall 2008 Meeting*, Boston, MA (2008).

9. F.G. Sen, A. Kinaci, M.K. Aydinol, "Effect of Alloying Elements on the Formation of FeTiH4: An Ab initio Study", *Proceedings X. International Conference Hydrogen Materials Science and Chemistry of Carbon Nanomaterials*, Crimea, Ukraine (2007).

10. F.G. Sen, M.K. Aydinol, "Molecular Dynamics of Electromigration in Aluminum and

Its Alloys", *Proceedings 13th International Metallurgy-Materials Congress and Exhibition*, Istanbul, Turkey (2006).

11. F.G. Sen, M.K. Aydinol, "Investigation of Electromigration Forces in Metals", *Proceedings 12th International Metallurgy-Materials Congress and Exhibition*, Istanbul, Turkey (2005).

12. F.G. Sen, M.K. Aydinol, "First principles study of C14 type Laves phase CaMg2 hydrides", *Proceedings International Hydrogen Energy Congress and Exhibition IHEC 2005*, Istanbul, Turkey (2005).

BOOK CHAPTERS, REPORTS AND THESIS

1. F.G. Sen, X. Meng-Burany, M. Lukitsch, Y. Qi, A.T. Alpas, "A new diamond-like carbon coating with humidity independent low friction against aluminum alloys", *General Motors Collaborative Report*, (March, 2012).

2. H. Guo, Y. Qi, F. G. Sen, A. Abou Gharam, M.J. Lukitsch, A.T. Alpas, "The effect of oxygen on adhesion, adhesive transfer and friction of carbon coatings", *General Motors Collaborative Report* CL-11/202/CML, (August, 2011).

3. F.G. Sen, Y. Qi, A.T. Alpas, "Anchoring Pt catalyst on graphene by metallic adatoms", *General Motors Collaborative Report*, (November, 2010).

4. F.G. Sen, Y. Qi, A.T. Alpas, "Adhesion of aluminum to fluorinated diamond-like carbon coatings", *General Motors Collaborative Report*, (April, 2010).

5. F.G. Sen, A. Kinaci, M.K. Aydinol, "Effect of Alloying Elements on the Formation of FeTiH4: an Ab Initio Study" in book ed. by B. Baranowski et al. *Carbon Nanomaterials in Clean Energy Hydrogen Systems*, p573-578 Springer, Netherlands (2009).

6. F.G. Sen, Y. Qi, A.T. Alpas, "Surface stability and electronic structure of hydrogen and fluorine terminated diamond surfaces: a first principles investigation", *General Motors Collaborative Report* (November 2008).

7. F.G. Sen, "Non-Equilibrium Molecular Dynamics of Electromigration in Aluminum and Its Alloys", *M.Sc. Thesis*, September 2006, supervisor: Prof. Dr. M. Kadri Aydinol.